

A Search for Supersymmetry in Multi-*b* Jet Events with the ATLAS Detector

by

Matthew Epland

Department of Physics
Duke University

Date: _____
Approved:

Ayana T. Arce, Supervisor

Steffen A. Bass

Alfred T. Goshaw

Mark C. Kruse

Roxanne P. Springer

Dissertation submitted in partial fulfillment of the requirements for the degree of
Doctor of Philosophy in the Department of Physics
in the Graduate School of Duke University
2019

ABSTRACT

A Search for Supersymmetry in Multi-*b* Jet Events with the ATLAS Detector

by

Matthew Epland

Department of Physics
Duke University

Date: _____

Approved:

Ayana T. Arce, Supervisor

Steffen A. Bass

Alfred T. Goshaw

Mark C. Kruse

Roxanne P. Springer

An abstract of a dissertation submitted in partial fulfillment of the requirements for
the degree of Doctor of Philosophy in the Department of Physics
in the Graduate School of Duke University
2019

Copyright © 2019 by Matthew Epland
All rights reserved

Abstract

A search for supersymmetry in pair-produced gluinos decaying via top squarks to the lightest neutralino is presented. Events with multiple hadronic jets, of which at least three must be identified as originating from b -quarks, and large amounts of missing transverse energy in the final state, are selected for study. The dataset utilized encompasses proton–proton collisions with a center-of-mass energy of $\sqrt{s} = 13\text{ TeV}$ and integrated luminosity of 79.9 fb^{-1} collected by the ATLAS experiment at the LHC from 2015 to 2017. The search employs a parameterized boosted decision tree (BDT) to separate supersymmetric signal events from standard model backgrounds. New methods for optimal BDT parameter point selection and signal region creation, as well as new soft kinematic variables, are exploited to increase the search’s expected exclusion limit beyond prior analyses of the same dataset by 100–200 GeV in the gluino and neutralino mass plane. No excess is observed in data above the predicted background, extending the previous exclusion limit at the 95 % confidence level by 250 GeV to approximately 1.4 TeV in neutralino mass. The analytical and machine learning techniques developed here will benefit future analysis of additional Run 2 data from 2018.

To my loving wife

Contents

Abstract	iv
List of Tables	xi
List of Figures	xii
List of Symbols and Abbreviations	xix
Acknowledgements	xxiii
Preface	xxv
1 Introduction	1
2 Theory	5
2.1 The Standard Model	5
2.1.1 Electroweak Interaction (EW)	7
2.1.2 Electroweak Symmetry Breaking (EWSB)	12
2.1.3 Strong Interaction: Quantum Chromodynamics (QCD)	15
2.1.4 Decay of the Top Quark	20
2.1.5 Shortcomings	22
2.2 Supersymmetry (SUSY)	24
2.2.1 The Wess-Zumino Model (WZM)	26
2.2.2 Soft SUSY Breaking and Naturalness	27
2.2.3 The Minimal Supersymmetric Standard Model (MSSM)	28
2.2.4 <i>R</i> -Parity	31

2.2.5	Gauge Coupling Unification	32
2.2.6	Simplified SUSY Models	33
3	The LHC and ATLAS Experiment	37
3.1	The Large Hadron Collider (LHC)	37
3.1.1	Luminosity	39
3.1.2	Pileup	40
3.2	The ATLAS experiment	41
3.2.1	Coordinate System	42
3.2.2	Inner Detector (ID)	44
3.2.3	Calorimeters	48
3.2.4	Muon Spectrometer (MS)	54
3.2.5	Trigger and Data Acquisition System (TDAQ)	56
4	Analysis Methods	60
4.1	Reconstructing Physics Objects	60
4.1.1	Tracks and Vertices	60
4.1.2	Jets	62
4.1.3	b -Tagging	64
4.1.4	Missing Transverse Energy	66
4.2	Jet Calibrations and Uncertainties	68
4.3	Boosted Decision Trees (BDT)	72
4.3.1	XGBOOST	77
4.3.2	Gain	77
4.4	Statistical Methods	78
4.4.1	Significance	78
4.4.2	Optimizing Significance	79

4.4.3	HISTFITTER	80
4.4.4	Likelihood Function	83
4.4.5	Profile-Likelihood Fit	83
5	The Multi-<i>b</i> Search	86
5.1	Signal and Background Samples	86
5.2	Physics Objects	87
5.2.1	Variables	89
5.3	Event Selection	92
5.4	BDT Analysis	93
5.4.1	Input Variable Selection	94
5.4.2	Hyperparameter Tuning	96
5.4.3	BDT Training	96
5.5	Parameter Point Selection	97
5.6	Control, Validation, and Signal Regions Selection	100
5.6.1	Fit Region Background Compositions	103
5.7	Uncertainties	105
5.7.1	Experimental Systematics	105
5.7.2	Theoretical Systematics	106
5.7.3	Statistical Uncertainties, Combining Uncertainties, Nuisance Parameters	108
5.8	Fit Construction	108
5.9	Results	112
5.9.1	Background Fits	112
5.9.2	Exclusion Fits	113
6	Conclusions	119

A Supplementary Multi-<i>b</i> Plots	121
A.1 Preselection Efficiency Studies	121
A.2 Input Variable Selection	125
A.3 Hyperparameter Tuning	128
A.4 Parameter Point Selection	129
A.5 Control, Validation, and Signal Regions Selection	133
A.6 Uncertainties	137
A.6.1 Uncertainty Tables	138
A.6.2 Fitted Nuisance Parameters	148
A.7 Fit Construction	154
A.8 Results	156
A.8.1 Individual Exclusion Limits	159
A.8.2 Event Yields	161
A.8.3 Expectation Limit Changes When Unblinding	168
A.9 Overfitting Studies	169
A.10 Input Variables	174
B Maximum Performance Studies	179
C The Look Elsewhere Effect	182
D Pseudocode	184
D.1 Z_B	184
D.2 Optimized \hat{y} Threshold	185
E In Situ γ+Jet Calibration	186
E.1 In Situ γ +Jet Calibration	186
E.1.1 Event Selection	188
E.1.2 Photon Purity Correction	189

E.1.3	Systematic Uncertainties	190
E.1.4	Results	192
E.2	<i>In Situ</i> Combination	193
E.3	Re-clustered Jet Studies	194
	Bibliography	197
	Biography	218

List of Tables

2.1	The fundamental interactions of nature and their properties. Adapted from [15].	7
2.2	MSSM fields and their quantum numbers. Adapted from [20].	29
2.3	MSSM sparticle gauge and mass eigenstates. Adapted from [62].	31
5.1	List of generators used for each simulated processes, adapted from [4].	88
5.2	Selected fit region definitions.	110
A.1	Uncertainties on background estimates in Gtt_0L_0_Gtt_1L_0.	139
A.2	Uncertainties on background estimates in Gtt_0L_1_Gtt_1L_0.	141
A.3	Uncertainties on background estimates in Gtt_0L_1_Gtt_1L_2.	143
A.4	Uncertainties on background estimates in Gtt_0L_3_Gtt_1L_2.	145
A.5	Uncertainties on background estimates in Gtt_0L_3_Gtt_1L_3.	147
A.6	Event yields for Gtt_0L_0.	162
A.7	Event yields for Gtt_0L_1.	163
A.8	Event yields for Gtt_0L_3.	164
A.9	Event yields for Gtt_1L_0.	165
A.10	Event yields for Gtt_1L_2.	166
A.11	Event yields for Gtt_1L_3.	167
A.12	5-fold cross-validation results.	170
E.1	γ +jet selections.	188
E.2	γ +jet systematic variation values.	192

List of Figures

1.1	Possible SUSY particle mass limits set by ATLAS [3].	3
1.2	ATLAS gluino to $t\bar{t}$ plus neutralino exclusion limits [3] from the multi- b [4, 11] and same sign lepton searches.	4
2.1	SM total production cross sections as measured by ATLAS compared to theoretical predictions [13].	6
2.2	The particles of the SM and their properties. Adapted from [16]. . .	8
2.3	Principal EW vertices. Adapted from [21].	11
2.4	Higgs potential $V_H(\phi^{(0)})$ of a single complex scalar Higgs field $\phi^{(0)}$. Adapted from [25].	13
2.5	Principal QCD vertices, adapted from [38].	16
2.6	Hadronization in a simulated hadron-hadron collision [42].	19
2.7	NNPDF3.1 NNLO PDFs [56].	21
2.8	Hadronic $t \rightarrow q\bar{q}b$ and leptonic $t \rightarrow l^+\nu_l b$ decays of the top quark. . .	22
2.9	Rotation curve of the NGC 3198 galaxy [61].	23
2.10	First order loop contributions to the Higgs squared mass correction Δm_H^2 for a fermion f and scalar S	24
2.11	Running of the inverse gauge couplings in the SM and MSSM. Adapted from [62].	33
2.12	Example diagram of \tilde{t} mass corrections due to a \tilde{g} loop.	34
2.13	NNLO _{Approx} +NNLL \tilde{q} and \tilde{g} production cross sections at the LHC [90].	35
2.14	Two potential mass orderings for the simplified SUSY model corresponding to on and off-shell \tilde{t} decays.	36

2.15	Feynman diagrams of $\tilde{g} \rightarrow \tilde{t}\tilde{t}_1 \rightarrow t\bar{t}\tilde{\chi}_1^0$ decay in a simplified SUSY model.	36
3.1	An overview of the LHC in relation to the surrounding geography [92].	38
3.2	A schematic view of the CERN accelerator complex [93].	38
3.3	The mean number of interactions per crossing in ATLAS [95].	40
3.4	A schematic representation of the ATLAS sub-detectors [98].	42
3.5	Coordinate system of the ATLAS detector. Image of ATLAS from [99].	43
3.6	The ATLAS inner detector [100].	45
3.7	Simplified operating schematic of a semiconductor detector.	45
3.8	Illustration of track measurements in the ATLAS TRT [110].	47
3.9	ATLAS ID endcaps [96].	48
3.10	The ATLAS calorimeter system [116].	49
3.11	ATLAS ECAL barrel geometry [96].	52
3.12	Illustrative sketches of EM showers in matter [115].	52
3.13	ATLAS HCAL tile barrel geometry [96].	53
3.14	Sketch of a hadronic shower in a calorimeter. Adapted from [115, 117].	53
3.15	The ATLAS Muon Spectrometer (MS) [121].	55
3.16	Cross sectional schematic of the ATLAS MS in the zy -plane [122].	57
3.17	Schematics of the MS monitored drift tubes (MDT) [96].	57
3.18	ATLAS trigger and data acquisition system (TDAQ) for Run 2 [125].	58
3.19	Illustration of the e, γ , and τ sliding window trigger algorithms [96].	59
4.1	Example reconstruction of tracks from hits in the ID [127].	61
4.2	ATLAS track transverse impact parameter d_0 and longitudinal impact parameter z_0 [131].	62
4.3	An illustration of the anti- k_t algorithm with $R = 1$ [132].	64
4.4	Signed impact parameter significances for $Z \rightarrow \mu\mu + \text{jets}$ events [139].	66
4.5	MV2c10 BDT output on simulated $t\bar{t}$ events [138].	67

4.6	The calibration sequence for small- R jets [143].	69
4.7	Average jet energy response of MC small- R jets at different p_T and η values [143].	69
4.8	Combination of small- R jet <i>in situ</i> JES calibrations [143].	71
4.9	Systematic uncertainties on the combined small- R JES calibration [143].	72
4.10	The JER and its uncertainty for small- R jets [147].	73
4.11	Simple classification and regression tree (CART).	75
4.12	Example receiver operating characteristic (ROC) curve.	80
4.13	Overview of a typical HISTFITTER analysis in terms of fit regions [164].	81
5.1	Construction of $H_T^{\text{leptons} + \text{soft jets}}$ Obfuscated.	91
5.2	Input variables used by the BDT in order of relative gain across all mass points.	95
5.3	Graph of mass parameter points and Louvain communities in the 0L channel.	99
5.4	Positions of representative parameter points in the 0L and 1L channel.	101
5.5	Smoothed S/B and S/\sqrt{B} for the parameter point P1L_0.	103
5.6	Fit region background compositions for parameter point P1L_0.	104
5.7	Event-driven theory systematic uncertainties for $t\bar{t}$ and single-top.	109
5.8	Relative uncertainties per SR.	111
5.9	Gtt_0L_0_Gtt_1L_0 fitted nuisance parameters at different levels of unblinding.	112
5.10	Control region fits.	113
5.11	Validation region fits.	114
5.12	Signal region fits.	115
5.13	Observed and expected exclusion limits for the 79.9 fb^{-1} BDT analysis.	116
5.14	Comparison of the expected and observed exclusion limits for the BDT analysis and standard 79.8 fb^{-1} result [4].	117

5.15 Observed CL_s and cross section limits for the 79.9 fb^{-1} BDT analysis.	118
A.1 Gtt signal efficiency of the full preselection.	121
A.2 Gtt signal efficiency of the E_T^{miss} trigger preselection.	122
A.3 Gtt signal efficiency of the $N_{\text{jet}} \geq 4$ preselection.	122
A.4 Gtt signal efficiency of the $N_{b\text{-jet}} \geq 3$ preselection.	123
A.5 Gtt signal efficiency of the $E_T^{\text{miss}} \geq 200 \text{ GeV}$ preselection.	123
A.6 Gtt signal efficiency of the $p_T^{\text{jet}1} > 30 \text{ GeV}$ preselection.	124
A.7 Gtt signal efficiency of the 0L $\Delta\phi_{\min}^{4j} > 0.4$ preselection.	124
A.8 BDT performance measured via mean Z_B on selected mass points during the iterative input variable selection process.	125
A.9 BDT performance measured via ROC AUC during the iterative input variable selection process.	125
A.10 Selected mass points for use in computing mean Z_B in the input variable selection and hyperparameter tuning processes.	126
A.11 Change in input variable gain when comparing the BDT over all signal parameter points to individual compressed and boosted points.	127
A.12 BDT performance during the Bayesian optimization of hyperparameters.	128
A.13 Graph of mass parameter points and Louvain communities in the 1L channel.	129
A.14 Graph of mass parameter points and Louvain communities in the 0L channel.	130
A.15 Graph of mass parameter points and Louvain communities in the 1L channel.	130
A.16 Graph of mass parameter points and Louvain communities in the 0L channel, when W_{ij} is only a function of the RMSD, <i>i.e.</i> $b = 0$.	131
A.17 Graph of mass parameter points and Louvain communities in the 0L channel, when W_{ij} is only a function of the radius in mass space.	131
A.18 Graph of mass parameter points and Louvain communities in the 0L channel, when W_{ij} is only a function of the RMSD, $b = 0$.	132

A.19 Graph of mass parameter points and Louvain communities in the 0L channel, when W_{ij} is only a function of the radius in mass space. . . .	132
A.20 Change in Gtt event weight per mass point after reweighting the production cross section to match 36.1 fb^{-1} exclusion limits [5]. . . .	133
A.21 Smoothed S/B & S/\sqrt{B} , and background composition for P0L_0. . .	134
A.22 Smoothed S/B & S/\sqrt{B} , and background composition for P0L_1. . .	134
A.23 Smoothed S/B & S/\sqrt{B} , and background composition for P0L_3. . .	135
A.24 Smoothed S/B & S/\sqrt{B} , and background composition for P1L_0. . .	135
A.25 Smoothed S/B & S/\sqrt{B} , and background composition for P1L_2. . .	136
A.26 Smoothed S/B & S/\sqrt{B} , and background composition for P1L_3. . .	136
A.27 $t\bar{t}$ generator theory systematic validation study.	137
A.28 Initial event-driven theory systematic uncertainties for $t\bar{t}$ and single-top.	138
A.29 Gtt_0L_0_Gtt_1L_0 fitted nuisance parameters.	149
A.30 Gtt_0L_1_Gtt_1L_0 fitted nuisance parameters.	150
A.31 Gtt_0L_1_Gtt_1L_2 fitted nuisance parameters.	151
A.32 Gtt_0L_3_Gtt_1L_2 fitted nuisance parameters.	152
A.33 Gtt_0L_3_Gtt_1L_3 fitted nuisance parameters.	153
A.34 Location of parameter points used in the final fit.	154
A.35 Individual expected exclusion limits per lepton channel combination.	155
A.36 Expected cross section limits for the 79.9 fb^{-1} BDT analysis. . . .	156
A.37 Validation regions before and after the $t\bar{t}$ normalizations are applied.	157
A.38 Observed and expected exclusion limits from the standard 79.8 fb^{-1} multi- b analysis [4]. .	158
A.39 Observed and expected exclusion limits for Gtt_0L_0_Gtt_1L_0. . .	159
A.40 Observed and expected exclusion limits for Gtt_0L_1_Gtt_1L_0. . .	159
A.41 Observed and expected exclusion limits for Gtt_0L_1_Gtt_1L_2. . .	160
A.42 Observed and expected exclusion limits for Gtt_0L_3_Gtt_1L_2. . .	160

A.43 Observed and expected exclusion limits for Gtt_0L_3_Gtt_1L_3. . .	161
A.44 Expected exclusion limits with blinded and unblinded SRs.	168
A.45 Change in the expected exclusion limit between the train and test sets.	169
A.46 Comparison of \hat{y} in the test and train sets for Gtt_0L_0.	171
A.47 Comparison of \hat{y} in the test and train sets for Gtt_0L_1.	171
A.48 Comparison of \hat{y} in the test and train sets for Gtt_0L_3.	172
A.49 Comparison of \hat{y} in the test and train sets for Gtt_1L_0.	172
A.50 Comparison of \hat{y} in the test and train sets for Gtt_1L_2.	173
A.51 Comparison of \hat{y} in the test and train sets for Gtt_1L_3.	173
A.52 $N_{\text{jet}}(p_T > 30 \text{ GeV}, \eta < 1.3)$ and $N_{\text{jet}}(p_T > 30 \text{ GeV}, \eta < 1.5)$ in data & MC with BDT split values.	174
A.53 $N_{\text{jet}}(p_T > 30 \text{ GeV}, \eta < 2.0)$ and $N_{\text{jet}}(p_T > 50 \text{ GeV}, \eta < 1.5)$ in data & MC with BDT split values.	174
A.54 $H_T^{\text{leptons + soft jets}}$ Obfuscated and m_T in data & MC with BDT split values.	175
A.55 E_T^{miss} and $N_{\text{sig lep}}$ in data & MC with BDT split values.	175
A.56 $N_{\text{RC jet}}(m > 80 \text{ GeV})$ and $N_{\text{jet}}(p_T > 30 \text{ GeV}, \eta < 1.0)$ in data & MC with BDT split values.	176
A.57 $N_{\text{jet}}(p_T > 50 \text{ GeV}, \eta < 1.0)$ and $N_{\text{jet}}(p_T > 50 \text{ GeV}, \eta < 1.3)$ in data & MC with BDT split values.	176
A.58 $H_T^{\text{soft jets}}$ and $m_{\text{eff}}^{\text{incl}}$ in data & MC with BDT split values.	177
A.59 $m_{T,\min}^{b\text{-jets}}$ and M_J^Σ in data & MC with BDT split values.	177
A.60 m_{eff}^{4j} and $p_T^{b\text{-jet}^4}$ in data & MC with BDT split values.	178
A.61 m_g and Δm in MC with BDT split values.	178
B.1 Expected “synthetic” exclusion limit of the BDT analysis on the train set.	181
E.1 Schematic representation of a well balanced $\gamma + \text{jet}$ event.	187
E.2 Photon purity regions.	189

E.3	Photon purity in the nominal region A [225].	191
E.4	γ +jet response with and without photon purity correction [225]. . .	191
E.5	Mean γ +jet transverse momentum balance in data and MC, and their ratio [218].	193
E.6	Systematic and statistical uncertainties on the γ +jet transverse momentum balance [218].	194
E.7	Data to MC ratio of the combined large- R <i>in situ</i> measurements [218].	195
E.8	Weight of each <i>in situ</i> measurement in the combination average as a function of the large- R jet p_T [218].	195
E.9	Mean γ +jet transverse momentum balance in data and MC for $R = 1.0$ re-clustered jets.	196

List of Symbols and Abbreviations

Symbols

\mathcal{L}	Lagrangian Density, or Instantaneous Luminosity
\sqrt{s}	Center-of-Mass Energy
η	Pseudorapidity
ϕ	Azimuthal Angle
m	Mass
p_T	Transverse Momentum
H_T	Scalar Sum of Transverse Momentum
E_T^{miss}	Missing Transverse Energy
\hat{y}	BDT Output Score
Z	Significance
Z_B	Significance, Incomplete Beta Function Approximation
CL_s	Signal Confidence Level
μ	CR Normalization Factor, or Average Interactions Per Crossing
γ	MC Statistical Uncertainty
α	(Fitted) Systematic Uncertainty Nuisance Parameter

Abbreviations

AUC	Area Under Curve
BDT	Boosted Decision Tree
CART	Classification and Regression Tree
CERN	European Organization for Nuclear Research
CKM	Cabibbo-Kobayashi-Maskawa (Quark Mixing Matrix)
CMB	Cosmic Microwave Background
cMSSM	Constrained Minimal Supersymmetric Standard Model
CR	Control Region
CTP	Central Trigger Processor
DM	Dark Matter
ECAL	Electromagnetic Calorimeter
EM	Electromagnetic
EW	Electroweak
EWSB	Electroweak Symmetry Breaking
FE	Front-End (Electronics)
FTK	Fast TracKer
GUT	Grand Unified Theory
h.c.	Hermitian Conjugate
HCAL	Hadronic Calorimeter
HLT	High-Level Trigger
IBL	Insertable B-Layer
ID	Inner Detector
IP	Interaction Point
JER	Jet Energy Resolution
JES	Jet Energy Scale

JVT	Jet Vertex Tagger
L1	Level-1 (Trigger)
LAr	Liquid Argon
LCW	Local Cluster Weighting (Scale)
LHC	Large Hadron Collider
LSP	Lightest Supersymmetric Particle
MC	Monte Carlo (Simulation)
MDT	Monitored Drift Tube
MJB	Multijet Balance
MNS	Maki-Nakagawa-Sakata (Lepton Mixing Matrix)
MS	Muon Spectrometer
MSSM	Minimal Supersymmetric Standard Model
NLL	Next-to-Leading Logarithmic
NLO	Next-to-Leading Order
NNLL	Next-to-Next-to-Leading Logarithmic
NNLO	Next-to-Next-to-Leading Order
PDF	Parton Distribution Function, or Probability Density Function
PID	Particle Identification
QCD	Quantum Chromodynamics
QED	Quantum Electrodynamics
RC	Re-clustered (Jet)
RF	Radio Frequency
RMSD	Root Mean Squared Deviation
ROC	Receiver Operating Characteristic
RoI	Region of Interest
SCT	Semiconductor Tracker

SM	Standard Model
SR	Signal Region
SUSY	Supersymmetry
TDAQ	Trigger and Data Acquisition
TR	Transition Radiation
TRF	Tag Rate Function
TRT	Transition Radiation Tracker
VEV	Vacuum Expectation Value
VR	Validation Region
WZM	Wess-Zumino Model

Acknowledgements

I would like to thank the many individuals who have helped inspire me to pursue a Ph.D. and complete my studies. First and foremost I must express my deepest gratitude to my amazing partner and wife, Jamie. Without her love and constant support I would not have been able to persevere though all the challenges of life and graduate school. Thank you for your help proofreading this dissertation even while you found many of the terms, such as “sleptons”, ridiculous.

My adviser, Professor Ayana Arce, has provided me with wonderful guidance and support during my time at Duke, from when I was a newly arrived REU student through today. Her knowledge of jet physics and ability to get to the heart of analysis questions is unmatched.

The multi-*b* search team was a phenomenal group to work with. Chiara Rizzi and Max Swiatlowski are excellent coordinators who steadfastly kept the team moving in the face of obstacles and offered a wider perspective on supersymmetry research. Louis-Guillaume Gagnon, with his concurrent work on neural network applications to multi-*b* events, was a very helpful source of second opinions. Giordon Stark’s coding prowess gave the team top-notch software tools and rapid-debugging support.

At Duke, my fellow graduate students in room 288; Doug, Mike, and Sourav, were great resources while going through course work and learning about the ATLAS detector. I owe a large debt of thanks to my committee members Professor Bass, Goshaw, Kruse, and Springer, for their guidance and critiques. Professor Goshaw’s

ready advice and fellowship support were particularly invaluable.

My passion for science growing up was nurtured by my parents Cindy and David taking me to museums, reading me books, and answering my endless questions about the world around me. I also credit my grandfather Tom Roan for sparking my curiosity in physics through our projects in model rocketry and electronics.

High energy particle physics is a field where scientific progress can only be made by large teams of people working together to tackle the innumerable challenges in running a collider experiment. If one thinks about the variety and number of technical problems encountered along the way, it is a wonder that we are able to produce anything at all from these enormously complex machines. That such physics results are possible is a testament to the hard work of thousands of dedicated people over many years inside the ATLAS collaboration and the larger community.

Preface

The search for supersymmetric particles presented in this dissertation would not have been possible without the extraordinary efforts of many collaborators. My own personal research contributions are summarized here.

As a new member of the ATLAS collaboration, I completed my qualification task developing the first *in situ* γ +jet calibration for large- R jets, described in Appendix E, including practical improvements to the photon purity correction. The calibration work spanned much of my time at Duke and gave me firsthand experience with the intricacies of experimental jet physics. I was able to contribute to the ATLAS jet performance group as a session chair at the 2017 Hadronic Calibration Workshop and poster presenter at the 2018 BOOST conference.

The main focus of my research activities has been the multi- b jet search for gluino pair production to the multi- b plus E_T^{miss} final state. The boosted decision tree (BDT) approach I developed, described in Chapter 5, was the first time machine learning was applied in this final state and led to a noticeable improvement in the search's exclusion limit. While carrying out this research I developed new methods for selecting parameter points, optimizing signal regions in output score, and identified new variables useful for classification. To support the wider efforts of the multi- b search team, I also validated the modeling of kinematic variables in simulation against data and worked to keep the software architecture up-to-date.

1

Introduction

While physics may be the study of the natural world writ large, particle physics focuses its attention on nature at the shortest distances and fastest times possible. The beauty to be found in understanding the fundamental processes of our universe on such scales is in one sense the ultimate end point of generations asking “How does that work?” To probe phenomena on these frontiers, extremely high energies are required, necessitating enormous experimental efforts such as those at the Large Hadron Collider (LHC). To date, our understanding of particle physics is best represented by the many successes of the standard model (SM), yet we know there is still more to the story. A potential next chapter to be explored is the theory of supersymmetry (SUSY) between fermions and bosons. The research presented here is on one such search for SUSY in the gluino to multiple b -jets plus missing energy channel at the LHC, as well as the necessary experimental and statistical tools, including machine learning, to realize it. Through the careful application of a boosted decision tree (BDT) to signal and background classification, the multi- b search’s exclusion limit was noticeably improved in the compressed region as compared to recent results on the same dataset.

Experimental Status of SUSY

Following the LHC Run 1 at 7–8 TeV ending in 2012 with $\sim 25 \text{ fb}^{-1}$ of total integrated luminosity, SUSY searches in the ATLAS and CMS experiments had excluded large portions of the constrained minimal supersymmetric standard model (cMSSM) [1, 2]. Today in the spring of 2019, data collection for the 13 TeV Run 2 has been completed, providing a much larger integrated luminosity of 150 fb^{-1} . It will be years before this dataset is fully explored, but in the meantime results from the first 36 fb^{-1} at 13 TeV taken through 2016 are available from both experiments in many channels and have begun to exclude significant portions of the MSSM. Limits on SUSY particle masses are now being raised to the 1–2 TeV scale, as shown in Figure 1.1, where the naturalness arguments for SUSY start breaking down. To meet the larger goal of discovering SUSY with Run 2 data, or thoroughly excluding it, requires each analysis to expand their search sensitivity in phase space as far as possible, thereby limiting the areas SUSY could hide unobserved. As new data will not be available until 2022, and even then only at similar energy scales, experimental physicists have an obligation to use the present dataset efficiently to answer these questions.

ATLAS has recently released results from 79.8 fb^{-1} of data which set the highest exclusion limits on the gluino to multi- b plus missing energy channel made public thus far [4]. This BDT re-analysis pushes these observed limits even further in the compressed region. In prior studies at 36 fb^{-1} the lower ATLAS [5] and CMS [6, 7, 8] limits were comparable. Searches for same sign lepton final states [9, 10] complement the multi- b results, extending the exclusion limit into a portion of the compressed region inaccessible to multi- b searches as shown in Figure 1.2.

Dissertation Outline

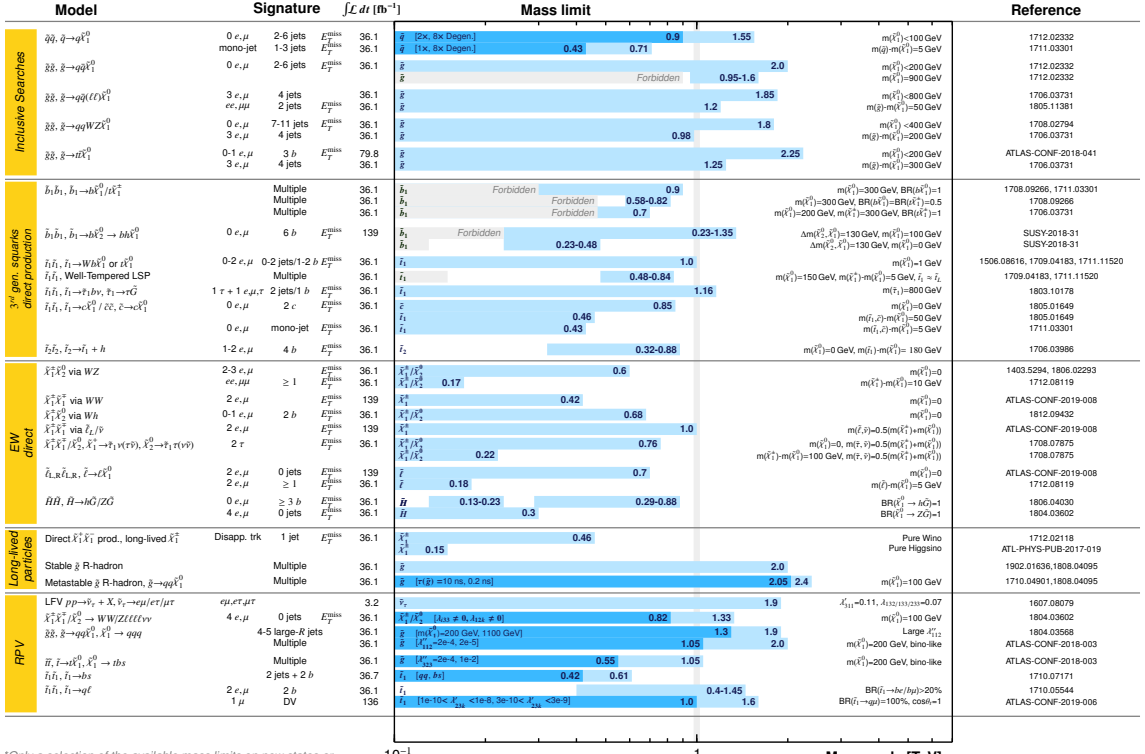
The contents of this dissertation are organized as follows: Chapter 2 lays out the theoretical framework of the SM and SUSY, Chapter 3 provides details of the LHC

ATLAS SUSY Searches* - 95% CL Lower Limits

March 2019

ATLAS Preliminary

$\sqrt{s} = 13 \text{ TeV}$



*Only a selection of the available mass limits on new states or phenomena is shown. Many of the limits are based on simplified models; c.f. refs. for the assumptions made.

FIGURE 1.1: Possible SUSY particle mass limits set by ATLAS [3]. The ATLAS-CONF-2018-041 line refers to the 79.8 fb^{-1} multi- b result [4] which sets a gluino mass limit of 2.25 TeV for neutralino masses of $< 800 \text{ GeV}$.

machine and ATLAS experiment, and Chapter 4 describes the experimental and statistical methods used in the analysis. The main focus of this research arrives in Chapter 5, where the multi- b BDT search and its results are presented in detail.

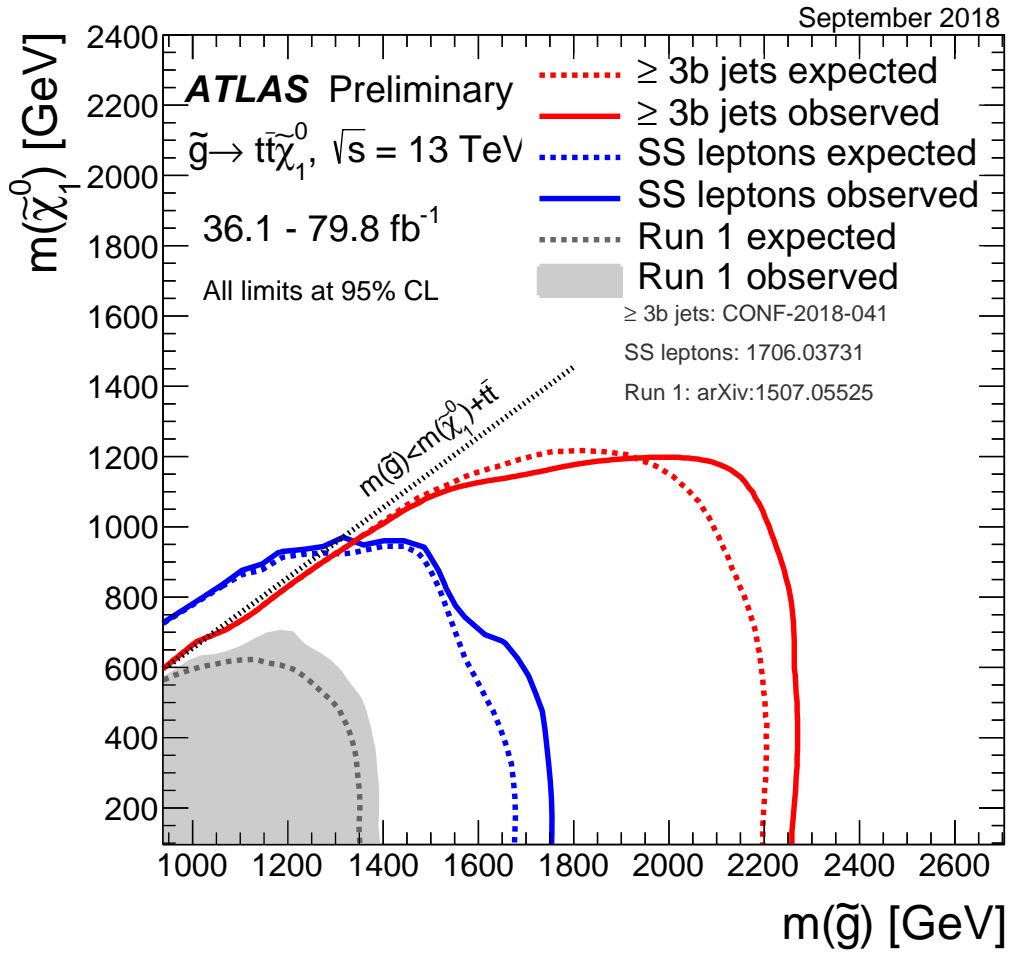


FIGURE 1.2: ATLAS gluino to $t\bar{t}$ plus neutralino exclusion limits [3] from the multi- b [4,11] and same sign lepton searches. The 36.1 fb^{-1} same sign lepton exclusion limit [9] extends into part of the compressed region kinematically forbidden in the multi- b search.

2

Theory

2.1 The Standard Model

The standard model (SM), as theoretically developed and experimentally tested over the past half century, is a remarkable scientific achievement able to make accurate predictions spanning 12 orders of magnitude for the probability of a particle physics process occurring, as illustrated in Figure 2.1. It is the most complete quantum field theory description of the fundamental interactions and elementary particles thus discovered in nature, with the conspicuous exception of gravity.¹ The relative strengths and properties of the four fundamental interactions are provided in Table 2.1. The theoretical core of the SM lies in its two principle interactions, each built on Yang-Mills gauge theory [12]: the electroweak interaction (EW), as described by the $SU(2)_L \otimes U(1)_Y$ Glashow-Weinberg-Salam theory encompassing the weak force and quantum electrodynamics (QED), and $SU(3)_C$ Quantum Chromodynamics (QCD), describing the strong force. Together these result in the overall $SU(3)_C \otimes SU(2)_L \otimes U(1)_Y$ SM symmetry group. The SM interactions will be explored

¹ Gravity, as mediated by some yet to be discovered graviton, is far too weak to have an effect on typical particle physics processes.

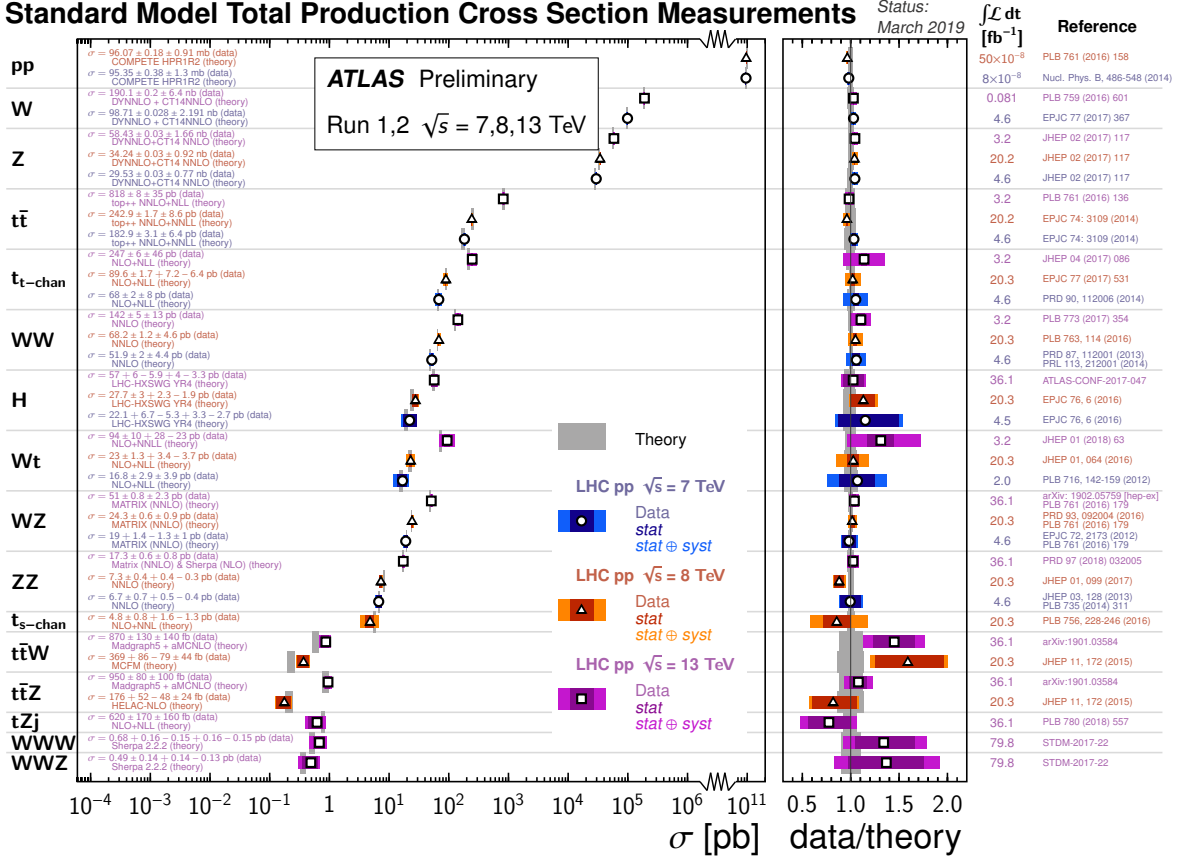


FIGURE 2.1: SM total production cross sections, σ , as measured by ATLAS compared to next-to-leading order (NLO) or higher theoretical predictions [13]. The agreement between data and theory for processes with probabilities ranging from the very rare, $\sigma \sim 10^{-1}$ pb, to the ubiquitous, $\sigma \sim 10^{11}$ pb, is a sensitive test of the SM.

in the following sections, along with the Higgs mechanism for generating mass and some shortcomings of the theory. For convenience natural units, $\hbar = c = 1$, and Einstein summation notation are used wherever possible in this dissertation.

SM Particles

The particle content of the SM, as shown in Figure 2.2, consists of three generations of fermion quarks and leptons, the interaction-mediating gauge bosons, and the mass-generating Higgs boson. Quarks q carry a single $SU(3)_C$ color charge and come in $+\frac{2}{3}$ up and $-\frac{1}{3}$ down-type flavors. Forced to remain in colorless composite states by confinement, typically in three quark hadrons or quark anti-quark mesons,

Table 2.1: The fundamental interactions of nature and their properties. The interaction strengths $|F/F_{\text{EM}}|$ are computed between two u quarks separated by $d = 10^{-18}$ m, on the order of the effective quark radius [14]. Adapted from [15].

Property	Interaction	Gravitational	Electroweak		Strong
			Weak	Electromagnetic	
Symmetry	–	$\text{SU}(2)_L$	$\text{U}(1)_Y$	$\text{SU}(3)_C$	
Acts On	Mass-Energy	Weak Isospin	Q_{EM}	Q_{Color}	
Particles Affected	All	q, l	All Charged	q, g	
Particles Mediating	Graviton	W^\pm, Z	γ	g	
$ F/F_{\text{EM}} $ at $\begin{cases} d \\ 30d \end{cases}$	10^{-41}	0.8	1	25	
	10^{-41}	10^{-4}	1	60	

their fractional electric charges are never observed directly. The leptons l consist of three -1 electric charged particles, e, μ, τ , plus their neutral, weakly interacting, and very light neutrino counterparts ν_e, ν_μ, ν_τ . Additionally, all quarks and leptons have anti-particle versions with opposite charges.

The W^\pm bosons mediate the flavor-changing weak charged current interaction, while the neutral Z mediates the flavor-preserving weak neutral current. Massless photons γ mediate the QED interaction between all charged particles. Gluons g mediate QCD interactions and are massless, but, unlike the neutral photon, carry a color and anti-color charge allowing for more complex behaviors. Completing the SM, the spin-0 Higgs boson H gives mass to the fermions and is evidence of the larger Higgs mechanism.

2.1.1 Electroweak Interaction (EW)

In the 1960s Glashow [17], Weinberg [18], and Salam [19] successfully derived the theoretical basis for unifying the electromagnetic (EM) and weak forces into one $\text{SU}(2)_L \otimes \text{U}(1)_Y$ electroweak (EW) interaction² at very high energies. Here we shall

² Here L denotes left-handed fields while Y represents weak hypercharge.

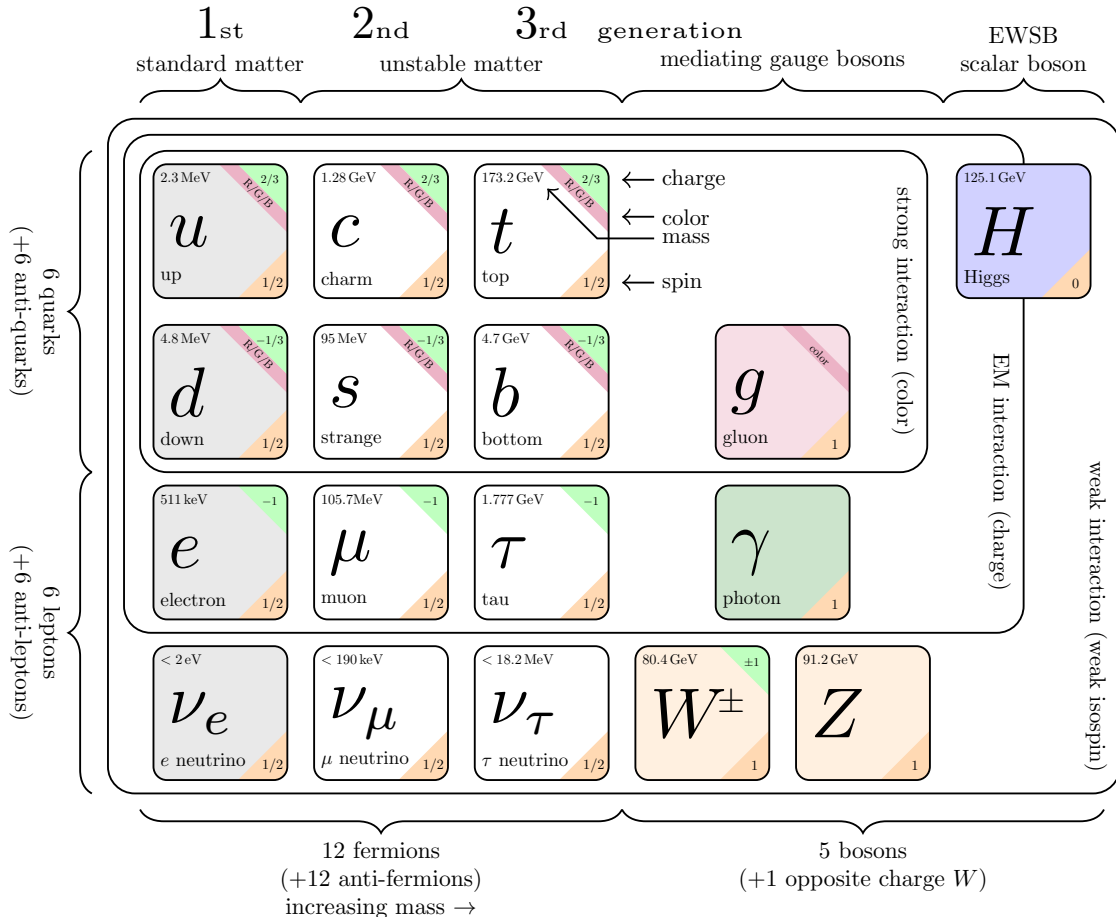


FIGURE 2.2: The particles of the SM and their properties; three generations of fermion quarks and leptons, the gauge bosons, and Higgs boson. Adapted from [16].

only consider processes on the order of $M_{\text{EW}} \sim 100 \text{ GeV}$, the EW scale, where they are distinct. For convenience we define $G \equiv \text{SU}(2)_L \otimes \text{U}(1)_Y$ to be the combined symmetry group. The $\text{SU}(2)_L$ group, representing rotations of 2-component spinors, is associated with the weak isospin W_μ^i gauge bosons and coupling constant g , where $i = 1, 2, 3$ denotes the fermion generation. The $\text{U}(1)_Y$ group, representing a rotation in the complex plane *i.e.* phase change, is associated with the weak hypercharge B_μ gauge boson and coupling constant g' . The left-handed fields of each fermion generation transform as $\text{SU}(2)_L$ doublets, while the right-handed fields transform as $\text{U}(1)_Y$ singlets [20, 21].

To begin describing the EW interaction quantitatively [21], we introduce the following fermion fields ψ for one generation of quarks (2.1a), or leptons (2.1b),

$$\psi_1(x) = \begin{pmatrix} u \\ d \end{pmatrix}_L, \quad \psi_2(x) = u_R, \quad \psi_3(x) = d_R, \quad (2.1a)$$

$$\psi_1(x) = \begin{pmatrix} \nu_e \\ e^- \end{pmatrix}_L, \quad \psi_2(x) = \nu_{eR}, \quad \psi_3(x) = e^-_R, \quad (2.1b)$$

each contributing to the kinetic Lagrangian density:

$$\mathcal{L}_0(x) = \sum_{j=1}^3 i\bar{\psi}_j(x) \gamma^\mu \partial_\mu \psi_j(x). \quad (2.2)$$

Here we have utilized the Dirac Lagrangian without mass terms, as they would mix the left- and right-handed fields and break the symmetry. Next we transform the fields under a local G gauge transformation,

$$\begin{aligned} \psi_1(x) &\xrightarrow{G} \psi'_1(x) \equiv \exp(iy_1\beta(x)) \exp(i\sigma_i\alpha^i(x)/2) \psi_1(x), \\ \psi_2(x) &\xrightarrow{G} \psi'_2(x) \equiv \exp(iy_2\beta(x)) \psi_2(x), \\ \psi_3(x) &\xrightarrow{G} \psi'_3(x) \equiv \exp(iy_3\beta(x)) \psi_3(x), \end{aligned} \quad (2.3)$$

where the y parameters are hypercharges of $U(1)_Y$, and the $SU(2)_L$ transformation, generated by the three σ_i Pauli matrices, only affects the ψ_1 left-handed doublet.

To keep \mathcal{L}_0 invariant under G , we must replace the ∂_μ derivatives with D_μ covariant versions (2.4) which are functions of four gauge boson fields W_μ^i, B_μ (2.5). Each gauge field also transforms under G and pairs with one of the gauge parameters α^i, β .

$$\mathcal{L}_{EW\ \psi} = \sum_{j=1}^3 i\bar{\psi}_j \gamma^\mu D_\mu \psi_j \quad (2.4)$$

$$\begin{aligned}
D_\mu \psi_1(x) &\equiv \left[\partial_\mu + ig \frac{\sigma_i}{2} W_\mu^i(x) + ig' y_1 B_\mu(x) \right] \psi_1(x) \\
D_\mu \psi_2(x) &\equiv \left[\partial_\mu + ig' y_2 B_\mu(x) \right] \psi_2(x) \\
D_\mu \psi_3(x) &\equiv \left[\partial_\mu + ig' y_3 B_\mu(x) \right] \psi_3(x)
\end{aligned} \tag{2.5}$$

As additional fields in the theory W_μ^i and B_μ require the introduction of new kinetic terms in the Lagrangian. After copious amounts of algebra, the resulting normalized $SU(2)_L \otimes U(1)_Y$ invariant gauge boson kinetic Lagrangian is

$$\mathcal{L}_{EW \text{ Gauge}} = -\frac{1}{4} B_{\mu\nu} B^{\mu\nu} - \frac{1}{4} W_{\mu\nu}^i W_i^{\mu\nu}, \tag{2.6}$$

where we define³:

$$\begin{aligned}
B_{\mu\nu} &\equiv \partial_\mu B_\nu - \partial_\nu B_\mu, \\
W_{\mu\nu}^i &\equiv \partial_\mu W_\nu^i - \partial_\nu W_\mu^i - g \epsilon^{ijk} W_\mu^j W_\nu^k.
\end{aligned} \tag{2.7}$$

The four physical gauge boson fields can then be written as

$$W^- = W_\mu \equiv (W_\mu^1 + iW_\mu^2) / \sqrt{2}, \tag{2.8a}$$

$$W^+ = W_\mu^\dagger \equiv (W_\mu^1 - iW_\mu^2) / \sqrt{2}, \tag{2.8b}$$

$$Z^0 = Z_\mu \equiv -B_\mu \sin \theta_W + W_\mu^3 \cos \theta_W, \tag{2.8c}$$

$$\gamma = A_\mu \equiv B_\mu \cos \theta_W + W_\mu^3 \sin \theta_W, \tag{2.8d}$$

where we have preemptively broken the symmetry by mixing B_μ and W_μ^3 in anticipation of generating the Z boson mass. The mixing is controlled via the weak angle θ_W with $\tan \theta_W = g'/g$.

³ Here ϵ^{ijk} is the totally antisymmetric Levi-Civita symbol.

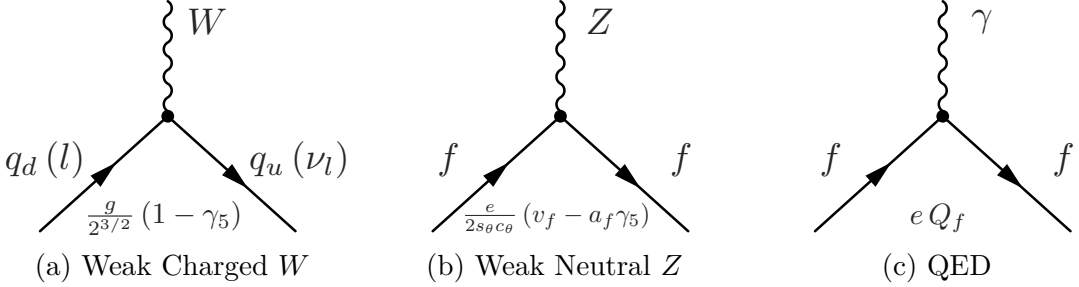


FIGURE 2.3: Principal EW vertices. Adapted from [21].

Interactions

Expanding $\mathcal{L}_{\text{EW}} \psi$ [21], we can identify the flavor-changing charged current interaction terms⁴ \mathcal{L}_{CC} (2.9) producing the quark and lepton vertices of Figure 2.3a.

$$\mathcal{L}_{\text{CC}} = -\frac{g}{2\sqrt{2}} \left\{ W_\mu^\dagger [\bar{u} \gamma^\mu (1 - \gamma_5) d + \bar{\nu}_e \gamma^\mu (1 - \gamma_5) e] + \text{h.c.} \right\} \quad (2.9)$$

Using the positron charge $e = g \sin \theta_W = g' \cos \theta_W$ with the operators for the third component of weak isospin $T_3 = \sigma_3/2$, weak hypercharge Y , and electric charge $Q_{\text{EM}} = \frac{1}{2}Y + T_3$, we can further isolate the quantum electrodynamic (QED) \mathcal{L}_{QED} (2.10) and Z neutral current $\mathcal{L}_{\text{NC}}^Z$ (2.11) terms producing the vertices of Figures 2.3b and 2.3c.

$$\mathcal{L}_{\text{QED}} = -e A_\mu \sum_j \bar{\psi}_j \gamma^\mu Q_j \psi_j \equiv -e A_\mu J_{\text{EM}}^\mu \quad (2.10)$$

$$\mathcal{L}_{\text{NC}}^Z = -\frac{e}{2 \sin \theta_W \cos \theta_W} Z_\mu \sum_j \bar{\psi}_j \gamma^\mu (\sigma_3 - 2 \sin^2 \theta_W Q_j) \psi_j \quad (2.11)$$

Expanding $\mathcal{L}_{\text{EW}} \text{Gauge}$ produces cubic and quartic gauge boson interaction terms generating vertices such as $\gamma \rightarrow WW$, $Z \rightarrow WW$, and $WW \rightarrow WW$.

⁴ Omitting the mirror hermitian conjugate (h.c.) terms.

2.1.2 Electroweak Symmetry Breaking (EWSB)

To maintain the gauge symmetry between the left- and right-handed fermion fields in the $SU(2)_L \otimes U(1)_Y$ EW theory, we were forced to make them massless — an uninteresting universe indeed. Fortunately, the vacuum EW symmetry is spontaneously broken (EWSB) via the Higgs mechanism [22, 23, 24], which allows for the generation of fermion and gauge boson masses. While exploring EWSB is worthwhile on its own merits, similar concepts about spontaneous broken symmetries return frequently in the development of supersymmetric theories, so it is useful to study EWSB in some detail here.

In addition to the ψ fermion fields of the EW theory we introduce a doublet of complex scalar fields ϕ with hypercharge⁵ $y_\phi = \frac{1}{2}$:

$$\phi(x) \equiv \begin{pmatrix} \phi^{(+)}(x) \\ \phi^{(0)}(x) \end{pmatrix}. \quad (2.12)$$

Following the same procedure as for ψ_1 we take the Klein-Gordon scalar Lagrangian and make it invariant under a local $SU(2)_L \otimes U(1)_Y$ gauge transformation [21],

$$\mathcal{L}_H = |D_\mu \phi|^2 - V_H, \quad (2.13)$$

where V_H is the Higgs potential with $\mu^2 < 0$:

$$V_H = \mu^2 \phi^\dagger \phi + \lambda (\phi^\dagger \phi)^2. \quad (2.14)$$

For $\mu^2 < 0$ the potential V_H takes the shape shown in Figure 2.4 where the minimum is infinitely degenerate. There can only be one ground state of ϕ , however,

⁵ $y_\phi = \frac{1}{2}$ is required to keep the neutral $\psi^{(0)}$ field from coupling to the photon. This will also lead to the photon not coupling to the physical Higgs field H , thus remaining massless.

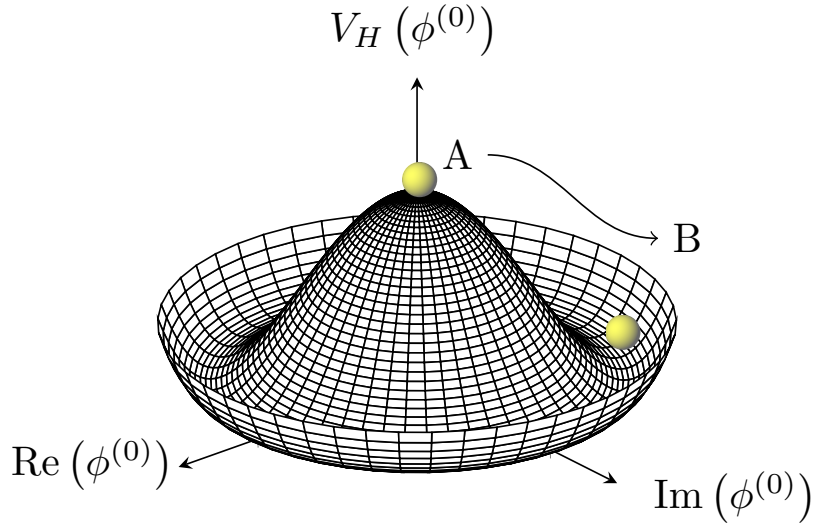


FIGURE 2.4: Higgs potential $V_H(\phi^{(0)})$ of a single complex scalar Higgs field $\phi^{(0)}$. The $SU(2)_L \otimes U(1)_Y$ symmetry is spontaneously broken $A \rightarrow B$ by the choice of a particular ground state B in the potential's minimum. Adapted from [25].

the choice of which spontaneously breaks the $SU(2)_L \otimes U(1)_Y$ symmetry and gives us a vacuum expectation value^{6,7} (VEV) v :

$$\left| \langle 0 | \phi^{(0)} | 0 \rangle \right| = \sqrt{\frac{-\mu^2}{2\lambda}} \equiv \frac{v}{\sqrt{2}}. \quad (2.15)$$

At this point we can expand ϕ about v ,

$$\phi(x) = \frac{1}{\sqrt{2}} \exp\left(i\sigma_i\theta^i(x)/2\right) \begin{pmatrix} 0 \\ v + H(x) \end{pmatrix}, \quad (2.16)$$

where $\theta^i(x)$ and $H(x)$ are real scalar fields. With the proper choice of gauge the θ^i fields can be rotated away⁸ leaving the single physical Higgs field H . Returning to

⁶ Due to charge conservation we can only have a non-zero VEV for the neutral $\phi^{(0)}$ component.

⁷ The measured VEV of $v \approx 246$ GeV provides a firmer description of the EW scale.

⁸ The θ^i fields become massless Goldstone bosons [26] which are the longitudinal polarization degrees of freedom for the now massive gauge bosons.

\mathcal{L}_H we find the kinetic portion now contains quadratic terms for the gauge bosons,

$$|D_\mu \phi|^2 = \frac{1}{2} |\partial_\mu H|^2 + \frac{g^2}{4} (v + H)^2 \left(|W_\mu|^2 + \frac{1}{2 \cos^2 \theta_W} |Z_\mu|^2 \right), \quad (2.17)$$

thereby generating their masses⁹:

$$m_W = \frac{gv}{2}, \quad (2.18a)$$

$$m_Z = \frac{gv}{2 \cos \theta_W} = \frac{m_W}{\cos \theta_W}, \quad (2.18b)$$

$$m_\gamma = 0. \quad (2.18c)$$

The Higgs boson itself has a mass of $m_H = \sqrt{-2\mu^2} = \sqrt{2\lambda}v$, as can be seen from the quadratic terms of V_H . Additional interaction terms in the gauged \mathcal{L}_H produce vertices for $H \rightarrow ZZ$, $H \rightarrow WW$, $H \rightarrow \gamma\gamma$, and $HH \rightarrow ZZ$ among others.

Fermion Masses

With the introduction of the scalar Higgs, new Yukawa terms $-c_i \bar{\psi}_i \phi \psi_i$ for the fermion fields can be added to the Lagrangian. After EWSB these Yukawa couplings give rise to the fermion mass terms,

$$\mathcal{L}_Y = - \left(1 + \frac{H}{v} \right) \left(m_d \bar{d}d + m_u \bar{u}u + m_e \bar{e}e \right), \quad (2.19)$$

with masses that are proportional to the Higgs coupling strengths:

$$m_d = c_1 \frac{v}{\sqrt{2}}, \quad m_u = c_2 \frac{v}{\sqrt{2}}, \quad m_e = c_3 \frac{v}{\sqrt{2}}. \quad (2.20)$$

⁹ The mass term for a boson field ϕ is $\mathcal{L} = \frac{1}{2} m^2 |\phi|^2$. For W^\pm , $|W_\mu| = \frac{1}{2} \left(|W_\mu|^2 + |W_\mu^\dagger|^2 \right)$.

The observed quark¹⁰ mass and flavor eigenstates are in fact linear combinations of the EW eigenstates ψ , as quantified by the Cabibbo-Kobayashi-Maskawa (CKM) mixing matrix [31, 32].

The 2012 discovery of the Higgs boson at $m_H = 125$ GeV by the ATLAS and CMS experiments [33, 34] completed our understanding of the SM, confirming mass generation via EWSB and the Higgs mechanism.

2.1.3 Strong Interaction: Quantum Chromodynamics (QCD)

To describe the strong interaction found between quarks and gluons, collectively named partons, we turn to the theory of quantum chromodynamics (QCD) [35, 36, 37]. The basis of QCD consists of three color charge states, indexed by $a = 1, 2, 3$ and traditionally labeled red, green, and blue. The proper symmetry group on this basis is $SU(3)_C$, representing rotations of complex 3-component vectors generated by the eight λ^A Gell-Mann matrices. Only color singlet, or colorless, states are allowed in nature, typically $|rgb\rangle$ ¹¹ hadrons or color anti-color $(|r\bar{r}\rangle + |g\bar{g}\rangle + |\bar{b}b\rangle)/\sqrt{3}$ mesons, though other exotic singlets are possible. Starting from the standard Dirac Lagrangian for massive fermions we construct the QCD Lagrangian to be invariant under local $SU(3)_C$ transformations [38]:

$$\mathcal{L}_{\text{QCD}} = \mathcal{L}_{\text{classical}} + \mathcal{L}_{\text{gauge-fixing}} + \mathcal{L}_{\text{ghost}}, \quad (2.21a)$$

$$\mathcal{L}_{\text{classical}} = -\frac{1}{4} F_{\alpha\beta}^A F_A^{\alpha\beta} + \sum_{\text{flavors}} \bar{q}_a (i\gamma_\mu D^\mu - m)_{ab} q_b, \quad (2.21b)$$

$$\mathcal{L}_{\text{gauge-fixing}} = -\frac{1}{2\lambda} (\partial^\alpha \mathcal{A}_\alpha^A)^2, \quad (2.21c)$$

$$\mathcal{L}_{\text{ghost}} = \partial_\alpha \eta^{A\dagger} (D_{AB}^\alpha \eta^B). \quad (2.21d)$$

¹⁰ Lepton mass state mixing quantified by the Maki-Nakagawa-Sakata (MNS) matrix and the generation of neutrino masses required for neutrino oscillations is omitted here for simplicity. For further reference see [20, 27, 28, 29, 30].

¹¹ Red, green, and blue are useful labels due to the analogy of mixing rgb light to form white light.

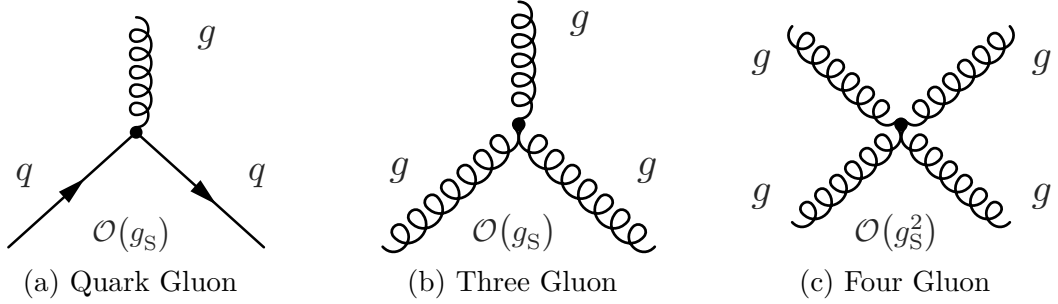


FIGURE 2.5: Principal QCD vertices, adapted from [38]. For vertex factors see [38].

The classical Lagrangian $\mathcal{L}_{\text{classical}}$ (2.21b) contains the covariant version of the Dirac Lagrangian for quark fields q_a , as well as terms for the quark gluon vertex of Figure 2.5a. Gluons mediate the strong force in a similar manner as gauge bosons in EW theory, albeit with some important differences. The gluon fields \mathcal{A}_α^A make up the field strength tensor,

$$F_{\alpha\beta}^A = \left[\partial_\alpha \mathcal{A}_\beta^A - \partial_\beta \mathcal{A}_\alpha^A - g_S f^{ABC} \mathcal{A}_\alpha^B \mathcal{A}_\beta^C \right], \quad (2.22)$$

where $A, B, C = 1, \dots, 8$ run over the gluon color degrees of freedom *i.e.* the eight $SU(3)_C$ generators, g_S is the $SU(3)_C$ coupling constant, and f^{ABC} are the $SU(3)_C$ non-abelian structure constants $[\lambda^A, \lambda^B] = 2i f^{ABC} \lambda^C$. The presence of the f^{ABC} term in (2.22) allows gluons themselves to carry color charge, thereby producing the three and four leg gluon self-interaction vertices of Figures 2.5b and 2.5c, as well as the phenomenon of asymptotic freedom which will be described shortly.

As $SU(3)_C$ is non-abelian choosing a gauge, accomplished by $\mathcal{L}_{\text{gauge-fixing}}$ (2.21c) with gauge parameter λ , is not enough to maintain invariance. Non-physical degrees of freedom remain and can propagate through the theory causing divergences. Fortunately, we can cancel these problematic degrees of freedom via the Faddeev-Popov method [39], which adds a ghost field η^A and additional Lagrangian term $\mathcal{L}_{\text{ghost}}$ (2.21d).

Renormalization, Running Couplings, and Asymptotic Freedom

When working with field theories it is inevitable that loop diagrams such as those of Figure 2.10 arise when computing corrections to many quantities, including coupling constants and particle masses. Unfortunately, the momentum carried by the virtual particles in the loop must be integrated over all possibilities, 0 to $+\infty$, leading to non-physical divergences. The calculation can be salvaged via renormalization, where we introduce an ultraviolet momentum cut-off Λ_{UV} to regulate the loop integral. Effectively, Λ_{UV} sets the scale where the SM breaks down and a more complete theory is required.

In the case of coupling constants $\alpha = g^2/4\pi$, the renormalization group equations at an energy scale Q include

$$Q^2 \frac{\partial \alpha}{\partial Q^2} = \beta(\alpha) , \quad (2.23)$$

where $\beta(\alpha)$ depends on the field in question. This differential equation defines the running coupling constant $\alpha(Q)$. For QCD, leading order perturbative calculations [38] result in

$$\beta(\alpha_S) = -\frac{11 n_{\text{colors}} - 2 n_f}{12\pi} \alpha_S^2 = -\frac{33 - 2 n_f}{12\pi} \alpha_S^2 , \quad (2.24)$$

for n_f active light flavors. With at most 6 SM quarks $\beta(\alpha_S)/\alpha_S^2 < 0$ and $\alpha_S(Q)$ decreases for higher energies Q , or equivalently at shorter length scales, enabling a perturbative approach. This counterintuitive behavior is known as asymptotic freedom¹² [37, 40]. One interpretation of asymptotic freedom envisions the color charge of adjacent quarks being diluted out over short distances by color-carrying virtual gluons, lessening the force between them in comparison to pure point charges.

¹² In contrast for leading order QED $\beta_{\text{QED}}(\alpha) = \alpha^2/3\pi$ and $\alpha(Q)$ increases for higher energies, shorter distances, as there is less vacuum polarization shielding the point electric charge.

Confinement and Hadronization

At low energies and large distances, approaching 1 fm, α_S increases to the point that perturbative calculations break down. In the non-perturbative regime the QCD interaction becomes so strong that the color charges are forced to form color singlet states. This can be shown with lattice calculations [41] and is known as confinement. As the distance between color charges grows and the strong force increases, there comes a point when it is more energetically favorable to create a new $q\bar{q}$ pair from the vacuum to cancel the charges rather than separate them further.

The transition between the perturbative and non-perturbative regimes is poorly understood, but partons leaving a vertex are experimentally observed to undergo hadronization, forming a shower of colorless hadrons and mesons. A simulated example of this process is shown in Figure 2.6. One parton from a vertex will also often radiate collinear gluons which then pair-produce quarks, beginning a larger shower that results in a highly collimated stream of stable hadrons and mesons along the original parton's trajectory. These streams are known as jets due to their appearance in detectors.

Several phenomenological theories have been developed to simulate the hadronization process [38]. PYTHIA [43] utilizes the Lund string model [44], where the non-perturbative evolution of the parton shower is represented as a string of the color field. The string has uniform energy density, kinks where perturbative gluons connect, and separations between perturbative $q\bar{q}$ pairs. The string is broken up into hadrons at kinks or when there is enough energy to produce new $q\bar{q}$ pairs.

SHERPA [45] and Herwig++ [46, 47] utilize the cluster model [48], where gluons are split into $q\bar{q}$ pairs non-perturbatively to form colorless clusters with the existing quarks. The fraction z of the gluon's original energy passed on to each quark is drawn from a probability distribution, known as the gluon splitting function, proportional

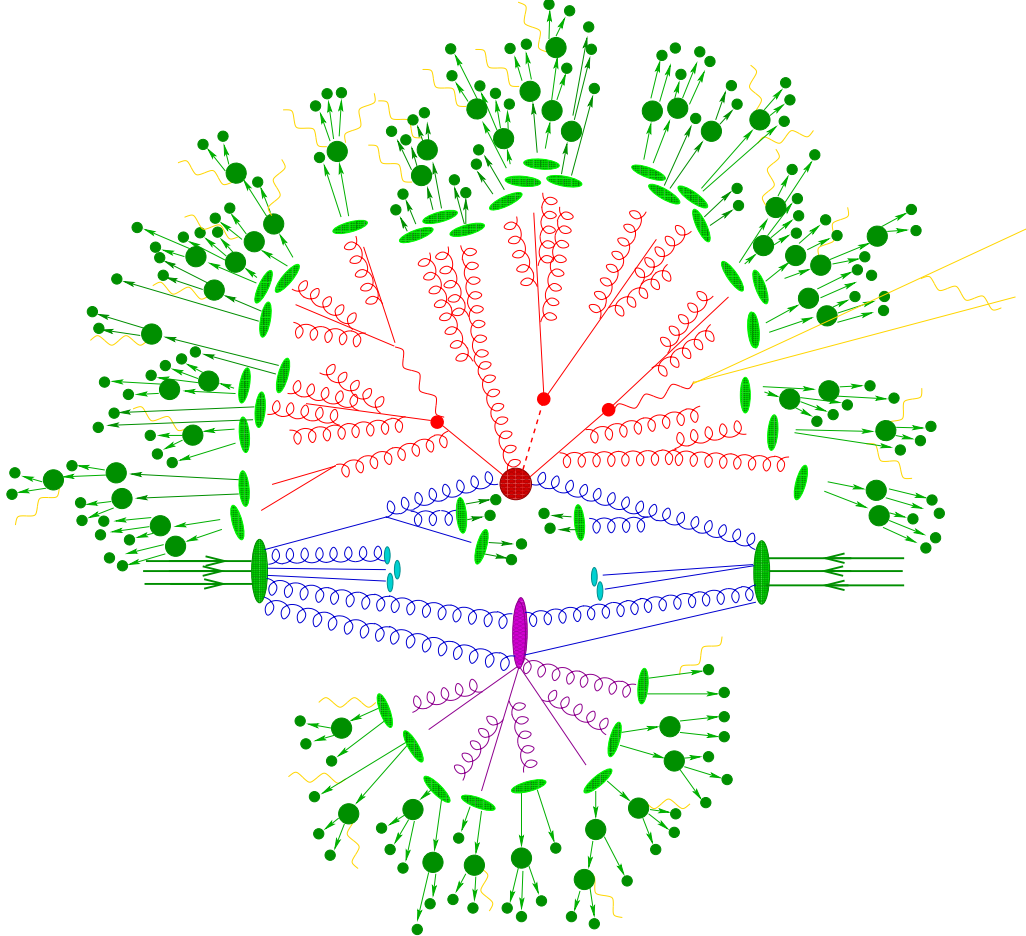


FIGURE 2.6: Hadronization in a simulated hadron-hadron collision [42]. Two colliding hadrons (large central green ellipses) interact via gluons in a primary hard scatter (red circle) producing a parton shower (red lines) which subsequently hadronizes (light green ellipses) into final state hadrons and mesons (dark green circles). The event also contains a secondary parton shower (purple elements), soft photon radiation (yellow lines), and beam remnants (light blue ellipses).

to $z^2 + (1 - z)^2$ [49]. Mesonic states are then formed in the clusters which go on to decay to the final hadrons.

Parton Distribution Functions (PDFs)

At the LHC protons are collided together at extremely high energies. Hadrons, including protons, are not fundamental particles, but are instead QCD bound states of quarks and gluons. Typically a proton is considered to be made up of *uud* quarks,

however at high energies, fluctuations in the proton's wave function can produce additional virtual $q\bar{q}$ pairs known as sea quarks. In a pp collision it is any of these partons within the protons that are really interacting.

Due to the nature of a collision, with particles starting at a distance then drawing ever closer, the parton-parton interaction must include both long-range non-perturbative and short-range perturbative components. Fortunately, QCD factorization theorems [50] allow us to separate these effects into experimentally measured parton distribution functions (PDF) [38, 51, 52] and standard perturbative QCD calculations, with the division between the two set by a factorization scale μ . PDFs $f(x, Q^2)$ are functions of the fraction x of the proton's total momentum carried by the interacting parton, and the energy scale Q of the interaction.¹³ Two example PDFs can be found in Figure 2.7. Once measured at a particular Q , PDFs can be evolved via the DGLAP [53, 54, 55] equations for use at higher energy scales.

2.1.4 Decay of the Top Quark

As the experimental signatures under investigation in this dissertation feature SM top quark decays we shall now address them specifically. The top quark t is quite massive at 173 GeV, making it the only quark that can decay to a real W boson. It does so readily, decaying semi-weakly to a W^+ and down-type quark with a branching fraction $\Gamma(Wq(q = b, s, d)) / \Gamma$ of nearly 100 %. This gives the top quark a very short lifetime of only $\sim 0.5 \times 10^{-24}$ s [20], too fast to hadronize or form any top bound states. The down-type quark q in $t \rightarrow Wq$ is overwhelmingly a b quark, $\Gamma(t \rightarrow Wb) / \Gamma(t \rightarrow Wq(q = b, s, d)) = 95.7 \pm 3.4$ %, while the W subsequently decays hadronically, $W \rightarrow q\bar{q}$, or leptonically, $W \rightarrow l^+ \nu_l$. In either case the top quark decays to at least one b quark, producing a b -jet via hadronization, along with additional jets or leptons from the W . The full top quark decay can be seen in Figure 2.8

¹³ In collider experiments the center-of-mass energy \sqrt{s} sets an upper bound on Q .

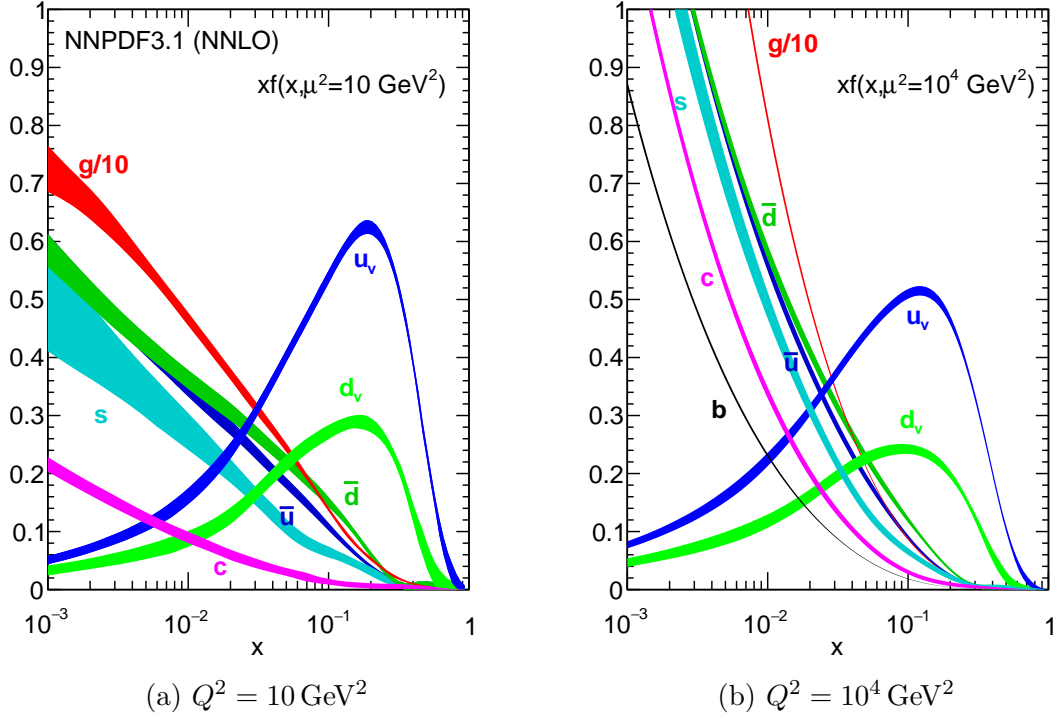


FIGURE 2.7: NNPDF3.1 NNLO PDFs [56]. Note that in these plots μ is set to Q and the vertical axis is the PDF $f(x, Q^2)$ multiplied by x . At the higher energy scale of (b) heavier c and b quarks begin to appear in the parton sea and subsequent collision interactions.

and has following branching ratios [57]:

$$\begin{aligned}
 \Gamma(t \rightarrow q\bar{q} b) / \Gamma &= 66.5 \pm 1.4\%, \\
 \Gamma(t \rightarrow e^+ \nu_e b) / \Gamma &= 13.3 \pm 0.6\%, \\
 \Gamma(t \rightarrow \mu^+ \nu_\mu b) / \Gamma &= 13.4 \pm 0.6\%, \\
 \Gamma(t \rightarrow \tau^+ \nu_\tau b) / \Gamma &= 7.1 \pm 0.6\%.
 \end{aligned} \tag{2.25}$$

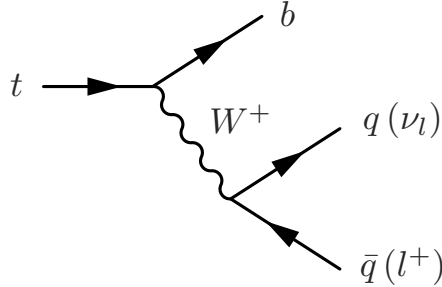


FIGURE 2.8: Hadronic $t \rightarrow q\bar{q}b$ and leptonic $t \rightarrow l^+\nu_l b$ decays of the top quark.

2.1.5 Shortcomings

Dark Matter

The relatively few SM particles of Figure 2.2 appear to be sufficient for explaining most, if not all, particle physics phenomena observed in collider experiments. However, from astrophysical measurements we know that some form of dark matter (DM) must exist that interacts gravitationally, yet has little to no EM interaction, rendering it non-luminous and non-absorbing. Aside from sterile neutrinos, the SM has no acceptable DM candidates and will likely require extension to incorporate any discovered DM particle(s). Despite intense experimental efforts there has been no conclusive direct detection of a DM particle to date. What we know of DM comes from its indirect effects on the cosmic microwave background (CMB) [58, 59], gravitational lensing of galaxies [60], and galactic rotation curves [61], an example of which is shown in Figure 2.9.

The Hierarchy Problem

While the SM can provide remarkably accurate predictions around the EW scale, $M_{\text{EW}} \sim 100 \text{ GeV}$, it is unable to unify the SM fields with gravity quantum mechanically at the Planck scale, $M_P = \sqrt{\hbar/8\pi G_{\text{Newton}}} = 2.4 \times 10^{18} \text{ GeV}$, where gravity and gauge interactions become comparable [20, 62]. The large hierarchy difference $M_P/M_{\text{EW}} \sim 10^{16}$ between these two scales is itself disturbing, but also causes fine-tuning issues in

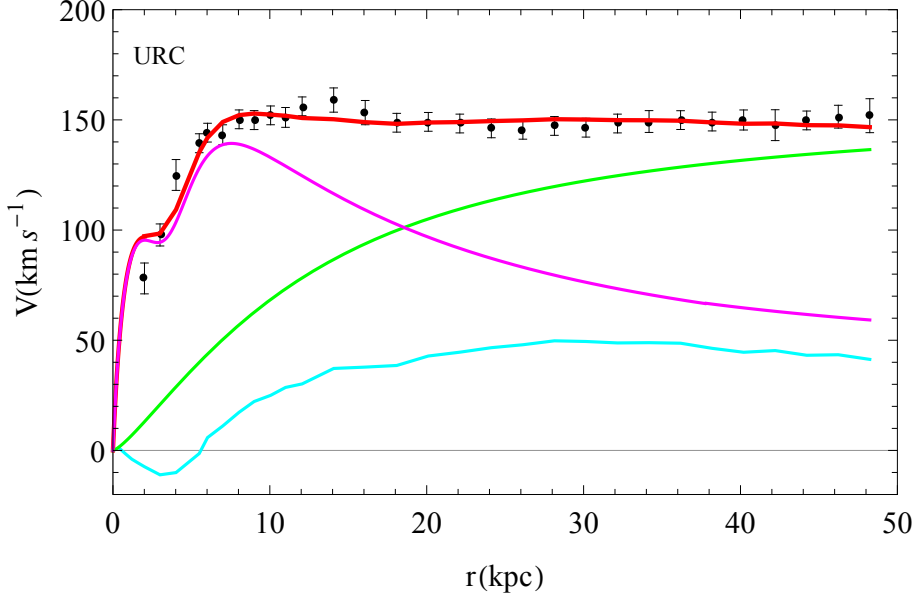


FIGURE 2.9: Rotation curve of the NGC 3198 galaxy [61]. The data points and model (red) with stellar disk (magenta), halo (green), and hydrogen line disk (azure) components are shown. The velocity of an object in orbit a distance r from the center of a galaxy should go as $v(r) \propto \sqrt{M_{\text{enc}}(r)/r}$, dropping as $1/\sqrt{r}$ outside the visible galactic core. However, as seen here $v(r)$ is approximately constant out to very large distances. This can be explained through the introduction of the DM halo.

loop corrections to the bare Higgs mass.

The Higgs field couples to all massive particles according to their mass, allowing for higher order self-loop diagrams. A fermion field f coupling to the Higgs via a $-\lambda_f \bar{f} H f$ Yukawa term in the Lagrangian creates the first order loop diagram shown in Figure 2.10a. This loop corrects the Higgs squared mass as in (2.26) [62], where Λ_{UV} regulates the integral and c_f is a color factor.¹⁴ Unfortunately, Δm_H^2 contains a quadratic divergence in Λ_{UV} , creating corrections of extremely large magnitudes.

$$\Delta m_H^2 = -c_f \frac{|\lambda_f|^2}{8\pi^2} \Lambda_{\text{UV}}^2 + \mathcal{O}(m_f^2 \ln(\Lambda_{\text{UV}})) \quad (2.26)$$

The strongest coupling fermion, *i.e.* the most massive, is the top quark with

¹⁴ $c_f = 3$ if f is a quark, and 1 if it is a lepton.

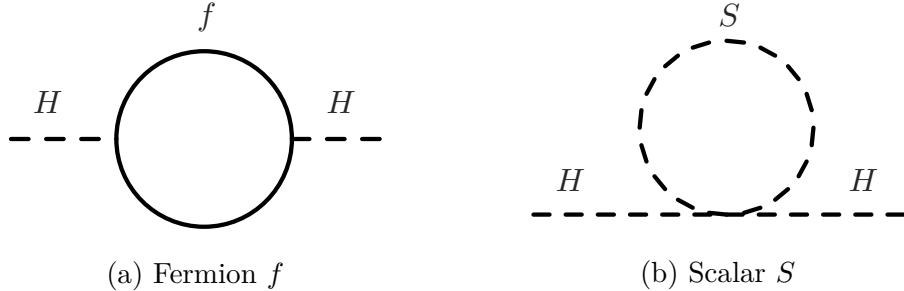


FIGURE 2.10: First order loop contributions to the Higgs squared mass correction Δm_H^2 for a fermion f and scalar S .

$\lambda_t \approx 0.94$. Taking Λ_{UV} to be M_P we find a correction of $\Delta m_H^2 \sim -(10^{17} \text{ GeV})^2$ from the top quark alone. As the measured mass of the Higgs is only $m_H = 125 \text{ GeV}$ an unreasonable amount of fine-tuning would be required for a mass of $\mathcal{O}(10^2)$ to result from $\mathcal{O}(10^{17})$ corrections on the bare mass.

In addition to fermions we can also consider how a complex scalar S would couple to the Higgs given a Lagrangian term of $-\lambda_S |H|^2 |S|^2$. The first order loop diagram shown in Figure 2.10b is similar, but the resulting Higgs squared mass correction (2.27) has the opposite sign [62]. This opens up the intriguing possibility of canceling fermion and (scalar) boson corrections within the right theoretical framework.

$$\Delta m_H^2 = \frac{\lambda_S}{16\pi^2} \Lambda_{\text{UV}}^2 + \mathcal{O}\left(m_S^2 \ln(\Lambda_{\text{UV}}/m_S)\right) \quad (2.27)$$

2.2 Supersymmetry (SUSY)

As alluded to in Section 2.1.5, hierarchy problems in the Higgs sector can be cleanly resolved by establishing a symmetry, or rather supersymmetry (SUSY) [63, 64, 65, 66], between fermions and bosons in such a way that a particle and its superpartner's Higgs squared mass corrections cancel exactly. The host of new SUSY particles, or sparticles, introduced by the theory also contain natural candidates for DM [67, 68],

thereby solving two thorny issues at once. Additionally, we shall see that SUSY allows for the unification of the SM gauge couplings near the Planck scale.

The essential SUSY transformation between bosons and fermions generated by an operator Q is simply:

$$Q |\text{Boson}\rangle = |\text{Fermion}\rangle, \quad Q |\text{Fermion}\rangle = |\text{Boson}\rangle.$$

To produce supersymmetric fermions by operating on SM bosons it follows that Q must be a spin- $\frac{1}{2}$ spinor, and thus SUSY is a symmetry of spacetime. Taking this fact along with the chirality of fermions in the SM, the Haag-Łopuszański-Sohnius generalization¹⁵ [69] of the Coleman-Mandula theorem [70] then gives us the following conditions on Q where P^μ is the four-momentum operator [62]:

$$\{Q, Q^\dagger\} = P^\mu, \tag{2.28a}$$

$$\{Q, Q\} = \{Q^\dagger, Q^\dagger\} = 0, \tag{2.28b}$$

$$[P^\mu, Q] = [P^\mu, Q^\dagger] = 0. \tag{2.28c}$$

The most interesting of these conditions is (2.28c) as it implies the squared-mass operator $-P^2$ commutes with Q, Q^\dagger , *i.e.* if SUSY is an unbroken symmetry SM particles and their superpartners, collectively forming a supermultiplet, must have the same mass. As we have yet to discover any sparticles they must have masses far heavier than the SM particles, thus if SUSY is physical it must be a broken symmetry. Q also commutes with gauge transformation generators, therefore superpartners must share the same electric charge, weak isospin, and color degrees of freedom as their SM counterparts.

¹⁵ The Haag-Łopuszański-Sohnius theorem also proves that SUSY is the only non-trivial extension to the internal (color, weak isospin...) and Poincaré (spacetime) symmetries of the SM [69].

2.2.1 The Wess-Zumino Model (WZM)

The Wess-Zumino model (WZM) [63] is the original and most straightforward field theory implementation of a SUSY transformation within a single massless supermultiplet. In the WZM the fermion state is represented by a left-handed 2-component Weyl spinor field ψ , while the boson state is a complex scalar field ϕ . Note that although ψ is a complex spinor field it only contains two degrees of freedom on-shell,¹⁶ the same number as the complex scalar ϕ . To begin we construct \mathcal{L}_{WZM} from the free Klein-Gordon and Dirac Lagrangians¹⁷ [62]:

$$\mathcal{L}_{\text{WZM}} = \mathcal{L}_{\text{KG}} + \mathcal{L}_{\text{Dirac}} = -|\partial_\mu \phi|^2 + i\psi^\dagger \bar{\sigma}^\mu \partial_\mu \psi. \quad (2.29)$$

A SUSY transformation on ϕ and ψ can be represented as

$$\begin{aligned} \delta_\epsilon \phi &= \epsilon \psi, \\ \delta_\epsilon \psi &= -i\sigma^\mu \epsilon^\dagger \partial_\mu \phi, \end{aligned} \quad (2.30)$$

where ϵ is an infinitesimal 2-component spinor parameterizing the global transformation, $\partial_\mu \epsilon = 0$. Applying (2.30) to \mathcal{L}_{WZM} we find that while $\delta \mathcal{L}_{\text{WZM}}$ (2.31) is not invariant, it is a total derivative. The action and resulting equations of motion are therefore invariant (2.32) under this infinitesimal SUSY transformation.¹⁸

$$\delta \mathcal{L}_{\text{WZM}} = -\partial_\mu (\epsilon \sigma^\nu \bar{\sigma}^\mu \psi \partial_\nu \phi^* + \epsilon \psi \partial^\mu \phi^* + \epsilon^\dagger \psi^\dagger \partial^\mu \phi) \quad (2.31)$$

$$\delta S = \int d^4x \partial_\mu (\dots) = 0 \quad (2.32)$$

¹⁶ Off-shell ψ has four degrees of freedom and we must introduce an auxiliary complex scalar field F , $\mathcal{L}_{\text{aux}} = |F|^2$, to correct the bookkeeping. The transformation remains invariant however [62].

¹⁷ Here $\sigma^\mu \equiv (I, \sigma^i)$, $\bar{\sigma}^\mu \equiv (I, -\sigma^i)$.

¹⁸ Additionally, the SUSY transformation of (2.30) can be shown to close via commutator arguments, while the conserved supercurrent and generator Q can be found via Noether's theorem [62].

As a simplified massless model the WZM is only a starting point. In practice each 4-component SM fermion partners with two complex scalar fields, one for each of its left- and right-handed 2-component spinor elements [62]. This makes intuitive sense as then four fermionic degrees of freedom pair with an equal number of bosonic degrees of freedom. When Higgs field interactions are added the two partner complex scalar fields provide exactly the right cancellation to the fermion correction, for $\lambda_S = |\lambda_f|^2 = \lambda$:

$$\begin{aligned} \Delta m_H^2 = & -\frac{\lambda}{8\pi^2} \Lambda_{\text{UV}}^2 \\ & + 2 \times \frac{\lambda}{16\pi^2} \Lambda_{\text{UV}}^2 \\ & + \mathcal{O}(m^2 \ln(\Lambda_{\text{UV}})). \end{aligned} \quad (2.33)$$

2.2.2 Soft SUSY Breaking and Naturalness

Having not discovered any light sparticles near their SM partner masses, we know that SUSY must be a broken symmetry. While the symmetry breaking may be spontaneous or explicit, in order to avoid reintroducing quadratic divergences in the Higgs mass corrections broken SUSY must keep the coupling constants $\lambda_S \approx |\lambda_f|^2$. This is possible with “soft” SUSY breaking where we only allow SUSY breaking mass terms and coupling constants with positive mass dimension to appear in the Lagrangian [62, 71]. Labeling the largest mass of the soft SUSY breaking terms m_{soft} we can find their contribution to the Higgs squared mass correction goes like:

$$\Delta m_H^2 = m_{\text{soft}}^2 \left(\frac{\lambda}{16\pi^2} \ln(\Lambda_{\text{UV}}/m_{\text{soft}}) + \dots \right). \quad (2.34)$$

Taking $\Lambda_{\text{UV}} \sim M_P$, $\lambda \sim 1$ we find that m_{soft} and thus the lighter sparticles, in

particular the stop \tilde{t} , should have masses no higher than a few TeV^{19,20} or the hierarchy and fine-tuning problems originally solved by SUSY will begin to re-emerge. Similar naturalness arguments resulting in TeV scale upper bounds for sparticle masses can also be made in terms of the top quark mass m_t [73].

2.2.3 The Minimal Supersymmetric Standard Model (MSSM)

Returning to the full SM, by introducing the minimum number of superfields required to perform one SUSY transformation Q over all the SM fields, we arrive at the Minimal Supersymmetric Standard Model (MSSM) [74, 75]. The MSSM supermultiplets, superfields, and sparticles are examined in the following paragraphs and summarized in Table 2.2. The MSSM Lagrangian $\mathcal{L}_{\text{MSSM}}$ is constructed from these fields to include all SUSY interactions which satisfy $SU(3)_C \otimes SU(2)_L \otimes U(1)_Y$ gauge invariance, baryon and lepton number conservation, as well as including generalized soft SUSY breaking terms [20]. The resulting theory contains a large number of free parameters, 105 new in addition to the 19 of the SM for a total of 124, though most are used to control the details of soft SUSY breaking.

Sfermions

Each spin- $\frac{1}{2}$ SM fermion field forms a chiral supermultiplet with two spin-0 complex scalar boson fields, one for each of its left- and right-handed components. These scalar fermion partners are simply named sfermions and, like all superpartners, are represented by a tilde above their SM symbols, \tilde{f} . The left- and right-handed gauge eigenstates can mix to form mass eigenstates, but this is typically suppressed in the first two sfermion generations due to soft SUSY breaking conditions [20]. The gauge and mass eigenstates for all the MSSM sparticles are summarized in Table 2.3.

¹⁹ For $m_{\text{soft}} = 1 \text{ TeV}$, $\Delta m_H^2 \sim (470 \text{ GeV})^2$, much more reasonable than $\Delta m_H^2 \sim (10^{17} \text{ GeV})^2$.

²⁰ See [72] for another argument for a light stop.

Table 2.2: MSSM fields and their quantum numbers. Additional fermion generations and anti-particle supermultiplets omitted for simplicity. Adapted from [20].

Super-multiplets	Super-fields	Bosonic Fields	Fermionic Partners	SU(3) _C	SU(2) _L	U(1) _Y
gluon/gluino	\widehat{V}_8	g	\tilde{g}	8	1	0
gauge boson/ gaugino	\widehat{V} \widehat{V}'	W^\pm, W^0 B	$\widetilde{W}^\pm, \widetilde{W}^0$ \widetilde{B}	1	3	0
slepton/ lepton	\widehat{L} \widehat{E}^c	$(\tilde{\nu}_L, \tilde{e}_L)$ \tilde{e}_R^*	$(\nu, e^-)_L$ e_L^c	1	2	-1
squark/ quark	\widehat{Q} \widehat{U}^c \widehat{D}^c	$(\tilde{u}_L, \tilde{d}_L)$ \tilde{u}_R^* \tilde{d}_R^*	$(u, d)_L$ u_L^c d_L^c	3 $\bar{3}$ $\bar{3}$	2 1 1	$\frac{1}{3}$ $-\frac{4}{3}$ $\frac{2}{3}$
Higgs/ Higgsino	\widehat{H}_u \widehat{H}_d	(H_u^+, H_u^0) (H_d^0, H_d^-)	$(\widetilde{H}_u^+, \widetilde{H}_u^0)$ $(\widetilde{H}_d^0, \widetilde{H}_d^-)$	1 1	2 2	1 -1

Gauginos

The spin-1 SM gauge bosons form gauge supermultiplets with their spin- $\frac{1}{2}$ fermion partners (gauginos) named gluinos, winos, and bino respectively for gluons, W bosons, and the B . Following EWSB \widetilde{Z}^0 , $\tilde{\gamma}$ superpartner mass eigenstates are formed via mixing the \widetilde{W}^0 , \widetilde{B}^0 gauge eigenstates as in the SM. The fermionic gluinos are still members of a color-octet and participate in SU(3)_C QCD color gauge interactions.

Higgsinos

While finding the superpartners of the fermion and gauge boson SM fields is a relatively straight forward process, things are not as simple in the Higgs sector. Two Higgs supermultiplets, each consisting of a complex Higgs doublet [76], are required in the MSSM to avoid EW gauge anomalies and give mass to the up and down-type quarks. The Higgs supermultiplets, labeled up and down, differ from each other in $Y = \pm 1$,

which is necessary for the gauge anomaly created by one to be canceled by the other. The doublet within each supermultiplet is a doublet of $T_3 = \pm\frac{1}{2}$. Altogether, the SM doublets of the Higgs supermultiplets are (H_u^+, H_u^0) , (H_d^0, H_d^-) where the electric charges follow from $Q_{\text{EM}} = T_3 + \frac{1}{2}Y$ [20, 62].

Due to the structure of the theory, only the $Y = +1$ up Higgs supermultiplet has a Yukawa coupling to the up-type quarks thereby generating their masses, while the $Y = -1$ down supermultiplet couples to the down-type quarks and charged leptons. This can most clearly been seen in the form of the superpotential W_{MSSM} (2.35) with respect to the fields \widehat{H}_u , \widehat{H}_d .

$$W_{\text{MSSM}} = \lambda_d \widehat{Q} \widehat{H}_d \widehat{D}^c - \lambda_u \widehat{Q} \widehat{H}_u \widehat{U}^c + \lambda_e \widehat{L} \widehat{H}_d \widehat{E}^c + \mu \widehat{H}_u \widehat{H}_d \quad (2.35)$$

Of the eight degrees of freedom present in the SM Higgs doublets, three become longitudinal modes of the Z^0 and W^\pm through EWSB, while the remaining five form mass eigenstates; H^\pm , CP-even h^0 & H^0 , and CP-odd A^0 . By convention $m_{h^0} < m_{H^0}$, identifying h^0 with the 125 GeV Higgs and leaving the remaining four SM Higgs particles to be discovered. The superpartner Higgs states, named Higgsinos, also mix with the gauginos through EWSB, forming model-dependent neutralino, $\tilde{\chi}^0$, and chargino, $\tilde{\chi}^\pm$, mass eigenstates. The neutralino mass matrix M_N (2.36) [20] is a function of two soft SUSY breaking mass parameters M_1 , M_2 , Higgs VEVs $v_u = \sqrt{2} |\langle 0 | H_u^0 | 0 \rangle|$, $v_d = \sqrt{2} |\langle 0 | H_d^0 | 0 \rangle|$, Higgs mass parameter μ , and the $SU(2)_L \otimes U(1)_Y$ gauge couplings g , g' . Taking $W^T M_N W$, where W is unitary, we find a diagonal matrix of the neutralino masses. The neutralinos (charginos) are customarily labeled in order of increasing mass, $\tilde{\chi}_1^0 < \tilde{\chi}_2^0 < \tilde{\chi}_3^0 < \tilde{\chi}_4^0$ ($\tilde{\chi}_1^\pm < \tilde{\chi}_2^\pm$).

Table 2.3: MSSM sparticle gauge and mass eigenstates, assuming negligible mixing for the first two sfermion generations. Adapted from [62].

Names	Spin	<i>R</i> -Parity	Gauge Eigenstates	Mass Eigenstates
Higgs bosons	0	+1	$H_u^0 \ H_d^0 \ H_u^+ \ H_d^-$	$h^0 \ H^0 \ A^0 \ H^\pm$
			$\tilde{u}_L \ \tilde{u}_R \ \tilde{d}_L \ \tilde{d}_R$	(same)
squarks	0	-1	$\tilde{s}_L \ \tilde{s}_R \ \tilde{c}_L \ \tilde{c}_R$	(same)
			$\tilde{t}_L \ \tilde{t}_R \ \tilde{b}_L \ \tilde{b}_R$	$\tilde{t}_1 \ \tilde{t}_2 \ \tilde{b}_1 \ \tilde{b}_2$
			$\tilde{e}_L \ \tilde{e}_R \ \tilde{\nu}_e$	(same)
sleptons	0	-1	$\tilde{\mu}_L \ \tilde{\mu}_R \ \tilde{\nu}_\mu$	(same)
			$\tilde{\tau}_L \ \tilde{\tau}_R \ \tilde{\nu}_\tau$	$\tilde{\tau}_1 \ \tilde{\tau}_2 \ \tilde{\nu}_\tau$
neutralinos	$\frac{1}{2}$	-1	$\tilde{B}^0 \ \tilde{W}^0 \ \tilde{H}_u^0 \ \tilde{H}_d^0$	$\tilde{\chi}_1^0 \ \tilde{\chi}_2^0 \ \tilde{\chi}_3^0 \ \tilde{\chi}_4^0$
charginos	$\frac{1}{2}$	-1	$\tilde{W}^\pm \ \tilde{H}_u^\pm \ \tilde{H}_d^\pm$	$\tilde{\chi}_1^\pm \ \tilde{\chi}_2^\pm$
gluino	$\frac{1}{2}$	-1	\tilde{g}	(same)
goldstino (gravitino)	$\frac{1}{2} \left(\frac{3}{2}\right)$	-1	\tilde{G}	(same)

$$M_N = \begin{pmatrix} M_1 & 0 & -\frac{1}{2}g'v_d & \frac{1}{2}g'v_u \\ 0 & M_2 & \frac{1}{2}gv_d & -\frac{1}{2}gv_u \\ -\frac{1}{2}g'v_d & \frac{1}{2}gv_d & 0 & -\mu \\ \frac{1}{2}g'v_u & -\frac{1}{2}gv_u & -\mu & 0 \end{pmatrix} \quad (2.36)$$

2.2.4 *R*-Parity

In the SM baryon number, B , and lepton number, L , are conserved due to the lack of possible renormalizable Lagrangian terms which violate $B-L$ symmetry. However, this is not the case for SUSY in general, as gauge invariant $B-L$ violating operators can be constructed from SM fields and their superfield partners. If allowed, such operators would lead to proton lifetimes orders of magnitude shorter than the measured $p \rightarrow e^+\pi^0$ mean lifetime of $> 8.2 \times 10^{33}$ years [20]. To match the experimentally

observed $B-L$ conservation, including its violation by non-perturbative EW effects, we impose an additional symmetry on $\mathcal{L}_{\text{MSSM}}$ in the form of multiplicative R -parity invariance (2.37) [77], where S is the spin of the particle in question.

$$R = (-1)^{3(B-L)+2S} \quad (2.37)$$

All SM particles have R -parity $R = +1$, while all SUSY squarks, sleptons, gauginos, and Higgsinos have $R = -1$. R -parity conservation has many important consequences beyond just fixing $B-L$ conservation: SM collisions can only produce even numbers of sparticles, SUSY states can never fully decay to SM particle final states, and, with nothing else to decay to, the lightest supersymmetric particle (LSP) is absolutely stable. Additionally, if the LSP is EM and QCD neutral, as implied by cosmological constraints [78], it will only weakly interact with SM particles, making it a DM candidate [67, 68] which appears as missing transverse energy $E_{\text{T}}^{\text{miss}}$ in collider experiments.

2.2.5 Gauge Coupling Unification

In the SM the EM and weak interactions are unified into a single $\text{SU}(2)_L \otimes \text{U}(1)_Y$ EW interaction at high energies. Simultaneously, their running g and g' gauge couplings converge via renormalization. Unfortunately, due to the particular particle content of the SM, the $\text{SU}(3)_C$ strong interaction gauge coupling g_S does not converge on the same scale. Intriguingly, including the additional sparticles of the MSSM in the renormalization group loops unifies²¹ all three interaction couplings at a scale $M_U \sim 1.5 \times 10^{16}$ GeV [62, 79, 80] approaching M_P as shown in Figure 2.11. This may only be coincidental, or it may be an inkling of a higher order grand unified theory (GUT) [81, 82, 83, 84] providing additional motivation for studying SUSY.

²¹ The convergence is not exact, with the $\text{SU}(3)_C$ strong coupling landing slightly off the intersection of the other two, but this is typically explained as an artifact of new particles on the M_U scale [62].

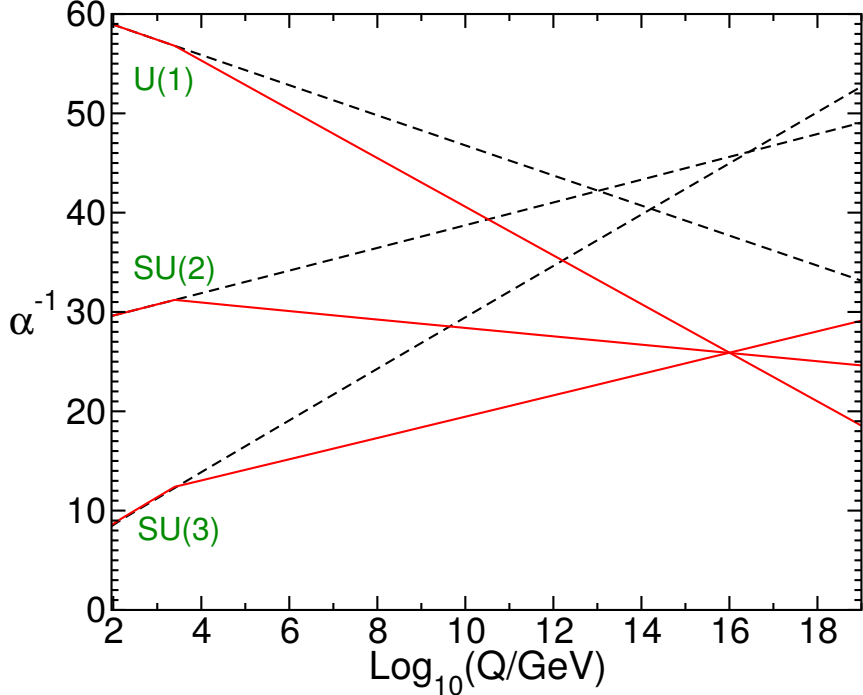


FIGURE 2.11: Running of the inverse gauge couplings $\alpha^{-1} = (g^2/4\pi)^{-1}$ in the SM (dashed black) and MSSM (solid red) calculated with two-loop renormalization groups at Q GeV. In the MSSM all three couplings unify around $M_U \sim 1.5 \times 10^{16}$ GeV. Adapted from [62].

2.2.6 Simplified SUSY Models

Trying to discover SUSY by searching for the full MSSM with its 124 free parameters is a daunting prospect. Fortunately for experimentalists, we can reduce the complexity considerably by utilizing simplified models [85, 86] where the majority of sparticles are assumed to be of high enough mass that they can be safely integrated out of the effective field theory. The few sparticles that remain are chosen with regards to the particular experimental signature under investigation while still taking naturalness considerations into account. The results from a search for one simplified model can often then be generalized to other models via methods such as RECAST [87].

The simplest model possible only consists of pair-produced LSPs, which has the additional benefit of requiring the lowest production center-of-mass energy. This is not,

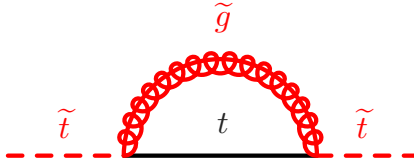


FIGURE 2.12: Example diagram of \tilde{t} mass corrections due to a \tilde{g} loop, which implies a light mass \tilde{g} due to naturalness considerations. Sparticle lines are drawn in red.

however, an optimal search strategy at the LHC due to its relatively low production cross section. Being a pp collider, the LHC is ultimately colliding color-carrying quarks and gluons, which couple strongly to the color-carrying squarks and gluinos, unlike the colorless LSP. Motivated by the naturalness arguments of Section 2.2.2 we include a light stop \tilde{t}_1 of a few TeV in the simplified model. Similar naturalness arguments [88,89] can be made for a light gluino \tilde{g} of $m_{\tilde{g}} > m_{\tilde{t}_1}$ as it corrects the scalar \tilde{t} mass through diagrams such as Figure 2.12. While \tilde{t}_1 and \tilde{g} are expected to have comparable TeV scale masses, gluinos have a higher pair production cross section due to their increased color charge as can be seen in Figure 2.13. To complete the model we must identify an EM and QCD neutral LSP. The lightest neutralino $\tilde{\chi}_1^0$ matches this description and should be light overall to satisfy cosmological constraints [78].

The simplified model resulting from these assumptions consists of three sparticles; \tilde{g} , \tilde{t}_1 , and $\tilde{\chi}_1^0$, with two potential mass orderings as shown in Figure 2.14. To search for evidence of this model at the LHC we may look for \tilde{g} pair production, taking advantage of the large cross section, decaying to a final state of four tops plus E_T^{miss} via $\tilde{g} \rightarrow \tilde{t}\tilde{t}_1 \rightarrow t\bar{t}\tilde{\chi}_1^0$ with the \tilde{t}_1 being on or off-shell as in Figure 2.15. The four tops subsequently decay to a multi- b final state with varying numbers of leptons as described in Section 2.1.4. While it is possible for the \tilde{g} pair to decay to other final states, to simplify the search we assume the $\tilde{g} \rightarrow t\bar{t}\tilde{\chi}_1^0$ branching ratio is 100 %. In the event of a SUSY discovery, multiple \tilde{g} searches in different final states, each making

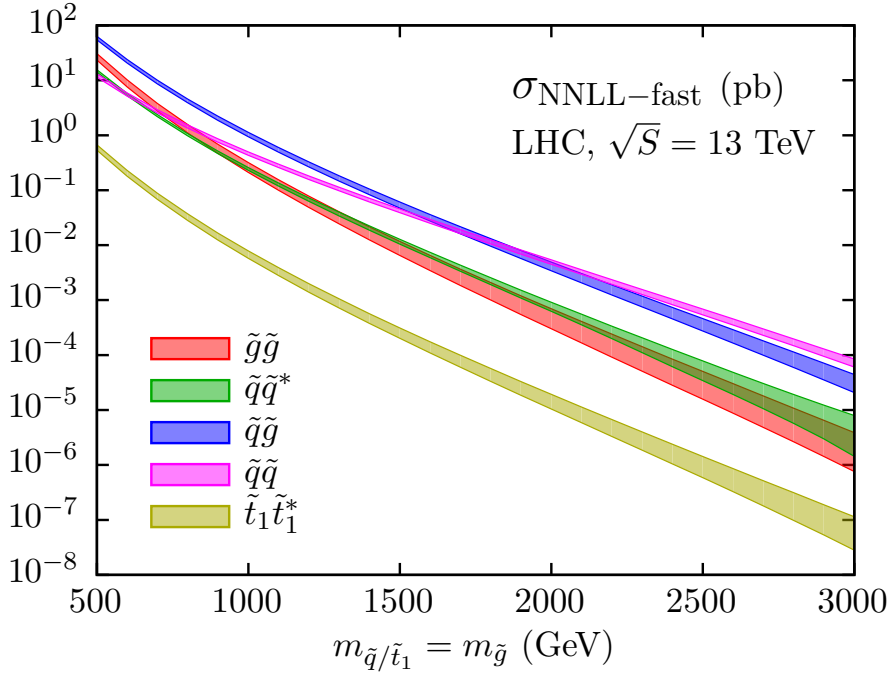


FIGURE 2.13: NNLO_{Approx}+NNLL \tilde{q} and \tilde{g} production cross sections at the LHC for $\sqrt{s} = 13$ TeV [90]. $\tilde{g}\tilde{g}$ has a higher pair production cross section than $\tilde{t}_1\tilde{t}_1^*$ due to the larger color charge, with both falling below inclusive $\tilde{q}\tilde{q}$, $\tilde{q}\tilde{g}$, and $\tilde{q}\tilde{q}^*$ production due to the increase in multiplicity. Error bands represent the theoretical uncertainty.

their own 100 % branching ratio assumption, could be linearly combined into a single measurement. For the on-shell decay where $m_{\tilde{g}} > m_{\tilde{t}_1}$ we can describe the entire simplified model with only three parameters; $m_{\tilde{g}}$, $m_{\tilde{t}_1}$,²² and $m_{\tilde{\chi}_1^0}$. In the off-shell decay where $m_{\tilde{t}_1} > m_{\tilde{g}}$ we can further reduce this to two parameters by assuming $m_{\tilde{t}_1}$ is an appropriately large²³ constant such as 5 TeV, thereby removing it from consideration. In this case $\tilde{g} \rightarrow t\bar{t}\tilde{\chi}_1^0$ can be modeled as an effective three-body decay with the final state tops having identical kinematic distributions.

²² The virtual \tilde{t}_1 alters the kinematics of the final state t and \bar{t} as a function of $m_{\tilde{t}_1}$.

²³ Setting $m_{\tilde{t}_1}$ to be a very high value, such as $\mathcal{O}(100)$ TeV, will suppress this decay channel for the \tilde{g} , thus it is best to keep $m_{\tilde{t}_1}$ $\mathcal{O}(1)$ TeV).

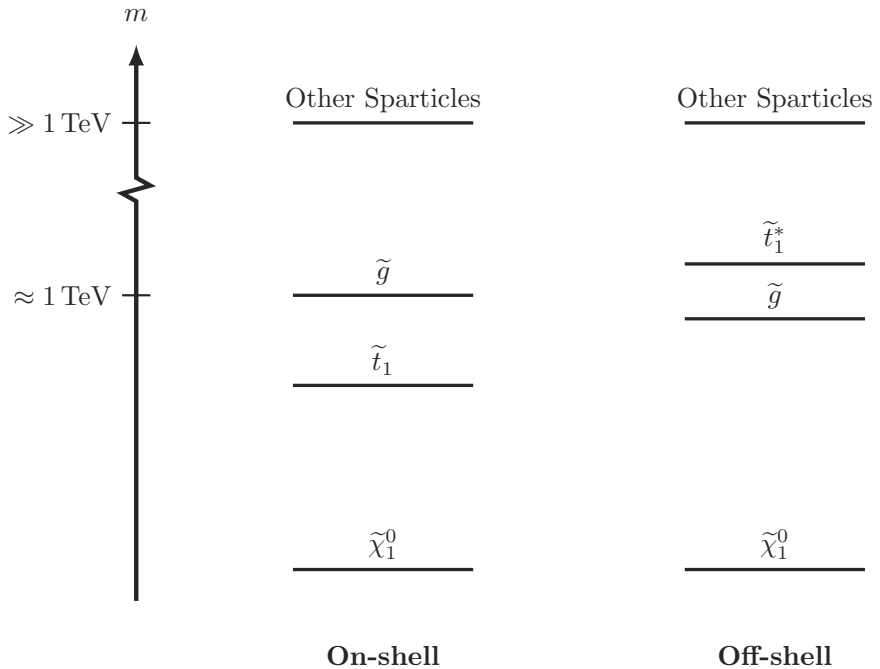


FIGURE 2.14: Two potential mass orderings for the simplified SUSY model corresponding to on and off-shell \tilde{t} decays.

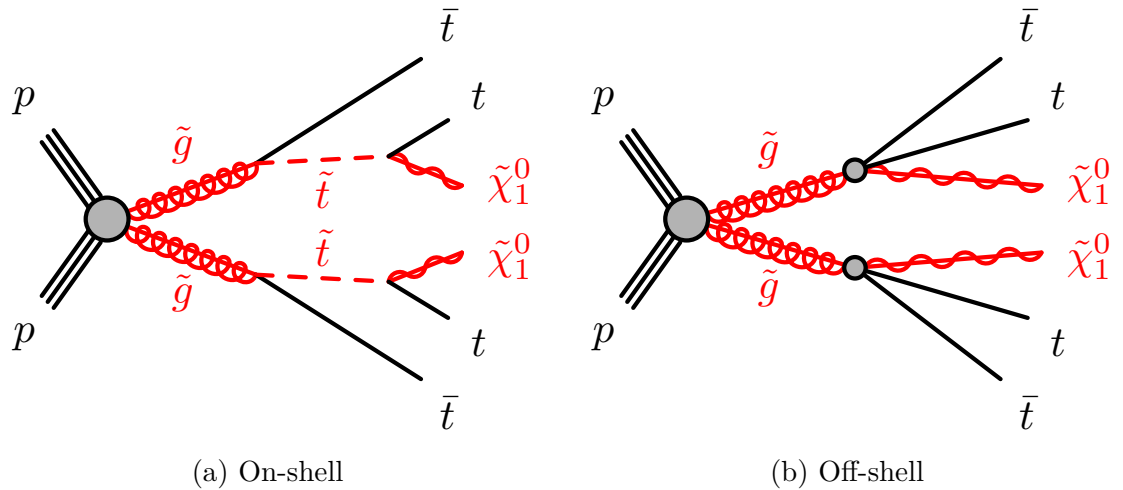


FIGURE 2.15: Feynman diagrams of $\tilde{g} \rightarrow \tilde{t}\tilde{t}_1 \rightarrow t\bar{t}\tilde{\chi}_1^0$ decay in a simplified SUSY model for on and off-shell \tilde{t}_1 . The final state consists of four tops plus E_T^{miss} in the form of two $\tilde{\chi}_1^0$ LSPs.

3

The LHC and ATLAS Experiment

3.1 The Large Hadron Collider (LHC)

As the name implies, the Large Hadron Collider (LHC) [91] is the largest particle accelerator ever constructed, considered by some to be the largest single machine in the world. The main LHC ring has a circumference of 27 km and is located ~ 100 m underground near Geneva, Switzerland at the European Organization for Nuclear Research (CERN), illustrated in Figure 3.1. The massive size of the accelerator is required to produce pp collisions at a center-of-mass energy $\sqrt{s} = 13$ TeV, the highest energy achieved by a collider. This energy is built up through a system of boosters shown in Figure 3.2, resulting in counter-circulating 6.5 TeV proton beams in the LHC itself. Collisions take place at four interaction points (IP) around the ring for the ATLAS, ALICE, CMS, and LHCb experiments.

At the heart of the LHC is its superconducting magnetic system consisting of 1232 8 T niobium-titanium (NbTi) dipole magnets used to direct protons around the ring, along with hundreds of beam focusing quadrupole and higher magnets. The actual acceleration is done in superconducting radio frequency (RF) cavities, 8 per beam,

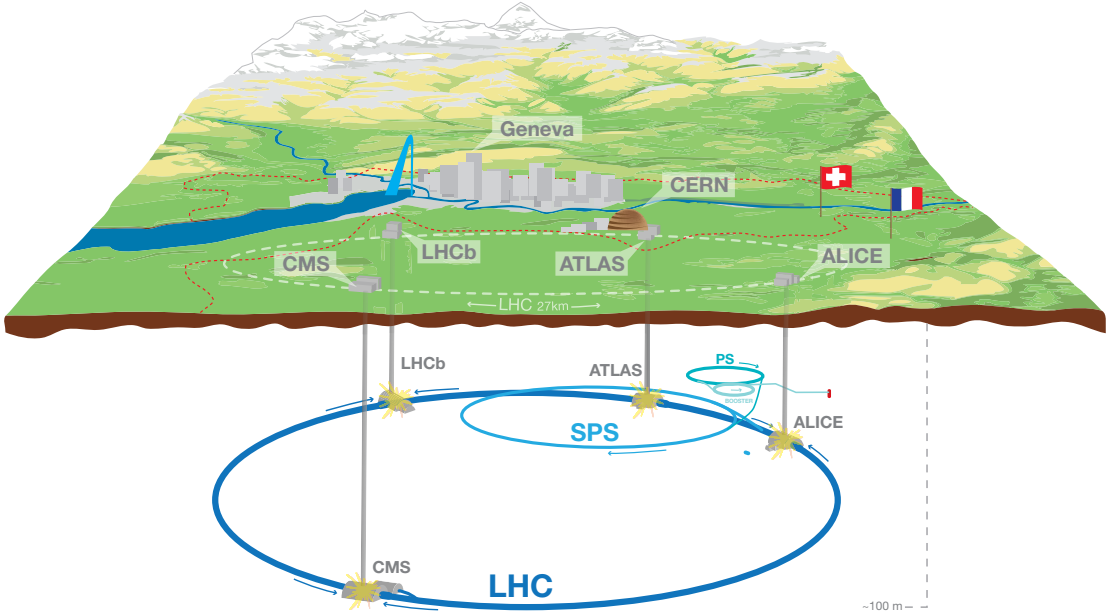


FIGURE 3.1: An overview of the LHC in relation to the surrounding geography [92].

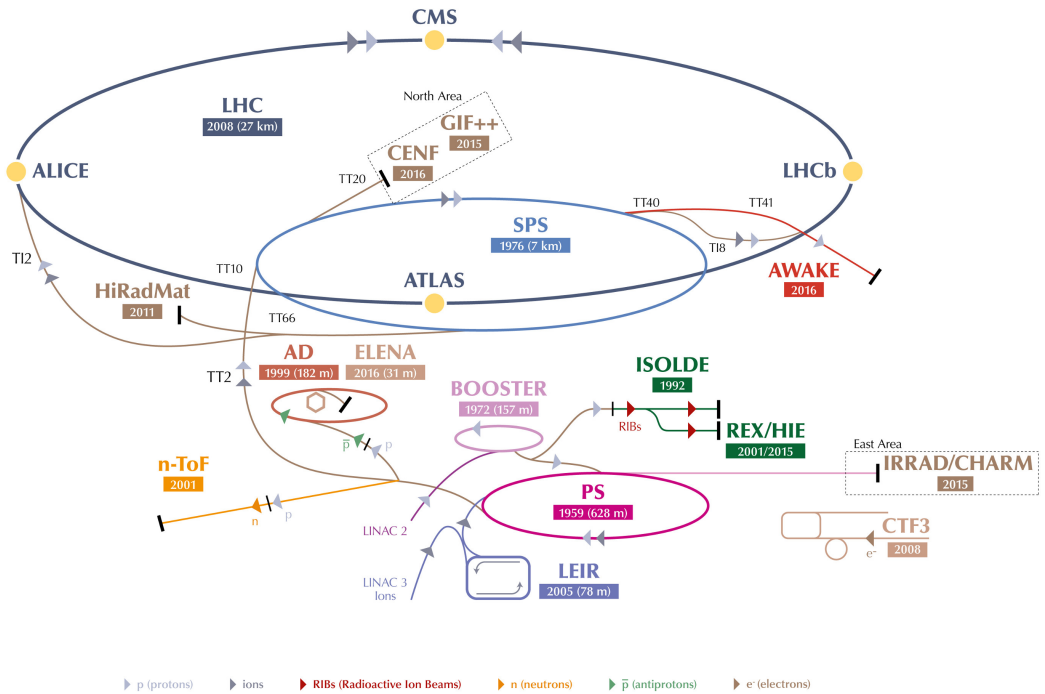


FIGURE 3.2: A schematic view of the CERN accelerator complex [93].

operating at 400 MHz and providing a 5.5 MV m^{-1} acceleration gradient [91]. During Run 2 [94] the LHC was filled with $n_b \sim 2000$ bunches of $N_b \sim 1.1 \times 10^{11}$ protons, spaced out by 25 ns, *i.e.* 10 RF periods. The beam itself contains $\approx 250 \text{ MJ}$ of stored energy, which when combined with the magnet system brings the total stored energy in the LHC to $\sim 1 \text{ GJ}$.

3.1.1 Luminosity

Particle physics is fundamentally concerned with measuring the probability of a quantum mechanical process occurring. Theorists can calculate these probabilities for scattering processes as cross sections¹ σ , but in order to find the experimental expected number of observed events we must also quantify the amount of times an interaction could potentially occur. This is done via the integrated luminosity L (3.1a) where the expected number of events is then simply $N_{\text{event}} = \sigma_{\text{event}} L$.

$$L = \int \mathcal{L} dt \quad (3.1a)$$

$$\mathcal{L} = \frac{N_b^2 n_b f_{\text{rev}} \gamma_r}{4\pi \epsilon_n \beta^*} \times F \quad (3.1b)$$

The instantaneous luminosity \mathcal{L} (3.1b) in turn depends on the parameters of the colliding beams; the frequency of revolution f_{rev} , the relativistic gamma factor γ_r , the normalized beam emittance ϵ_n , the beta function at the IP β^* , and a geometric factor related to the beam crossing angle F [91]. Together ϵ_n and β^* describe the elliptical area of the beam at the IP, hence their location in the denominator. In Run 2 $\mathcal{L}_{\text{max}} \sim 10^{-5} \text{ fb}^{-1} \text{ s}^{-1}$ [94] for a total of $L = 148.5 \text{ fb}^{-1}$ recorded by ATLAS in 2015–2018 [95].

¹ Cross sections have units of area typically expressed in barns, $1 \text{ b} = 10^{-28} \text{ m}^2$, to better handle the very low cross sections of many processes.

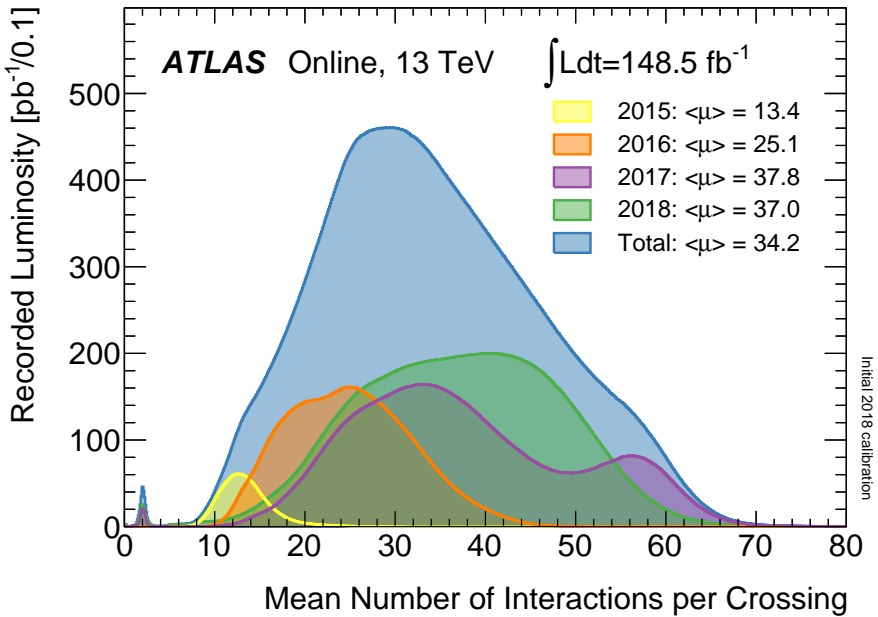


FIGURE 3.3: The mean number of interactions per crossing $\langle\mu\rangle$, *i.e.* pileup, in ATLAS for 2015–2018 [95]. Changing LHC operating conditions over time, along with the decay of $\langle\mu\rangle$ within a beam fill, are responsible for the spread of values.

3.1.2 Pileup

In order to increase luminosity the LHC is designed to pack as many protons as possible into as small a volume as possible. This results in a high \mathcal{L} due to multiple pp interactions per bunch crossing, also known as in-time pileup. Pileup is measured by the mean number of interactions per crossing $\langle\mu\rangle$, and by the number of interaction vertices in a single event N_{vtx} . The LHC provided ATLAS with a wide range of $\langle\mu\rangle$ values over the course of Run 2, from 10 to upwards of 60 depending on the year as shown in Figure 3.3. The spread of $\langle\mu\rangle$ values is brought on by changing LHC operating conditions, as well as the natural decay in the number of interactions per crossing within the lifetime of a single beam fill.

Along with in-time pileup, LHC experiments such as ATLAS must also contend with out-of-time pileup where particles from past crossings are still being measured by the detector hardware as new crossings take place. Whatever the source, physics

analyses must each study the effects of pileup on their measurements. Fortunately, pileup has been found to have a negligible impact on the results presented in this dissertation.

3.2 The ATLAS experiment

The ATLAS experiment [96] is one of two general purpose particle physics detectors at the LHC, joined by the CMS experiment across the ring. Design work on the detector began in the early 1990s followed by construction in the mid-2000s. Since the beginning of high energy pp collisions in 2009² ATLAS has produced hundreds of scientific results, including the joint discovery of the Higgs boson with CMS in 2012. Today ATLAS continues to test the physics of the SM at the highest energies to date, while searching for what may lie beyond.

To best measure the many types of final state particles radiating outward from a collision, the ATLAS detector consists of multiple specialized sub-detectors arranged in layers around the IP, illustrated in Figure 3.4. Starting near the beam pipe, charged particle tracking is performed by the Insertable B-Layer (IBL), pixel detector, Semiconductor Tracker (SCT), and Transition Radiation Tracker (TRT); collectively known as the inner detector (ID). The ID is enclosed by a superconducting solenoid magnet producing a 2 T axial field. This field strength is required to appreciably curve the highly energetic charged particles, thereby allowing for momentum measurements. Beyond the solenoid magnet particle energies are measured using two calorimeters; the electromagnetic (ECAL) and hadronic (HCAL). At the outermost layer, the Muon Spectrometer (MS) sits within the eponymous³ 0.2–3.5 T superconducting toroid magnets, tracking muons which are poorly measured in the ID and calorimeters.

² Unfortunately delayed by a destructive 2008 magnet quenching incident in the LHC brought on by an electrical fault in one of the superconducting interconnections [97].

³ ATLAS: A Toroidal LHC ApparatuS.

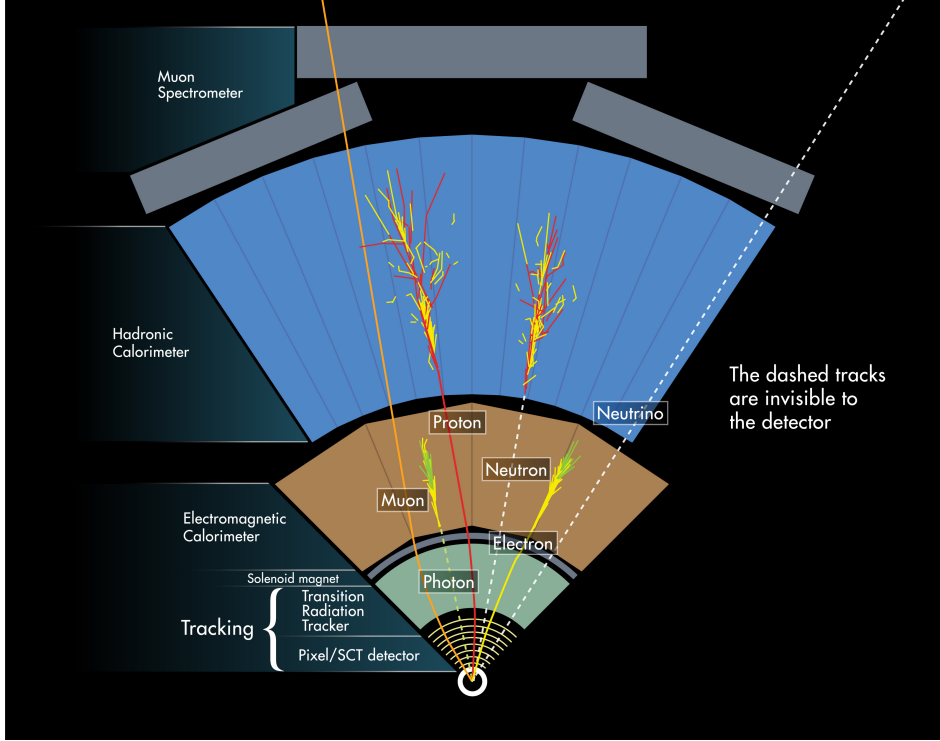


FIGURE 3.4: A schematic representation of the ATLAS sub-detectors [98]. Charged particles, such as p and e , are tracked by the inner detector (ID) within a solenoidal magnetic field. Particle energies are then measured in the Electromagnetic (ECAL) or Hadronic (HCAL) Calorimeters, depending on if they primarily experience EM interactions; γ , e , or strong interactions; p , n . The Muon Spectrometer (MS) located within a toroid magnet system tracks muons. Neutrinos escape undetected as missing energy. Track curvature has been vastly exaggerated for illustration.

A high frequency trigger and data acquisition system (TDAQ) reads out all of the sub-detectors, identifying interesting events and saving them to disk for later analysis.

3.2.1 Coordinate System

ATLAS utilizes a right-handed coordinate system, illustrated in Figure 3.5, with the x -axis directed into the center of the LHC ring and the y -axis directed upward out of the ground. As is common in particle physics experiments the pseudorapidity η (3.2a) is frequently used in lieu of the polar angle θ . The transverse xy -plane corresponds to $\eta = 0$, the most forward detector components stop at $|\eta| \approx 5$, and the beam line aligns with $|\eta| \rightarrow \infty$. The pseudorapidity can also be defined in terms of momentum (3.2b)

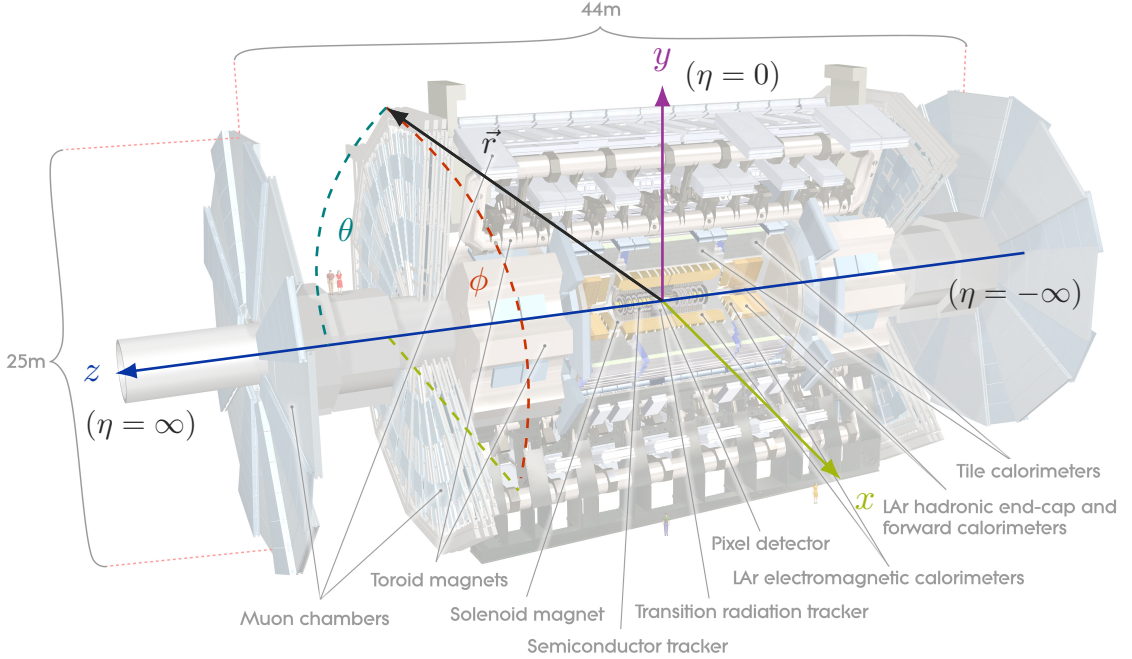


FIGURE 3.5: Coordinate system of the ATLAS detector. The x -axis points to the center of the LHC ring, while the y -axis is directed upward, and the z -axis is along the LHC beam line. ϕ is the azimuthal angle from the xy -plane, while θ is the polar angle from the z -axis. The pseudorapidity η is defined in terms of θ (3.2a). Image of ATLAS from [99].

and approximates the rapidity y (3.2c) for directly observed high energy particles where $E \gg m$ as is almost always the case at the LHC.

$$\eta = -\ln \left(\tan \frac{\theta}{2} \right) \quad (3.2a)$$

$$\eta = \frac{1}{2} \ln \left(\frac{|\vec{p}| + p_x}{|\vec{p}| - p_x} \right) \quad (3.2b)$$

$$y = \frac{1}{2} \ln \left(\frac{E + p_z}{E - p_z} \right) \quad (3.2c)$$

A collision's center-of-mass momentum along the beam line, p_z , is not zero as the actual interacting parton momentum fractions are uncorrelated. Rapidity, and thus

pseudorapidity, is a particularly useful quantity in these circumstances as differences in rapidity $\Delta y \approx \Delta\eta$ are invariant under the Lorentz boosts along z caused by $p_z \neq 0$. For the same reason the separation of two objects is often defined in terms of η and azimuthal angle ϕ as ΔR (3.3a). The transverse momentum of a collision p_T (3.3b) is approximately zero, leading to its extensive use when describing a particle's four-momentum. The transverse energy E_T , and missing transverse energy E_T^{miss} , are similarly useful variables.

$$\Delta R = \sqrt{(\Delta\eta)^2 + (\Delta\phi)^2} \quad (3.3a)$$

$$p_T = p \sin \theta = \frac{p}{\cosh \eta} \quad (3.3b)$$

3.2.2 Inner Detector (ID)

The ID, made up of the IBL, pixel detector, SCT, and TRT as shown in Figure 3.6, occupies the innermost $\approx 1\text{ m}$ of ATLAS. This central location allows for precise charged particle tracking in the solenoidal magnetic field with minimal interference from non-active support material. Once a track has been reconstructed from the many hits it leaves in the different layers of the ID, the originating vertex position can be measured along with the momentum and sign of the charge. The TRT additionally provides particle identification (PID) information for electrons.

Insertable B-Layer (IBL), Pixel Detector, and Semiconductor Tracker (SCT)

The IBL [101, 102], pixel detector [103, 104], and SCT [105, 106] are all semiconductor detectors chosen for their high spatial resolution and ability to be radiation hardened. When a charged particle passes through a semiconductor it leaves an ionized track behind as shown in Figure 3.7. The charge carriers, negative electrons or positive holes respectively for n or p-type doped semiconductors, then produce ionization currents under an applied bias voltage which can be picked up by readout electronics.

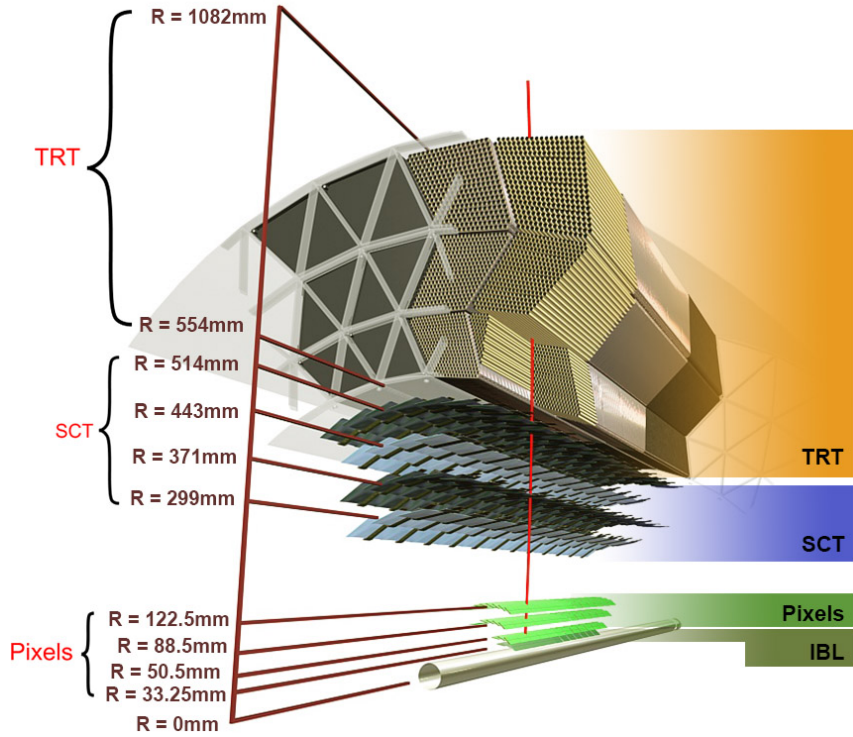


FIGURE 3.6: The ATLAS inner detector [100].

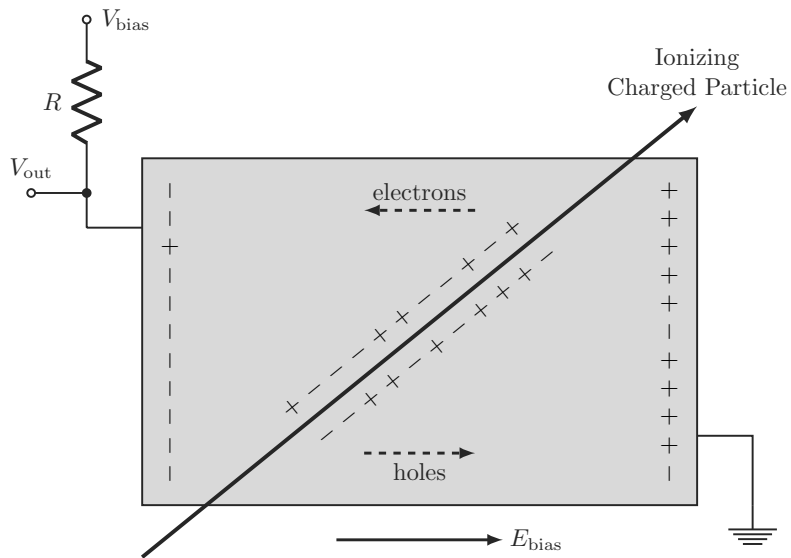


FIGURE 3.7: Simplified operating schematic of a semiconductor detector. The charge carriers left in the wake of an ionizing particle produce detectable currents when the semiconductor is put under a bias voltage. The doping details of the semiconductor shown in grey are omitted for simplicity as they vary between sub-detectors.

The pixel detector is made up of three barrel layers and three endcap disks. Each detector module is finely segmented with a minimum pixel size in cylindrical coordinates of $R - \phi \times z = 50\text{ }\mu\text{m} \times 400\text{ }\mu\text{m}$ producing an intrinsic accuracy of $10\text{ }\mu\text{m} \times 115\text{ }\mu\text{m}$. Between the layers and disks there are a staggering $\sim 80 \times 10^6$ readout channels [96]. The IBL can be thought of as a fourth, innermost, pixel layer and was added to ATLAS in 2014 to improve tracking precision and b -tagging performance, while preparing for the higher luminosities of Run 2 and beyond. It contributes $\sim 12 \times 10^6$ additional pixel readout channels as well. Together the IBL and pixel detector give ATLAS a vertex reconstruction resolution of $11\text{ }\mu\text{m}$ in x and y , and $24\text{ }\mu\text{m}$ in z [101].

To reduce costs and readout bandwidth in the larger volume outside the pixel detector, the four layers of the SCT utilize double-sided strip detector modules. The strips on either side of a module are set at a 40 mrad stereo angle to one another, allowing for 2D reconstruction in the module plane without pixels. This simplifies fabrication and lowers the total readout channels to $\sim 6 \times 10^6$, at the cost of a reduced intrinsic accuracy of $17\text{ }\mu\text{m} \times 580\text{ }\mu\text{m}$ per module [96]. The SCT and pixel endcaps provide full coverage up to $|\eta| < 2.5$ as illustrated in Figure 3.9.

Transition Radiation Tracker (TRT)

The TRT [107, 108, 109] is a gas drift tube detector constructed out of thousands of polyimide straws 4 mm in diameter. When a charged particle travels through a straw it ionizes pockets of gas along its track. These ionization clusters are drifted to a central wire under high voltage where they initiate cascades in the increasing electric field and are collected. By measuring the drift time of collected charge, the distance from the track to the wire can be estimated, as demonstrated in Figure 3.8.

The large cylindrical ID volume of $R = 554\text{--}1092\text{ mm}$ covered by the TRT allows it to capture many more hits per track, $\approx 35\text{--}40$, than the semiconductor detectors

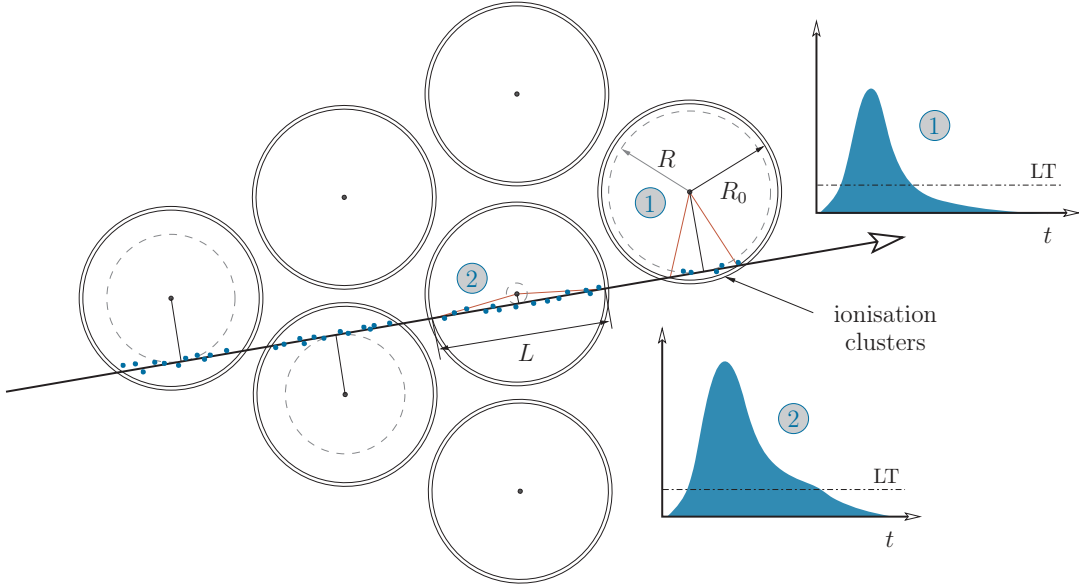


FIGURE 3.8: Illustration of track measurements in the ATLAS TRT [110]. As a charged particle travels through the TRT straws it forms ionization clusters in the enclosed gas. The ionized charges are drifted to a central wire under high voltage where they are collected. Clusters formed at a larger radius (1) all travel similar distances to the wire, leading to a shorter time over threshold when compared to clusters from a smaller radius (2) which must cover a wider range of distances.

alone, greatly improving the performance of track pattern recognition. To efficiently instrument such a sizable volume the TRT straws are quite long, 144 cm in the barrel aligned parallel to the beam line with the wires divided in two at $\eta = 0$, and 37 cm aligned radially in the endcap wheels as shown in Figure 3.9. This covers $|\eta| < 2$ with a total of $\sim 350\,000$ readout channels. Due to length of the straws, the TRT only provides $R - \phi$ hit measurements at an intrinsic accuracy of $130\,\mu\text{m}$ per straw [96].

Along with measuring hits the TRT also performs a PID function for electrons. Relativistic charged particles entering a TRT straw emit transition radiation (TR) photons of a few keV which are detected through the same charge ionization process as tracks. The TR itself is caused by the particle's EM fields being forced to satisfy boundary conditions between the gas and surrounding material of different dielectric

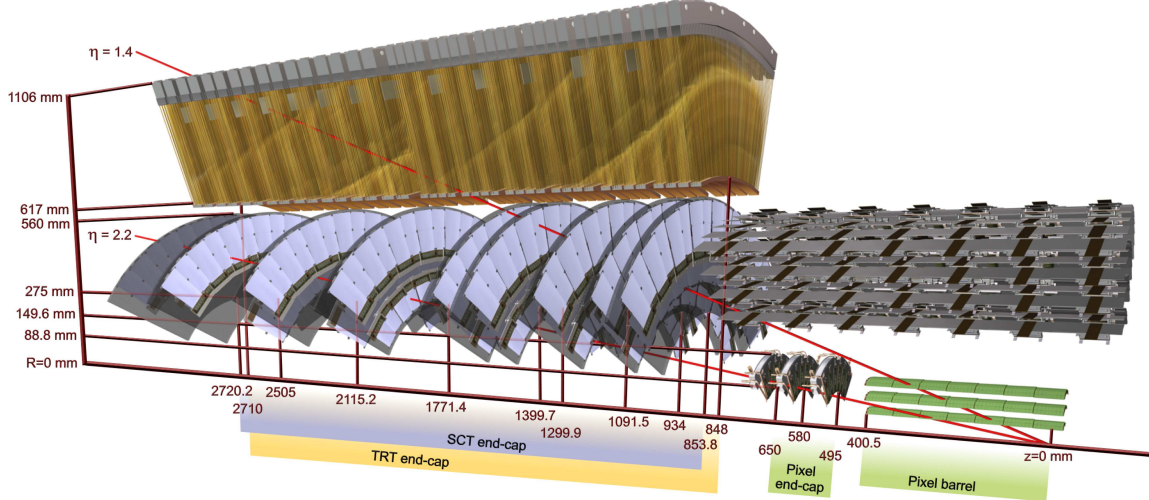


FIGURE 3.9: ATLAS ID endcaps [96]. The pixel and SCT cover up to $|\eta| < 2.5$, while the TRT covers $|\eta| < 2$. Two $p_T = 10$ GeV tracks are displayed in red. The $\eta = 1.4$ track leaves hits in the IBL (not shown), three pixel barrel layers, four SCT endcap disks, and ≈ 40 straws the TRT endcap wheels. At $\eta = 2.2$ the track only intersects the IBL, first pixel barrel layer, two pixel endcap disks, and four SCT endcap disks.

constants. The intensity of the TR, and resulting ionization, is proportional to the Lorentz factor $\gamma = E/m$ [111], and thus for a particular amplitude of collected charge we can identify the particle by mass. In practice this allows the TRT to identify electrons from other particles due to their very light masses. In order to increase PID efficiency the excellent TR absorber Xe is used as the active gas⁴ while polypropylene radiator material is placed around the straws. The TR photons deposit much more energy than a track and can be distinguished with a high threshold of 6–7 keV versus the track’s low threshold of 250–300 eV.

3.2.3 Calorimeters

The ATLAS calorimeter system [112, 113, 114] is split into multiple electromagnetic and hadronic sub-detectors, as illustrated in Figure 3.10, collectively providing hermetic coverage out to $|\eta| < 4.9$. All of the calorimeters used in ATLAS are non-

⁴ Xe readily absorbs TR photons with energies from 6–15 keV [108], but is prohibitively expensive in Run 2 after irreparable gas leaks formed in the TRT. The leaking regions are now filled with significantly less costly Ar, sacrificing some PID performance in the process [109].

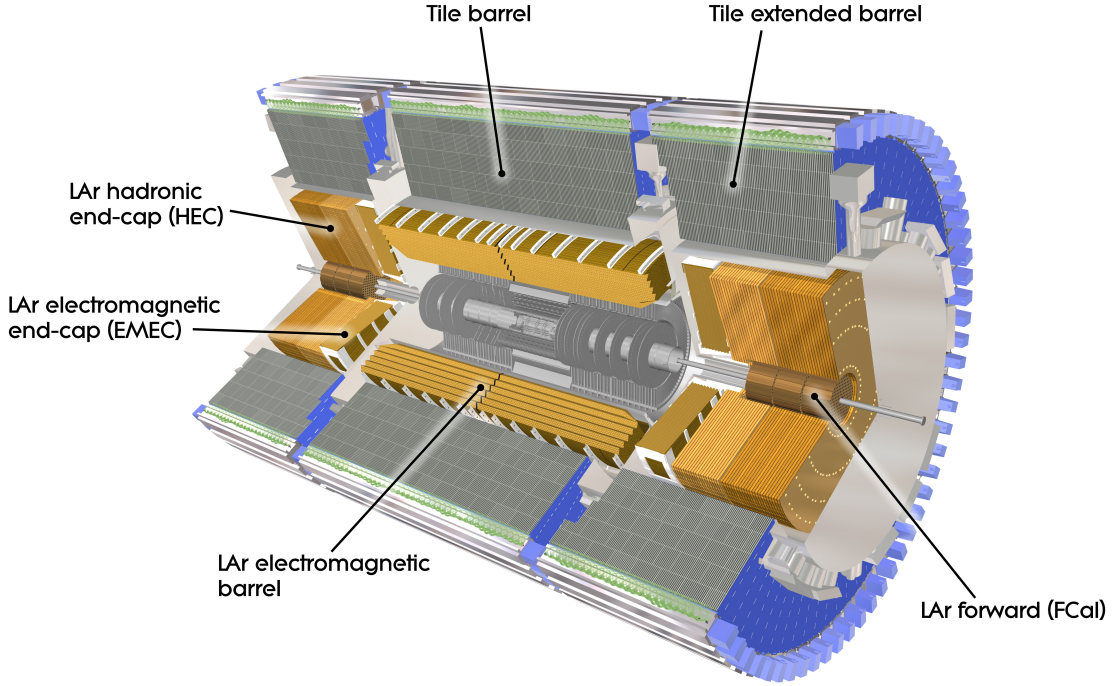


FIGURE 3.10: The ATLAS calorimeter system [116].

compensating sampling calorimeters, constructed out of alternating layers of dense absorbing material, such as lead or steel, and active detector material. The absorbing layers slow down incoming particles and promote showering while the active material samples the energy of the resulting showers, through ionization or scintillation in the case of ATLAS. This process repeats itself numerous times through the layers of the calorimeters until all particles, excluding muons and neutrinos, are stopped with their energy fully measured. Energy is lost in the absorbing layers requiring careful calibration of the detector response in order to recover the original particle's energy. Fluctuations in the development of showers in the absorbing layers put a limit on the calibrated energy resolution for sampling calorimeters [115], but the resulting performance is satisfactory and the simple design lowers complexity and cost.

Electromagnetic Calorimeter (ECAL)

The electromagnetic calorimeter (ECAL) measures the energy of photons and electrons in EM showers and is the first layer of the ATLAS calorimeter system. It consists of three major components of a similar lead-liquid Argon (LAr) design; the barrel covering $|\eta| < 1.475$, outer wheel covering $1.375 < |\eta| < 2.5$, and inner wheel covering $2.5 < |\eta| < 3.2$. The ECAL uses an accordion style geometry for its lead-LAr layers in order to provide ϕ symmetry without azimuthal cracks, and is itself divided into two or three radial segments of different $\Delta\eta \times \Delta\phi$ granularities depending on location [96] as shown in Figure 3.11. The calorimeter cell size can be safely increased at larger radii due to the growing lateral spread of the showers. The outermost layer is read out in $\Delta\eta \times \Delta\phi \approx 0.1 \times 0.1$ trigger towers by the first level of the trigger system.

At high energies photons undergo e^+e^- pair production while electrons radiate bremsstrahlung photons. Between these two effects an EM shower of additional photons and electrons is created, illustrated in Figure 3.12, spreading out the original particle's energy until it can be easily measured. An EM shower in the ECAL ionizes Ar atoms which are drifted and recorded on electrode plates in a similar manner as gas ions in the TRT. The longitudinal length scale of an EM shower in a particular material is described by the radiation length⁵ X_0 . The ECAL has a minimum radial thickness of $22X_0$ to ensure it captures EM showers in their entirety. The measured fractional energy resolution in the ECAL barrel (3.4) consists of an energy dependent stochastic term due to EM shower fluctuations, and a 0.17% constant term resulting from local non-uniformities summed in quadrature [96]. For ~ 100 GeV electrons the energy resolution is $\sim 1\%$ which improves with increasing energy.

⁵ For electrons, the radiative energy loss can be described as $\frac{dE}{dx} = -\frac{1}{X_0} E$ where the radiation length X_0 is the distance traveled for E to be reduced by a factor of $1/e$. For photons, the pair production probability can be described as $\frac{dw}{dx} = \frac{1}{\lambda_{\text{prod}}} \exp(-x/\lambda_{\text{prod}})$ where $\lambda_{\text{prod}} = \frac{9}{7}X_0$ [115].

$$\frac{\sigma(E)}{E} = \frac{10\%}{\sqrt{E \text{ (GeV)}}} \oplus 0.17\% \quad (3.4)$$

Hadronic Calorimeter (HCAL)

The hadronic calorimeter (HCAL) encompasses the ECAL and measures the energy of hadronic particles which have not been stopped earlier due to their longer interaction lengths⁶ λ . Like the ECAL, the HCAL endcaps, covering $1.5 < |\eta| < 3.2$, employ LAr as the active material in combination with copper absorbing layers. In the barrel region of $|\eta| < 1.7$ scintillating plastic tiles are used with steel absorbers, as illustrated in Figure 3.13, organized into three readout layers with a total thickness of 7.4λ . The first two barrel layers are segmented into $\Delta\eta \times \Delta\phi = 0.1 \times 0.1$ cells while the third is coarser at 0.2×0.1 [96]. A hadronic shower traversing the HCAL tile calorimeter excites molecules of the polystyrene tiles which release UV scintillation light upon returning to the ground state. This UV light is wavelength-shifted to the visible spectrum by organic fluors embedded in the polystyrene, collected in fiber optic cables, and measured by photomultipliers tubes located on the outer edge of the calorimeter.

Hadronic showers are considerably more complex and challenging to measure than pure EM showers. An example shower is illustrated in Figure 3.14. Energy lost to nuclear interactions in the absorbing material is invisible to the calorimeter, as is the energy which escapes in the form of long-lived neutral decay products, such as neutrinos, neutrons, and kaons. The total fraction of unmeasured energy in a hadronic shower can be as high as 30–40 % [115]. Additionally, the relative proportions of the EM and hadronic components of a shower change with energy, producing a non-linear

⁶ The average nuclear interaction length λ is the distance required to reduce the number of particles by a factor of $1/e$. For hadrons in lead $\lambda = 17.59 \text{ cm}$, in comparison to a radiation length of only $X_0 = 0.5612 \text{ cm}$ [20].

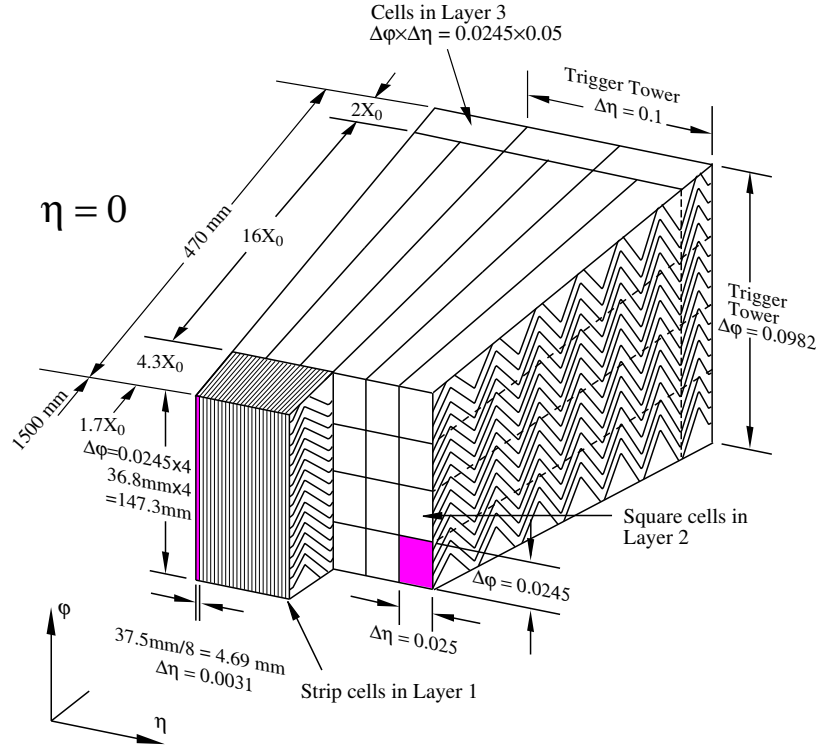


FIGURE 3.11: ATLAS ECAL barrel geometry [96]. Note the folded accordion design to prevent azimuthal cracks and three layers of different $\Delta\eta \times \Delta\phi$ granularities. The cells of layer 3 are grouped together by the first level of the trigger (L1) to form $\Delta\eta \times \Delta\phi \approx 0.1 \times 0.1$ trigger towers.

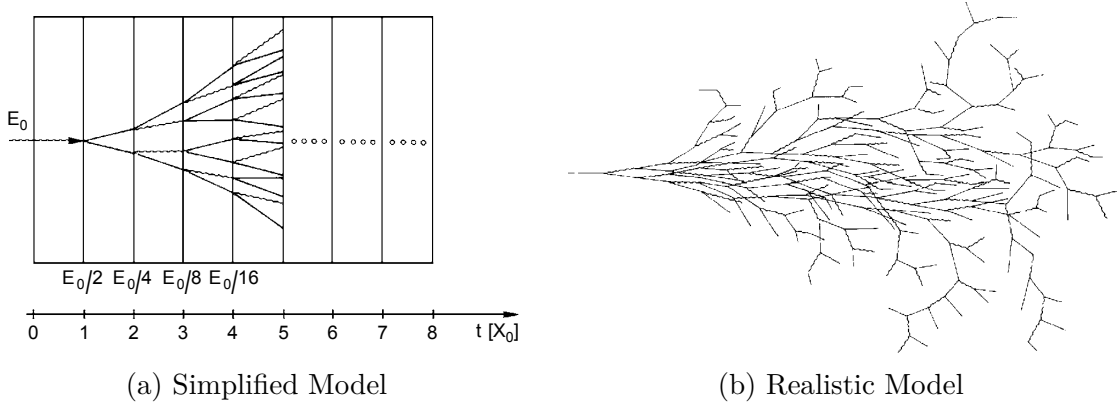


FIGURE 3.12: Illustrative sketches of EM showers in matter [115]. In the simplified model an incident photon creates a shower with equal energy branches splitting once per radiation length X_0 . This is a useful model for representing how energy is diffused in a shower and the rough scale of X_0 . In a realistic model the branching behavior is a stochastic process resulting in a complex shower.

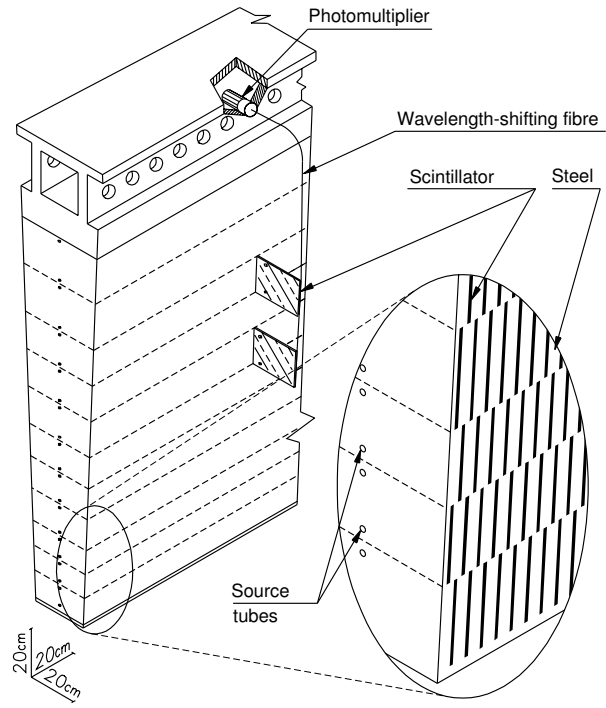


FIGURE 3.13: ATLAS HCAL tile barrel geometry [96].

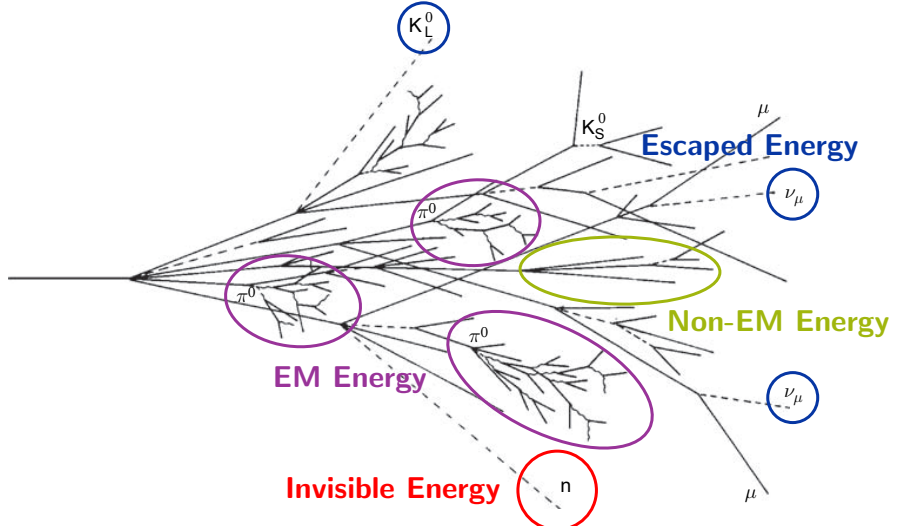


FIGURE 3.14: Sketch of a hadronic shower in a calorimeter. As the shower progresses energy is deposited in the calorimeter through daughter EM showers and the ionization losses of charged hadrons. A significant fraction of the energy is invisibly deposited via nuclear interactions in the absorbing material, or escapes the calorimeter in the form of long-lived neutral decay products. Adapted from [115, 117].

response [117]. Together these effects limit the HCAL resolution for pions (3.5) to 6.6% at 350 GeV and $\eta = 0.25$ [96].

$$\frac{\sigma(E)}{E} = \frac{56.4\%}{\sqrt{E \text{ (GeV)}}} \oplus 5.5\% \quad (3.5)$$

To account for the differences between the EM and hadronic components of a shower, topological clusters of calorimeter cells are created and calibrated with factors derived from pion simulations. Such clusters are said to be at the Local Cluster Weighting (LCW) scale [118]. An EM scale which only calibrates the EM components of showers is also available.

3.2.4 Muon Spectrometer (MS)

The components of the Muon Spectrometer (MS) [119, 120], shown in Figure 3.15, form the final layers of the ATLAS detector and provide tracking information for muons curving in the toroidal magnetic fields out to $|\eta| < 2.7$. Due to their relatively large mass and lack of strong interactions, muons easily penetrate the numerous calorimeter layers while retaining the majority of their original energy.⁷ With its large mass a muon will also curve less in the ID, negatively impacting the momentum resolution. The MS was designed to addresses both points by identifying muons as tracks which make it through the calorimeter, and producing a stand-alone p_T measurement⁸ with a resolution of 10% for 1 TeV tracks [96]. Additionally, portions of the MS within $|\eta| < 2.4$ are used in the first level of the trigger system.

The MS consists of three layers of different detector technologies spread over a large volume as shown in Figure 3.16. Monitored drift tubes (MDT) are the primary

⁷ High energy charged particles primarily loose energy in matter via bremsstrahlung with $-\frac{dE}{dx} \propto \frac{E}{m^2}$ [115]. Muons being 200 times lighter than electrons therefore loose energy $\sim 40\,000$ times slower. Taus would be even more penetrating, but are halted by their short lifetime of $c\tau = 87.03 \mu\text{m}$ [20].

⁸ Hits in the ID and MS are combined offline to further improve muon track reconstruction.

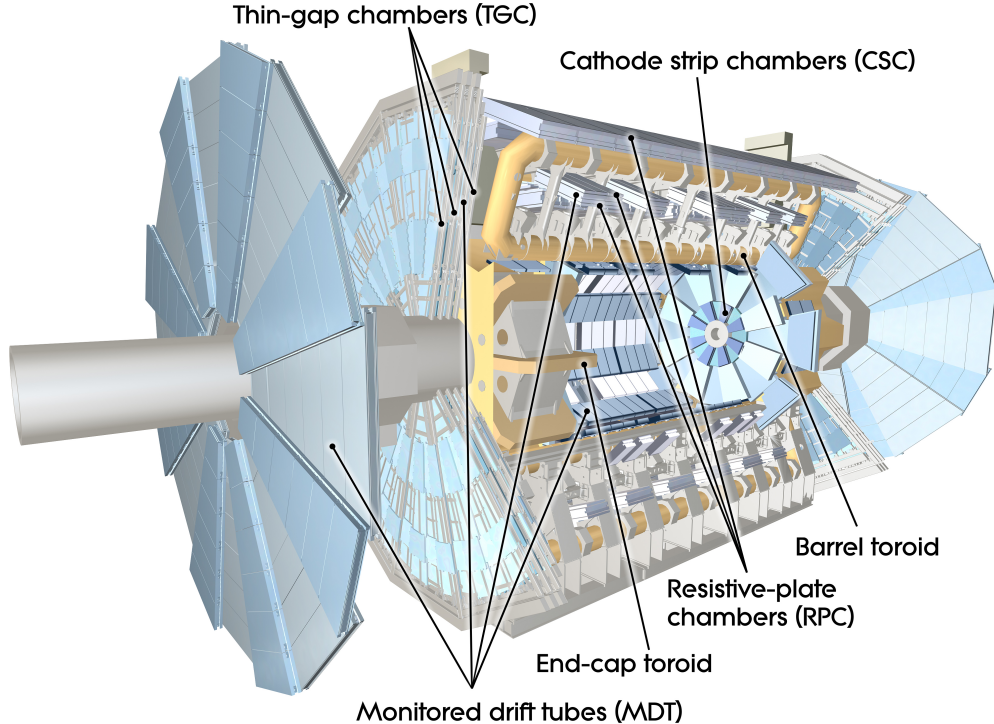


FIGURE 3.15: The ATLAS Muon Spectrometer (MS) [121].

detector technology and are used for precision tracking. The MDTs are arranged in modules, or chambers, with three or four layers of 3cm diameter Al tubes on either side of a mechanical support frame as illustrated in Figure 3.17. The tubes are filled with a 93 % Ar, 7 % CO₂ gas mixture at 3 bar and operate via ionization charge collection. Together the tubes of each chamber have an average resolution of 35 μm [96]. An optical alignment system built into the support frame monitors deformations with temperature fluctuations and time so that they may be accounted for during track reconstruction.

Cathode strip chambers are used for precision tracking in place of MDTs in the high particle flux $2 < |\eta| < 2.7$ forward region near the IP. These chambers are multi-wire proportional detectors with cathodes segmented into strips and benefit from a higher granularity, rate capability, and time resolution. The triggering functionality of the

MS is made possible by resistive plate chambers in the barrel and thin gap chambers in the endcaps. Both are simpler detector technologies with lower resolutions, but can quickly provide track information to the trigger system within a few tens of nanoseconds. They also measure the last muon spatial coordinate orthogonal to those found by the precision tracking chambers.

3.2.5 Trigger and Data Acquisition System (TDAQ)

Collectively the sub-detectors of ATLAS are read out through $\sim 10^8$ channels producing events 1–2 MB in size. As collisions occur in the LHC at a rate of 40 MHz it is completely impractical to readout and save every collision.⁹ Instead interesting events from a physics perspective must be selected in real-time and recorded via a trigger and data acquisition system (TDAQ) [123, 124] to conserve readout bandwidth and storage space. After a major upgrade before Run 2 [125] the TDAQ now consists of two levels, the hardware-based level-1 (L1) trigger and the software-based high-level trigger (HLT) as illustrated in Figure 3.18. The TDAQ system reduces the 40 MHz event rate to 100 kHz in L1, limited by the detector readout hardware, and 1 kHz in the HLT, limited by computing resources. While the trigger decisions are being made the raw data is buffered on the detector itself in front-end (FE) electronic systems.

The L1 trigger uses custom electronics to process a reduced set of inputs from the calorimeter and MS detectors in order to rapidly return a L1 acceptance decision and regions of interest (RoI) in $\eta - \phi$ for the HLT. Calorimeter trigger towers with large granularities are fed into sliding window algorithms to identify candidate e, γ and τ energy deposits, illustrated in Figure 3.19, as well as jets, E_T , and E_T^{miss} . Trigger muons are identified by simplified linear track finding algorithms while requiring varying levels of coincidence between MS layers to reduce the false positive rate. The calorimeter and muon information is further analyzed in a topological trigger

⁹ Which would require operating at an astounding rate of 40–80 TB s⁻¹!

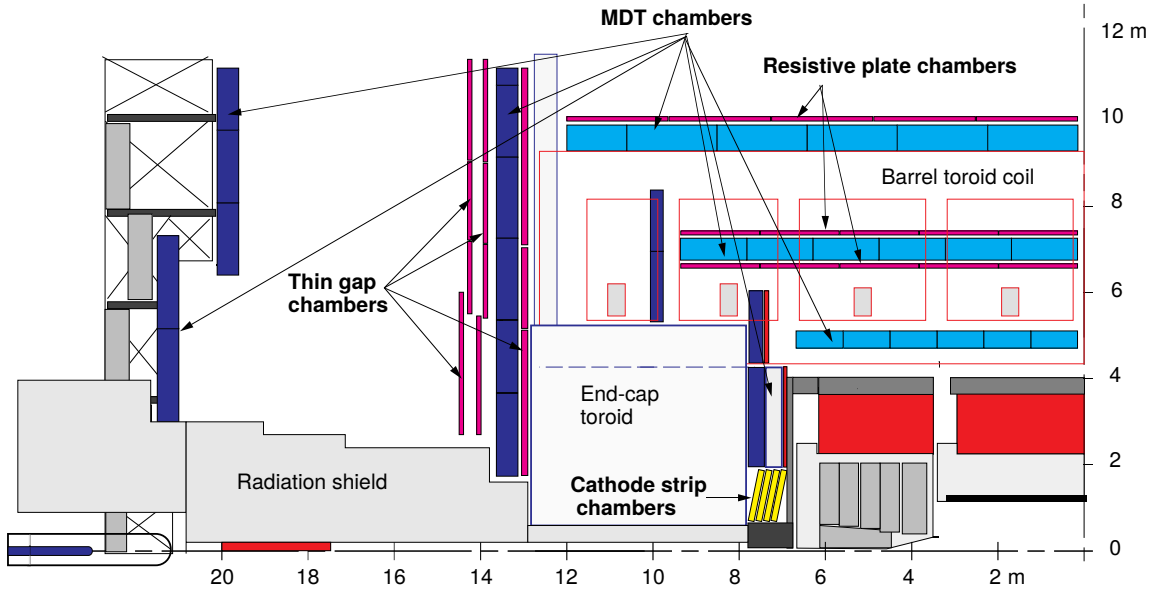


FIGURE 3.16: Cross sectional schematic of the ATLAS MS in the zy -plane [122]. Note the three layer design, distribution of detector technologies, and position within the toroid magnet system.

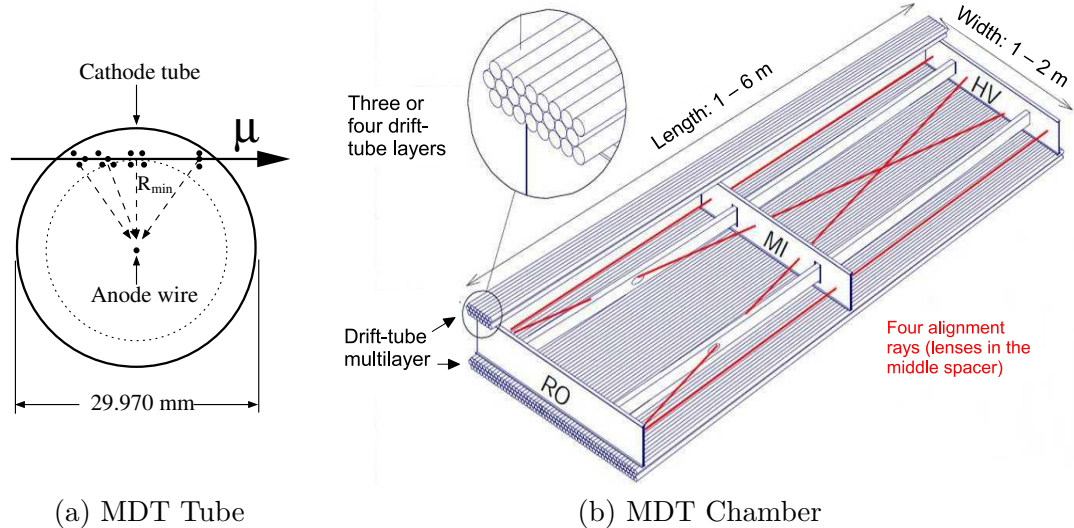


FIGURE 3.17: Schematics of the MS monitored drift tubes (MDT) [96]. The cross section of a single drift tube is shown in (a), while the geometry of a MDT chamber with layers of tubes on both sides of a mechanical support frame is illustrated in (b). An optical alignment system built into the support frame continually monitors for any deformations.

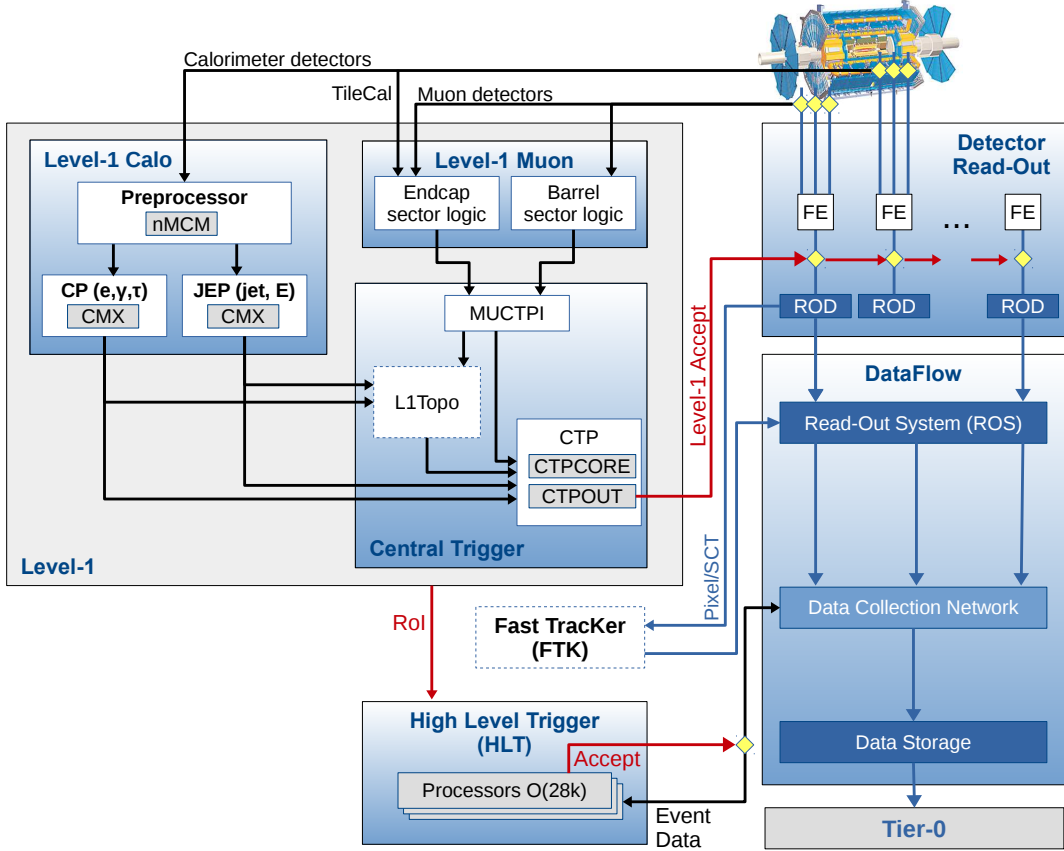


FIGURE 3.18: ATLAS trigger and data acquisition system (TDAQ) for Run 2 [125].

to capitalize on spatial and kinematic associations between L1 trigger objects. The final L1 decision combining all elements is made in the central trigger processor (CTP) which also enforces dead-time to avoid overlapping readout windows and overflowing FE buffers.

Following a L1 acceptance, the HLT retrieves precision information from the calorimeters and MS beyond what was used in L1. Tracking information from the ID is also incorporated after being reconstructed by the fast tracker (FTK), a hardware accelerated track pattern recognition system [126]. The HLT considers thousands of trigger chains, each focused on a particular physics object such as photons or E_T^{miss} , at near offline precision on a cluster of commercial CPUs. The HLT trigger signals

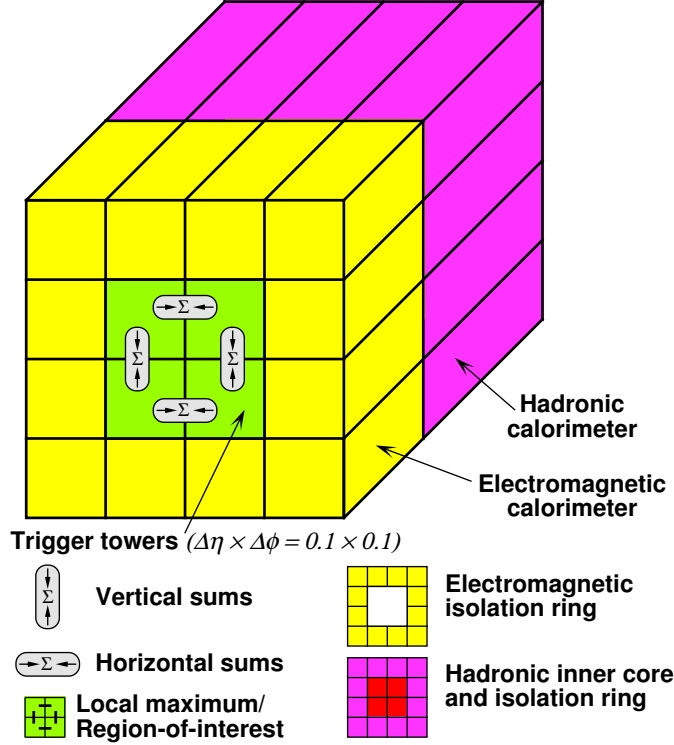


FIGURE 3.19: Illustration of the e , γ , and τ sliding window trigger algorithms [96]. The algorithms search for 2×2 clusters of ECAL trigger towers containing 1×2 or 2×1 sub-clusters with energies above a set threshold, surrounded by ECAL and HCAL towers below an isolation threshold. Similar sliding window algorithms without isolation criteria are used to identify jets, E_T , and E_T^{miss} .

are generally localized to the RoIs identified by the L1 trigger, but can also utilize the full detector if required. Events passing a HLT chain are subsequently saved to permanent storage for later offline reconstruction and analysis. Depending on the trigger rate, prescaling may be applied to lower the required bandwidth for more common events, typically at low p_T .

4

Analysis Methods

4.1 Reconstructing Physics Objects

4.1.1 *Tracks and Vertices*

Charged particles are measured in ATLAS as a series of space-point hits in the silicon inner detectors and TRT. Track reconstruction algorithms [127, 128] are then used to build particle tracks from these many individual hits. Sets of three space-points in the silicon detectors start the process as seed tracks, subject to quality criteria on their momentum and impact parameters, while also requiring at least one additional hit be consistent with the seed’s trajectory. These seeds are grown into candidate tracks containing many matching points through the use of a combinatorial Kalman filter. The candidate track’s quality is estimated based upon the number and type of hits in the track, while holes where a hit should have appeared in a layer but was not observed are penalized. An example track visualization is provided in Figure 4.1. Hits shared between candidate tracks are resolved with an ambiguity solving algorithm based on a maximum likelihood approach which takes the candidate track quality into account, until no hit is contained in more than two tracks and no track has more

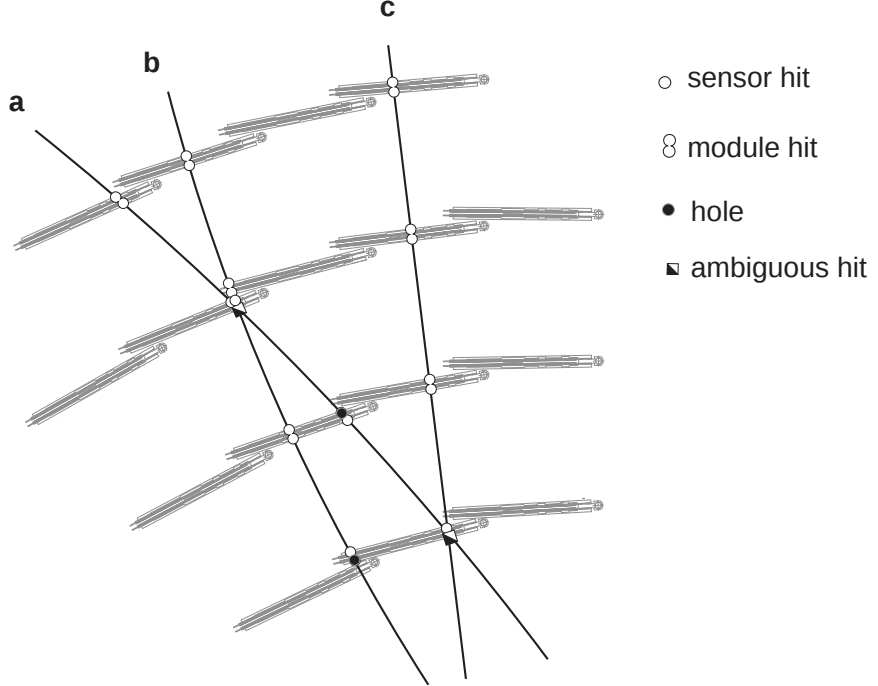


FIGURE 4.1: Example reconstruction of tracks from hits in the ID [127]. Hits are scored according to type, holes are penalized, and ambiguous hits are resolved.

than two shared hits.

Once the ID tracks have been reconstructed the multiple primary vertices underpinning the collision can be found [129]. A seed vertex is picked near the nominal interaction point and its position and associated tracks are fit in an annealing procedure [130]. On each iteration the tracks are weighted according to their compatibility with the vertex, the fit is re-run, and the vertex position is updated. Upon completion of the annealing process compatible tracks are assigned to the final vertex and the process is begun again with the remaining tracks until no further vertices can be created.

Having constructed a primary vertex it is useful to define a coordinate system for tracks relative to it in the form of impact parameters. The transverse impact parameter d_0 is the distance of closest approach between the track and primary vertex in the transverse xy -plane as illustrated in Figure 4.2. Likewise, the longitudinal

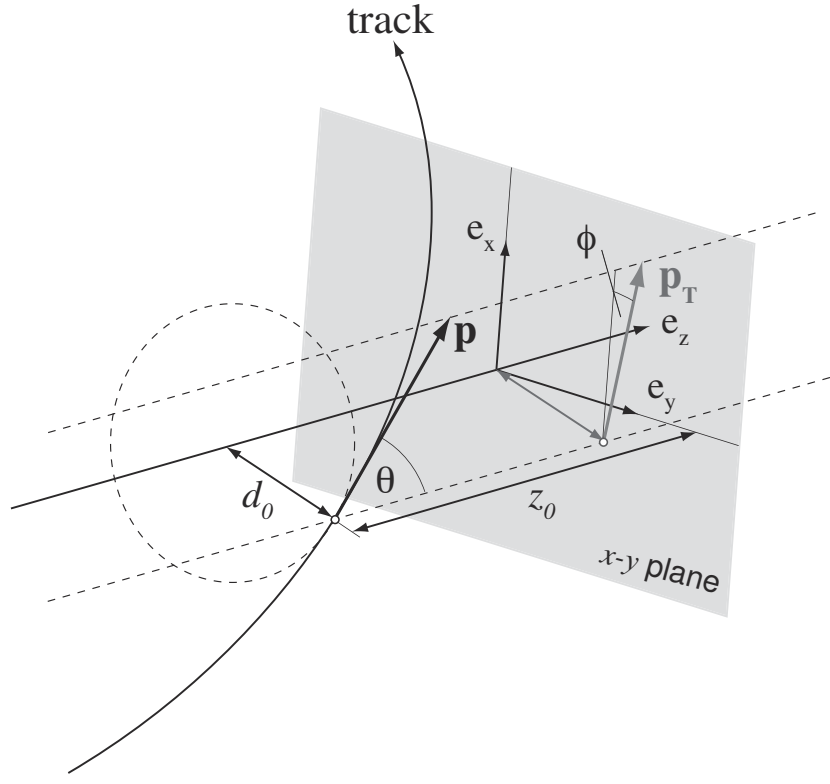


FIGURE 4.2: ATLAS track transverse impact parameter d_0 and longitudinal impact parameter z_0 [131].

impact parameter z_0 is distance of closest approach along the z -axis.

4.1.2 Jets

Jets resulting from the hadronization of color-carrying partons appear in the detector as sprays of tracks in the ID and pockets of energy in the calorimeters. ATLAS typically reconstructs jets with the anti- k_t jet algorithm [132] from topological clusters of hadronic calorimeter cells. The anti- k_t algorithm sequentially combines input objects, topological clusters in this case, to form stable conical jets of radius R specified as a parameter. The order in which objects are combined is decided by the “distance” d_{ij} between objects i and j , and d_{iB} between object i and the beam line:

$$d_{ij} = \min \left(1/p_{\mathrm{T}}^2 i, 1/p_{\mathrm{T}}^2 j \right) \frac{\Delta R_{ij}^2}{R^2}, \quad (4.1a)$$

$$d_{iB} = 1/p_{\mathrm{T}}^2 i. \quad (4.1b)$$

The algorithm computes all d_{ij} , d_{iB} values and finds the minimum. If d_{ij} is the minimum, objects i and j are merged. Otherwise, if d_{iB} is the minimum, the i th object is declared to be a jet and removed from consideration. The process repeats until all objects have been assigned to a jet. Effectively, high p_{T} objects will clear out a radius R in $\eta - \phi$ around themselves, or $y - \phi$ as shown in Figure 4.3, joining with lower and lower p_{T} objects. This has the advantage of forming consistently shaped jets while maintaining infrared and collinear safety, *i.e.* being tolerant of soft radiation changes and collinear splittings.

In practice a radius of $R = 0.4$ has been found to be optimal for many purposes and is the standard in ATLAS. Jets with larger radii such as $R = 1.0$ are also used in situations where energetic decays boost neighboring jets until they substantially overlap and form one large- R jet. To limit the effects of pileup radiation on large- R jets, low p_{T} components are commonly trimmed away [133]. The trimming procedure re-clusters the constituents of a jet into $R = 0.2$ subjets via the k_t algorithm¹ [134]. Subjets with $p_{\mathrm{T}}^{\mathrm{subjett}}/p_{\mathrm{T}}^{\mathrm{jet}} < f_{\mathrm{cut}} = 0.05$ or 0.1 are then removed.

Once constructed, a jet's calorimeter mass [135] is computed from its constituent topological clusters as

$$M^{\mathrm{calo}} = \sqrt{\left(\sum_{i=1} E_i \right)^2 - \left(\sum_{i=1} \vec{p}_i \right)^2}, \quad (4.2)$$

where the clusters are assumed to be massless, $|\vec{p}_i| = |E_i|$, for consistency.

¹ Identical in operation to the anti- k_t algorithm, but with p_{T} in place of $1/p_{\mathrm{T}}$.

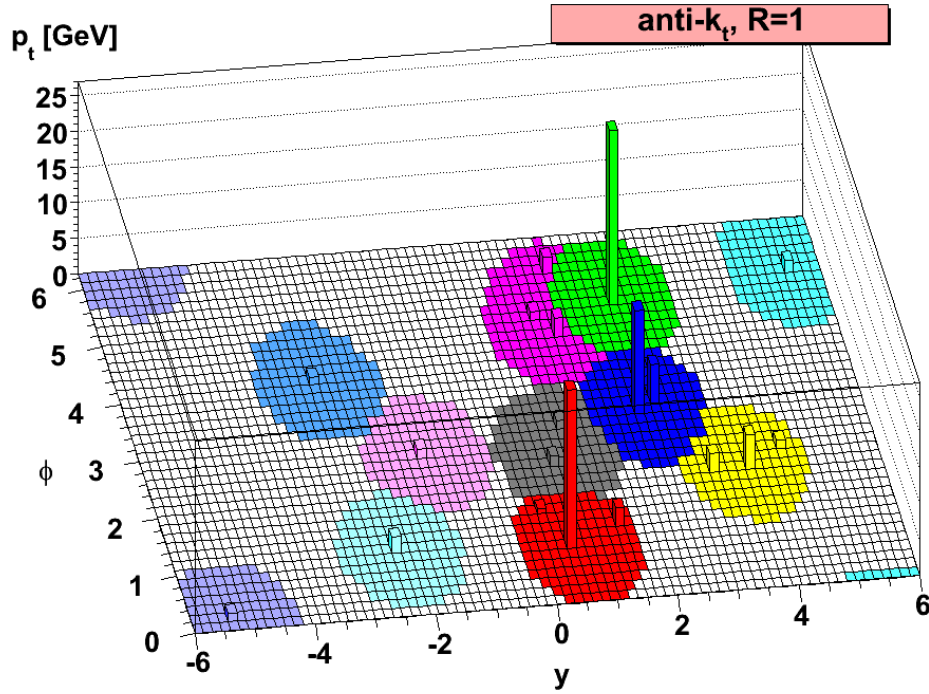


FIGURE 4.3: An illustration of the anti- k_t algorithm with $R = 1$ applied to simulated data [132]. The resulting jets are circular and centered on high p_T objects.

When a massive particle decays the magnitude of its decay product's angular separation grows as $\sim 2m/p_T$, implying that the physical jet radius will also depend on the initiating particle's m and p_T . Ideally each analysis using jets would optimize their own R value, but it is not feasible to produce jet calibrations for all the resulting radii. Instead calibrated small- R jets with $R = 0.4$ can be re-clustered [136] into larger radius jets of arbitrary size while the original calibration seamlessly propagates through to the re-clustered jet. Re-clustered jets with $R = 0.8$ are utilized in this dissertation analysis.

4.1.3 b -Tagging

To extract the multi- b final state under consideration in this dissertation from the overwhelming SM backgrounds it is crucial to have a high performance b -tagger.

Using a variety of techniques ATLAS has developed a mature b -tagging procedure [137, 138, 139] constructed out of multiple basic taggers working in unison. B -hadrons have a relatively long lifetime of ≈ 1.5 ps allowing them to travel appreciable distances, $c\tau \approx 450 \mu\text{m}$, from the primary interaction vertex before decaying. The ID can reconstruct these displaced secondary B -hadron vertices, particularly when enhanced by the IBL in Run 2, thereby forming the basis of most b -tagging methods. Tracks from the ID are matched to calorimeter jets with a p_{T} dependent ΔR selection before their use in the tagger.

The first class of basic taggers operate on track impact parameters to estimate the probability of a jet being a b , c , or light flavor jet. In a log-likelihood approach, the transverse and longitudinal impact parameter significances, d_0/σ_{d_0} and z_0/σ_{z_0} , for each track associated to the jet are computed and compared to reference probability distributions from simulation. The impact parameters are signed with respect to the jet direction; positive for events with the primary vertex, secondary vertex, and jet inline as expected for a displaced B -hadron, and negative for events with the secondary vertex and jet on opposite sides of the primary vertex. As shown in Figure 4.4, tracks from b -jets have larger impact parameter significances on average facilitating their identification.

The second class of basic taggers consists of two modified vertex finding algorithms. The secondary vertex finding algorithm explicitly reconstructs a single secondary vertex within the jet. All two-track vertices within the jet, that pass quality and impact parameter selections designed to remove non- B -hadron vertices, are found and ordered by p_{T} . The leading tracks are then used to reconstruct the secondary vertex that will appear displaced for b -jets. For an inclusive approach, the decay chain multi-vertex reconstruction algorithm attempts to identify the full B -hadron decay. Tracks within the jet are input to a Kalman filter to locate the probable B -hadron flight path, from primary, to bottom, and then charm vertex. The bottom and charm

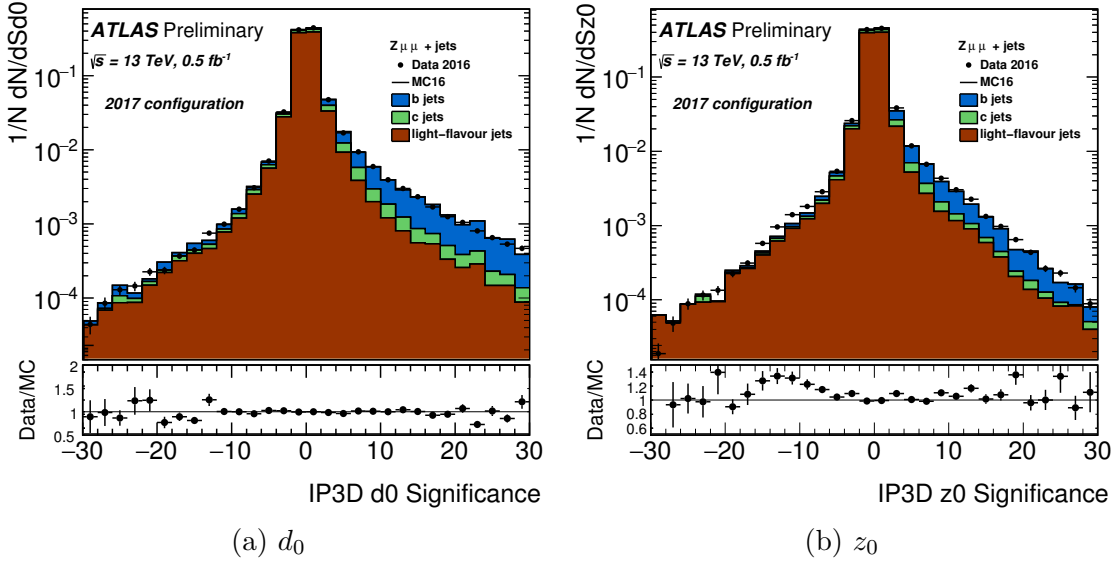


FIGURE 4.4: Signed impact parameter significances for $Z \rightarrow \mu\mu + \text{jets}$ events [139]. Tracks from b -jets tend to have larger positive values due to their origin in displaced B -hadron secondary vertices.

vertices can then be resolved even from single tracks along the flight path, subject to ID resolution constraints.

Taking the results from all of the basic taggers along with the jet p_T and η , a high-level BDT is trained on simulated data to classify b , c , and light flavor jets. The particular multivariate tagger used in this dissertation analysis, MV2c10, was trained to identify b -jets from a background sample of 10 % c , 90 % light flavor jets. The multi- b analysis [4] has previously found the 77 % b -jet efficiency working point to be the optimal trade-off between b -jet acceptance and background rejection, reducing c and light flavor jets by factors of 6 and 134 respectively [138]. The performance of the MV2c10 b -tagger can be seen in Figure 4.5.

4.1.4 Missing Transverse Energy

While the ATLAS detector has been designed to record as many particles from an event as possible, weakly interacting stable particles such as SM neutrinos or hypoth-

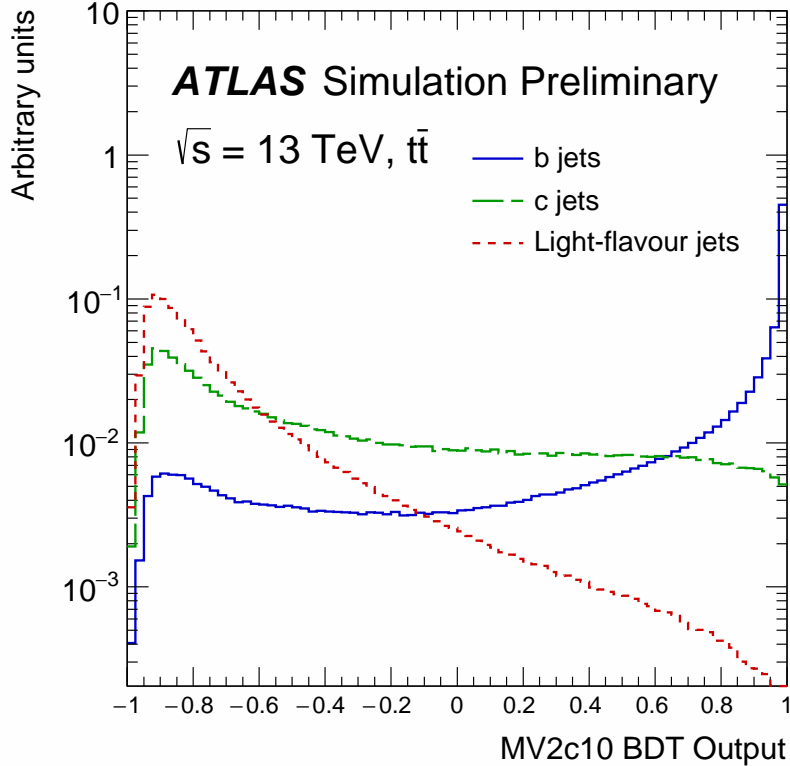


FIGURE 4.5: MV2c10 BDT output on simulated $t\bar{t}$ events [138]. The selected 77% working point corresponds to a decision threshold of 0.6459.

esized SUSY neutralinos will escape the detector unseen. However, as momentum is conserved in the transverse plane and the initial p_T is zero, the missing transverse momentum, or energy E_T^{miss} , can be measured by summing the p_T of all observed particles:

$$E_T^{\text{miss}} = - \sum \vec{p}_T. \quad (4.3)$$

Consequently, E_T^{miss} is a vital quantity for SUSY searches as a means of identifying final state neutralinos. Being a function of all observed particles, E_T^{miss} is sensitive to double counting in overlapping objects, visible particles escaping the detector as punch-through, the inclusion of unassociated particles from pileup, and otherwise poorly

measured or reconstructed objects. Care must be taken during $E_{\mathrm{T}}^{\mathrm{miss}}$ reconstruction and calibration that these effects are well understood and minimized where possible [140]. In particular, a “track soft term” computed using ID tracks [141, 142] is often added to incorporate energy from the primary vertex which is not included in any reconstructed object, thereby reducing the sensitivity of $E_{\mathrm{T}}^{\mathrm{miss}}$ to pileup beyond what can be achieved with calorimeter variables alone.

4.2 Jet Calibrations and Uncertainties

After reconstruction jets must be carefully calibrated to account for a myriad of experimental complications such that their measured energy matches that of the original parton as closely as possible. The non-compensating nature of the ATLAS calorimeters, loss of energy to dead material or punch-through, and extra energy from pileup all affect the jet energy scale (JES) and resolution (JER). The JES calibration sequence for small- R jets [143] is quite extensive and will be summarized here. It consists of 7 main steps as shown in Figure 4.6. First, the jets are reconstructed from EM scale calorimeter clusters with the anti- k_t algorithm. The jet direction is then adjusted to point to the actual primary vertex instead of the geometric center of the detector. Next, energy contributions from pileup are removed in two stages, with an area-based p_{T} density subtraction [144] and Monte Carlo (MC) simulation-based residual correction as a function of η and the number of primary vertices.

The primary correction of the calibration is derived from comparisons of MC truth and reconstructed jets in bins of p_{T} and η . This absolute MC calibration corrects for the detector’s varying geometric arrangement and non-compensating calorimeters, as well as particulars of the reconstruction algorithms and software. Isolated reconstructed jets are matched to truth jets within a $\Delta R = 0.3$ cone and the jet energy response $R = E_{\mathrm{reco}}/E_{\mathrm{truth}}$ is computed. The core of the energy response function is fit to a Gaussian in different $p_{\mathrm{T}} - \eta$ bins with the mean $\langle R \rangle$ then

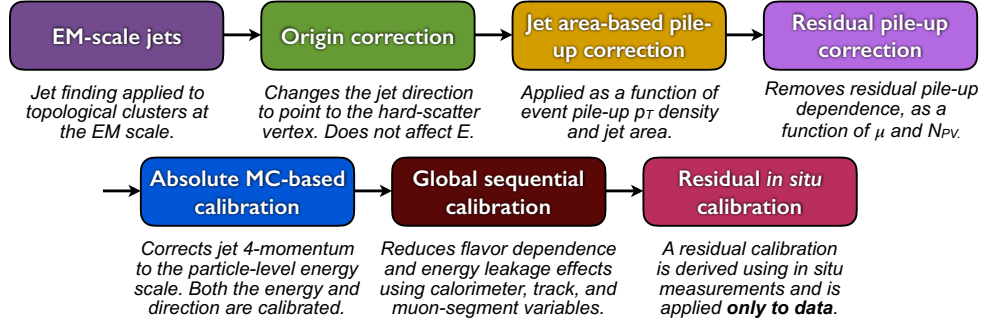


FIGURE 4.6: The calibration sequence for small- R jets [143].

being numerically inverted [145] to derive appropriate JES calibration factors for reconstructed jets. The fitted $\langle R \rangle$ values are provided in Figure 4.7.

Following the MC calibration there are still some residual dependencies of the JES on the composition and distribution of energy within a jet. In particular, due to their large color factor, gluon-initiated jets have increased particle multiplicities and softer

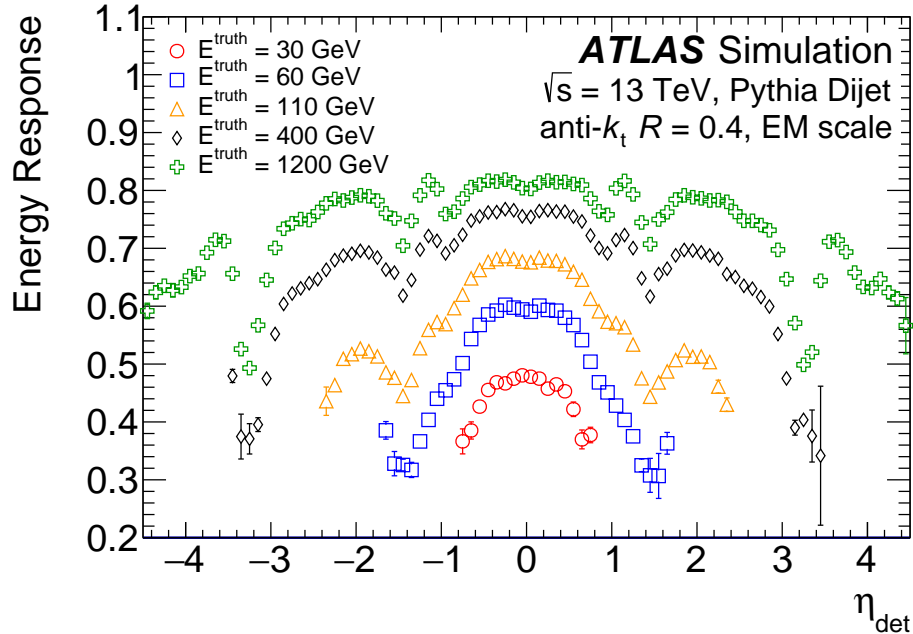


FIGURE 4.7: Average jet energy response of MC small- R jets at different p_T and η values [143]. As $\langle E_{\text{reco}}/E_{\text{truth}} \rangle < 1.0$ the absolute MC calibration increases the energy of reconstructed jets to better match the truth energy, as well as flattening out the dependence on η . The response values and error bars are derived from Gaussian fits.

p_T components, leading to a wider calorimeter shower shape. Quark-initiated jets, on the other hand, tend to have more of their p_T carried by hadrons which penetrate further into the calorimeters. The global sequential calibration accounts for these flavor dependencies with five additional corrections based on shower and calorimeter jet variables.

Lastly, *in situ* calibrations derived from real events in data are used to correct for any mismodelings in the prior MC-based calibration steps. Nearly all *in situ* calibrations exploit some form of p_T conservation between the jet to be calibrated and a well-measured reference object. The mean response $\langle \mathcal{R}_{in\ situ} \rangle$ between the jet p_T and appropriate reference p_T ,

$$\langle \mathcal{R}_{in\ situ} \rangle = \left\langle \frac{p_T^{\text{jet}}}{p_T^{\text{ref}}} \right\rangle, \quad (4.4)$$

is found in each case by fitting the response in data and MC. The ratio $\langle \mathcal{R}_{in\ situ}^{\text{data}} \rangle / \langle \mathcal{R}_{in\ situ}^{\text{MC}} \rangle$ between the two can then be used to make the actual calibration factors. An *in situ* η -intercalibration on dijet events corrects remaining response differences between the forward and central η regions. Momentum balance measurements with reference photons² and leptonically decaying Z bosons provide *in situ* JES corrections for jets with $p_T < 950$ GeV. These corrections are then propagated to higher p_T values by the multijet balance (MJB) calibration which uses a system of low p_T recoiling jets to balance one high p_T jet. All of the *in situ* calibrations are combined statistically, as shown in Figure 4.8, before use in the final calibration.

In the end, an unwieldy 80 correlated JES systematic uncertainties in p_T and η are created by the many calibrations, grouped for easier display in Figure 4.9. The total uncertainty is $\sim 1\%$ for much of the p_T range. For this research the 80 individual

² See Appendix E for a detailed discussion of the author's work on the complementary large- R γ +jet calibration.

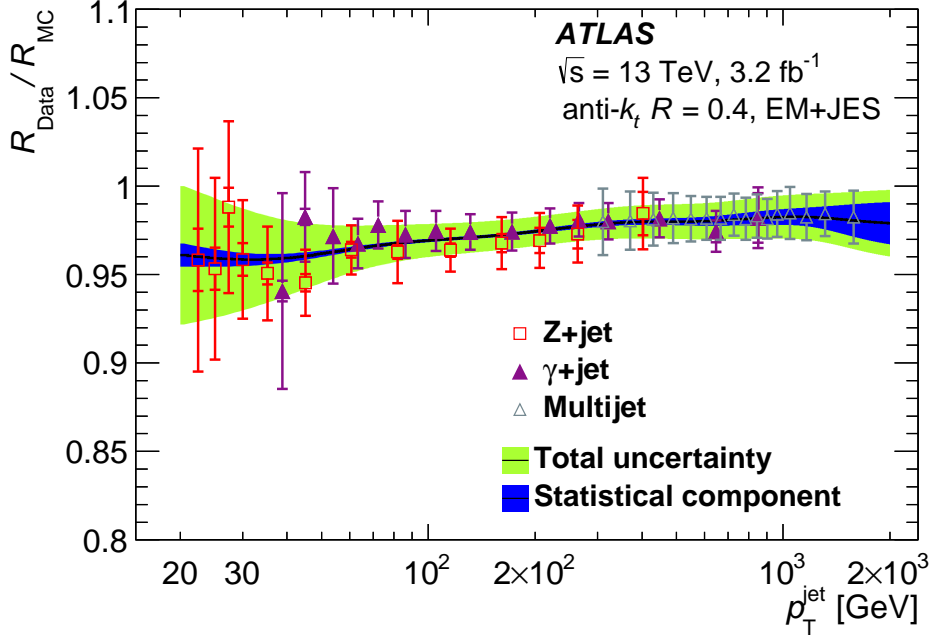


FIGURE 4.8: Combination of small- R jet *in situ* JES calibrations [143]. The Z and photon jet balance measurements provide calibrations for low p_T jets, which are then propagated to higher p_T values by the multijet balance calibration.

uncertainties are simplified to 3 nuisance parameters via eigenvector decomposition [143,146], JES1, JES2, and JES3, plus 3 nuisance parameters for the η -intercalibration, JES_EtaInter_highE, JES_EtaInter_negEta, and JES_EtaInter_posEta.

The JER can be thought of as the standard deviation of a Gaussian fit to the jet energy response $R = E_{\text{reco}}/E_{\text{truth}}$. Experimentally the resolution is a function of pile-up and electronic noise, stochastic variations due to the sampling design of the calorimeters, and constant energy smearing caused by passive material in the detector. The noise term is measured from the energy in random $\Delta R = 0.4$ cones, while the other terms are determined via momentum balances in dijet events. All measurements are performed *in situ* and on MC to allow for corrections to be made to MC jets. Systematic uncertainties on the JER include the JES uncertainty, modeling uncertainties on the dijet events, and method non-closure. 34 correlated uncertainties are needed for a full description of the JER uncertainty, but for this research a

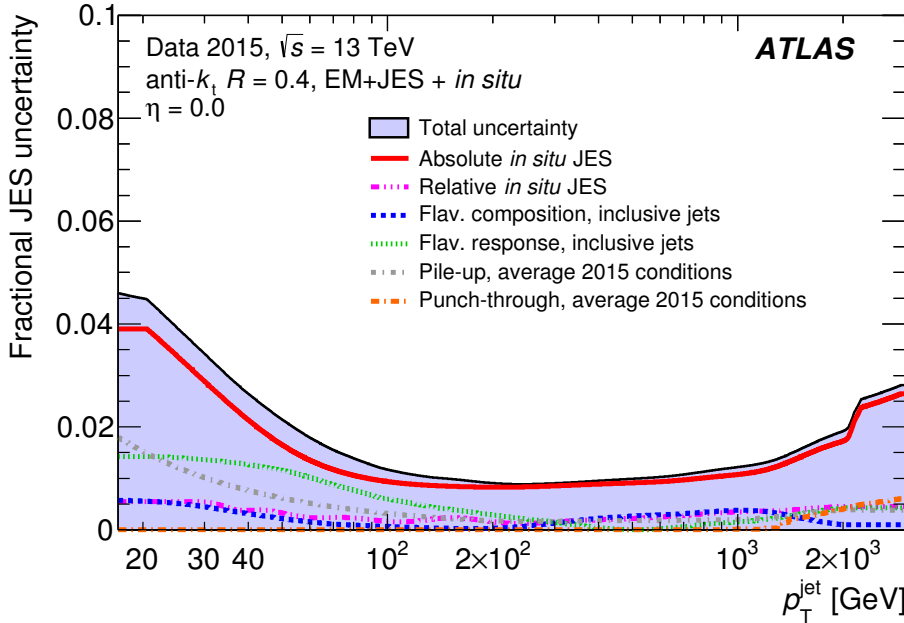


FIGURE 4.9: Systematic uncertainties on the combined small- R JES calibration versus p_T for $\eta = 0$ jets [143]. The 80 individual uncertainties have been grouped for easier interpretation. Note that the total uncertainty is $< 2\%$ for a wide range of p_T .

simplified set of 8 JER nuisance parameters, JER1–JER7 plus JER_DataVsMC, was used. As can be seen in Figure 4.10, the JER is 0.5–2% with an uncertainty of $< 1\%$ for jets seen in this dissertation.

4.3 Boosted Decision Trees (BDT)

Boosted decision trees (BDT) are a form of supervised machine learning useful for classification problems such as the separation of SUSY signal and SM background events found in this dissertation. In supervised learning a model is trained over many known examples to use input features, *i.e.* event level variables, \vec{x} to make a prediction \hat{y} about the true value y . During the training process parameters θ of the model are adjusted to minimize a two-part objective function, $\text{obj}(\theta) = L(\theta) + \Omega(\theta)$. The training loss $L(\theta)$ measures the model’s predictive performance while $\Omega(\theta)$ is a regularization term to penalize model complexity. Note that L is a measure of

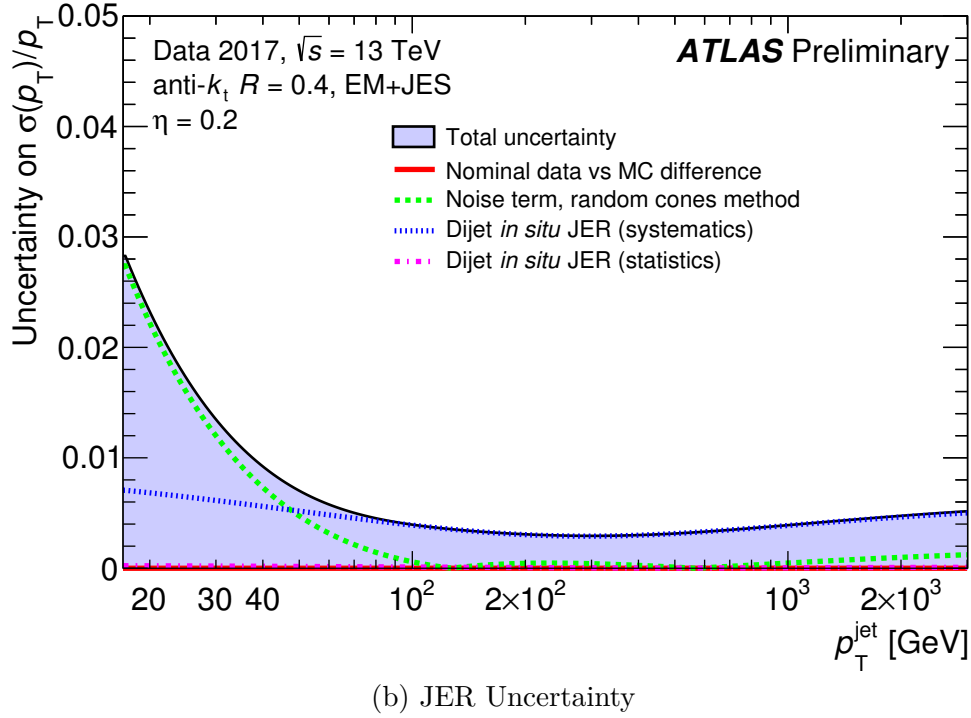
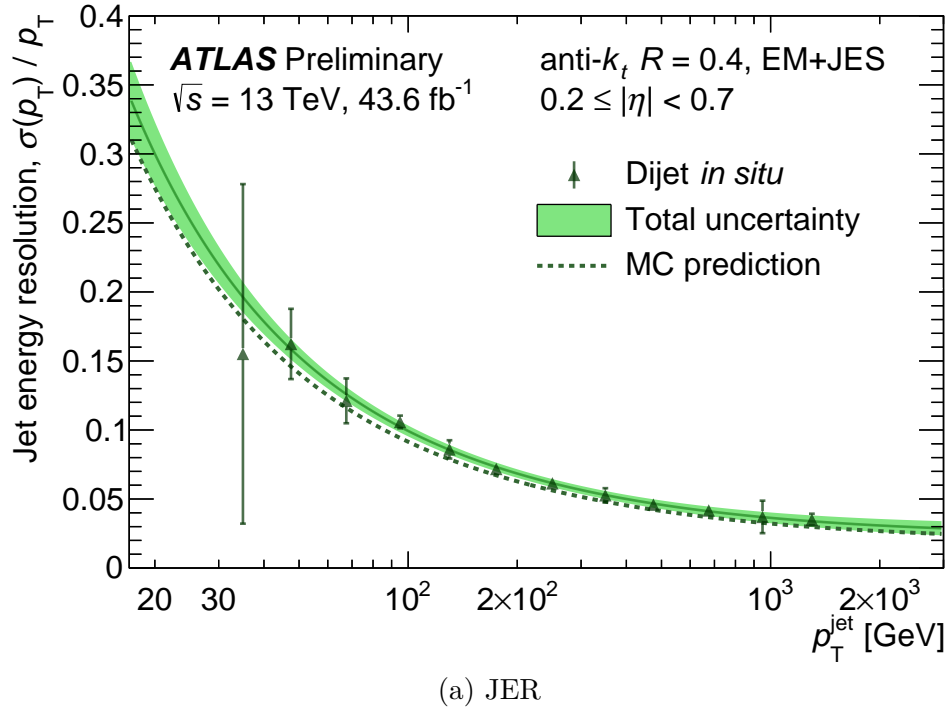


FIGURE 4.10: The JER and its uncertainty for small- R jets [147]. The JER is 0.5–2 % with an uncertainty of < 1 % for the p_T values seen in this dissertation.

the model's bias³ and Ω is a measure of its variance,⁴ so the joint $\text{obj}(\theta)$ is a good demonstration of the bias-variance tradeoff in action [148].

In signal and background classification problems, with $y = 1$ and $y = 0$ respectively, the binary logistic function,

$$L = \sum_i [y_i \ln(1 + \exp(-\hat{y}_i)) + (1 - y_i) \ln(1 + \exp(\hat{y}_i))], \quad (4.5)$$

is an appropriate choice of loss function. Regularization can be carried out in a variety of ways, but two of the primary methods are known as L1 and L2 regularization⁵ for the power of their dependence on the norm of θ :

$$\Omega_{\text{L1}}(\theta) \sim \|\theta\|, \quad (4.6a)$$

$$\Omega_{\text{L2}}(\theta) \sim \|\theta\|^2. \quad (4.6b)$$

A basic classifier can be created from a tree of selections on \vec{x} designed to separate signal and background events at each branch, or split, in the tree. Such a model is known as a classification and regression tree (CART) [149] and a simple example can be found in Figure 4.11. As the splits are just selections on the input variables, they are — somewhat — possible to understand physically, and conveniently do not need any kind of feature scaling, unlike other machine learning methods. To make a prediction for an event the tree and its branches are traversed until the event lands in one of the weighted leaves. The weight of the leaf w is positive (negative) for signal-like (background-like) events. A logistic function is used to properly transform w into an output score $\hat{y} = 1 / (1 + e^{-w})$ within $0 < \hat{y} < 1$.

³ Errors due to the model not learning about relationships between features, *i.e.* underfitting.

⁴ Errors due to a complex model failing to generalize beyond the training data, *i.e.* overfitting.

⁵ L1 regularization produces sparse parameters and thus acts as a form of inherent feature selection, while L2 regularization is more computationally efficient.

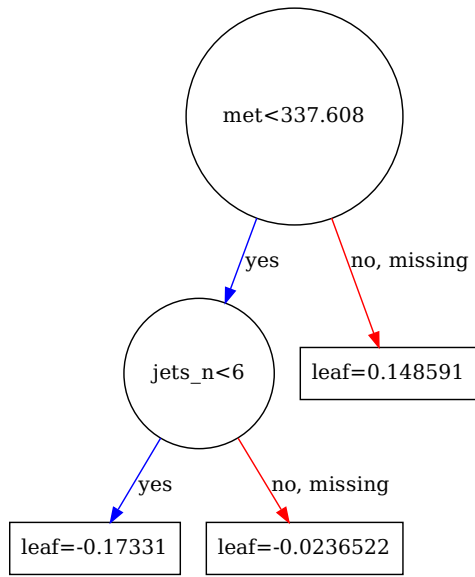


FIGURE 4.11: Simple classification and regression tree (CART) of only two splittings on E_T^{miss} and N_{jet} . Signal-like (background-like) events receive positive (negative) weights in the leaves.

While simple in operation, individual CARTs are rather poor and limited models in terms of the behaviors they can successfully predict. However, by taking an ensemble of K complementary trees, *i.e.* boosting [150, 151], and summing each CART’s individual weight w_k a much more flexible BDT⁶ is formed. The component trees of a BDT are generated by iteratively adding new trees $f_k(x_i)$ to those which came before [152],

⁶ As the leaf weights are variable real numbers rather than integer classes this approach may be better described as a boosted regression tree, and can indeed handle regression problems without the logistic function, but in particle physics is colloquially known as a BDT.

$$\begin{aligned}
\hat{y}_i^{(0)} &= 0, \\
\hat{y}_i^{(1)} &= f_1(x_i) = \hat{y}_i^{(0)} + f_1(x_i), \\
\hat{y}_i^{(2)} &= f_1(x_i) + f_2(x_i) = \hat{y}_i^{(1)} + f_2(x_i), \\
&\vdots \\
\hat{y}_i^{(t)} &= \sum_{k=1}^t f_k(x_i) = \hat{y}_i^{(t-1)} + f_t(x_i),
\end{aligned} \tag{4.7}$$

where each tree f_k is grown from zero branches while minimizing $\text{obj}(\theta)$. Through the ingenious use of a second order Taylor expansion this process can be recast as a form of gradient descent, and thus is known as stochastic gradient boosting [153, 154].

Event weights, essential in MC samples but seldom encountered in machine learning outside of particle physics, are multiplied with the gradient thereby allowing the model to proportionally “learn” more from higher weight events. Negative event weights created by higher order interference terms in MC are a bit harder to address. In this research such events were dropped while training for safety as XGBoost did not appear to be using them anyway. Note that the MC event weight is not a factor when making predictions, so as long as the final BDT’s performance is acceptable when negative weights are included, this is not an issue.

The number of boosting rounds, and thus trees, K can be chosen in advance but is better optimized during the training process via early stopping. A small validation set of events is withheld from the training data and is used to compute a validation error based on a predefined classification threshold. The validation error will decrease initially as the BDT is trained until at some point it begins to grow as the model begins overfitting the training data. The training is stopped when the validation error has not improved in a specified number of rounds, and the number of trees with the lowest validation error, K_{best} , are retained as the final BDT.

4.3.1 XGBOOST

The XGBOOST⁷ library [152] is a modern open source implementation of gradient boosted decision tree methods. Through various algorithmic and memory optimizations XGBOOST enjoys faster performance⁸ than the traditional particle physics machine learning package, TMVA [157], and has been used in numerous high profile projects such as the Higgs challenge [158]. L1 and L2 regularization is incorporated via

$$\Omega(f) = \alpha T + \frac{1}{2} \lambda \sum_{j=1}^T w_j^2, \quad (4.8)$$

where T is the number of leaves in a tree and w_j are the leaf weights; however, the default hyperparameters $\alpha = 0$ and $\lambda = 1$ only enable L2 regularization. Other important hyperparameters in XGBOOST include the learning rate η , which scales the corrections added by each new tree, maximum tree depth, which sets a limit on the complexity of any tree via its depth, and the early stopping validation threshold. For reference $\eta = 0.3$ and a maximum depth of 6 are the default values.

4.3.2 Gain

To attempt to attain an understanding of what a trained BDT has learned, we can compute the Gini importance [149], or mean decrease in impurity, from its trees. At each split in the BDT the decrease in classification impurity, *i.e.* how well the split reduces overlap between classes, is found. The decrease in impurity is then weighted by the probability of reaching the split⁹ and averaged over all the trees in the BDT. Variables which are more influential to the classification therefore receive higher Gini

⁷ XGBOOST: eXtreme Gradient Boosting, github.com/dmlc/xgboost.

⁸ XGBOOST has lost its speed crown in recent years to newer libraries such as LightGBM [155] and CatBoost [156].

⁹ Approximated by the fraction of events which do reach the split.

importance scores. The Gini importance can also be thought of approximately as the gain in loss function L at each split, and hence is known in XGBoost simply as the gain. We can also plot the split values from all trees directly to see where the BDT has decided the best divisions in each input variable lie, although this doesn't show the correlations learned between variables which give a BDT much of its predictive power.

4.4 Statistical Methods

4.4.1 Significance

When evaluating an experimental result it is essential to understand the significance of the observation, *i.e.* estimate the likelihood that the new data is incompatible with known behaviors. In physics the significance Z is typically thought of in terms of the fluctuation of a standard Gaussian variable¹⁰ rather than the p -value¹¹ as is common in other fields. To convert between the p -value and Z we take

$$Z = \Phi^{-1} (1 - p), \quad (4.9)$$

where Φ^{-1} is the inverse of the standard Gaussian cumulative probability distribution [159]. As a point of reference, a $Z = 3$ result is considered to show evidence of new physics while a $Z = 5$ result is the gold standard for discovery.¹² Statistically, Z can be computed from the expected number of signal and background events, s and b , in many ways [159], each appropriate under different sets of assumptions. The simplest approximation $Z = s/\sqrt{b}$ when $s \ll b$ is a commonly used shorthand for the significance, but quickly breaks down in regions with low amounts of expected b .

¹⁰ Similar to a Z score, *i.e.* how many standard deviations σ away from the mean.

¹¹ $p = \frac{1}{\sqrt{2\pi}} \int_Z^\infty e^{-x^2/2} dx = 1 - \Phi(Z)$ [159]. The p -value is the probability that a subsequent observation disagrees with the hypothesis being tested by more than the current observation.

¹² One-tailed $Z = 1.64 \leftrightarrow p = 0.05$, $Z = 3 \leftrightarrow p = 1.35 \times 10^{-3}$, $Z = 5 \leftrightarrow p = 2.87 \times 10^{-7}$.

Additionally, for discovery purposes the estimate of Z should ideally incorporate the statistical uncertainty on b , σ_b . A better approximation¹³ which takes both of these concerns into account is

$$Z_B = \Phi^{-1} \left(1 - B \left(\frac{1}{1 + \tau}; s + b, 1 + b\tau \right) \right), \quad (4.10a)$$

$$\tau = \frac{b}{\sigma_b^2}, \quad (4.10b)$$

$$B(x; y, z) = \frac{1}{B(y, z)} \int_0^x t^{y-1} (1-t)^{z-1} dt, \quad (4.10c)$$

$$B(y, z) = \int_0^1 t^{y-1} (1-t)^{z-1} dt = \frac{\Gamma(y)\Gamma(z)}{\Gamma(y+z)}, \quad (4.10d)$$

where $B(x; y, z)$ is the regularized incomplete beta function. The Z_B approximation is fast to compute and thus is used widely when developing aspects of the BDT, typically with a relative σ_b of 50 % as was observed in [5].

4.4.2 Optimizing Significance

To compute significance results for a machine learning model, like a BDT, in practice we must first decide a classification threshold to set on the output score \hat{y} between the signal and background classes. Receiver operating characteristic (ROC) curves comparing the true and false positive error rates at different thresholds are one way of visualizing this choice as is done in Figure 4.12. The integrated area under the curve (AUC) is equivalent to the probability that a randomly chosen signal event has a lower \hat{y} score than a randomly chosen background event [163]. By selecting a threshold at which to operate the classifier, we are picking one point along the ROC curve and making a trade-off between false positives and false negatives.

¹³ In ROOT [160] as `BinomialExpZ`. The SciPy [161] pseudocode actually used is provided in Appendix D.1. For a derivation see Appendix E of [162], with the slight difference that there $y = s$ has been approximated for $y = s + b$ as now $b < s$.

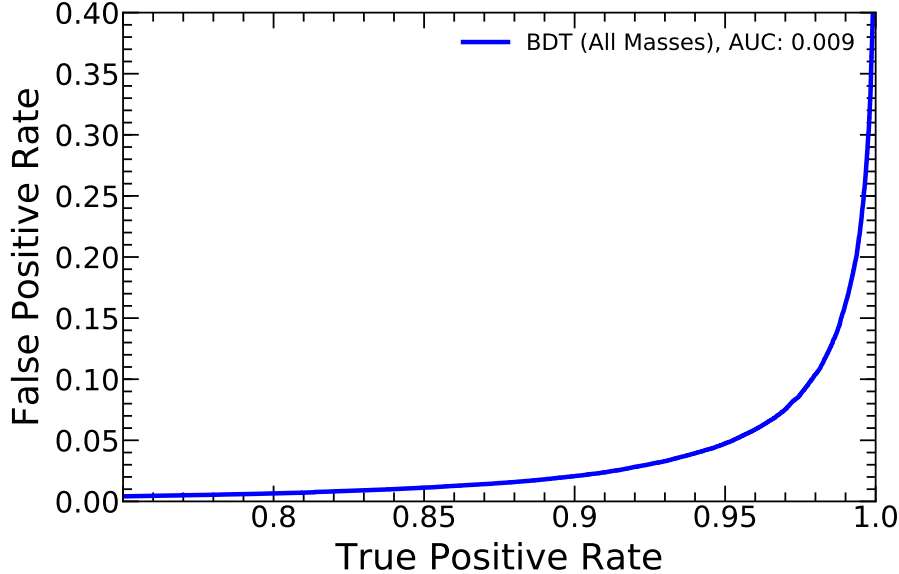


FIGURE 4.12: Example receiver operating characteristic (ROC) curve from the BDT developed in this dissertation. The average ROC curve over all signal mass points is shown. The lower-right corner with high true positive rate and low false positive rate, and hence a small area under the curve (AUC), is desirable.

A simple, but effective, way of making this choice is through brute force; compute the ROC curve on some small binning in \hat{y} threshold, loop through all points evaluating the true background and signal yields, b and s , at each, and then compute Z via Z_B or some other approximation. The point which maximizes Z can then be used to make the optimal, in terms of expected significance, division between signal and background classes. To keep the background statistics in the selected signal region from dropping to zero, thereby causing large background uncertainties to overshadow any significance gains, as the \hat{y} threshold is raised ever closer to 1.0, we also require $b > 0.5$ and the leading background, $t\bar{t}$, statistical uncertainty to be $< 30\%$. Pseudocode of this significance optimization process can be found in Appendix D.2.

4.4.3 HISTFITTER

While Z_B is a good first step toward understanding the performance of the BDT it is not a sufficient tool for fully describing the significance and signal exclusion potential of

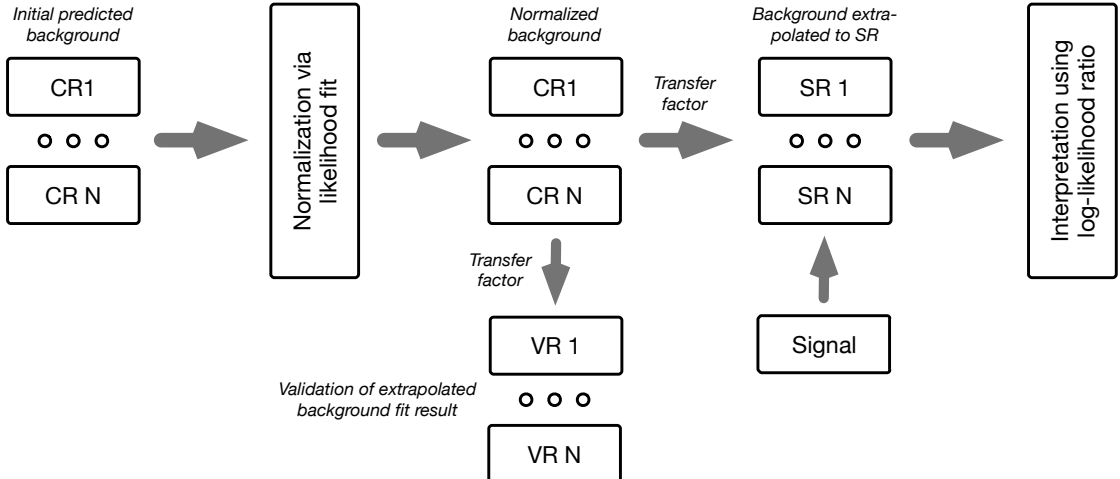


FIGURE 4.13: Overview of a typical HISTFITTER analysis in terms of fit regions [164].

the analysis across the parameter space of possible SUSY masses. The ATLAS SUSY group has developed a statistical software framework known as `HISTFITTER` [164] to address these issues, while also taking care of background normalizations in a semi-data-driven way and managing all sources of uncertainty with their correlations. `HISTFITTER` is a convenient SUSY focused wrapper around `HISTFACTORY` [165] and `RooStats` [166], underpinned by `RooFit` [167] and `ROOT` [160]. Control regions (CRs) with low amounts of signal contamination are constructed to measure the data via likelihood fits and produce the normalizations needed to bring data and MC into close agreement. The normalizations are then checked in validation regions (VRs) before being transferred to signal regions (SRs) where the real question, was signal observed or not, is answered. A flowchart of the `HISTFITTER` architecture can be found in Figure 4.13. Note that in this method the real data in the SRs is blinded until the analysis procedure has been verified, and that the VRs are used to validate the fit before unblinding but are not actually included in the fit itself.

The CR fits are converted to SR normalizations through the use of transfer factors defined as the square bracketed term of

$$N_p(\text{SR, est.}) = N_p(\text{CR, obs.}) \times \left[\frac{N_p(\text{SR, MC})}{N_p(\text{CR, MC})} \right] = \mu_p \times N_p(\text{SR, MC}), \quad (4.11)$$

where $N_p(\text{SR, est.})$ is the estimated SR background yield for a normalized simulated processes p , $N_p(\text{CR, obs.})$ is the number of CR events observed in data minus the expected MC yield for processes other than p , and $N_p(\text{CR, MC})$ ($N_p(\text{SR, MC})$) is the original estimate of the background yield in the CR (SR) from the MC simulation. For convenience μ_p is defined to be the ratio of the data and MC yields of p in the CR as this is the normalization factor ultimately applied to p in the SR.¹⁴ It is up to the physicist performing the analysis to determine what dominate processes p should be normalized with dedicated CRs.

As a benefit of this approach, many experimental and theoretical systematic uncertainties on background processes drop out in ratios, reducing their impact on the SRs. Only changes to the transfer factors, not the raw yields themselves, affect the SR uncertainty. The systematic uncertainty in a SR is then only made up of residual systematics which survive the extrapolation process and systematics on non-normalized backgrounds. Additionally, the total SR uncertainty also includes MC statistical uncertainties propagated from the CR fit, statistical uncertainties on MC backgrounds in the SR,¹⁵ and statistical uncertainties on the data itself. To allow for reasonable extrapolations between regions it is crucial that the CRs, VRs, and SRs be kept as close together kinematically as possible. CRs are also constructed with background yields many times that of SRs to reduce the effects of statistical uncertainties.

¹⁴ μ_p is the factor p is rescaled by to have data to MC agreement in the CR.

¹⁵ Later represented in `HISTFITTER` by γ nuisance parameters.

4.4.4 Likelihood Function

The likelihood function used in HISTFITTER (4.12a) [164] is constructed from products of Poisson distributions, $P(n|\lambda) = \frac{1}{n!} \lambda^n e^{-\lambda}$, for the events in each SR¹⁶ and CR, \mathbf{n} , as well as standard Gaussian distributions, G , which constrain the systematic uncertainties (4.12c). Each systematic $k \in \mathcal{S}$ is represented by its own nuisance parameter, θ_k , which is varied about its nominal auxiliary measurement, θ_k^0 . The auxiliary measurement fluctuations are constrained by the Gaussian to range from $\pm 1\sigma$ about the nominal value of $\theta_k^0 = 0$ when $\theta_k = \pm 1$.

$$L(\mathbf{n}, \boldsymbol{\theta}^0 | \mu_{\text{sig}}, s, \boldsymbol{\mu}, \mathbf{b}, \boldsymbol{\theta}) = P_{\text{SR}} \times P_{\text{CR}} \times C_{\text{syst}} \\ = \prod_{i \in \text{SR}} P(n_i, \lambda_i) \times \prod_{j \in \text{CR}} P(n_j, \lambda_j) \times C_{\text{syst}}(\boldsymbol{\theta}^0, \boldsymbol{\theta}) \quad (4.12\text{a})$$

$$\lambda_i = \lambda_i(\mu_{\text{sig}}, s, \boldsymbol{\mu}, \mathbf{b}, \boldsymbol{\theta}) \quad (4.12\text{b})$$

$$C_{\text{syst}}(\boldsymbol{\theta}^0, \boldsymbol{\theta}) = \prod_{k \in \mathcal{S}} G(\theta_k^0 - \theta_k) \quad (4.12\text{c})$$

The Poisson means λ_i and λ_j are functions¹⁷ (4.12b) of the signal strength parameter μ_{sig} , signal predictions s , background normalization factors $\boldsymbol{\mu}$, background predictions¹⁸ \mathbf{b} , and nuisance parameters $\boldsymbol{\theta}$. μ_{sig} is used to control the amount of simulated signal included in the fit, from no signal with $\mu_{\text{sig}} = 0$ to the nominal expectation with $\mu_{\text{sig}} = 1$.

4.4.5 Profile-Likelihood Fit

Once constructed, the likelihood function L (4.12a) can be used to find the p -value of a particular observation through the employment of a log-likelihood ratio [164, 168, 169]

¹⁶ Here $i \in \text{SR}$ refers to orthogonal SR bins, *i.e.* a multi-bin fit. Additional likelihood functions are needed for non-orthogonal SRs, *i.e.* a single-bin fit.

¹⁷ $\lambda \sim W(\boldsymbol{\theta})(\mu_{\text{sig}} s + \boldsymbol{\mu} \cdot \mathbf{b})$ where $W(\boldsymbol{\theta})$ represents any systematics that are applied as weights.

¹⁸ In the notation of (4.11) $\boldsymbol{\mu}$ is a vector of μ_p values, while \mathbf{b} is a vector of $N_p(\text{MC})$ values.

test statistic,¹⁹

$$q_{\mu_{\text{sig}}} = -2 \log \left(\frac{L(\mu_{\text{sig}}, \hat{\boldsymbol{\theta}})}{L(\hat{\mu}_{\text{sig}}, \hat{\boldsymbol{\theta}})} \right), \quad (4.13)$$

where $\hat{\mu}_{\text{sig}}$, $\hat{\boldsymbol{\theta}}$ maximize L absolutely²⁰ and $\hat{\boldsymbol{\theta}}$ maximizes L for a specific value of μ_{sig} . The largest, *i.e.* most conservative, p -value of a particular μ_{sig} null hypothesis is then calculated by integrating the probability distribution function (PDF) of the test statistic, $f(q_{\mu_{\text{sig}}} | \mu_{\text{sig}}, \boldsymbol{\theta})$:

$$p_{\mu_{\text{sig}}} = \int_{q_{\mu_{\text{sig}}}}^{\infty} f(q | \mu_{\text{sig}}, \boldsymbol{\theta}) dq. \quad (4.14)$$

The PDF can be estimated by throwing large numbers of pseudo-experiments with random values of \mathbf{n} and $\boldsymbol{\theta}^0$. However, due to the copious amounts of nuisance parameters encountered in a physics analysis, this is very computationally expensive. Instead the nuisance parameters are “profiled”, *i.e.* fit, in data to find the value of $\boldsymbol{\theta}^0$ which best matches²¹ the observations and thus leads to the largest p -value. For the sake of consistency, it is convention at the LHC to use the same profiled $\boldsymbol{\theta}^0$ values for both the expected and observed p -values. By doing so the expected p -values and exclusion limits indirectly depend on the observed data in the SRs, and can change slightly when the data is unblinded.²² The fitted nuisance parameters are displayed by HISTFITTER as α values where the displacement from 0 represents any change to the nominal auxiliary measurement θ_k^0 and the width represents any fitted constraints

¹⁹ The Neyman-Pearson lemma [170] proves that the log-likelihood ratio q is the most powerful hypothesis test statistic in this case.

²⁰ If the signal contribution is negative, $\hat{\mu}_{\text{sig}} < 0$, we should not allow the background to be reduced non-physically. This is enforced by turning $q_{\mu_{\text{sig}}}$ into an appropriate piecewise function, see [168].

²¹ Formally $\boldsymbol{\theta}^0$ is the maximum likelihood estimation of the nuisance parameters.

²² See Figure A.44 for a demonstration of the effect in this analysis.

on the $\pm 1\sigma$ variation parameterized by θ_k . An example of fitted nuisance parameters from this analysis can be found in Figure 5.9. If the width of α is < 1 (> 1) the corresponding systematic variation originally provided to HISTFITTER was found to be too large (small) by the fit. Lastly, in the limit of large numbers of events, even only $\mathcal{O}(10)$, the profiled PDF can be approximated asymptotically [168] via Wilks' theorem [171] as a χ^2 distribution and no pseudo-experiments are required.

With $\mu_{\text{sig}} = 1$, the profile-likelihood fit gives a p -value of $p_1 = p_{s+b}$ for the signal plus background hypothesis test. However, p_{s+b} has the undesirable tendency to set overly optimistic limits when there is a downwards background fluctuation in b . To address this, a background-only fit with $\mu_{\text{sig}} = 0$, $p_0 = p_b$ is also performed and the two are combined to form a signal confidence level CL_s [172],

$$CL_s = \frac{p_{s+b}}{1 - p_b}, \quad (4.15)$$

where $1 - p_b$ is the p -value at which the observed data is incompatible with the background-only hypothesis. For the purposes of excluding new physics the standard approach in SUSY searches is to reject phase space at the 95 % CL_s level.

5

The Multi-*b* Search

The multi-*b* search [4, 5, 173] is a model dependent search for SUSY in the form of gluino pair production decaying strongly, via $\tilde{g} \rightarrow \tilde{t}\tilde{t}_1 \rightarrow t\bar{t}\tilde{\chi}_1^0$ and the top decays of Section 2.1.4, to a final state of multiple *b*-jets, neutralinos which appear as E_T^{miss} , and a variable number of leptons. As described in Section 2.2.6 a simplified model for this decay, known as the Gtt model, only requires two parameters, $m_{\tilde{g}}$ and $m_{\tilde{\chi}_1^0}$, in the off-shell case¹ where $m_{\tilde{t}} > m_{\tilde{g}}$. In this dissertation a re-analysis of the 2015–2017 79.8 fb^{-1} search [4] is presented utilizing a BDT classifier to increase the explored parameter space.

5.1 Signal and Background Samples

The data and MC samples used in this analysis are very similar to those of the 2015–2017 79.8 fb^{-1} analysis [4]. An updated event quality cleaning procedure produced a final dataset with an integrated luminosity of 79.9 fb^{-1} . The MC signal and background samples are nearly identical to those of [4] though they have been reprocessed in the current version of the ATLAS offline software. The backgrounds

¹ MADGRAPH models $\tilde{g} \rightarrow t\bar{t}\tilde{\chi}_1^0$ as an effective three-body decay and $m_{\tilde{t}}$ is set to a constant 5 TeV.

include $t\bar{t}$, single-top, $t\bar{t} + X$ ², $W + \text{jets}$, $Z + \text{jets}$, and diboson samples. $t\bar{t}$ is the leading background and is generated with POWHEG-Box [174] v2 and the NNPDF3.0 [175] PDF set. The generators used for each MC sample can be found in Table 5.1. The data-driven multijet background sample was not available in recent offline software versions and is omitted from this analysis as it was not a major background in [4]. The kinematic correction³ to address data to MC discrepancies in the 1L channel developed in [4] has been retained.

The Gtt signal mass grid extends along $m_{\tilde{g}}$ from 1100–2400 GeV in 100 GeV increments, and along $m_{\tilde{\chi}_1^0}$ from 1–2000 GeV in roughly 200 GeV increments up to the kinematically forbidden $m_{\tilde{g}} = m_{\tilde{\chi}_1^0} + 2m_t$ line. Only off-shell \tilde{t} decays are considered.⁴ The signal production cross section and its associated uncertainty are derived with an envelope of predictions from different PDF sets, factorization and renormalization scales [176].

5.2 Physics Objects

The object selections used in the prior 79.8 fb^{-1} result are reused in this analysis for consistency. A summary of the final object definitions is provided below; for full details on the reconstruction and overlap removal process see [4].

Lepton candidates are selected to increase object quality based on various particle identification, isolation, impact parameter, and kinematic selections. Both electrons and muons must have $p_T > 20 \text{ GeV}$ and $|z_0 \sin \theta| < 0.5 \text{ mm}$. Electrons are selected which have $|\eta| < 2.47$, $|d_0| / \sigma_{d_0} < 5$, and pass “tight” identification requirements [190]. The electron identification decision is made from ECAL shower shape variables and ID

² Sometimes grouped together as topEW, or partially grouped as topEW*.

³ Known as RW_1CR.

⁴ Limited on-shell signal simulation samples were available at the time of analysis, but preliminary studies appeared to indicate similar BDT classification performance as compared to off-shell events.

Table 5.1: List of generators used for each simulated processes, adapted from [4].

Process	Generator + Fragmentation/Hadronization	Tune	PDF Set	Cross Section Order
Gtt	MADGRAPH5_aMC@NLO 2.3.3 + PYTHIA 8.212	A14	NNPDF2.3	NLO+NLL [176, 177, 178, 179, 180, 181]
t̄t	POWHEG-BOX v2 + PYTHIA 8.230	A14	NNPDF3.0	NNLO+NNLL [182]
Single-top Wt-channel (<i>s/t</i>)	POWHEG-BOX v1 (v2) + PYTHIA 6.428 (8.230)	PERUGIA2012	CT10	NNLO+NNLL [183, 184, 185]
t̄tW/t̄tZ	MADGRAPH5_aMC@NLO 2.2.2 + PYTHIA 8.186	A14	NNPDF2.3	NLO [186]
4-tops	MADGRAPH 2.2.2 + PYTHIA 8.186	A14	NNPDF2.3	NLO [186]
t̄tH	MADGRAPH5_aMC@NLO 2.2.1 + HERWIG++ 2.7.1	UEEE5	CT10	NLO [187]
Dibosons WW, WZ, ZZ	SHERPA 2.2.1	Default	NNPDF3.0	NLO [45, 188]
W/Z+jets	SHERPA 2.2.1	Default	NNPDF3.0	NNLO [189]

track variables, including TR measurements from the TRT, combined in a likelihood-based approach. Muons are selected which have $|\eta| < 2.5$, $|d_0| / \sigma_{d_0} < 3$, and pass “medium” identification requirements [191]. The muon identification decision is based on ID and MS track variables, and the compatibility of the momentum independently measured in each detector system.

Small- R jets are reconstructed from EM scale calorimeter clusters with the anti- k_t algorithm at a radius of $R = 0.4$. The jets are then calibrated, as described in Section 4.2, and cleaned to remove jets from non-collision sources⁵ [192] and pileup [193]. Overlap with leptons is removed, and the jets are required to have $p_T > 30\text{ GeV}$ and $|\eta| < 2.8$. The calibrated small- R jets are then re-clustered into large- R anti- k_t $R = 0.8$ jets which are subsequently trimmed with $f_{\text{cut}} = 0.1$ and required to have $p_T > 100\text{ GeV}$, $|\eta| < 2.0$. The small- R calibration propagates through to the

⁵ Such “jets” are due to non-collision muons depositing energy in the calorimeters then being falsely reconstructed as jets. These muons may come from upstream proton beam losses or cosmic-ray showers [192].

re-clustered jets as demonstrated in Appendix E.3. The radius of $R = 0.8$ was chosen in earlier versions of the analysis [5] to best capture boosted top quark decays in re-clustered jets, as quantified via the performance of the M_J^{Σ} variable (5.5). The small- R jets are also tagged as b -jets according to the MV2c10 b -tagger operating at the 77 % efficiency working point.

The E_T^{miss} is constructed from all of the reconstructed and calibrated objects in the event following Section 4.1.4 and includes the track soft term.

5.2.1 Variables

With the above physics objects reconstructed it is useful to create higher level variables designed to have differing distributions between SM background and SUSY Gtt signal events. For events with at least one lepton, known as the 1L channel, we define the transverse mass m_T between E_T^{miss} and the leading lepton to be:

$$m_T = \sqrt{2p_T^{\text{lepton}}E_T^{\text{miss}}(1 - \cos(\Delta\phi(\vec{p}_T^{\text{miss}}, \vec{p}_T^{\text{lepton}})))}. \quad (5.1)$$

m_T is useful for reducing $t\bar{t}$ and $W+\text{jets}$ backgrounds with leptonic W decays where it peaks at the W mass while being typically larger in Gtt events. Similarly the minimum transverse mass between E_T^{miss} and the three leading b -jets,

$$m_{T,\min}^{b\text{-jets}} = \min_{i \leq 3} \left(\sqrt{2p_T^{b\text{-jet } i}E_T^{\text{miss}}(1 - \cos(\Delta\phi(\vec{p}_T^{\text{miss}}, \vec{p}_T^{b\text{-jet } i})))} \right), \quad (5.2)$$

has a kinematic endpoint near m_t for $t\bar{t}$ background events, while taking higher values for Gtt as E_T^{miss} from neutralinos is largely independent of the b -jets. The inclusive effective mass of the event, defined to be E_T^{miss} plus the p_T of all jets and leptons,

$$m_{\text{eff}}^{\text{incl}} = E_T^{\text{miss}} + \sum_i p_T^{\text{jet } i} + \sum_j p_T^{\text{lep } j}, \quad (5.3)$$

and effective mass of E_T^{miss} and the four leading jets,

$$m_{\text{eff}}^{4j} = E_T^{\text{miss}} + \sum_{i=1}^4 p_T^{\text{jet } i}, \quad (5.4)$$

are both larger for Gtt signal compared to SM backgrounds as they correlate to the mass scale of the original decaying particles. The total mass of the four leading re-clustered jets,

$$M_J^\Sigma = \sum_{i \leq 4} m_{\text{RCjet } i}, \quad (5.5)$$

is also much larger for Gtt events with their up-to-four top decays in comparison to the leading $t\bar{t}$ background's two. The minimum $\Delta\phi$ between E_T^{miss} and the p_T of any of the four leading jets in the event,

$$\Delta\phi_{\min}^{4j} = \min_{i \leq 4} (\left| \phi_{\text{jet } i} - \phi_{\vec{p}_T^{\text{miss}}} \right|), \quad (5.6)$$

is useful in the zero lepton channel, 0L, for reducing the effects of SM multijet background events which can appear to possess large amounts of E_T^{miss} if some jets are poorly measured or happen to have coaxial neutrinos.

In addition to the above variables from the standard multi- b search which focus on leading p_T objects, new variables sensitive to soft components of the event were developed during the course of this research. The scalar sum of p_T from the fifth and softer jets,

$$H_T^{\text{soft jets}} = \sum_{5 \leq i} p_T^{\text{jet } i}, \quad (5.7)$$

and its combination with the lepton p_T sum,

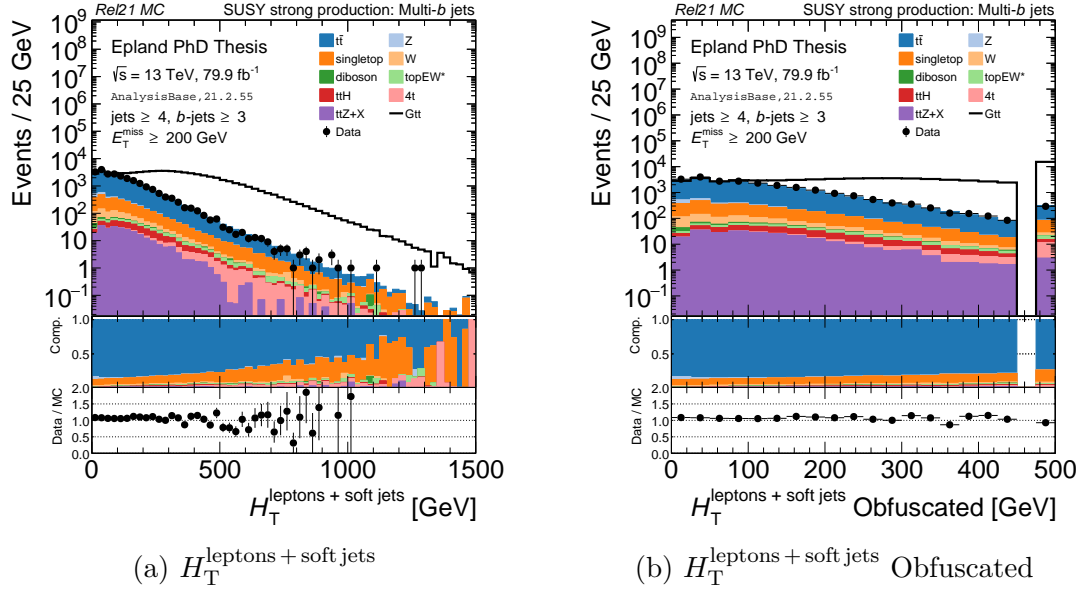


FIGURE 5.1: Construction of $H_T^{\text{leptons} + \text{soft jets}}$ Obfuscated. The data to MC mismatch seen above 500 GeV in $H_T^{\text{leptons} + \text{soft jets}}$ can be alleviated by setting values above 450 GeV to 480 GeV, forming the still useful $H_T^{\text{leptons} + \text{soft jets}}$ Obfuscated.

$$H_T^{\text{leptons} + \text{soft jets}} = \sum_{5 \leq i} p_T^{\text{jet } i} + \sum_j p_T^{\text{lep } j}, \quad (5.8)$$

are high for Gtt events with their many jets and low for SM backgrounds like $t\bar{t}$ which do not produce more than four jets from the hard scatter. The modeling of these soft jets in background processes is poorer than for the hard components, and indeed $H_T^{\text{leptons} + \text{soft jets}}$ shows some data to MC discrepancies above 500 GeV. However, creating “ $H_T^{\text{leptons} + \text{soft jets}}$ Obfuscated” by setting values above 450 GeV to 480 GeV was found to fix the mismodeling while still remaining a useful variable, as shown in Figure 5.1.

Along with standard object multiplicity variables for jets, b -jets, and signal leptons, N_{jet} , $N_{b\text{-jet}}$, $N_{\text{sig lep}}$, the number of small- R jets with $p_T > X \text{ GeV}$ in $|\eta| < Y$, $N_{\text{jet}}(p_T > X \text{ GeV}, \eta < Y)$, and re-clustered jets with $m > Z \text{ GeV}$, $N_{\text{RC jet}}(m > Z \text{ GeV})$

are also used.

Lastly, to more simply parameterize the Gtt signal we define

$$\Delta m = m_{\tilde{g}} - m_{\tilde{\chi}_1^0} \quad (5.9)$$

to be the mass difference between the gluino and neutralino signal masses. A larger Δm will allow an event to impart more energy to the final state neutralinos, thereby increasing the potential E_T^{miss} . Gtt events of this type are considered to be “boosted”, while those with small values of Δm , and thus low expected E_T^{miss} , are considered to be “compressed”.

5.3 Event Selection

Preliminary event quality cleaning is performed to ensure nominal beam, detector, and data conditions for all events under consideration. Events are required to have a primary vertex that contains at least two $p_T > 0.4 \text{ GeV}$ tracks and is consistent with the IP beam spot. In events with multiple primary vertices, the vertex with the largest sum of track p_T is defined to be the true primary vertex.

Events were required to pass the lowest unprescaled HLT E_T^{miss} trigger available in each data taking period, and have $E_T^{\text{miss}} \geq 200 \text{ GeV}$ such that the trigger efficiency was $\approx 100\%$. Additional preselections shared with the standard multi- b analysis further suppressed SM backgrounds; $N_{\text{jet}} \geq 4$, $N_{b\text{-jet}} \geq 3$, $p_T^{\text{jet}1} > 30 \text{ GeV}$, and if $N_{\text{sig lep}} = 0$ *i.e.* 0L, $\Delta\phi_{\min}^{4j} > 0.4$. This comes at the cost of a reduced Gtt efficiency of $\approx 30\text{--}50\%$ across the studied mass parameters. Signal efficiency results for the preselection and each individual selection can be found in Appendix [A.1](#).

5.4 BDT Analysis

In order to improve on the results obtained by the standard 2015–2017 79.8 fb^{-1} analysis [4] a BDT approach in XGBoost⁶ [152] was chosen to increase the signal and background classification performance, thereby producing higher performance signal regions and using the available data more efficiently. As the characteristics of the Gtt final state vary with $m_{\tilde{g}}$ and Δm these variables were input to the BDT as parameters following the approach presented in [197]. For Gtt events $m_{\tilde{g}}$, Δm take their true values, while for SM background events they are selected uniformly from the signal mass point distribution. When it comes time to make predictions⁷ particular values of the $m_{\tilde{g}}$, Δm parameters can be chosen, effectively returning a distinct BDT by making constant splits on $m_{\tilde{g}}$ and Δm branches. In this way one BDT can be trained across the whole mass parameter space, while still being sensitive to changes in the signal characteristics in different regions.

To avoid and quantify any overfitting the MC samples were divided into three sets, the train set with 53.6 % of the data by MC event weight,⁸ validation set at 13.3 %, and test set at 33 %. The train and validation sets were regularly used to train the BDT and engineer the signal regions, while the test set was used sparingly to check for overfitting⁹ and to produce the final results. All of the MC samples were divided individually between the three sets to ensure an equal proportion of event types in each.

⁶ Data processing performed in PYTHON with UPROOT [194], PANDAS [195], and NUMPY [196].

⁷ BDTs have not been shown to interpolate well between parameter points used in training [197], thus we shall only pick parameter points used in training when making predictions to be safe.

⁸ 33 % of the data was first set aside for the test set, while the remaining 67 % was divided into 5 folds, one of which was used for validation and the other 4 for training. The folds were also used independently for cross-validation studies reported in Table A.12.

⁹ For comparisons between the test and train set in terms of the output \hat{y} score see Appendix A.9, and in terms of expected exclusion limit see Figure A.45. No evidence of overtraining was observed.

5.4.1 Input Variable Selection

The first step in the process of any machine learning analysis is selecting an appropriate set of input variables, or features. 70 kinematic and high-level variables were initially considered after verifying each was free of MC mismodeling.¹⁰ Input variables were ranked in an iterative process; the BDT was trained on all variables under consideration, the lowest variable by gain was removed, and the process was repeated until only the signal parameters remained. For best results the variable ranking process was performed a second time on the top 45 variables from the first run. The final set of 18 input variables, plus the two mass parameters for a total of 20, were chosen by hand based on the BDT performance as measured by Z_B vs mass point, the mean Z_B over select points near the edge of the prior expected exclusion limit, and the area under the receiver operating characteristic curve (AUC ROC). Detailed results are provided in Appendix A.2.

The 18 input variables can be divided into two rough groups; a core set of 7 which provide $\sim 80\%$ of the performance:

- $N_{\text{jet}}(p_T > 30 \text{ GeV}, \eta < 1.3)$, $N_{\text{jet}}(p_T > 30 \text{ GeV}, \eta < 1.5)$,
- $N_{\text{jet}}(p_T > 30 \text{ GeV}, \eta < 2.0)$, $N_{\text{jet}}(p_T > 50 \text{ GeV}, \eta < 1.5)$,
- $H_T^{\text{leptons} + \text{soft jets}}$ Obfuscated, m_T , E_T^{miss} ,

and the remaining 11:

- $N_{\text{sig lep}}$, $N_{\text{RC jet}}(m > 80 \text{ GeV})$, $N_{\text{jet}}(p_T > 30 \text{ GeV}, \eta < 1.0)$,
- $N_{\text{jet}}(p_T > 50 \text{ GeV}, \eta < 1.0)$, $N_{\text{jet}}(p_T > 50 \text{ GeV}, \eta < 1.3)$,
- $H_T^{\text{soft jets}}$, $m_{\text{eff}}^{\text{incl}}$, $m_{T,\text{min}}^{b\text{-jets}}$, M_J^Σ , m_{eff}^{4j} , $p_T^{b\text{-jet } 4}$,

which help performance at higher masses and in the compressed corner in particular.

¹⁰ For data to MC comparisons of the final 18 input variables see Appendix A.10.

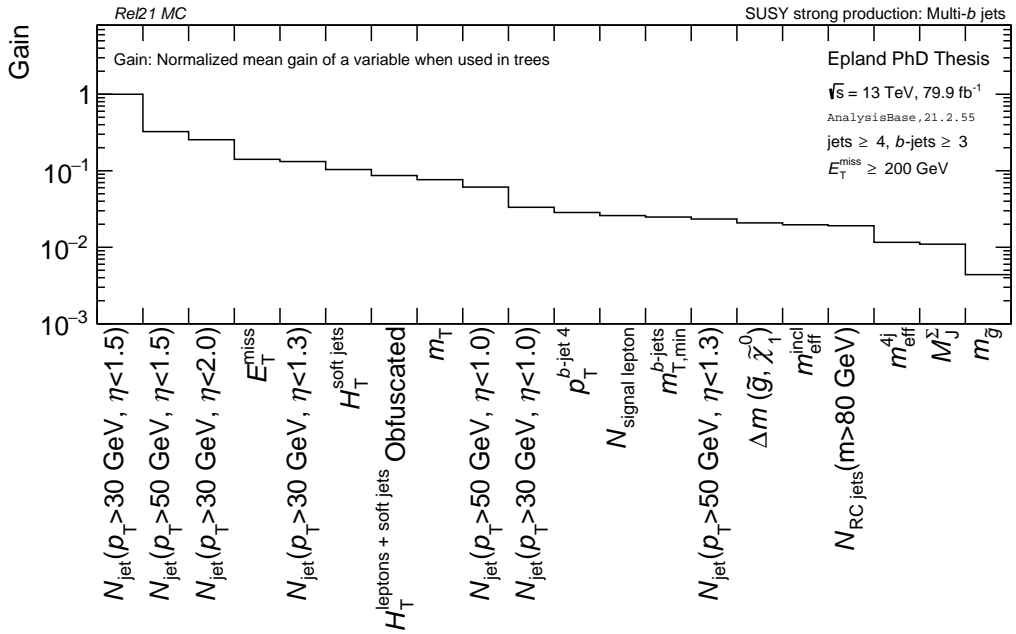


FIGURE 5.2: Input variables used by the BDT in order of relative gain across all mass points.

Plotting the input variables by gain as in Figure 5.2 is a valuable way of visualizing their relative classification utility. The $N_{\text{jet}}(p_T > X \text{ GeV}, \eta < Y)$ variables are markedly useful, providing some p_T and η information about the final state to the BDT without all the details of each jet's four vector. Along with E_T^{miss} , $H_T^{\text{soft jets}}$, and $H_T^{\text{leptons + soft jets}}$ they easily outperform the standard effective mass variables $m_{T,\min}^{b\text{-jets}}$, $m_{\text{eff}}^{\text{incl}}$, and M_J^Σ at the heart of prior analyses. The signal parameters $m_{\tilde{g}}$, Δm rank in the bottom quarter of input variables, showing that they do have some effect on the BDT, but not to an undesirably large degree. Ideally the relative rankings of the input variables may change with the particular signal parameters under consideration while the parameters themselves always have low gains. This was observed in the cross checks of Figure A.11.

5.4.2 Hyperparameter Tuning

With the input variables in hand, we can next tune the hyperparameters of the BDT to maximize its performance. Starting from the default hyperparameters of XGBOOST the learning rate η , maximum tree depth, and early stopping validation threshold¹¹ are simultaneously optimized via Bayesian optimization with a random forest¹² regressor in SCIKIT-OPTIMIZE [200, 201, 202, 203]. This hyperparameter tuning netted a 3.4% improvement in the BDT performance as measured by the mean Z_B over select points. Full results are provided in Appendix A.3. The final tuned hyperparameter values are¹³:

- Learning rate $\eta = 0.0722758514998$,
- Maximum tree depth = 7,
- Early stopping validation threshold = 0.769402992287.

5.4.3 BDT Training

To train the BDT, MC event weights are rescaled such that each signal mass point has an equal total weight of signal and background events. This fixes the class imbalance problem, resulting in a more unbiased classifier for both signal and background. Since the SM background events are uniformly assigned between the signal mass points, each point effectively receives $w_{\text{all}}^{\text{bkg}} / N_{\text{mass points}}^{\text{sig}}$ background events which are then upscaled to match the uniform amount of signal at the mass point. The rescaled training weights are only used in training the BDT, all subsequent predictions and analysis utilize the physical MC weights. The BDT is then trained with early stopping

¹¹ The number of early stopping rounds was set to 10.

¹² Bayesian optimization with Gaussian processes [198, 199] was also run, but the random forest optimization found a slightly better result.

¹³ Note that all of the digits reported here are not significant. However, this is what was returned by the optimizer and was used while training the final BDT.

enabled on the validation set, halting after $K_{\text{best}} = 197$ boosting rounds¹⁴ in ≈ 2 min on 4 CPU cores.¹⁵ For reference, all input variables displayed with their split values from the trained BDT, and data to MC comparisons, are provided in Appendix A.10.

5.5 Parameter Point Selection

While the BDT can make predictions from any number of signal mass parameter points it is unwise to attempt to use all possible 115 points when searching for SUSY as the eventual HISTFITTER fit may start to be potentially impacted by the look elsewhere effect, described in Appendix C, as well as being enormously unwieldy. It is therefore essential to pick a handful of representative points from the mass grid to simplify matters while still providing good coverage, particularly in the area of the expected exclusion limit. These points also may differ between the 0L and 1L channels. Choosing representative points could be performed by hand, with the physicist selecting particular points via their subjective judgment, as is effectively the case in many standard cut-and-count analyses of this type. Instead, over the course of this research, a new approach was developed to identify interesting regions in parameter space algorithmically.

To group related parameter points we must first define a metric for their similarity. The parameterized BDT itself can be of great use in this area, as comparable parameter points should produce similar predictions for the same input events. Quantitatively this idea can be expressed as the root mean squared deviation (RMSD) between BDT

¹⁴ The upper limit K_{max} was set to 200 as prior versions of the BDT trained in 100–150 rounds. The best iteration of $K_{\text{best}} = 197$ was noticed after all of the final results had been produced, and together with an early stopping window of 10 rounds implies that the training halted due to K_{max} rather than early stopping. However, $K_{\text{best}} = 191 \pm 8$ in the cross-validation studies presented in Table A.12, so $K_{\text{best}} = 197$ is probably not being severely constrained by K_{max} . In any case, as the BDT performance is acceptable this is not a problem, but could mean that another BDT trained with additional boosting rounds might have produced slightly better results.

¹⁵ This is quite reasonable as far as some machine learning algorithms go, and is what enables the input variable and hyperparameter optimization processes to use so many iterations of the BDT. For reference, all of the training variables fill ≈ 260 MB of memory across the train and test sets.

output scores,

$$\text{RMSD}(p_i, p_j) = \sqrt{\sum_k w_k (\hat{y}_k^{p_i} - \hat{y}_k^{p_j})^2 / \sum_k w_k}, \quad (5.10)$$

where $\hat{y}_k^{p_i}$ and $\hat{y}_k^{p_j}$ are output scores for the same train set event k with different parameter points, and w_k is the appropriate event weight. The RMSD¹⁶ is small, or even zero, for parameter points that result in similar predictions. Thus it is convenient to transform the raw RMSD values by adding the minimal non-zero RMSD observed then taking the inverse, $1/(\text{RMSD} + \text{RMSD}_{\min > 0})$, such that division by zero issues are avoided and similar points return higher scores. The radius in mass space,

$$R_m(p_i, p_j) = \sqrt{(\Delta m_{\tilde{g}})^2 + (\Delta m_{\tilde{\chi}_1^0})^2}, \quad (5.11)$$

is also useful for relating parameter points as it tends to form compact clusters in mass space. Again taking the inverse $1/R_m$ is necessary to have the correct scaling.

Defining the combined similarity metric to be

$$W_{ij} = 1/(\text{RMSD} + \text{RMSD}_{\min > 0}) + b/R_m, \quad (5.12)$$

where b is a scaling factor, a connected graph or network¹⁷ can be formed with parameter points as nodes and variable weight edges between them set by W_{ij} . Related clusters, or communities, within the graph can then be identified via the Louvain method [205, 206], which forms communities such that their internal (external) weighted edge densities are maximized (minimized). Reasonable communities were found to be created with $b = 1$ as shown in Figure 5.3 and Appendix A.4.

¹⁶ The Pearson correlation coefficient and reflective Pearson correlation coefficient were also studied in place of the RMSD, but the correlation between points was too high globally to be a useful metric for identifying individual clusters.

¹⁷ Carried out computationally in NETWORKX [204].

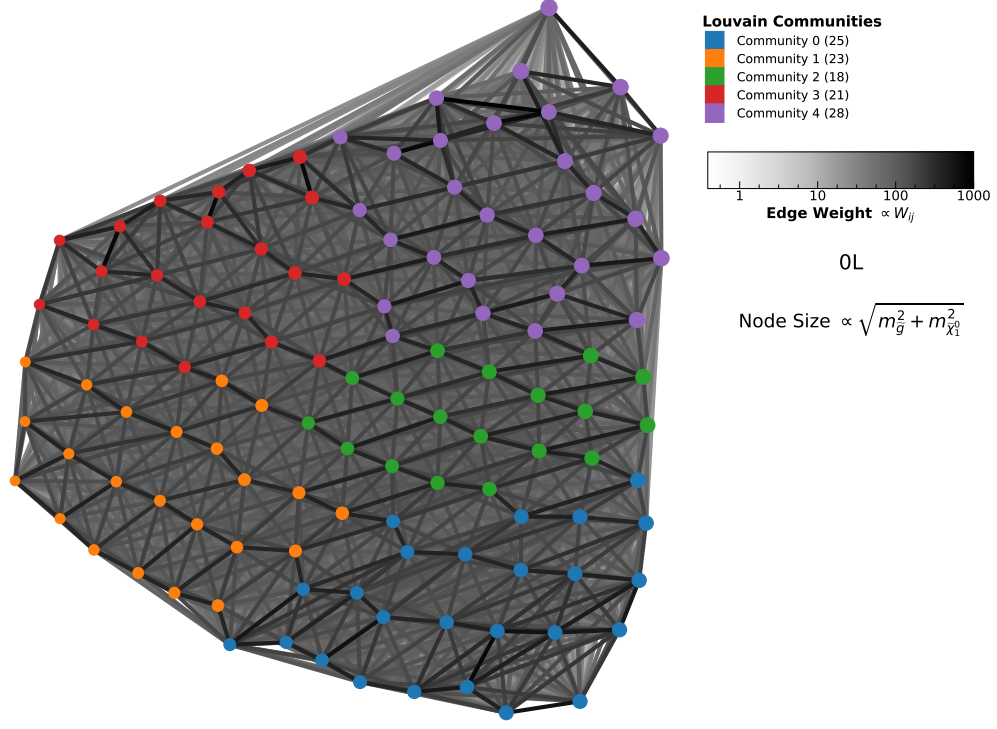


FIGURE 5.3: Graph of mass parameter points and Louvain communities in the OL channel. The position of nodes is set via a spring relaxation algorithm and their size corresponds to their masses. The edge shading is proportional to W_{ij} and is darker for stronger edges.

Having formed related communities in parameter space the next simplification is to reduce each community to a single best representative point. The node with maximum eigenvector centrality and the node nearest to the center-of-mass were considered as possibilities for this point, but better results were found with a more physically-based algorithm. For every community, the algorithm loops over the constituent points using each in turn to make predictions about all signal events with mass points in the community. Z_B is computed at each point using all available background events with the proper rescaling. The signal event weights are also uniformly normalized across mass points to remove any effects from the varying Gtt production cross section. A significance metric is then formed from the average of these results, with each

individual significance first capped at $Z = 5.0$ to reduce the impact of outliers:

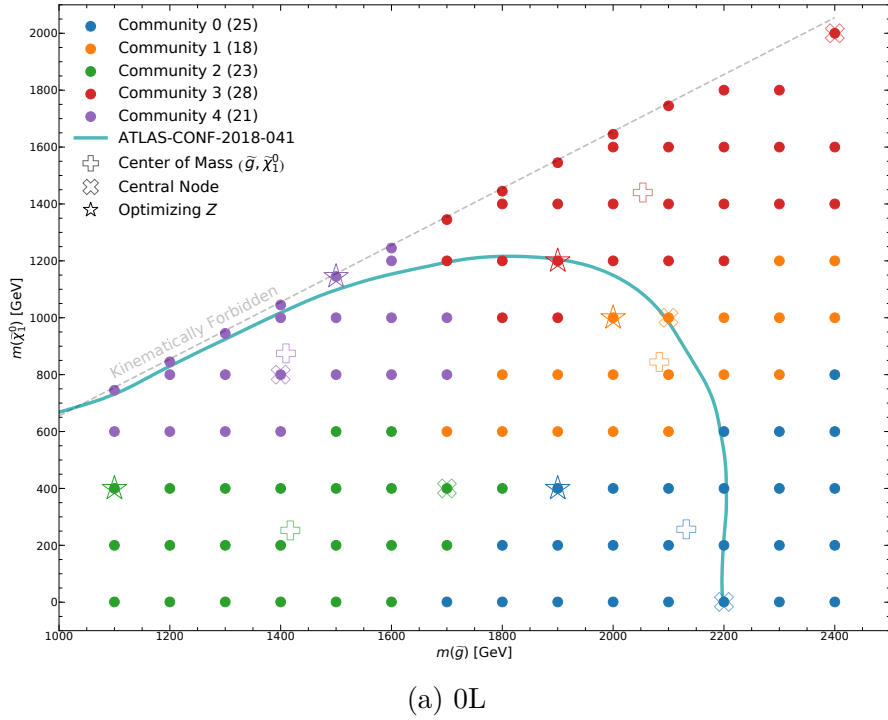
$$Z_{\text{metric}} = \langle \min(5.0, Z) \rangle. \quad (5.13)$$

The point with the highest Z_{metric} is considered to be the best point for representing the whole community, as it maximizes the significance at other points when substituted for them. Plots of these representative parameter points are shown in Figure 5.4 for the 0L and 1L channels. Both leptonic channels have the community 2 (green) point in the same location, while the rest are generally near each other and the prior expected exclusion limit. To simplify the nomenclature parameter points are labeled according to their lepton channel and community number, *i.e.* P1L_0 for the 1L community 0 point.

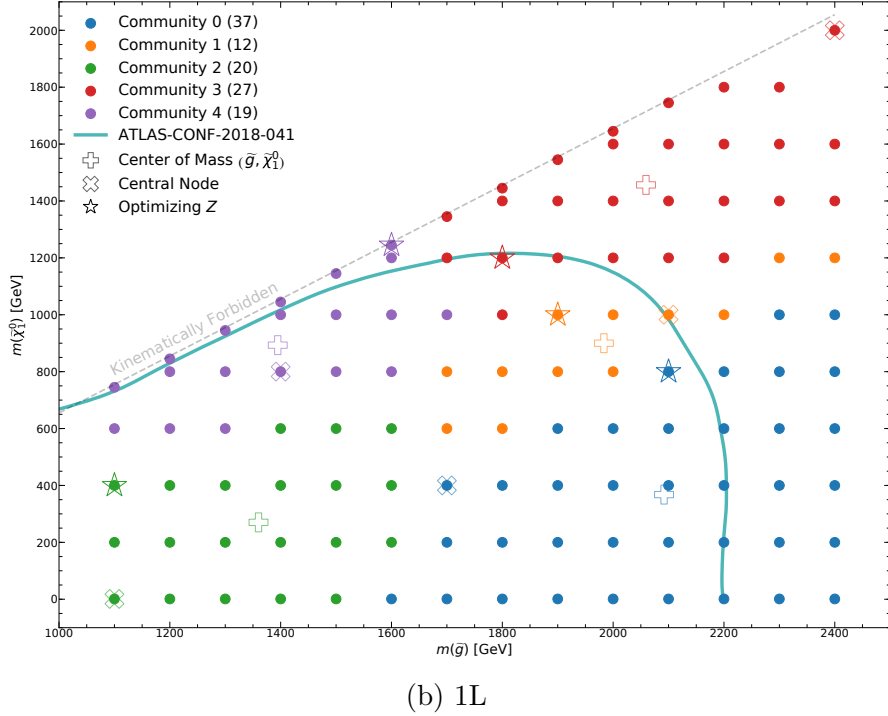
5.6 Control, Validation, and Signal Regions Selection

While identifying representative parameter points was non-trivial they alone do not define usable control, validation, and signal regions (CRs, VRs, and SRs) for the final fit. Fortunately, with a solid BDT classifier it is possible to create the necessary regions from bins in the output score $\hat{y}_{\text{SUSY}, \text{BDT}}$ with precisely the desired levels of signal contamination. SRs are placed at the upper end of \hat{y} near 1.0 to afford them the maximum amount of signal acceptance. Lying below the SRs are the CRs needed to find the proper normalization and the VRs to validate it. As very background-like events are easy to identify and subsequently receive very low scores near $\hat{y} = 0$ they do not meaningfully contaminate the SR. Instead it is signal-like background events that score in the ≈ 0.9 –0.95 range which are likely to be misclassified by the BDT and end up in the SR, and thus are where the normalization should be calculated for the best extrapolation performance.

Within the particular output score defined by each parameter point, $\hat{y}(m_{\tilde{g}}, \Delta m)$,



(a) 0L



(b) 1L

FIGURE 5.4: Positions of representative parameter points (stars) in the 0L and 1L channel with the center-of-mass and central node also shown for reference.

the CR, VR, and SR are algorithmically determined with the following procedure. A useful binning of \hat{y} is created starting from 0.002 width bins, rebinned so that each has $W_{\text{bkg}} \geq 0.5$ with the leading background, $t\bar{t}$, statistical uncertainty $\leq 30\%$. S/B and S/\sqrt{B} are plotted after being smoothed with a Gaussian kernel of $\sigma = 0.01$ to reduce statistical fluctuations. Only signal events from the parameter point under consideration are included in the calculation, and if possible the Gtt production cross section is reweighted to match the observed 36.1 fb^{-1} exclusion limits [5]. This allows for tighter SRs, and larger limits, to be created at low masses where Gtt has already been excluded to some degree and is the first time such an approach has been used in an ATLAS SUSY search. The changes to the integrated signal event weights per mass point can be found in Figure A.20.

The potential range for the SR is defined to be from $\hat{y} = 1.0$ to where $S/B \geq 1.0$, $W_{\text{sig}} \geq 4.0$, and $W_{\text{bkg}} \geq 1.0$. From this initial range multiple SR bins can be formed to include signal shape information in the fit.¹⁸ The highest SR bin is selected in the same way as the optimized threshold for the Z_B calculation, with the expected background target raised to 1.0, and is thus the best individual SR bin. Up to 4 additional bins of varying widths are allowed below the top bin, sized so they each have roughly the same amount of expected background events and a minimum of 1.0. The SR bins are labeled SR0 through SR4 with SR4 being the top bin. To avoid signal contamination the VR is constructed to begin where $S/B \leq 0.2$, $S/\sqrt{B} \leq 3$, and continue until $W_{\text{bkg}} \geq 20$. Lastly, the CR starts at $S/B \leq 0.1$ or the end of the VR, whichever is lower, and continues until $W_{\text{bkg}} \geq 30$. The sizes of the CR and VR were chosen to provide enough statistics for the normalization while keeping them as close as possible to the SR. Though it contains many steps this procedure can create tunable fit regions which are relatively simple to understand, particularly visually as seen in Figure 5.5. S/B results for all parameter points can be found in

¹⁸ Shape fitting in SR \hat{y} bins has been used previously by the $t\bar{t} \rightarrow 1\text{L}$ search [207], Tables 7 & 15.

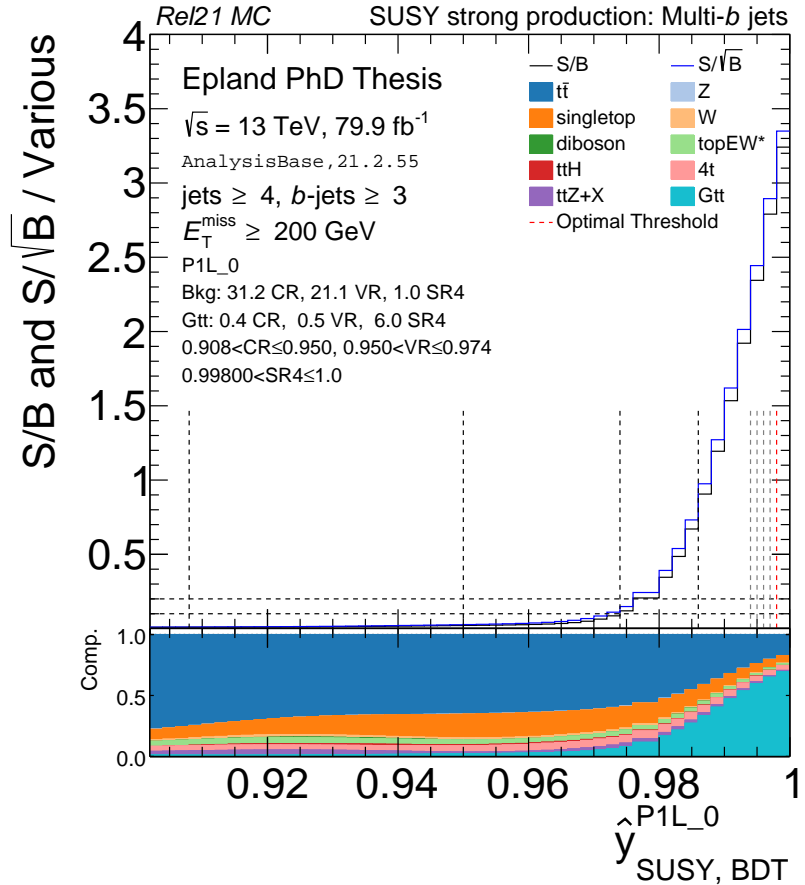


FIGURE 5.5: Smoothed S/B and S/\sqrt{B} for the parameter point P1L_0. The SR bins start at $\hat{y} = 1.0$ on the right with the top optimized SR4 bin in red, and continue in the light grey down to SR0. The SR bins only take up around half of the available SR range, after which there is another unused segment where $0.2 \leq S/B < 1.0$. The VR and CR then follow from right to left as the wide \hat{y} ranges required to collect the desired statistics. A summary of the fit region limits and expected event content can be found in the annotation.

Appendix A.5.

5.6.1 Fit Region Background Compositions

The expected background composition in each fit region of P1L_0 can be seen in Figure 5.6. $t\bar{t}$ is the leading background in all regions, followed by single-top. This is the case as well for the other 1L parameter points. On the train set in the 0L regions single-top makes up a larger fraction of the SR bins, as seen in Appendix A.5,

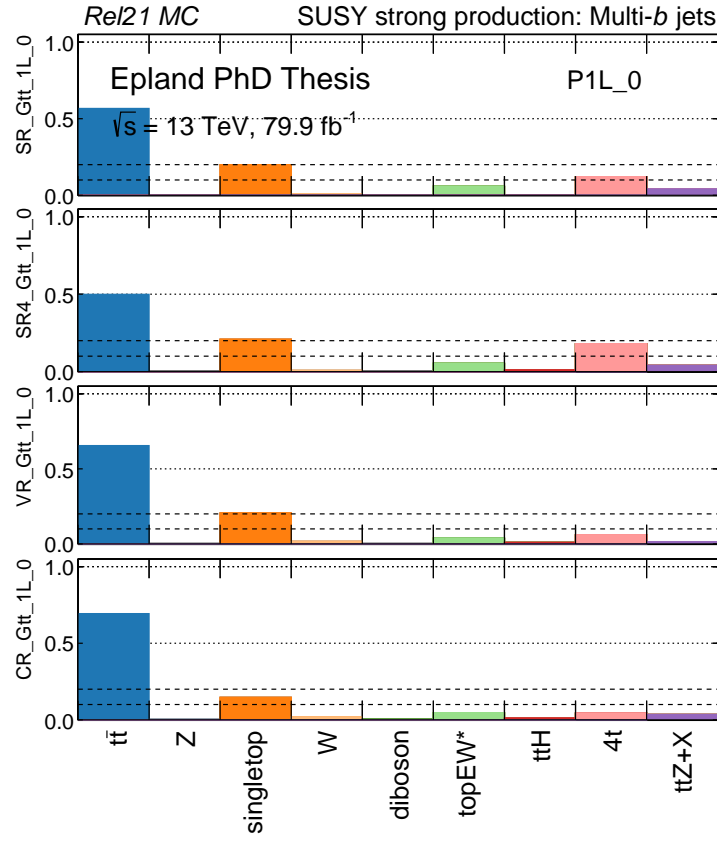


FIGURE 5.6: Fit region background compositions for parameter point P1L_0. $t\bar{t}$ is the leading background followed by single-top. Here $SR_Gtt_1L_0$ represents the union of all SR bins, $SR0$ through $SR4$, while $SR4_Gtt_1L_0$ is the top bin alone. Reference lines are provided at 0.1, 0.2, and 0.5. Events are drawn from the train set.

particularly in the top SR4 bins which are ultimately¹⁹ the only bins included in the 0L fits. It was decided to only normalize the $t\bar{t}$ background with $t\bar{t}$ dominated CRs and VRs, constructed via the above procedure, when the single-top fraction was lower²⁰ before these SR bins were removed.

An additional complication was discovered when switching to the test set during the final stages of the analysis. As can be seen in Figure 5.12, the 0L bin's single-top fraction is smaller in the test set and $t\bar{t}$ is again the leading background. While the

¹⁹ See the following discussion in Section 5.7.2.

²⁰ See $SR_Gtt_0L_1$ of Figure A.22b.

train and test set were created in a stratified manner, the low SR bin background yields, ~ 1.0 by design, induce enough MC statistical uncertainty to cause background composition fluctuations of this magnitude. In the end, however, only normalizing the $t\bar{t}$ background is sufficient as the test set used in the final results is majority $t\bar{t}$ in all SR bins, and HISTFITTER properly accounts for systematic and statistical uncertainties on the other backgrounds in the SRs. To increase the background statistics in the SRs while maintaining a low background yield, future work could employ the “ k -ensemble construction” technique²¹ currently emerging in ATLAS.

If required, future BDT-driven searches could also create independent flavor-specific CRs and VRs per SR for each prominent background through the use of an additional multi-class BDT. The second BDT can be trained on signal-like background events, with high $\hat{y}_{\text{SUSY}, \text{BDT}}$ scores from the first two-class BDT, to identify different background types.²² Together orthogonal selections on $\hat{y}_{\text{SUSY}, \text{BDT}}$ and the second BDT’s background-specific \hat{y} scores could then define flavor-specific CRs and VRs. This approach was investigated during the course of this research but was not ultimately pursued.

5.7 Uncertainties

5.7.1 Experimental Systematics

Experimental systematic uncertainties developed by the various ATLAS performance groups are applied to the underlying events in signal and background samples, before being propagated through the preselections, BDT predictions, and fit itself. The

²¹ The k -ensemble construction divides the MC into k folds and trains k machine learning models over them, while withholding one fold from each model. When the final unblinded test set results are needed each model is used only to make predictions on events from its withheld fold. In this way no event’s \hat{y} score comes from a model that saw that event in training, while still making use of all available MC statistics in the final result.

²² One multi-class BDT on its own is likely not sufficient as the per class \hat{y} scores are constrained to $\sum_i \hat{y}_i = 1$, at least in XGBOOST. It is therefore extremely challenging to construct pure flavor-specific CRs with high $\hat{y}_{\text{SUSY}, \text{BDT}}$ scores and retain enough statistics.

leading experimental uncertainty for this analysis was the JER²³ [143]. Additional sources of experimental uncertainty include the JES [143], jet vertex tagger (JVT) [208], b -tagging efficiencies and mis-tagging rates [138, 139], and integrated luminosity [209]. A systematic uncertainty arising from the kinematic correction to the 1L channel is also included. To fix issues in the flavor tagging calibration a constant 40 % uncertainty is applied to $W/Z + \text{jets}$ and diboson samples. Other experimental systematics have been shown previously to be negligible in this final state [4, 5].

5.7.2 Theoretical Systematics

Many theoretical systematic uncertainties are included in this analysis, each affecting different MC samples. Starting with $t\bar{t}$, hadronization and parton shower systematic variations are evaluated by generating events in POWHEG then comparing the results of showering with HERWIG++ 2.7.1 [47] via the cluster model, and PYTHIA 6.428 [5] via the Lund string model. Initial and final state radiation is varied in the POWHEG samples by showering with the radHi and radLo settings of PYTHIA 6.428 [210], which change the renormalization scale to $\alpha_S(2Q)$ and $\alpha_S(\frac{1}{2}Q)$ respectively. The effect of the choice of $t\bar{t}$ matrix-element generator²⁴ is evaluated by comparing results from samples generated with POWHEG and MADGRAPH5_aMC@NLO. For $t\bar{t}$ events produced with extra heavy-flavor jets, *i.e.* $t\bar{t}+ \geq 1b$ and $t\bar{t}+ \geq 1c$, an additional uncertainty derived by varying the cross section of such events by 30 % [5] is included to account for the large theoretical uncertainties on these processes.

Single-top samples receive radiation systematic variations from PYTHIA 6.428

²³ The simplified 8 nuisance parameter version of the JER systematic was used as it had been shown to be sufficient in prior multi- b results [4]. As can be seen in Figure 5.9 the JER nuisance parameters are slightly constrained, indicating that the full set of correlated nuisance parameters may be a better option going forward.

²⁴ In reality more than two generator variations should be considered, but using two is common practice with the justification that the final results do not strongly depend on the generator systematic. This is the case for this analysis shown in Figure A.27 where doubling the size of the estimated generator systematic does little to change the final exclusion limit.

in the same manner as $t\bar{t}$, and a constant 5% uncertainty on their cross sections from HATHOR predictions [211]. Additionally, single-top is particularly sensitive to interference between the $t\bar{t}$ and Wt processes. This interference is modeled with inclusive WWb events, generated with MADGRAPH5_aMC@NLO, which are compared to the sum of $t\bar{t}$ and Wt .

The $W/Z + \text{jets}$ samples receive uncertainties from varying the scale used to match between jets originating from the matrix element and in the parton shower. The factorization, renormalization, and resummation scales are also varied by factors of 0.5 and 2 [5]. A constant, uncorrelated 50% uncertainty is applied to the normalization of the minor $t\bar{t} + W/Z/H$, $t\bar{t}t\bar{t}$ and diboson backgrounds. Lastly, the Gtt signal samples receive an uncertainty on their production cross sections from an envelope of predictions [176].

The theory systematic uncertainties, when not fixed values, are derived from MC truth samples processed with continuous b -tagging via the tag rate function (TRF) [212] to improve statistics.²⁵ Unfortunately, some of the regions formed by the strict selections on $\hat{y}_{\text{SUSY}, \text{BDT}}$ still have limited MC statistics. Additionally, as the truth samples are not reconstructed some of their nominal input variable distributions differ from the corresponding standard MC samples. While these were not issues for the standard analysis [4] they result in some BDT SR bins having extremely large calculated theory systematics for $t\bar{t}$ and single-top. To address this issue it was decided, before unblinding, to prune any SR bins where the combined $t\bar{t}$ or single-top theory uncertainty plus its error was so large it would translate to ± 1 in the event yield.²⁶ For $t\bar{t}$ (single-top) with ≈ 0.5 (≈ 0.25) events in each SR bin, this works out

²⁵ Events failing the nominal b -jet selections are not rejected outright, but are instead weighted according to the probability they might contain mis-tagged jet(s).

²⁶ The full Run 2 multi- b analysis can request the generation of additional samples to improve MC statistics, and pass them through the reconstruction process to feed the BDT the same kind of variables it was trained on.

to be a threshold of $\geq 200\%$ ($\geq 400\%$). The event-driven $t\bar{t}$ and single-top theory systematic relative uncertainties for the remaining regions are provided in Figure 5.7, with their initial versions in Figure A.28.

5.7.3 Statistical Uncertainties, Combining Uncertainties, Nuisance Parameters

Two types of statistical uncertainties are encountered in the fit; uncertainties from the extrapolation of the $t\bar{t}$ normalization from CR to SR, $\mu_{t\bar{t}}$, and uncertainties on the yields of sub-leading backgrounds in SRs as predicted from the MC samples, γ . All of the uncertainties are given to the fit individually, allowing the proper correlations to be taken into account as needed. Tables of each uncertainty in every region can be found in Appendix A.6.1. To concisely summarize the many uncertainties they have been grouped by type and region in Figure 5.8. An example of the fitted nuisance parameters in one region is displayed in Figure 5.9, with all regions provided in Appendix A.6.2.

5.8 Fit Construction

Fit regions from different parameter points are non-orthogonal within a lepton channel as $\hat{y}_{\text{SUSY}, \text{BDT}}$ is correlated between regions. This is most easily seen in the low ranking of $m_{\tilde{g}}$ and Δm in Figure 5.2 and the RMSD-only graph of Figure A.16. However, across lepton channels, fit regions are orthogonal by definition. To make use of all regions in the fit we therefore construct orthogonal²⁷ combinations of 0L and 1L regions, such as Gtt_0L_1_Gtt_1L_2, and then combine these into one larger non-orthogonal fit. Individual regions with large VR pulls indicating a poor normalization extrapolation from CR to SR, such as Gtt_1L_1, are first dropped to improve the fit quality. All possible 0L, 1L combinations are initially considered, however not all are equally useful as, like a dot product, the best gains come from combining regions with

²⁷ Here orthogonal (non-orthogonal) refers to a multi-bin (single-bin) fit in HISTFITTER.

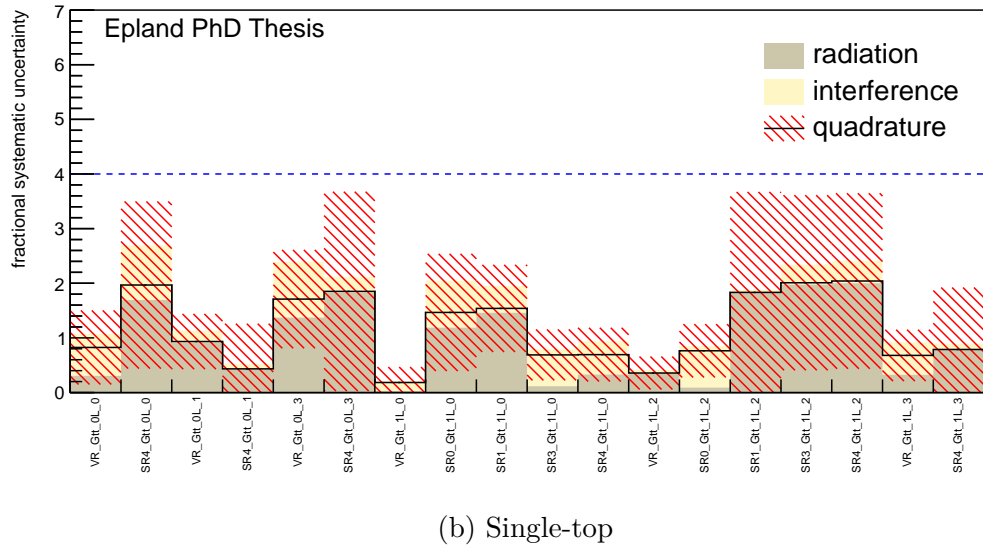
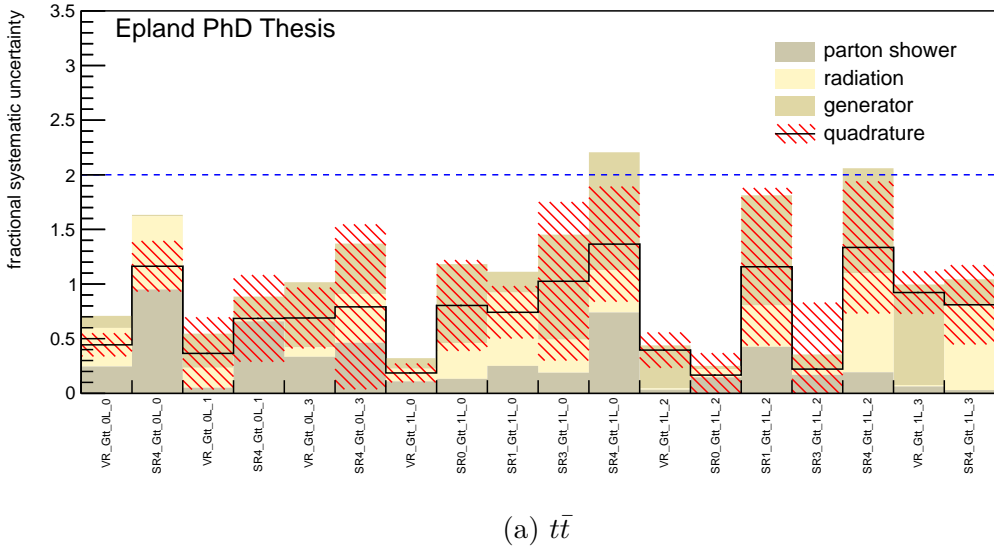


FIGURE 5.7: Event-driven theory systematic uncertainties for $t\bar{t}$ and single-top. The $t\bar{t}$ uncertainties include parton shower, radiation, and generator systematics components, while single-top includes radiation and interference. The quadrature sum, with error, is also displayed. SR bins with a quadrature sum plus error greater than the blue dashed thresholds are removed from the fit before unblinding. This has the effect of removing all of Gtt_0L_4, while Gtt_0L_2, Gtt_1L_1, and Gtt_1L_4 were removed for other reasons detailed in Section 5.8.

Table 5.2: Selected fit region definitions. Note that regions in different lepton channels are orthogonal by construction, while regions within a lepton channel are non-orthogonal. For regions of a particular parameter point the selections on \hat{y} make each CR, VR, and SR bin orthogonal among themselves.

Region	$m_{\tilde{g}}$	$m_{\tilde{\chi}_1^0}$	$N_{\text{sig lep}}$	Type	\hat{y} Selection
Gtt_0L_0	1900 GeV	400 GeV	0	CR	$0.88400 \leq \hat{y}_{0L_0} < 0.94200$
				VR	$0.94200 \leq \hat{y}_{0L_0} < 0.97200$
				SR4	$0.99836 \leq \hat{y}_{0L_0} \leq 1.00000$
Gtt_0L_1	2000 GeV	1000 GeV	0	CR	$0.91800 \leq \hat{y}_{0L_1} < 0.95000$
				VR	$0.95000 \leq \hat{y}_{0L_1} < 0.97200$
				SR4	$0.99717 \leq \hat{y}_{0L_1} \leq 1.00000$
Gtt_0L_3	1900 GeV	1200 GeV	0	CR	$0.93000 \leq \hat{y}_{0L_3} < 0.95400$
				VR	$0.95400 \leq \hat{y}_{0L_3} < 0.97000$
				SR4	$0.99621 \leq \hat{y}_{0L_3} \leq 1.00000$
Gtt_1L_0	2100 GeV	800 GeV	≥ 1	CR	$0.90800 \leq \hat{y}_{1L_0} < 0.95000$
				VR	$0.95000 \leq \hat{y}_{1L_0} < 0.97400$
				SR0	$0.99400 \leq \hat{y}_{1L_0} < 0.99500$
				SR1	$0.99500 \leq \hat{y}_{1L_0} < 0.99600$
				SR3	$0.99700 \leq \hat{y}_{1L_0} < 0.99800$
				SR4	$0.99800 \leq \hat{y}_{1L_0} \leq 1.00000$
				CR	$0.93400 \leq \hat{y}_{1L_2} < 0.95200$
				VR	$0.95200 \leq \hat{y}_{1L_2} < 0.96600$
Gtt_1L_2	1100 GeV	400 GeV	≥ 1	SR0	$0.99300 \leq \hat{y}_{1L_2} < 0.99400$
				SR1	$0.99400 \leq \hat{y}_{1L_2} < 0.99500$
				SR3	$0.99600 \leq \hat{y}_{1L_2} < 0.99706$
				SR4	$0.99706 \leq \hat{y}_{1L_2} \leq 1.00000$
Gtt_1L_3	1800 GeV	1200 GeV	≥ 1	CR	$0.91800 \leq \hat{y}_{1L_3} < 0.94400$
				VR	$0.94400 \leq \hat{y}_{1L_3} < 0.96200$
				SR4	$0.99562 \leq \hat{y}_{1L_3} \leq 1.00000$

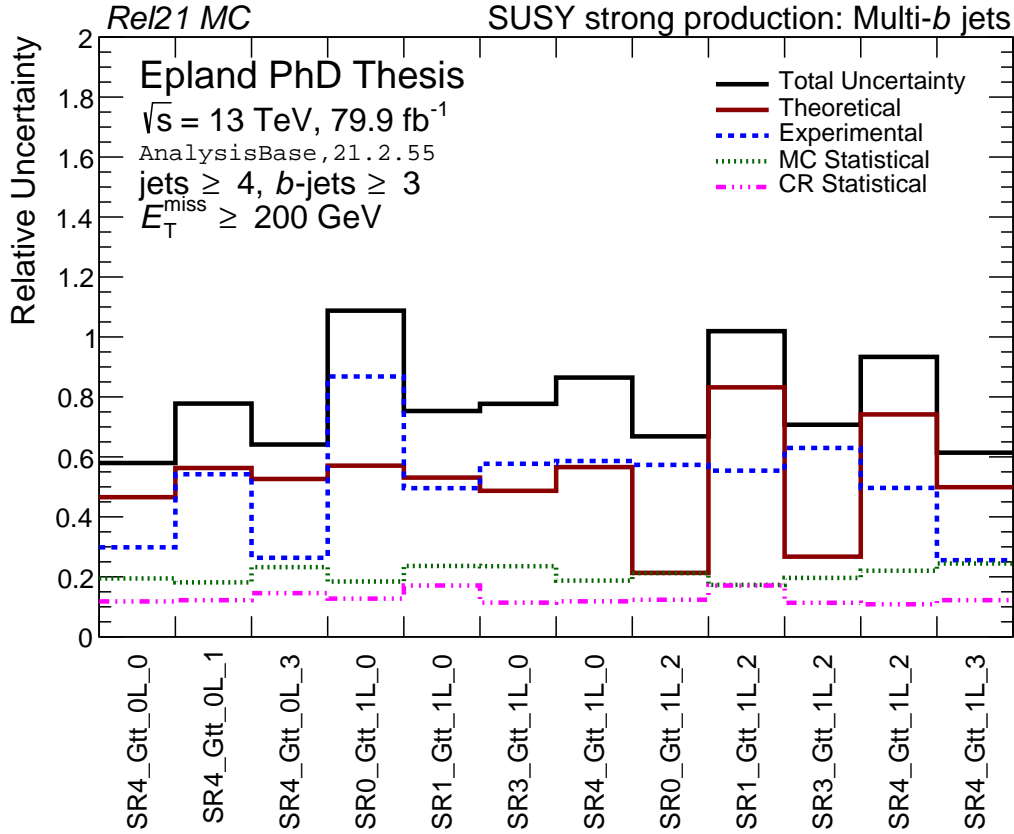


FIGURE 5.8: Relative uncertainties per SR. The displayed theoretical and experimental components are simple quadrature sums of all the relevant individual systematic uncertainties. The total uncertainty produced by the fit takes into account all of the proper correlations.

similar parameter points, *i.e.* both boosted or compressed. Redundant combinations which do not contribute to the non-orthogonal fit are removed. This has the effect of dropping Gtt_0L_2 and Gtt_1L_4 as they are no longer needed in any combination. The expected individual exclusion limits of the retained combinations can be seen in Figure A.35. Upon cross referencing the parameter point locations shown in Figure A.34 one can see that the BDT parameterization is working as intended, with boosted points driving the boosted limit particularly when two boosted points are in combination, and vice versa for compressed. A summary of all regions used in the final fit, with SR bins pruned according to Section 5.7.2, can be found in Table 5.2.

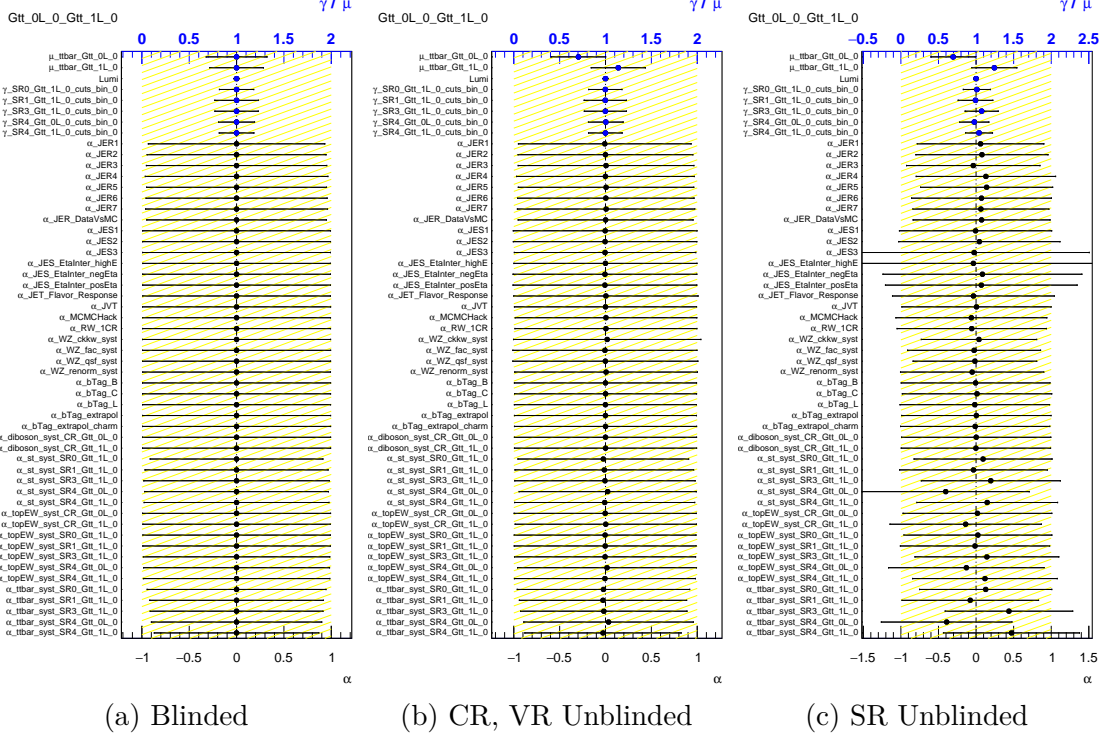


FIGURE 5.9: Gtt_0L_0_Gtt_1L_0 fitted nuisance parameters at different levels of unblinding. $\mu_{t\bar{t}}$ represents statistical uncertainties on the normalization extrapolation from CR to SR. γ represents statistical uncertainties on SR background yields in MC. α represents the fitted nuisance parameter for a particular systematic. The displacement from 0 represents any change to the nominal measurement and the width represents any fitted constraints to the $\pm 1\sigma$ variations. Here some of the JER and theory systematics appear to be slightly constrained. When the fit is fully blinded only the constraints can be estimated from MC, after unblinding the CR and VR the displacements from nominal are added. The unblinded SRs can have a large impact on the nuisance parameter displacements, as discussed in Section 4.4.5, but as long as they remain within $|\alpha| < 1$ as seen here there is no cause for concern.

5.9 Results

5.9.1 Background Fits

Having constructed effective fit regions, the data and MC samples are first fit in the CRs and VRs as shown in Figures 5.10 and 5.11. The CRs have event yields of ≈ 30 as designed, and the fits show reasonable agreement between the data and expected MC with $t\bar{t}$ normalization factors near $\mu \approx 1.0$. Extrapolating to the VRs, the normalizations produce satisfactorily small pulls between the expected and observed

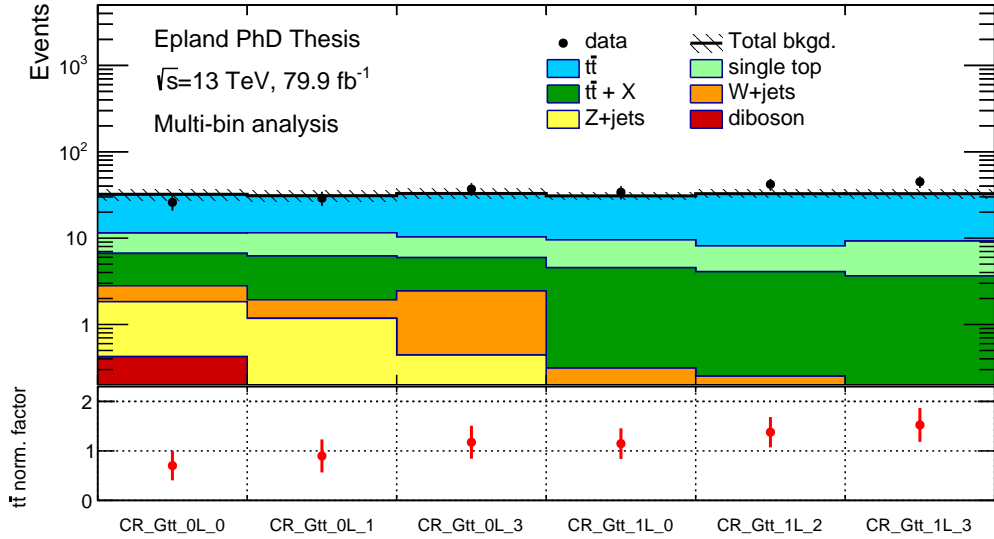


FIGURE 5.10: Control region fits. The $t\bar{t}$ normalization factors, μ , are distributed near 1.0 and each CR has an yield of ≈ 30 events as expected.

yields of ≈ 20 . Most VRs either showed an improvement in the data to MC agreement after application of the $t\bar{t}$ normalization factors or remained the same, as illustrated by Figure A.37.

5.9.2 Exclusion Fits

After verifying that the analysis strategy, uncertainties, and background fits were all acceptable the decision was made to unblind the analysis and look at the data in the SRs. The resulting yields are displayed in Figure 5.12. As constructed, the MC background yields in each SR bin were $\approx 1\text{--}2$ events and no significant excesses were observed in data. The largest pulls between observed and expected of $\approx 1.5\sigma$ were seen in SR3_Gtt_1L_0 and SR4_Gtt_1L_3. Detailed event yields for each region are provided in Appendix A.8.2.

No events were observed in data for any of the three non-orthogonal 0L SR bins. Additional studies were conducted to estimate the probability of this result occurring

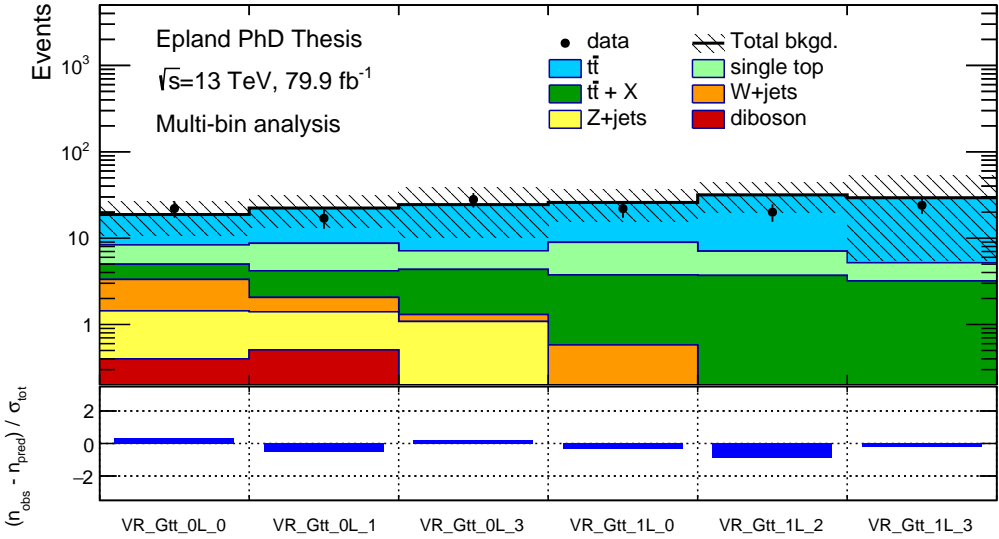


FIGURE 5.11: Validation region fits. The $t\bar{t}$ normalization factors produce relatively small pulls between expected and observed event yields. Each VR has a yield of ≈ 20 events as expected.

with the expected background distributions. The total number of background events in the 0L SR bins without double counting was found from the MC samples and used as the mean λ of a Poisson distribution to produce the probability $p(n = 0 | \lambda) = e^{-\lambda}$. On the train set²⁸ $p(0 | \lambda) = 0.15$ with a maximum and minimum value of 0.16 and 0.07 respectively over all the systematic variations. These studies show that the probability of observing zero 0L events by chance with these SRs is not insignificant, though a re-examination of the differences between 0L and 1L events in future work may be prudent.

The observed exclusion limit is consistent with the expected limit across the whole contour as seen in Figure 5.13. As could be anticipated from the lack of excesses in the SR bins, there are no suspicious dips in the observed exclusion limit hinting at a possible Gtt signal. Compared to the prior results from this

²⁸ On the test set $p = 0.09$, while together $p = 0.13$. This is another area where the k -ensemble construction could be useful for eliminating the differences between fixed train and test sets.

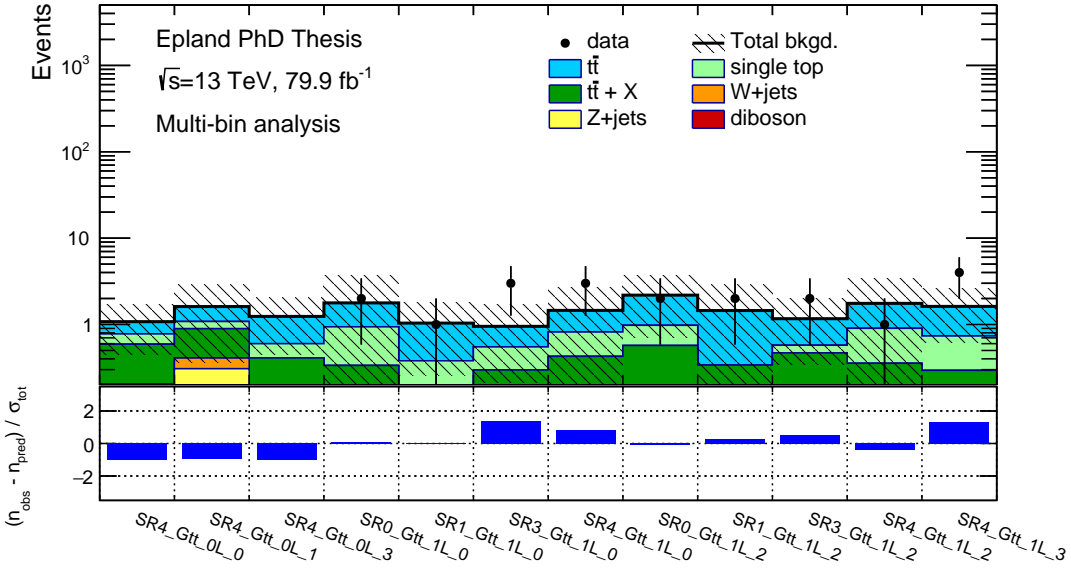


FIGURE 5.12: Signal region fits. No significant excesses above the expected $\approx 1\text{--}2$ events per SR bin were observed, while no events at all were seen in data for any of the three non-orthogonal 0L SR bins.

dataset, provided in Figure A.38 for reference, the BDT analysis appreciably extended the expected exclusion limit²⁹ by 100–200 GeV across the whole contour as seen in Figure 5.14a. This resulted in 250 GeV of new phase space along $m_{\tilde{\chi}_1^0}$ in the compressed region, up to approximately $m_{\tilde{\chi}_1^0} = 1.4$ TeV, being excluded by the observed limit as shown in Figure 5.14b. Individual exclusion limits for each region can be found in Appendix A.8.1.

The exclusion limit results can also be displayed in terms of the underlying CL_s values and cross section upper limits per mass point as is done in Figure 5.15. The slight outward bump in the upper-right corner of the observed contour is due to the $m_{\tilde{g}} = 2300$ GeV, $m_{\tilde{\chi}_1^0} = 1400$ GeV mass point pulling the extrapolated curve in its direction.

²⁹ See Appendix B for additional discussion in terms of the maximum potential performance.

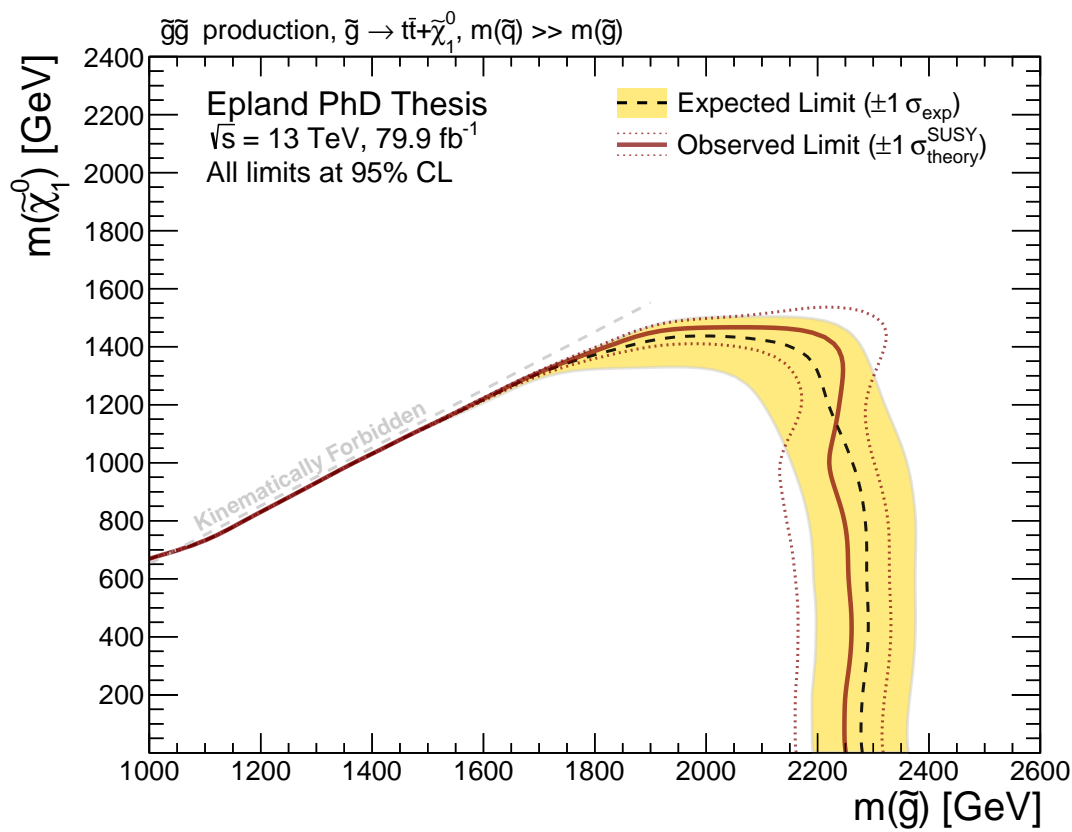
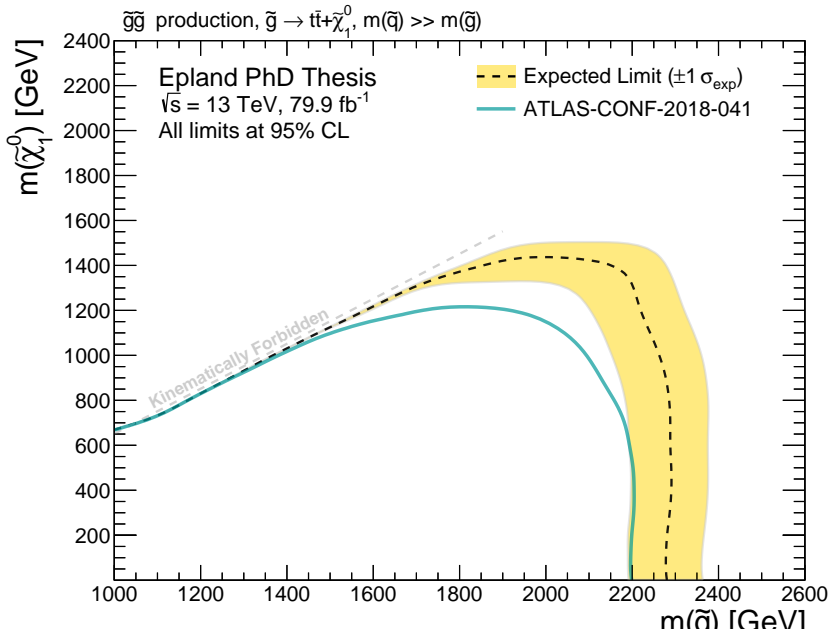
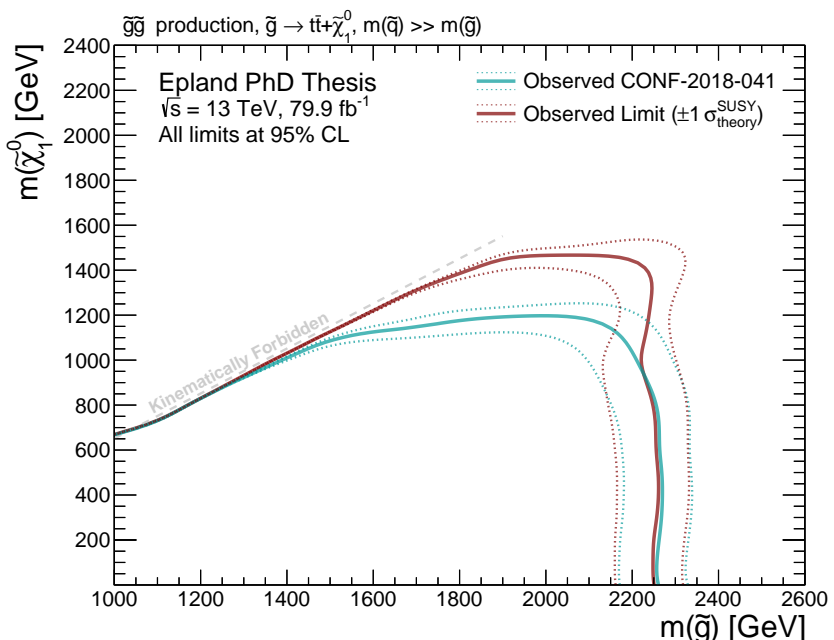


FIGURE 5.13: Observed and expected exclusion limits for the 79.9 fb^{-1} BDT analysis. Good agreement was found between the observed and expected limits.

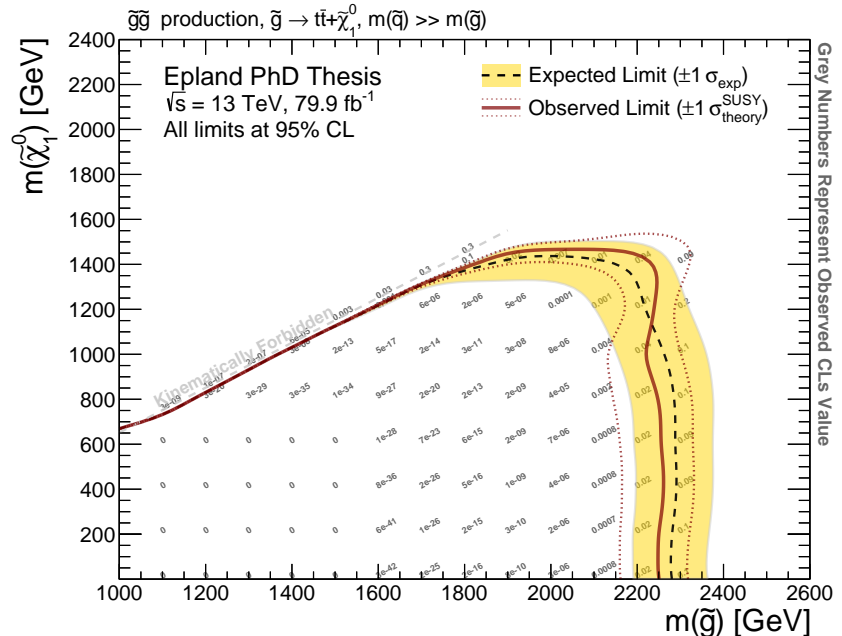


(a) Expected

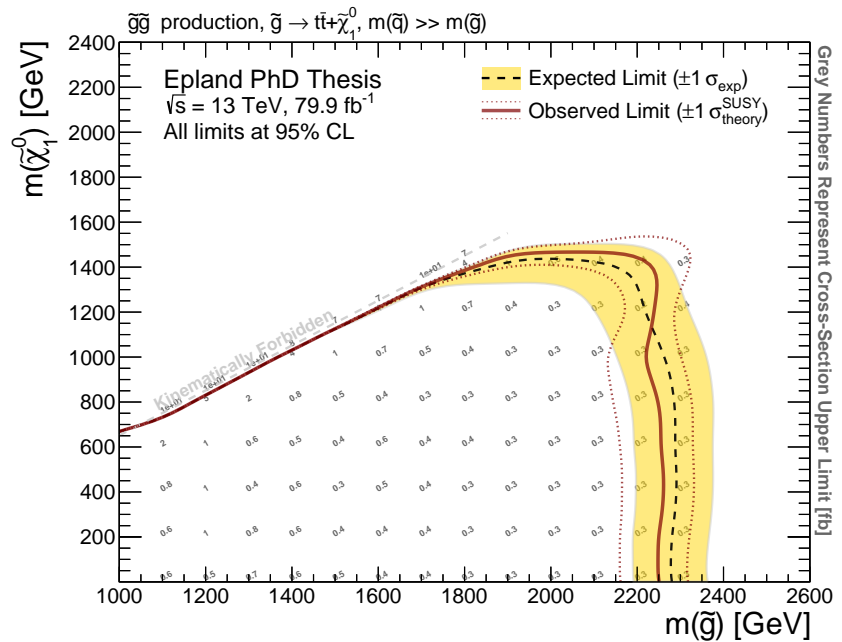


(b) Observed

FIGURE 5.14: Comparison of the expected and observed exclusion limits for the BDT analysis and standard 79.8 fb^{-1} result [4]. The BDT analysis extended the expected exclusion limit by 100–200 GeV across the whole contour, and the observed limit by 250 GeV in $m_{\tilde{\chi}_1^0}$ up to approximately 1.4 TeV.



(a) CL_s Limits



(b) Cross Section Limits

FIGURE 5.15: Observed CL_s and cross section limits for the 79.9 fb^{-1} BDT analysis. For the expected cross section limits see Figure A.36.

6

Conclusions

Over the course of the research presented in this dissertation, machine learning methods in the form of a BDT were first applied to the multi- b plus E_T^{miss} Gtt final state, leading to an increase of 100–200 GeV in the expected exclusion limit across the whole contour. The observed results were consistent with the expected limit, and extended the excluded region¹ by an additional 250 GeV to approximately 1.4 TeV in $m_{\tilde{\chi}_1^0}$. No evidence for SUSY was observed. If followed by similar negative results with the full Run 2 dataset in all channels at ATLAS and CMS, as has been the trend thus far, significant experimental constraints will be placed on SUSY. This will likely necessitate a major theoretical reassessment of SUSY’s naturalness and beauty in resolving the SM’s Higgs sector hierarchy problems and lack of a natural DM candidate.

While constructing the BDT analysis a new approach was developed to algorithmically select Gtt mass parameter points for signal region creation through the use of a weighted graph structure. At each parameter point fit regions were algorithmically created from the output $\hat{y}_{\text{SUSY,BDT}}$ score and expected S/B ratio. Cross section

¹ From the standard analysis on the same dataset [4].

exclusion limits from prior analyses were incorporated for the first time in this signal region optimization process. New variables aimed at measuring signal to background differences in the low p_T components of the event, $H_T^{\text{soft jets}}$ and $H_T^{\text{leptons} + \text{soft jets}}$, were identified and observed to give good performance when used appropriately. Variables of the form $N_{\text{jet}}(p_T > X\text{GeV}, \eta < Y)$ were found to be surprisingly useful, and together with E_T^{miss} , $H_T^{\text{soft jets}}$, and $H_T^{\text{leptons} + \text{soft jets}}$ had much higher gains in the BDT than the $m_{T,\text{min}}^{b\text{-jets}}$, $m_{\text{eff}}^{\text{incl}}$, and M_J^Σ mass variables central to prior analyses. While useful in its own right, this research also directly contributes to the analytical techniques that will be utilized by the full Run 2 multi- b search, helping to maximize its signal sensitivity and thereby hopefully discover, or substantially exclude, SUSY at the LHC.

Appendix A

Supplementary Multi-*b* Plots

A.1 Preselection Efficiency Studies

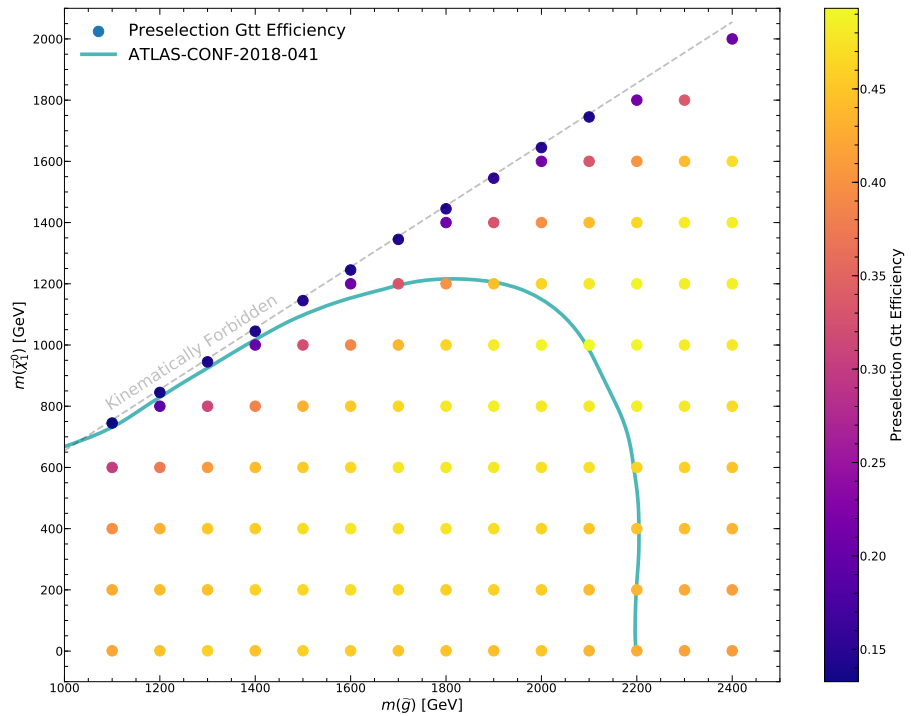


FIGURE A.1: Gtt signal efficiency of the full preselection.

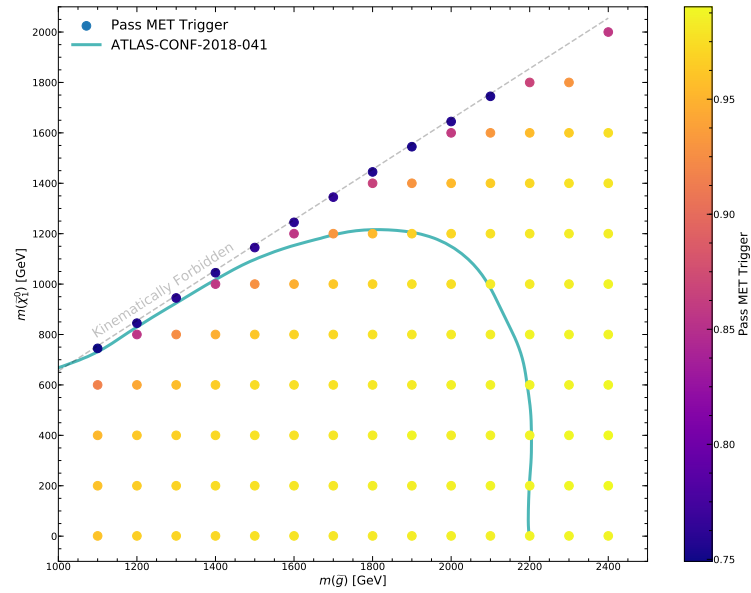


FIGURE A.2: Gtt signal efficiency of the E_T^{miss} trigger preselection.

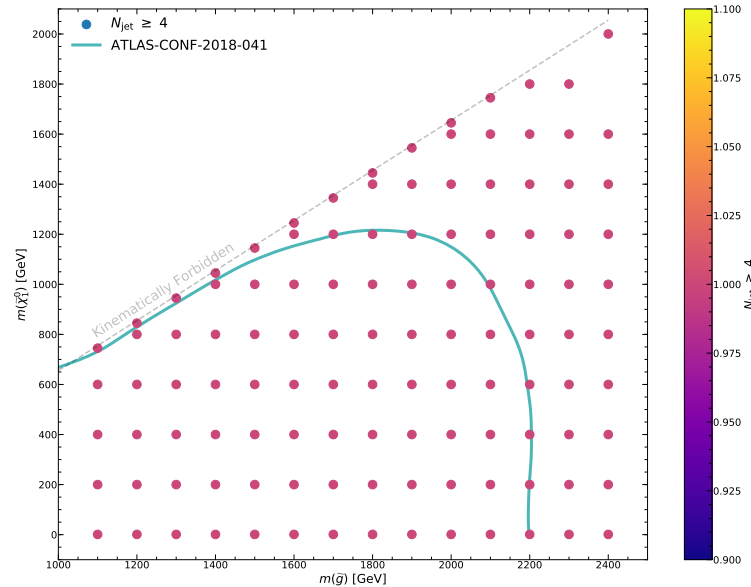


FIGURE A.3: Gtt signal efficiency of the $N_{\text{jet}} \geq 4$ preselection.

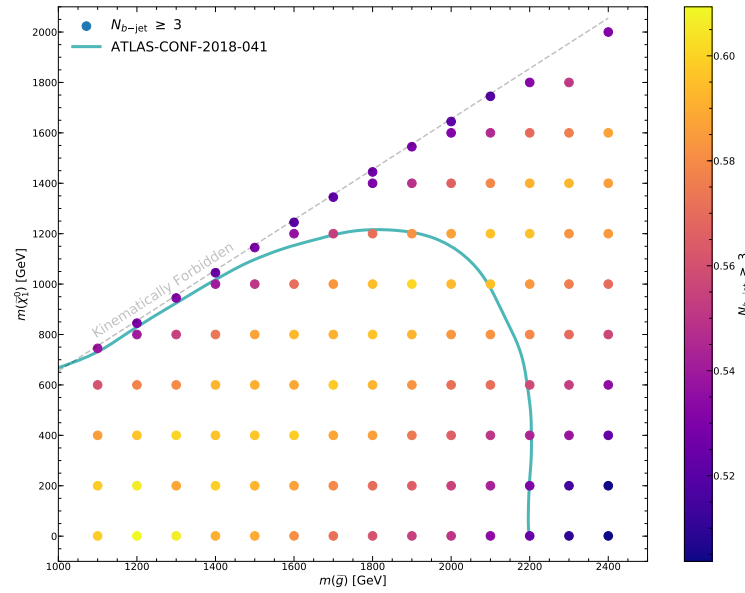


FIGURE A.4: Gtt signal efficiency of the $N_{b\text{-jet}} \geq 3$ preselection.

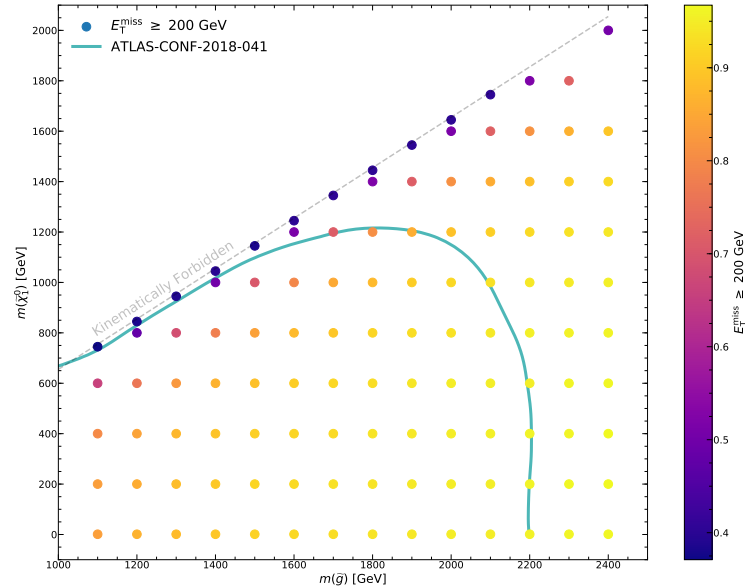


FIGURE A.5: Gtt signal efficiency of the $E_T^{\text{miss}} \geq 200 \text{ GeV}$ preselection.

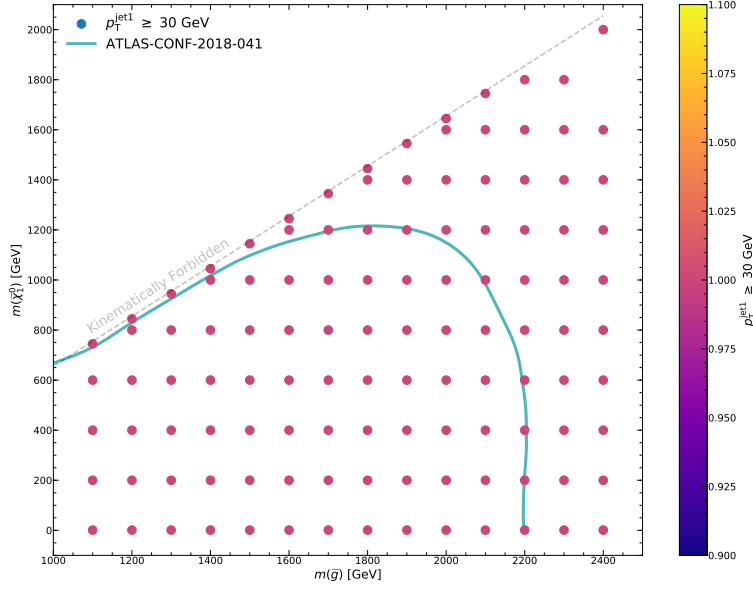


FIGURE A.6: Gtt signal efficiency of the $p_T^{\text{jet1}} > 30 \text{ GeV}$ preselection.

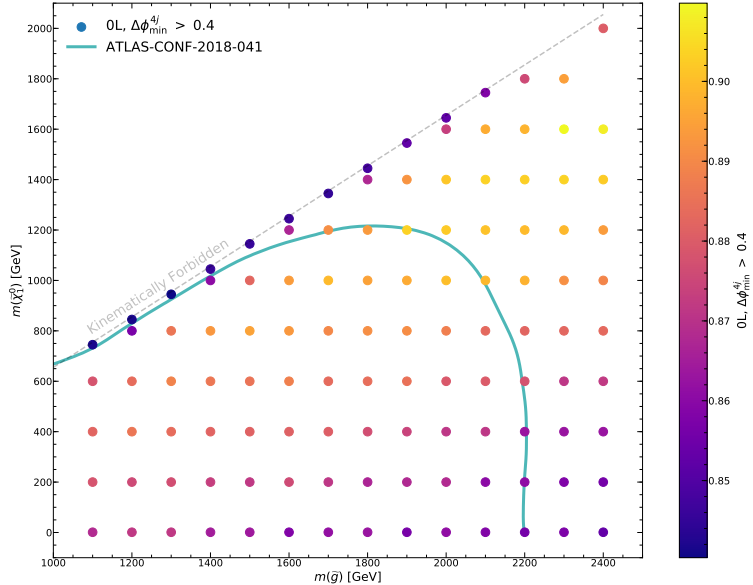


FIGURE A.7: Gtt signal efficiency of the $0L, \Delta\phi_{\min}^{4j} > 0.4$ preselection.

A.2 Input Variable Selection

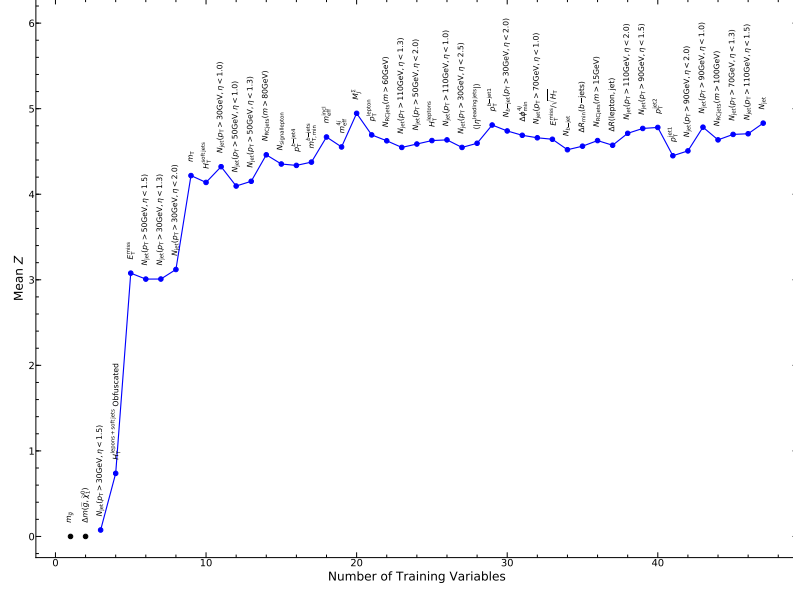


FIGURE A.8: BDT performance measured via mean Z_B on selected mass points during the iterative input variable selection process.

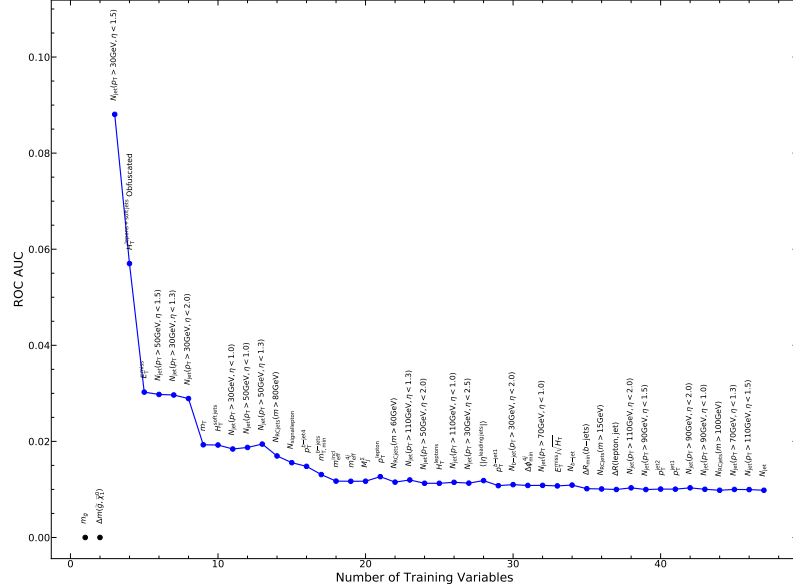


FIGURE A.9: BDT performance measured via ROC AUC during the iterative input variable selection process.

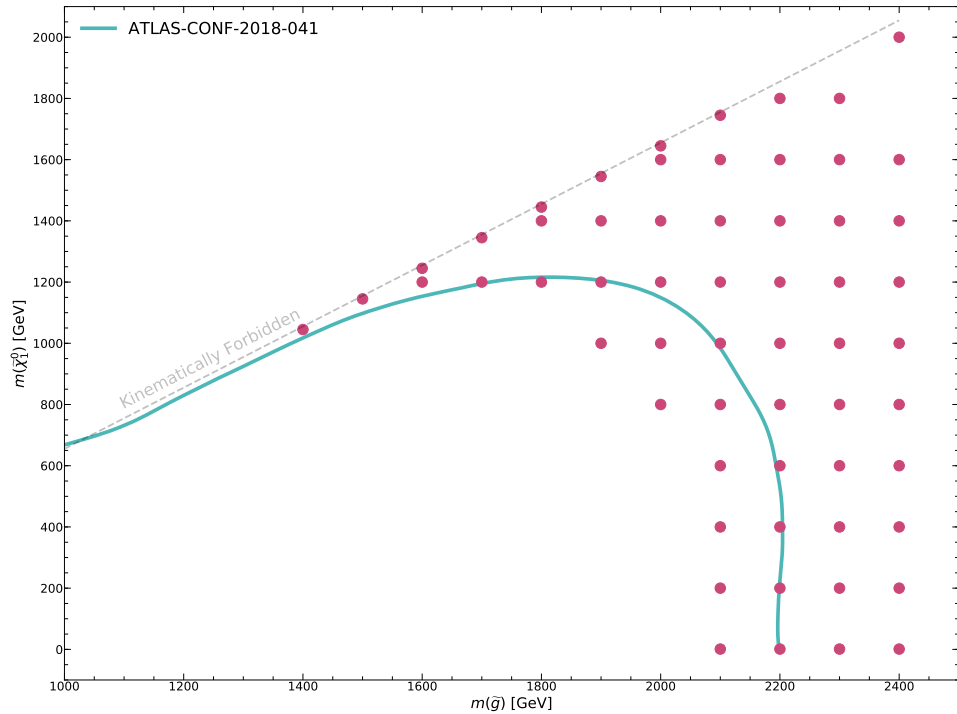


FIGURE A.10: Selected mass points for use in computing mean Z_B in the input variable selection and hyperparameter tuning processes.

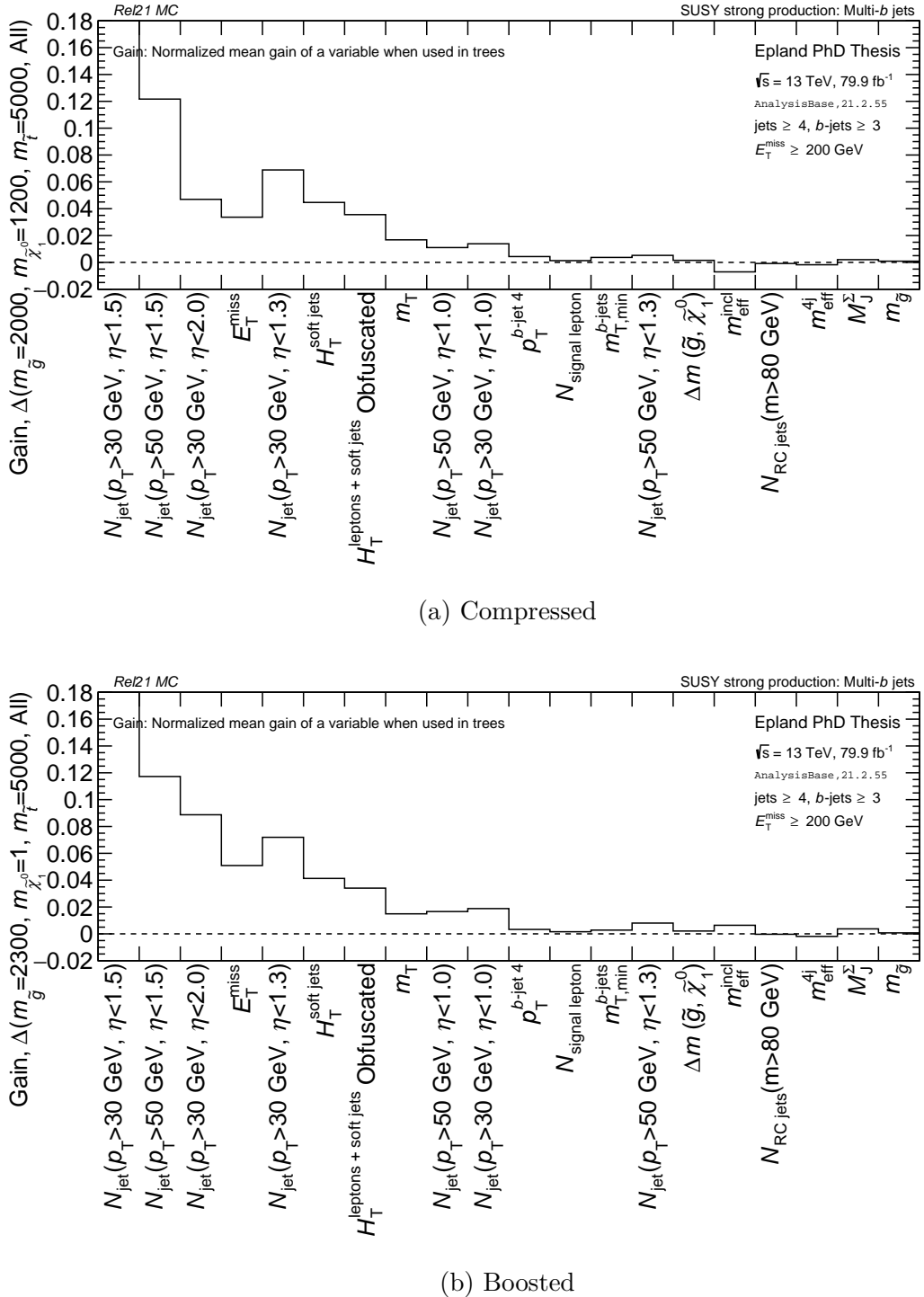


FIGURE A.11: Change in input variable gain when comparing the BDT over all signal parameter points to individual compressed and boosted points. The trial compressed point is located at $m_{\tilde{g}} = 2 \text{ TeV}$, $m_{\tilde{\chi}_1^0} = 1.2 \text{ TeV}$, while the boosted point is located at $m_{\tilde{g}} = 2.3 \text{ TeV}$, $m_{\tilde{\chi}_1^0} = 1 \text{ GeV}$.

A.3 Hyperparameter Tuning

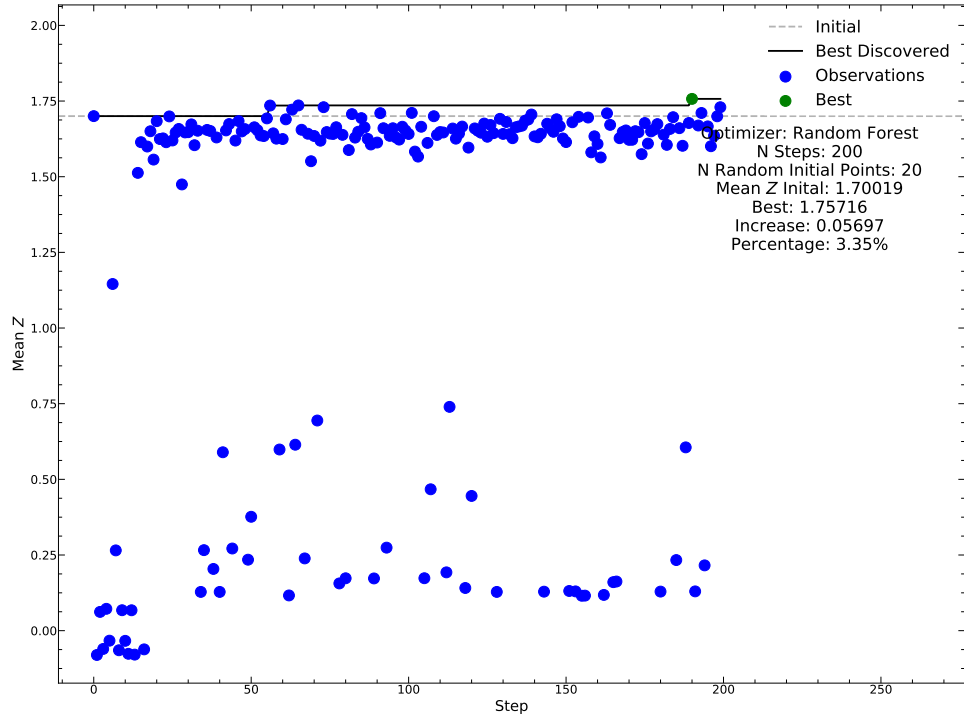


FIGURE A.12: BDT performance measured via mean Z_B on selected mass points during the Bayesian optimization of hyperparameters with a random forest regressor and 200 iterations. The learning rate η , maximum tree depth, and early stopping validation threshold were optimized simultaneously. The optimal point, marked in green, showed a 3.4 % improvement over the initial values.

A.4 Parameter Point Selection

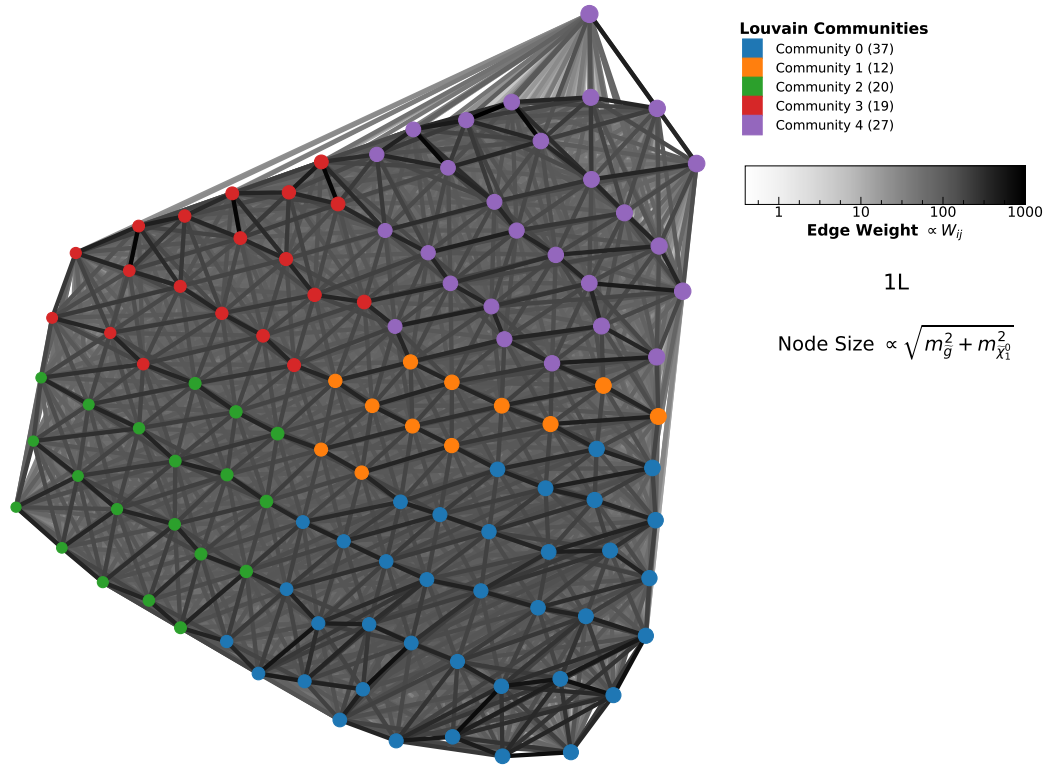


FIGURE A.13: Graph of mass parameter points and Louvain communities in the 1L channel. The position of nodes is set via a spring relaxation algorithm and their size corresponds to their masses. The edge shading is proportional to W_{ij} and is darker for stronger edges.

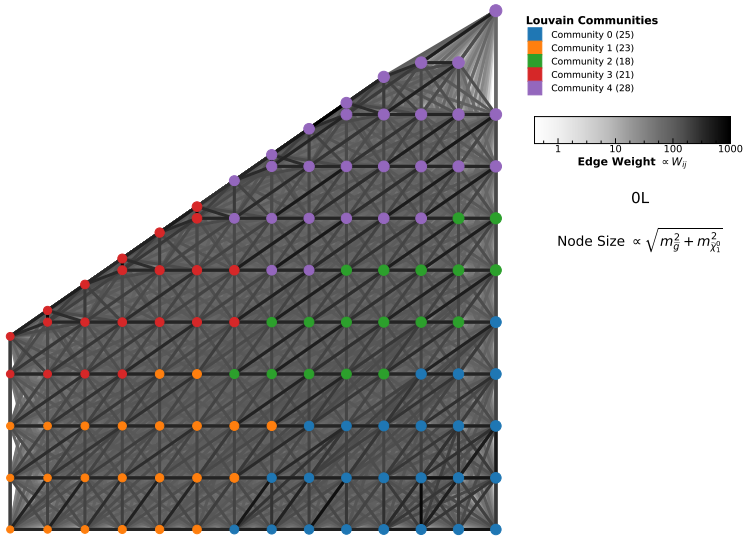


FIGURE A.14: Graph of mass parameter points and Louvain communities in the 0L channel. The position of nodes is set on the standard $m_{\tilde{g}}$, $m_{\tilde{\chi}_1^0}$ mass grid and their size corresponds to their masses. The edge shading is proportional to W_{ij} and is darker for stronger edges.

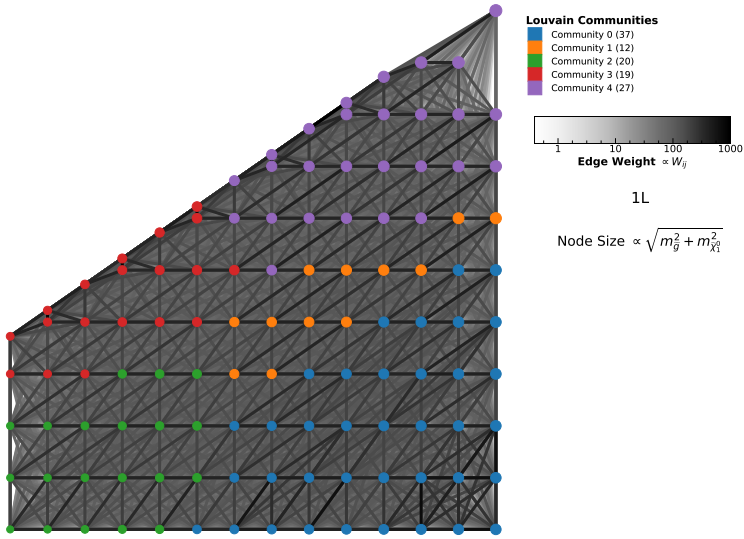


FIGURE A.15: Graph of mass parameter points and Louvain communities in the 1L channel. The position of nodes is set on the standard $m_{\tilde{g}}$, $m_{\tilde{\chi}_1^0}$ mass grid and their size corresponds to their masses. The edge shading is proportional to W_{ij} and is darker for stronger edges.

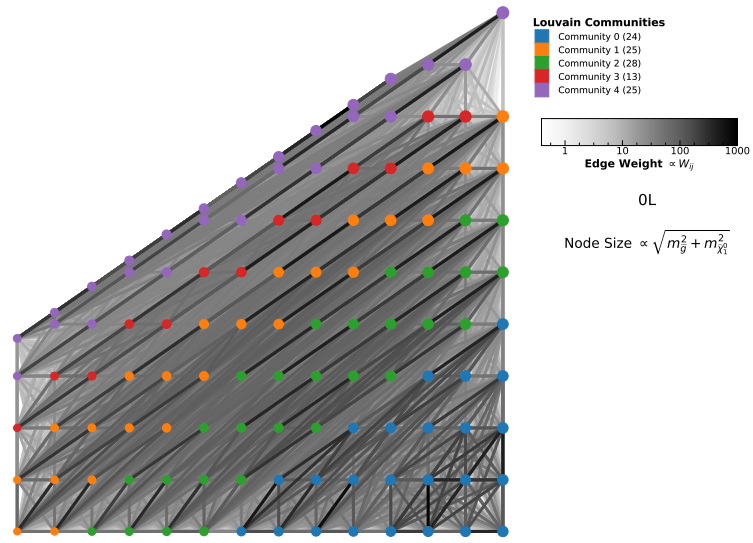


FIGURE A.16: Graph of mass parameter points and Louvain communities in the 0L channel, when W_{ij} is only a function of the RMSD, *i.e.* $b = 0$.

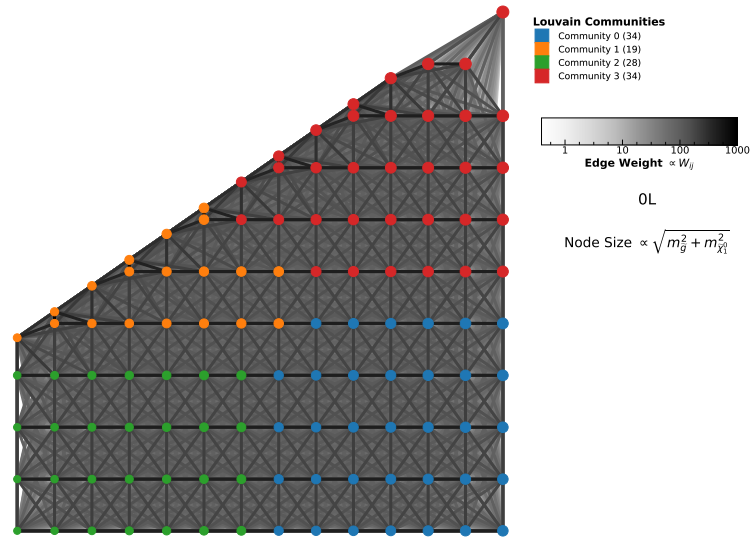


FIGURE A.17: Graph of mass parameter points and Louvain communities in the 0L channel, when W_{ij} is only a function of the radius in mass space $R_m(p_i, p_j)$.

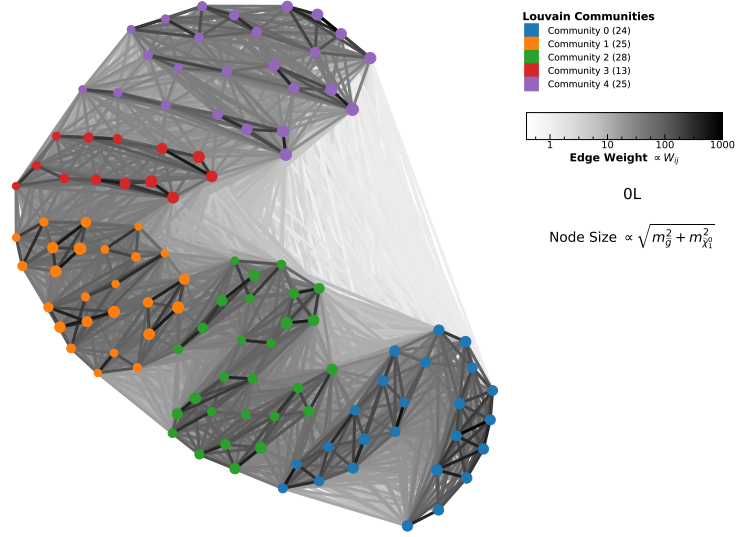


FIGURE A.18: Graph of mass parameter points and Louvain communities in the 0L channel, when W_{ij} is only a function of the RMSD, $b = 0$. The position of nodes is set via a spring relaxation algorithm.

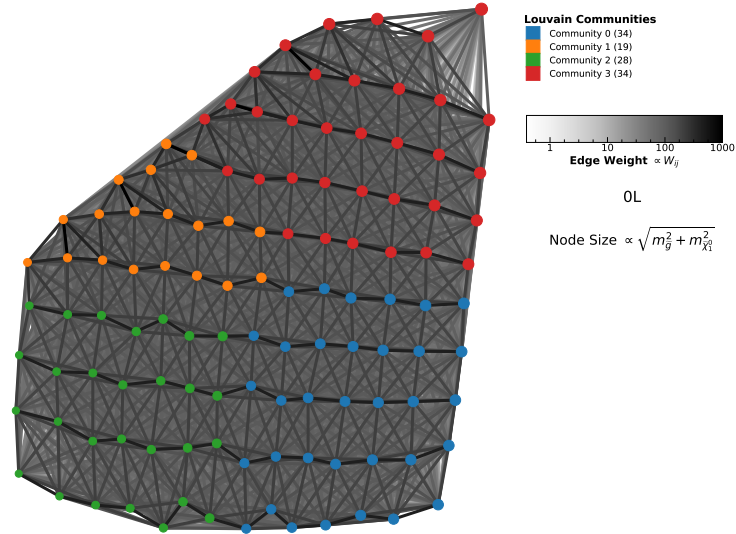


FIGURE A.19: Graph of mass parameter points and Louvain communities in the 0L channel, when W_{ij} is only a function of the radius in mass space $R_m(p_i, p_j)$. The position of nodes is set via a spring relaxation algorithm.

A.5 Control, Validation, and Signal Regions Selection

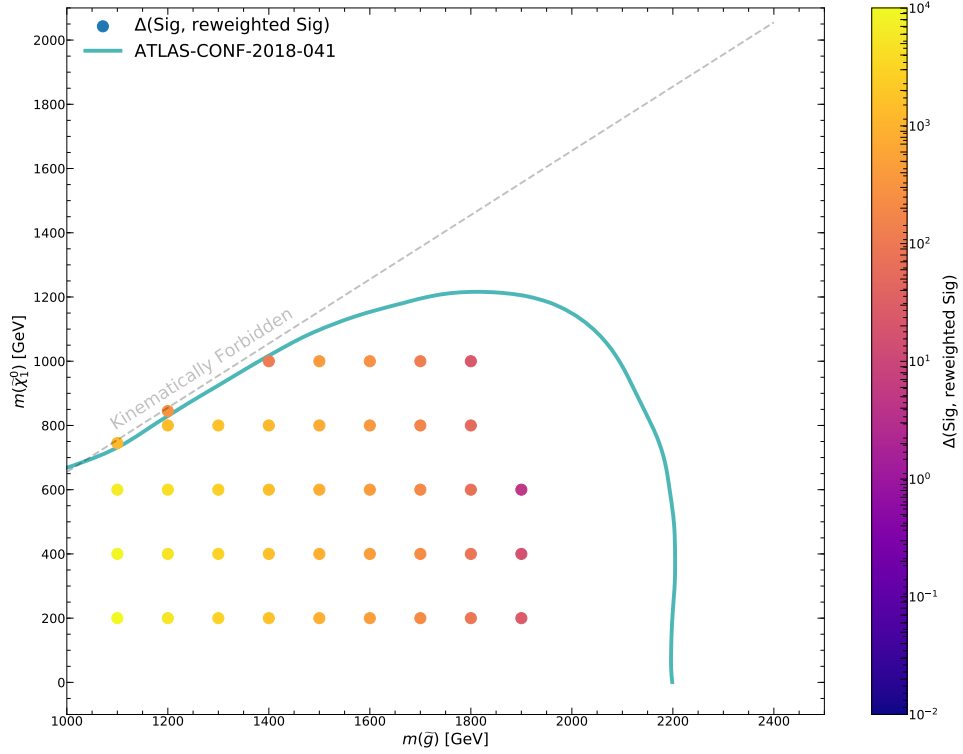


FIGURE A.20: Change in total Gtt event weight per mass point after reweighting the production cross section to match the observed 36.1 fb^{-1} exclusion limits [5].

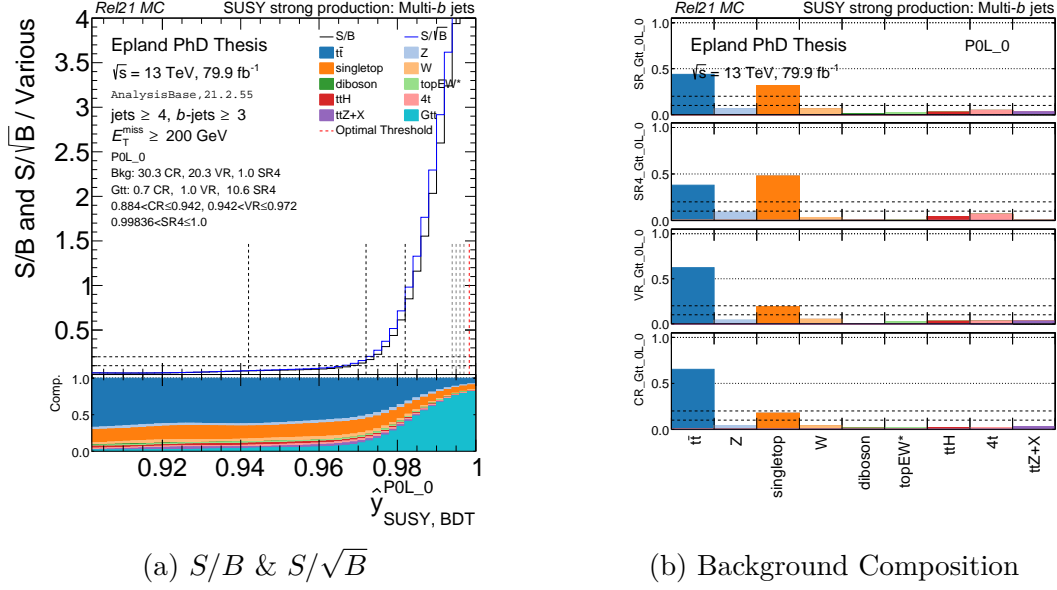


FIGURE A.21: Smoothed S/B & S/\sqrt{B} , and background composition for P0L_0.

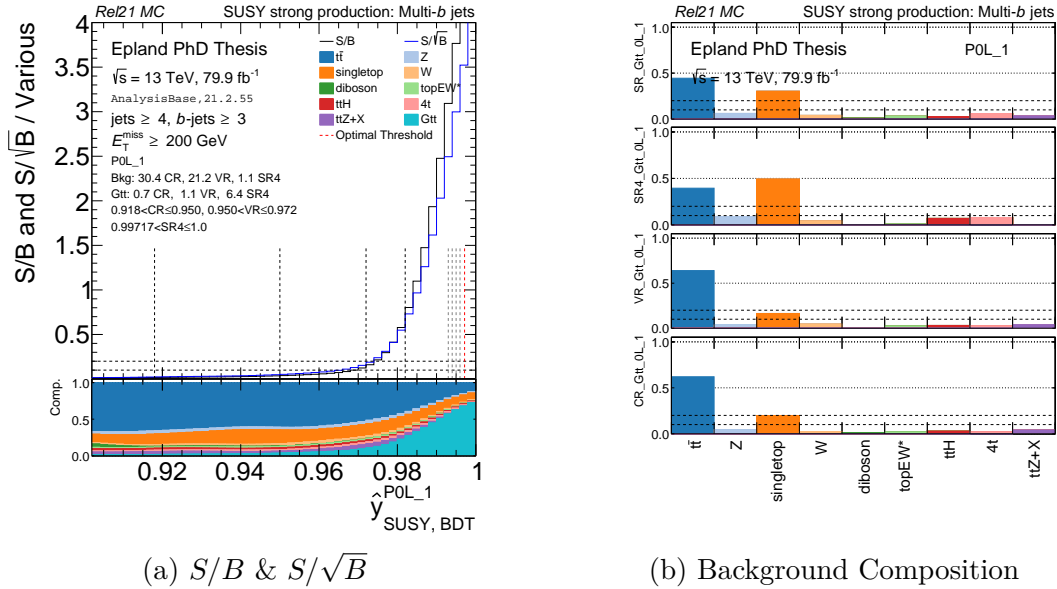


FIGURE A.22: Smoothed S/B & S/\sqrt{B} , and background composition for P0L_1.

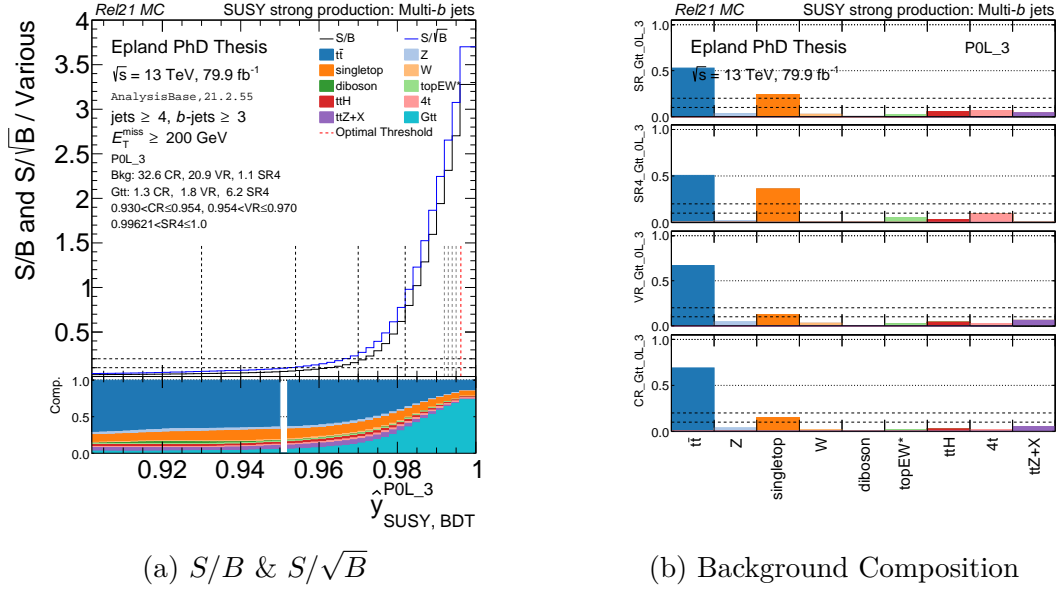


FIGURE A.23: Smoothed S/B & S/\sqrt{B} , and background composition for P0L_3.

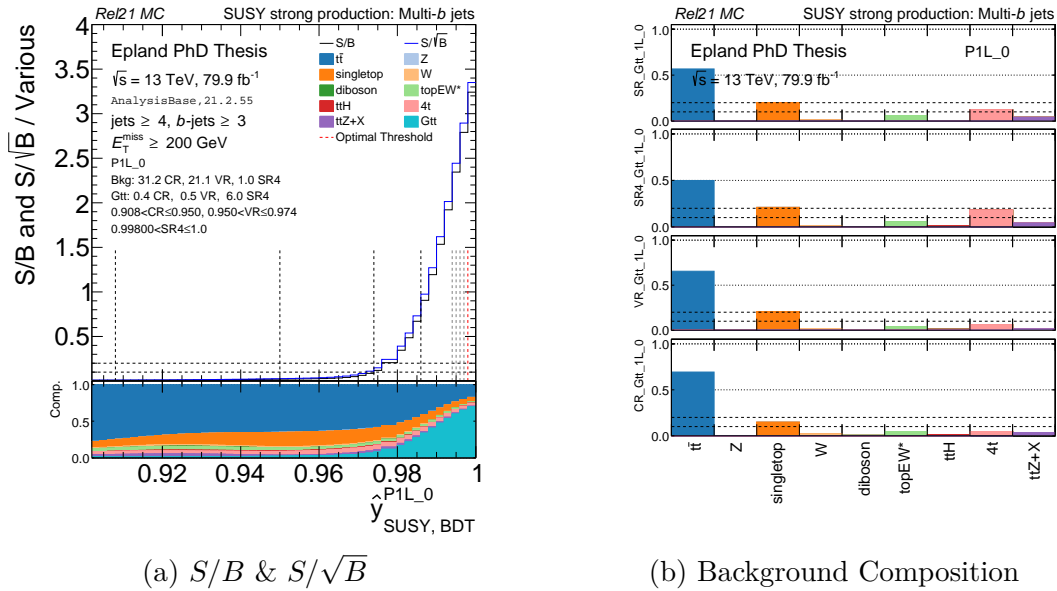


FIGURE A.24: Smoothed S/B & S/\sqrt{B} , and background composition for P1L_0.

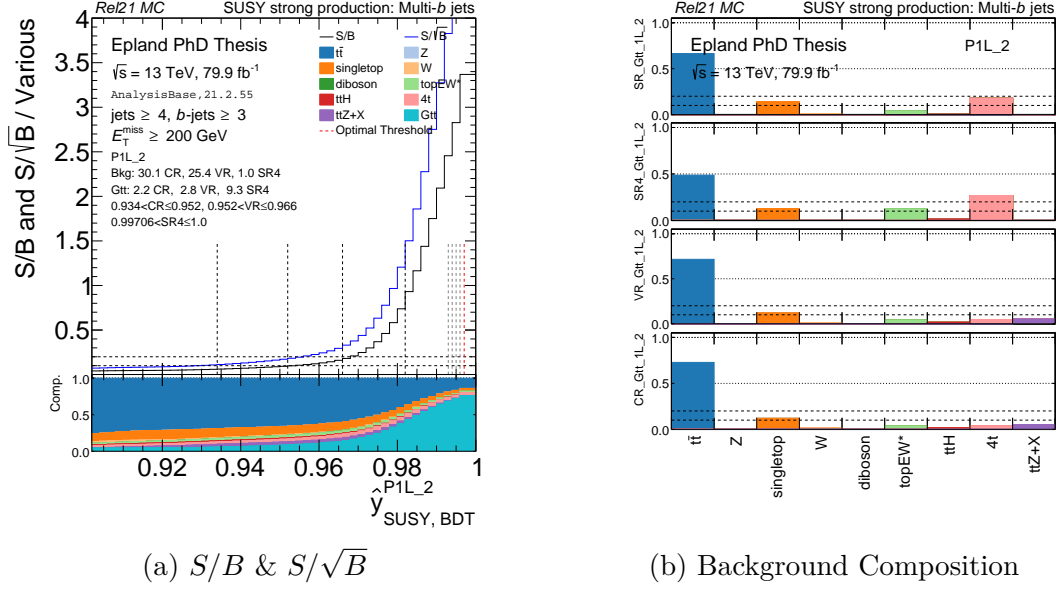


FIGURE A.25: Smoothed S/B & S/\sqrt{B} , and background composition for P1L_2.

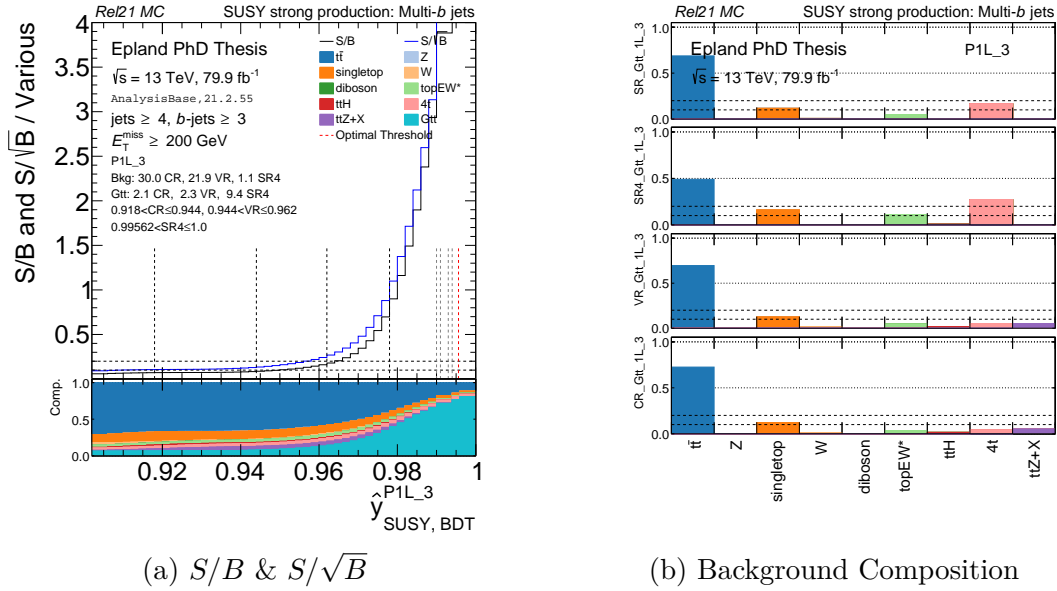


FIGURE A.26: Smoothed S/B & S/\sqrt{B} , and background composition for P1L_3.

A.6 Uncertainties

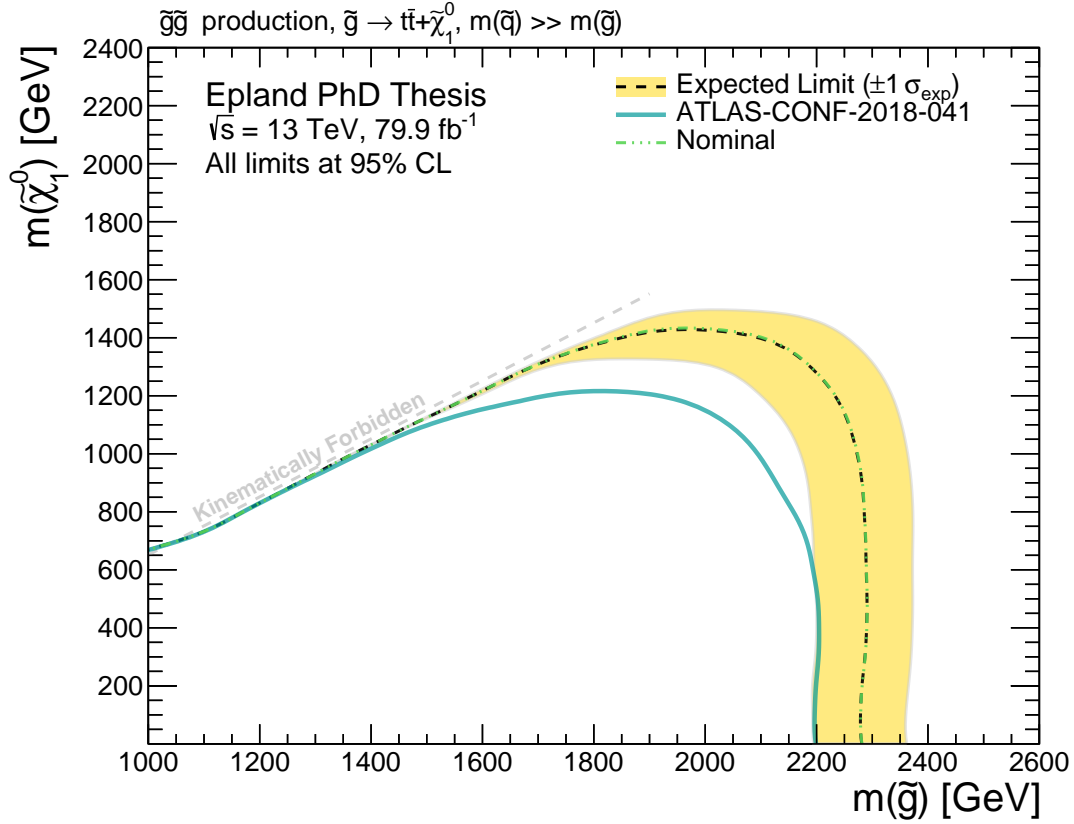
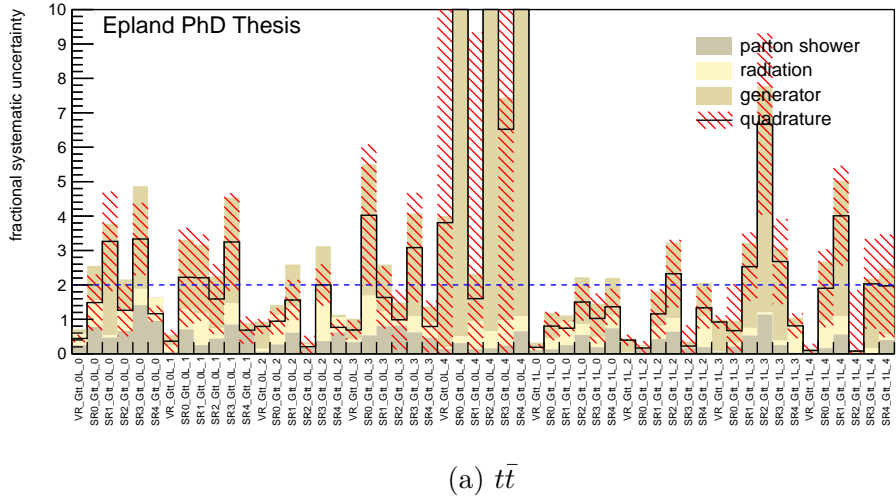
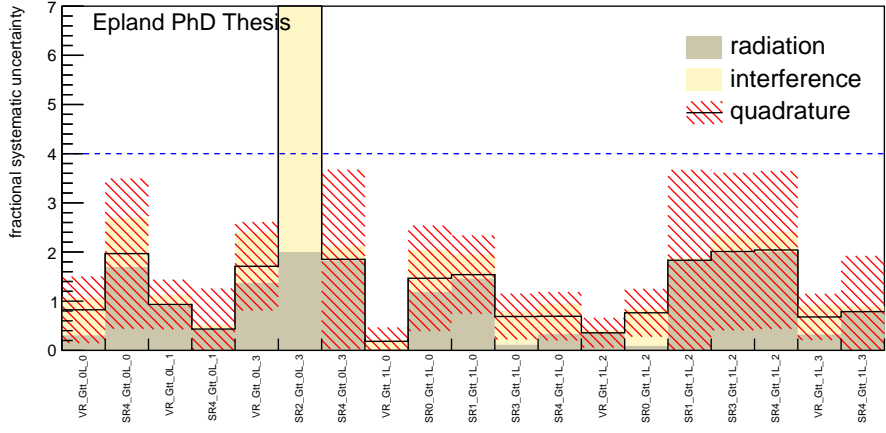


FIGURE A.27: $t\bar{t}$ generator theory systematic validation study. Here the simplistic $t\bar{t}$ generator systematic created from only two variations has been doubled in the fit, with little to no effect on the exclusion limit results when compared to the nominal result. This shows that it is acceptable to use the simplified two-variation approach.



(a) $t\bar{t}$



(b) Single-top

FIGURE A.28: Initial event-driven theory systematic uncertainties for $t\bar{t}$ and single-top. The $t\bar{t}$ uncertainties include parton shower, radiation, and generator systematics components, while single-top includes radiation and interference. The quadrature sum, with error, is also displayed. SR bins with a quadrature sum plus error greater than the blue dashed thresholds are removed from the fit before unblinding. Such SR bins in the $t\bar{t}$ uncertainty, including all of Gtt_0L_4, have already been removed from the single-top results shown here. Gtt_1L_1, Gtt_0L_2, and Gtt_1L_4 were removed for other reasons detailed in Section 5.8.

A.6.1 Uncertainty Tables

Table A.1: Breakdown of the dominant systematic uncertainties on background estimates in the Gtt_0L_0_Gtt_1L_0 signal regions. Note that the individual uncertainties can be correlated, and do not necessarily add up quadratically to the total background uncertainty. The percentages show the size of the uncertainty relative to the total expected background.

Uncertainty of channel	CR_Gtt_0L_0CR_Gtt_1L_0VR_Gtt_0L_0VR_Gtt_1L_0SR4_Gtt_0L_0SR0_Gtt_1L_0SR1_Gtt_1L_0SR3_Gtt_1L_0SR4_Gtt_1L_0								
Total background expectation	26.01	34.02	18.77	25.86	1.08	1.76	1.04	0.96	1.45
Total statistical ($\sqrt{N_{\text{exp}}}$)	± 5.10	± 5.83	± 4.33	± 5.08	± 1.04	± 1.33	± 1.02	± 0.98	± 1.20
Total background systematic	± 5.51 [21.16%]	± 5.81 [17.09%]	± 7.91 [42.16%]	± 10.23 [39.57%]	± 0.62 [57.96%]	± 1.91 [108.41%]	± 0.79 [75.36%]	± 0.75 [77.81%]	± 1.25 [86.46%]
Lumi	± 0.33 [1.3%]	± 0.28 [0.81%]	± 0.24 [1.3%]	± 0.26 [1.00%]	± 0.02 [2.1%]	± 0.03 [1.5%]	± 0.01 [1.1%]	± 0.02 [1.7%]	± 0.02 [1.6%]
$\mu_{\text{ttbar, Gtt}_0\text{L}_0}$	± 6.17 [23.7%]	± 0.00 [0.00%]	± 4.42 [23.5%]	± 0.00 [0.00%]	± 0.13 [11.8%]	± 0.00 [0.00%]	± 0.00 [0.00%]	± 0.00 [0.00%]	± 0.00 [0.00%]
$\mu_{\text{ttbar, Gtt}_1\text{L}_0}$	± 0.00 [0.00%]	± 6.61 [19.4%]	± 0.00 [0.00%]	± 4.58 [17.7%]	± 0.00 [0.00%]	± 0.23 [12.8%]	± 0.18 [17.1%]	± 0.11 [11.4%]	± 0.17 [11.9%]
$\gamma_{\text{stat, SR0, Gtt}_1\text{L}_0}$	± 0.00 [0.00%]	± 0.00 [0.00%]	± 0.00 [0.00%]	± 0.00 [0.00%]	± 0.00 [0.00%]	± 0.33 [18.4%]	± 0.00 [0.00%]	± 0.00 [0.00%]	± 0.00 [0.00%]
$\gamma_{\text{stat, SR1, Gtt}_1\text{L}_0}$	± 0.00 [0.00%]	± 0.00 [0.00%]	± 0.00 [0.00%]	± 0.00 [0.00%]	± 0.00 [0.00%]	± 0.00 [0.00%]	± 0.25 [23.6%]	± 0.00 [0.00%]	± 0.00 [0.00%]
$\gamma_{\text{stat, SR3, Gtt}_1\text{L}_0}$	± 0.00 [0.00%]	± 0.00 [0.00%]	± 0.00 [0.00%]	± 0.00 [0.00%]	± 0.00 [0.00%]	± 0.00 [0.00%]	± 0.23 [23.5%]	± 0.00 [0.00%]	± 0.00 [0.00%]
$\gamma_{\text{stat, SR4, Gtt}_0\text{L}_0}$	± 0.00 [0.00%]	± 0.00 [0.00%]	± 0.00 [0.00%]	± 0.00 [0.00%]	± 0.21 [19.5%]	± 0.00 [0.00%]	± 0.00 [0.00%]	± 0.00 [0.00%]	± 0.00 [0.00%]
$\gamma_{\text{stat, SR4, Gtt}_1\text{L}_0}$	± 0.00 [0.00%]	± 0.00 [0.00%]	± 0.00 [0.00%]	± 0.00 [0.00%]	± 0.00 [0.00%]	± 0.00 [0.00%]	± 0.00 [0.00%]	± 0.00 [0.00%]	± 0.27 [18.7%]
$\gamma_{\text{stat, VR, Gtt}_0\text{L}_0}$	± 0.00 [0.00%]	± 0.00 [0.00%]	± 1.45 [7.7%]	± 0.00 [0.00%]	± 0.00 [0.00%]	± 0.00 [0.00%]	± 0.00 [0.00%]	± 0.00 [0.00%]	± 0.00 [0.00%]
$\gamma_{\text{stat, VR, Gtt}_1\text{L}_0}$	± 0.00 [0.00%]	± 0.00 [0.00%]	± 0.00 [0.00%]	± 1.37 [5.3%]	± 0.00 [0.00%]	± 0.00 [0.00%]	± 0.00 [0.00%]	± 0.00 [0.00%]	± 0.00 [0.00%]
α_{JER1}	± 0.09 [0.34%]	± 0.87 [2.6%]	± 0.73 [3.9%]	± 2.34 [9.0%]	± 0.10 [9.0%]	± 0.53 [30.3%]	± 0.32 [31.0%]	± 0.23 [23.5%]	± 0.34 [23.3%]
α_{JER2}	± 0.22 [0.86%]	± 0.76 [2.2%]	± 1.13 [6.0%]	± 2.18 [8.4%]	± 0.06 [5.2%]	± 0.53 [30.1%]	± 0.25 [23.9%]	± 0.23 [24.2%]	± 0.31 [21.2%]
α_{JER3}	± 0.04 [0.14%]	± 1.14 [3.4%]	± 1.58 [8.4%]	± 3.08 [11.9%]	± 0.10 [8.9%]	± 0.53 [30.2%]	± 0.15 [14.3%]	± 0.16 [16.4%]	± 0.35 [24.0%]
α_{JER4}	± 0.28 [1.1%]	± 0.41 [1.2%]	± 1.17 [6.2%]	± 1.97 [7.6%]	± 0.10 [9.7%]	± 0.46 [25.8%]	± 0.12 [11.6%]	± 0.18 [19.1%]	± 0.26 [18.0%]
α_{JER5}	± 0.02 [0.08%]	± 0.30 [0.89%]	± 1.21 [6.5%]	± 2.39 [9.3%]	± 0.08 [7.4%]	± 0.55 [31.0%]	± 0.08 [7.8%]	± 0.25 [25.8%]	± 0.30 [20.7%]
α_{JER6}	± 0.27 [1.1%]	± 0.64 [1.9%]	± 1.25 [6.6%]	± 2.85 [11.0%]	± 0.10 [9.7%]	± 0.56 [31.6%]	± 0.11 [10.7%]	± 0.17 [17.3%]	± 0.25 [17.4%]
α_{JER7}	± 0.36 [1.4%]	± 0.72 [2.1%]	± 1.00 [5.3%]	± 2.76 [10.7%]	± 0.08 [7.2%]	± 0.50 [28.3%]	± 0.08 [7.4%]	± 0.18 [18.5%]	± 0.28 [19.6%]
$\alpha_{\text{JER, DataVsMC}}$	± 0.31 [1.2%]	± 0.10 [0.28%]	± 1.75 [9.3%]	± 2.25 [8.7%]	± 0.13 [11.7%]	± 0.60 [34.0%]	± 0.18 [16.9%]	± 0.14 [14.8%]	± 0.26 [18.2%]
α_{JES1}	± 1.14 [4.4%]	± 0.57 [1.7%]	± 0.43 [2.3%]	± 0.00 [0.00%]	± 0.00 [0.44%]	± 0.09 [5.2%]	± 0.02 [1.9%]	± 0.02 [2.5%]	± 0.06 [4.5%]
α_{JES2}	± 1.20 [4.6%]	± 0.33 [0.96%]	± 0.42 [2.3%]	± 0.11 [0.42%]	± 0.03 [2.7%]	± 0.12 [6.7%]	± 0.01 [1.0%]	± 0.00 [0.51%]	± 0.06 [4.4%]
α_{JES3}	± 0.27 [1.1%]	± 0.13 [0.38%]	± 0.04 [0.19%]	± 0.31 [1.2%]	± 0.01 [1.2%]	± 0.05 [2.7%]	± 0.02 [1.6%]	± 0.03 [3.5%]	± 0.03 [2.0%]
$\alpha_{\text{JES, EtaInter, highE}}$	± 0.64 [2.4%]	± 0.28 [0.83%]	± 0.27 [1.5%]	± 0.97 [3.7%]	± 0.11 [10.0%]	± 0.01 [0.63%]	± 0.06 [5.3%]	± 0.00 [0.03%]	± 0.07 [4.9%]
$\alpha_{\text{JES, EtaInter, negEta}}$	± 0.04 [0.16%]	± 0.00 [0.00%]	± 0.06 [0.34%]	± 0.01 [0.03%]	± 0.07 [6.7%]	± 0.01 [0.43%]	± 0.00 [0.03%]	± 0.01 [0.94%]	± 0.00 [0.04%]
$\alpha_{\text{JES, EtaInter, posEta}}$	± 0.00 [0.01%]	± 0.01 [0.02%]	± 0.88 [4.7%]	± 0.00 [0.02%]	± 0.07 [6.8%]	± 0.00 [0.10%]	± 0.01 [0.87%]	± 0.00 [0.02%]	± 0.00 [0.06%]
$\alpha_{\text{JET, Flavor, Response}}$	± 0.87 [3.3%]	± 0.11 [0.32%]	± 0.21 [1.1%]	± 0.02 [0.08%]	± 0.01 [0.82%]	± 0.09 [5.2%]	± 0.06 [5.3%]	± 0.01 [1.6%]	± 0.04 [2.6%]

Uncertainty of channel	CR_Gtt_0L_0CR_Gtt_1L_0VR_Gtt_0L_0VR_Gtt_1L_0SR4_Gtt_0L_0SR0_Gtt_1L_0SR1_Gtt_1L_0SR3_Gtt_1L_0SR4_Gtt_1L_0
α_{JVT}	$\pm 0.13 [0.52\%]$ $\pm 0.08 [0.25\%]$ $\pm 0.07 [0.38\%]$ $\pm 0.07 [0.28\%]$ $\pm 0.00 [0.35\%]$ $\pm 0.01 [0.48\%]$ $\pm 0.00 [0.38\%]$ $\pm 0.01 [0.72\%]$ $\pm 0.00 [0.29\%]$
α_{MCMCHack}	$\pm 1.11 [4.3\%]$ $\pm 0.13 [0.37\%]$ $\pm 1.32 [7.0\%]$ $\pm 0.23 [0.89\%]$ $\pm 0.08 [7.6\%]$ $\pm 0.01 [0.38\%]$ $\pm 0.01 [1.1\%]$ $\pm 0.00 [0.43\%]$ $\pm 0.01 [0.66\%]$
$\alpha_{\text{RW_1CR}}$	$\pm 0.00 [0.00\%]$ $\pm 0.53 [1.6\%]$ $\pm 0.00 [0.00\%]$ $\pm 0.50 [1.9\%]$ $\pm 0.00 [0.00\%]$ $\pm 0.07 [3.8\%]$ $\pm 0.03 [2.8\%]$ $\pm 0.04 [3.7\%]$ $\pm 0.06 [3.9\%]$
$\alpha_{\text{WZ_ckkw_syst}}$	$\pm 2.96 [11.4\%]$ $\pm 0.04 [0.12\%]$ $\pm 2.04 [10.9\%]$ $\pm 0.02 [0.08\%]$ $\pm 0.15 [13.7\%]$ $\pm 0.00 [0.13\%]$ $\pm 0.00 [0.36\%]$ $\pm 0.00 [0.20\%]$ $\pm 0.00 [0.22\%]$
$\alpha_{\text{WZ_fac_syst}}$	$\pm 1.32 [5.1\%]$ $\pm 0.09 [0.26\%]$ $\pm 0.55 [3.0\%]$ $\pm 0.10 [0.39\%]$ $\pm 0.04 [3.9\%]$ $\pm 0.01 [0.36\%]$ $\pm 0.01 [1.0\%]$ $\pm 0.00 [0.11\%]$ $\pm 0.01 [0.61\%]$
$\alpha_{\text{WZ_qsf_syst}}$	$\pm 0.17 [0.64\%]$ $\pm 0.09 [0.27\%]$ $\pm 0.49 [2.6\%]$ $\pm 0.09 [0.35\%]$ $\pm 0.03 [3.1\%]$ $\pm 0.01 [0.30\%]$ $\pm 0.01 [0.86\%]$ $\pm 0.00 [0.42\%]$ $\pm 0.01 [0.52\%]$
$\alpha_{\text{WZ_renorm_syst}}$	$\pm 0.85 [3.3\%]$ $\pm 0.15 [0.45\%]$ $\pm 1.37 [7.3\%]$ $\pm 0.19 [0.75\%]$ $\pm 0.10 [8.9\%]$ $\pm 0.01 [0.61\%]$ $\pm 0.02 [1.8\%]$ $\pm 0.00 [0.19\%]$ $\pm 0.02 [1.1\%]$
$\alpha_{\text{bTag_B}}$	$\pm 0.19 [0.74\%]$ $\pm 0.30 [0.87\%]$ $\pm 0.21 [1.1\%]$ $\pm 0.22 [0.86\%]$ $\pm 0.01 [0.75\%]$ $\pm 0.04 [2.3\%]$ $\pm 0.00 [0.43\%]$ $\pm 0.00 [0.32\%]$ $\pm 0.01 [1.0\%]$
$\alpha_{\text{bTag_C}}$	$\pm 0.43 [1.7\%]$ $\pm 0.31 [0.91\%]$ $\pm 0.17 [0.93\%]$ $\pm 0.24 [0.94\%]$ $\pm 0.03 [2.6\%]$ $\pm 0.06 [3.2\%]$ $\pm 0.00 [0.09\%]$ $\pm 0.02 [2.4\%]$ $\pm 0.01 [0.78\%]$
$\alpha_{\text{bTag_L}}$	$\pm 0.37 [1.4\%]$ $\pm 0.33 [0.96\%]$ $\pm 0.54 [2.9\%]$ $\pm 0.78 [3.0\%]$ $\pm 0.01 [1.0\%]$ $\pm 0.01 [0.42\%]$ $\pm 0.05 [4.7\%]$ $\pm 0.00 [0.45\%]$ $\pm 0.03 [1.8\%]$
$\alpha_{\text{bTag_extrapol}}$	$\pm 0.00 [0.00\%]$ $\pm 0.03 [0.09\%]$ $\pm 0.23 [1.2\%]$ $\pm 0.09 [0.36\%]$ $\pm 0.01 [1.3\%]$ $\pm 0.06 [3.2\%]$ $\pm 0.00 [0.43\%]$ $\pm 0.00 [0.01\%]$ $\pm 0.00 [0.11\%]$
$\alpha_{\text{bTag_extrapol_charm}}$	$\pm 0.11 [0.43\%]$ $\pm 0.12 [0.35\%]$ $\pm 0.01 [0.07\%]$ $\pm 0.14 [0.55\%]$ $\pm 0.01 [0.65\%]$ $\pm 0.03 [2.0\%]$ $\pm 0.00 [0.27\%]$ $\pm 0.00 [0.40\%]$ $\pm 0.00 [0.22\%]$
$\alpha_{\text{diboson_syst_CR_Gtt_0L_0}}$	$\pm 0.21 [0.81\%]$ $\pm 0.00 [0.00\%]$
$\alpha_{\text{diboson_syst_CR_Gtt_1L_0}}$	$\pm 0.00 [0.00\%]$ $\pm 0.02 [0.06\%]$ $\pm 0.00 [0.00\%]$
$\alpha_{\text{diboson_syst_VR_Gtt_0L_0}}$	$\pm 0.00 [0.00\%]$ $\pm 0.00 [0.00\%]$ $\pm 0.20 [1.1\%]$ $\pm 0.00 [0.00\%]$
$\alpha_{\text{st_syst_SR0_Gtt_1L_0}}$	$\pm 0.00 [0.00\%]$ $\pm 0.73 [41.3\%]$ $\pm 0.00 [0.00\%]$ $\pm 0.00 [0.00\%]$ $\pm 0.00 [0.00\%]$
$\alpha_{\text{st_syst_SR1_Gtt_1L_0}}$	$\pm 0.00 [0.00\%]$ $\pm 0.24 [23.3\%]$ $\pm 0.00 [0.00\%]$ $\pm 0.00 [0.00\%]$
$\alpha_{\text{st_syst_SR3_Gtt_1L_0}}$	$\pm 0.00 [0.00\%]$ $\pm 0.18 [18.3\%]$ $\pm 0.00 [0.00\%]$ $\pm 0.00 [0.00\%]$
$\alpha_{\text{st_syst_SR4_Gtt_0L_0}}$	$\pm 0.00 [0.00\%]$ $\pm 0.00 [0.00\%]$ $\pm 0.00 [0.00\%]$ $\pm 0.00 [0.00\%]$ $\pm 0.28 [25.6\%]$ $\pm 0.00 [0.00\%]$ $\pm 0.00 [0.00\%]$ $\pm 0.00 [0.00\%]$ $\pm 0.00 [0.00\%]$
$\alpha_{\text{st_syst_SR4_Gtt_1L_0}}$	$\pm 0.00 [0.00\%]$ $\pm 0.27 [18.6\%]$
$\alpha_{\text{st_syst_VR_Gtt_0L_0}}$	$\pm 0.00 [0.00\%]$ $\pm 0.00 [0.00\%]$ $\pm 2.78 [14.8\%]$ $\pm 0.00 [0.00\%]$
$\alpha_{\text{st_syst_VR_Gtt_1L_0}}$	$\pm 0.00 [0.00\%]$ $\pm 0.00 [0.00\%]$ $\pm 0.00 [0.00\%]$ $\pm 0.95 [3.7\%]$ $\pm 0.00 [0.00\%]$
$\alpha_{\text{topEW_syst_CR_Gtt_0L_0}}$	$\pm 1.91 [7.3\%]$ $\pm 0.00 [0.00\%]$
$\alpha_{\text{topEW_syst_CR_Gtt_1L_0}}$	$\pm 0.00 [0.00\%]$ $\pm 2.11 [6.2\%]$ $\pm 0.00 [0.00\%]$
$\alpha_{\text{topEW_syst_SR0_Gtt_1L_0}}$	$\pm 0.00 [0.00\%]$ $\pm 0.16 [8.9\%]$ $\pm 0.00 [0.00\%]$ $\pm 0.00 [0.00\%]$ $\pm 0.00 [0.00\%]$
$\alpha_{\text{topEW_syst_SR1_Gtt_1L_0}}$	$\pm 0.00 [0.00\%]$ $\pm 0.08 [7.8\%]$ $\pm 0.00 [0.00\%]$ $\pm 0.00 [0.00\%]$
$\alpha_{\text{topEW_syst_SR3_Gtt_1L_0}}$	$\pm 0.00 [0.00\%]$ $\pm 0.14 [15.0\%]$ $\pm 0.00 [0.00\%]$ $\pm 0.00 [0.00\%]$
$\alpha_{\text{topEW_syst_SR4_Gtt_0L_0}}$	$\pm 0.00 [0.00\%]$ $\pm 0.00 [0.00\%]$ $\pm 0.00 [0.00\%]$ $\pm 0.00 [0.00\%]$ $\pm 0.19 [17.9\%]$ $\pm 0.00 [0.00\%]$ $\pm 0.00 [0.00\%]$ $\pm 0.00 [0.00\%]$ $\pm 0.00 [0.00\%]$
$\alpha_{\text{topEW_syst_SR4_Gtt_1L_0}}$	$\pm 0.00 [0.00\%]$ $\pm 0.20 [13.8\%]$
$\alpha_{\text{topEW_syst_VR_Gtt_0L_0}}$	$\pm 0.00 [0.00\%]$ $\pm 0.00 [0.00\%]$ $\pm 0.83 [4.4\%]$ $\pm 0.00 [0.00\%]$
$\alpha_{\text{topEW_syst_VR_Gtt_1L_0}}$	$\pm 0.00 [0.00\%]$ $\pm 0.00 [0.00\%]$ $\pm 0.00 [0.00\%]$ $\pm 1.58 [6.1\%]$ $\pm 0.00 [0.00\%]$
$\alpha_{\text{ttbar_syst_SR0_Gtt_1L_0}}$	$\pm 0.00 [0.00\%]$ $\pm 0.67 [38.2\%]$ $\pm 0.00 [0.00\%]$ $\pm 0.00 [0.00\%]$ $\pm 0.00 [0.00\%]$
$\alpha_{\text{ttbar_syst_SR1_Gtt_1L_0}}$	$\pm 0.00 [0.00\%]$ $\pm 0.49 [46.9\%]$ $\pm 0.00 [0.00\%]$ $\pm 0.00 [0.00\%]$ $\pm 0.00 [0.00\%]$
$\alpha_{\text{ttbar_syst_SR3_Gtt_1L_0}}$	$\pm 0.00 [0.00\%]$ $\pm 0.41 [42.7\%]$ $\pm 0.00 [0.00\%]$ $\pm 0.00 [0.00\%]$ $\pm 0.00 [0.00\%]$
$\alpha_{\text{ttbar_syst_SR4_Gtt_0L_0}}$	$\pm 0.00 [0.00\%]$ $\pm 0.00 [0.00\%]$ $\pm 0.00 [0.00\%]$ $\pm 0.00 [0.00\%]$ $\pm 0.32 [30.0\%]$ $\pm 0.00 [0.00\%]$ $\pm 0.00 [0.00\%]$ $\pm 0.00 [0.00\%]$ $\pm 0.00 [0.00\%]$
$\alpha_{\text{ttbar_syst_SR4_Gtt_1L_0}}$	$\pm 0.00 [0.00\%]$ $\pm 0.75 [51.7\%]$
$\alpha_{\text{ttbar_syst_VR_Gtt_0L_0}}$	$\pm 0.00 [0.00\%]$ $\pm 0.00 [0.00\%]$ $\pm 4.62 [24.6\%]$ $\pm 0.00 [0.00\%]$
$\alpha_{\text{ttbar_syst_VR_Gtt_1L_0}}$	$\pm 0.00 [0.00\%]$ $\pm 0.00 [0.00\%]$ $\pm 0.00 [0.00\%]$ $\pm 3.15 [12.2\%]$ $\pm 0.00 [0.00\%]$

Table A.2: Breakdown of the dominant systematic uncertainties on background estimates in the Gtt_0L_1_Gtt_1L_0 signal regions. Note that the individual uncertainties can be correlated, and do not necessarily add up quadratically to the total background uncertainty. The percentages show the size of the uncertainty relative to the total expected background.

Uncertainty of channel	CR_Gtt_0L_1CR_Gtt_1L_0VR_Gtt_0L_1VR_Gtt_1L_0SR4_Gtt_0L_1SR0_Gtt_1L_0SR1_Gtt_1L_0SR3_Gtt_1L_0SR4_Gtt_1L_0								
Total background expectation	28.99	34.01	22.32	25.91	1.61	1.78	1.04	0.95	1.46
Total statistical ($\sqrt{N_{\text{exp}}}$)	± 5.38	± 5.83	± 4.72	± 5.09	± 1.27	± 1.33	± 1.02	± 0.98	± 1.21
Total background systematic	± 5.56 [19.19%]	± 5.81 [17.09%]	± 9.00 [40.32%]	± 10.25 [39.56%]	± 1.25 [77.78%]	± 1.93 [108.77%]	± 0.78 [75.31%]	± 0.74 [77.70%]	± 1.26 [86.45%]
Lumi	± 0.33 [1.1%]	± 0.28 [0.81%]	± 0.25 [1.1%]	± 0.26 [1.00%]	± 0.03 [1.9%]	± 0.03 [1.5%]	± 0.01 [1.1%]	± 0.02 [1.7%]	± 0.02 [1.6%]
$\mu_{\text{ttbar}}_{\text{Gtt}_0\text{L}_1}$	± 6.50 [22.4%]	± 0.00 [0.00%]	± 5.06 [22.7%]	± 0.00 [0.00%]	± 0.20 [12.2%]	± 0.00 [0.00%]	± 0.00 [0.00%]	± 0.00 [0.00%]	± 0.00 [0.00%]
$\mu_{\text{ttbar}}_{\text{Gtt}_1\text{L}_0}$	± 0.00 [0.00%]	± 6.60 [19.4%]	± 0.00 [0.00%]	± 4.58 [17.7%]	± 0.00 [0.00%]	± 0.23 [12.7%]	± 0.18 [17.1%]	± 0.11 [11.4%]	± 0.17 [11.8%]
$\gamma_{\text{stat}}_{\text{SR0}}_{\text{Gtt}_1\text{L}_0}$	± 0.00 [0.00%]	± 0.00 [0.00%]	± 0.00 [0.00%]	± 0.00 [0.00%]	± 0.00 [0.00%]	± 0.33 [18.4%]	± 0.00 [0.00%]	± 0.00 [0.00%]	± 0.00 [0.00%]
$\gamma_{\text{stat}}_{\text{SR1}}_{\text{Gtt}_1\text{L}_0}$	± 0.00 [0.00%]	± 0.00 [0.00%]	± 0.00 [0.00%]	± 0.00 [0.00%]	± 0.00 [0.00%]	± 0.00 [0.00%]	± 0.25 [23.6%]	± 0.00 [0.00%]	± 0.00 [0.00%]
$\gamma_{\text{stat}}_{\text{SR3}}_{\text{Gtt}_1\text{L}_0}$	± 0.00 [0.00%]	± 0.00 [0.00%]	± 0.00 [0.00%]	± 0.00 [0.00%]	± 0.00 [0.00%]	± 0.00 [0.00%]	± 0.22 [23.5%]	± 0.00 [0.00%]	± 0.00 [0.00%]
$\gamma_{\text{stat}}_{\text{SR4}}_{\text{Gtt}_0\text{L}_1}$	± 0.00 [0.00%]	± 0.00 [0.00%]	± 0.00 [0.00%]	± 0.00 [0.00%]	± 0.29 [18.1%]	± 0.00 [0.00%]	± 0.00 [0.00%]	± 0.00 [0.00%]	± 0.00 [0.00%]
$\gamma_{\text{stat}}_{\text{SR4}}_{\text{Gtt}_1\text{L}_0}$	± 0.00 [0.00%]	± 0.00 [0.00%]	± 0.00 [0.00%]	± 0.00 [0.00%]	± 0.00 [0.00%]	± 0.00 [0.00%]	± 0.00 [0.00%]	± 0.00 [0.00%]	± 0.27 [18.7%]
$\gamma_{\text{stat}}_{\text{VR}}_{\text{Gtt}_0\text{L}_1}$	± 0.00 [0.00%]	± 0.00 [0.00%]	± 1.40 [6.3%]	± 0.00 [0.00%]	± 0.00 [0.00%]	± 0.00 [0.00%]	± 0.00 [0.00%]	± 0.00 [0.00%]	± 0.00 [0.00%]
$\gamma_{\text{stat}}_{\text{VR}}_{\text{Gtt}_1\text{L}_0}$	± 0.00 [0.00%]	± 0.00 [0.00%]	± 0.00 [0.00%]	± 1.38 [5.3%]	± 0.00 [0.00%]	± 0.00 [0.00%]	± 0.00 [0.00%]	± 0.00 [0.00%]	± 0.00 [0.00%]
α_{JER1}	± 0.50 [1.7%]	± 0.86 [2.5%]	± 1.87 [8.4%]	± 2.34 [9.0%]	± 0.20 [12.7%]	± 0.54 [30.4%]	± 0.32 [30.9%]	± 0.22 [23.5%]	± 0.34 [23.2%]
α_{JER2}	± 0.85 [2.9%]	± 0.75 [2.2%]	± 1.51 [6.8%]	± 2.19 [8.4%]	± 0.20 [12.6%]	± 0.54 [30.2%]	± 0.25 [23.8%]	± 0.23 [24.2%]	± 0.31 [21.2%]
α_{JER3}	± 0.52 [1.8%]	± 1.14 [3.3%]	± 1.88 [8.4%]	± 3.09 [11.9%]	± 0.20 [12.3%]	± 0.54 [30.3%]	± 0.15 [14.2%]	± 0.16 [16.3%]	± 0.35 [24.0%]
α_{JER4}	± 0.74 [2.5%]	± 0.40 [1.2%]	± 1.60 [7.2%]	± 1.98 [7.6%]	± 0.29 [17.7%]	± 0.46 [25.9%]	± 0.12 [11.5%]	± 0.18 [19.0%]	± 0.26 [18.0%]
α_{JER5}	± 0.63 [2.2%]	± 0.30 [0.88%]	± 0.80 [3.6%]	± 2.40 [9.3%]	± 0.26 [16.2%]	± 0.55 [31.1%]	± 0.08 [7.8%]	± 0.25 [25.8%]	± 0.30 [20.7%]
α_{JER6}	± 0.27 [0.92%]	± 0.64 [1.9%]	± 1.64 [7.3%]	± 2.85 [11.0%]	± 0.30 [18.6%]	± 0.56 [31.7%]	± 0.11 [10.6%]	± 0.16 [17.3%]	± 0.25 [17.4%]
α_{JER7}	± 0.56 [1.9%]	± 0.71 [2.1%]	± 1.86 [8.3%]	± 2.77 [10.7%]	± 0.23 [14.3%]	± 0.50 [28.4%]	± 0.08 [7.2%]	± 0.18 [18.4%]	± 0.29 [19.6%]
$\alpha_{\text{JER}}_{\text{DataVsMC}}$	± 0.63 [2.2%]	± 0.09 [0.27%]	± 1.34 [6.0%]	± 2.26 [8.7%]	± 0.31 [19.4%]	± 0.61 [34.2%]	± 0.17 [16.8%]	± 0.14 [14.7%]	± 0.27 [18.3%]
α_{JES1}	± 1.12 [3.9%]	± 0.57 [1.7%]	± 0.76 [3.4%]	± 0.01 [0.04%]	± 0.06 [3.9%]	± 0.09 [5.2%]	± 0.02 [1.8%]	± 0.02 [2.5%]	± 0.07 [4.5%]
α_{JES2}	± 0.93 [3.2%]	± 0.32 [0.95%]	± 0.68 [3.0%]	± 0.12 [0.46%]	± 0.11 [7.1%]	± 0.12 [6.7%]	± 0.01 [1.1%]	± 0.01 [0.56%]	± 0.06 [4.5%]
α_{JES3}	± 0.02 [0.07%]	± 0.13 [0.38%]	± 0.25 [1.1%]	± 0.30 [1.2%]	± 0.00 [0.08%]	± 0.05 [2.8%]	± 0.02 [1.6%]	± 0.03 [3.3%]	± 0.03 [1.9%]
$\alpha_{\text{JES}}_{\text{EtaInter_highE}}$	± 0.23 [0.79%]	± 0.28 [0.83%]	± 1.30 [5.8%]	± 0.97 [3.7%]	± 0.38 [23.5%]	± 0.01 [0.68%]	± 0.06 [5.3%]	± 0.00 [0.02%]	± 0.07 [5.0%]
$\alpha_{\text{JES}}_{\text{EtaInter_negEta}}$	± 0.34 [1.2%]	± 0.00 [0.01%]	± 0.24 [1.1%]	± 0.01 [0.05%]	± 0.18 [11.2%]	± 0.01 [0.36%]	± 0.00 [0.02%]	± 0.01 [0.85%]	± 0.00 [0.02%]
$\alpha_{\text{JES}}_{\text{EtaInter_posEta}}$	± 0.11 [0.38%]	± 0.01 [0.02%]	± 0.04 [0.18%]	± 0.01 [0.02%]	± 0.17 [10.5%]	± 0.00 [0.09%]	± 0.01 [0.87%]	± 0.00 [0.03%]	± 0.00 [0.07%]
$\alpha_{\text{JET}}_{\text{Flavor_Response}}$	± 0.75 [2.6%]	± 0.11 [0.33%]	± 0.55 [2.5%]	± 0.03 [0.12%]	± 0.01 [0.61%]	± 0.09 [5.0%]	± 0.05 [5.3%]	± 0.01 [1.5%]	± 0.04 [2.6%]

Uncertainty of channel	CR_Gtt_0L_1CR_Gtt_1L_0VR_Gtt_0L_1VR_Gtt_1L_0SR4_Gtt_0L_1SR0_Gtt_1L_0SR1_Gtt_1L_0SR3_Gtt_1L_0SR4_Gtt_1L_0
α_{JVT}	$\pm 0.12 [0.41\%]$ $\pm 0.08 [0.25\%]$ $\pm 0.12 [0.54\%]$ $\pm 0.07 [0.28\%]$ $\pm 0.01 [0.55\%]$ $\pm 0.01 [0.48\%]$ $\pm 0.00 [0.38\%]$ $\pm 0.01 [0.72\%]$ $\pm 0.00 [0.29\%]$
α_{MCMCHack}	$\pm 0.76 [2.6\%]$ $\pm 0.12 [0.36\%]$ $\pm 0.82 [3.7\%]$ $\pm 0.23 [0.89\%]$ $\pm 0.16 [10.1\%]$ $\pm 0.01 [0.38\%]$ $\pm 0.01 [1.1\%]$ $\pm 0.00 [0.44\%]$ $\pm 0.01 [0.66\%]$
$\alpha_{\text{RW_1CR}}$	$\pm 0.00 [0.00\%]$ $\pm 0.53 [1.6\%]$ $\pm 0.00 [0.00\%]$ $\pm 0.50 [1.9\%]$ $\pm 0.00 [0.00\%]$ $\pm 0.07 [3.8\%]$ $\pm 0.03 [2.8\%]$ $\pm 0.03 [3.7\%]$ $\pm 0.06 [3.9\%]$
$\alpha_{\text{WZ_ckkw_syst}}$	$\pm 2.21 [7.6\%]$ $\pm 0.04 [0.10\%]$ $\pm 2.01 [9.0\%]$ $\pm 0.02 [0.06\%]$ $\pm 0.70 [43.7\%]$ $\pm 0.00 [0.11\%]$ $\pm 0.00 [0.33\%]$ $\pm 0.00 [0.21\%]$ $\pm 0.00 [0.19\%]$
$\alpha_{\text{WZ_fac_syst}}$	$\pm 0.94 [3.2\%]$ $\pm 0.09 [0.25\%]$ $\pm 0.86 [3.8\%]$ $\pm 0.10 [0.39\%]$ $\pm 0.34 [21.2\%]$ $\pm 0.01 [0.35\%]$ $\pm 0.01 [1.0\%]$ $\pm 0.00 [0.11\%]$ $\pm 0.01 [0.61\%]$
$\alpha_{\text{WZ_qsf_syst}}$	$\pm 0.16 [0.54\%]$ $\pm 0.09 [0.26\%]$ $\pm 0.13 [0.57\%]$ $\pm 0.09 [0.35\%]$ $\pm 0.01 [0.33\%]$ $\pm 0.01 [0.30\%]$ $\pm 0.01 [0.87\%]$ $\pm 0.00 [0.43\%]$ $\pm 0.01 [0.52\%]$
$\alpha_{\text{WZ_renorm_syst}}$	$\pm 0.65 [2.2\%]$ $\pm 0.15 [0.43\%]$ $\pm 0.56 [2.5\%]$ $\pm 0.19 [0.74\%]$ $\pm 0.12 [7.1\%]$ $\pm 0.01 [0.61\%]$ $\pm 0.02 [1.8\%]$ $\pm 0.00 [0.20\%]$ $\pm 0.02 [1.1\%]$
$\alpha_{\text{bTag_B}}$	$\pm 0.31 [1.1\%]$ $\pm 0.30 [0.87\%]$ $\pm 0.13 [0.56\%]$ $\pm 0.22 [0.86\%]$ $\pm 0.00 [0.04\%]$ $\pm 0.04 [2.4\%]$ $\pm 0.00 [0.43\%]$ $\pm 0.00 [0.33\%]$ $\pm 0.02 [1.0\%]$
$\alpha_{\text{bTag_C}}$	$\pm 0.51 [1.7\%]$ $\pm 0.31 [0.91\%]$ $\pm 0.45 [2.0\%]$ $\pm 0.24 [0.94\%]$ $\pm 0.03 [2.0\%]$ $\pm 0.06 [3.2\%]$ $\pm 0.00 [0.07\%]$ $\pm 0.02 [2.4\%]$ $\pm 0.01 [0.79\%]$
$\alpha_{\text{bTag_L}}$	$\pm 0.38 [1.3\%]$ $\pm 0.33 [0.96\%]$ $\pm 0.33 [1.5\%]$ $\pm 0.78 [3.0\%]$ $\pm 0.01 [0.49\%]$ $\pm 0.01 [0.42\%]$ $\pm 0.05 [4.8\%]$ $\pm 0.00 [0.45\%]$ $\pm 0.03 [1.8\%]$
$\alpha_{\text{bTag_extrapol}}$	$\pm 0.12 [0.42\%]$ $\pm 0.03 [0.09\%]$ $\pm 0.06 [0.28\%]$ $\pm 0.09 [0.36\%]$ $\pm 0.00 [0.15\%]$ $\pm 0.06 [3.2\%]$ $\pm 0.00 [0.43\%]$ $\pm 0.00 [0.01\%]$ $\pm 0.00 [0.11\%]$
$\alpha_{\text{bTag_extrapol_charm}}$	$\pm 0.16 [0.54\%]$ $\pm 0.12 [0.35\%]$ $\pm 0.07 [0.30\%]$ $\pm 0.14 [0.55\%]$ $\pm 0.00 [0.29\%]$ $\pm 0.04 [2.0\%]$ $\pm 0.00 [0.27\%]$ $\pm 0.00 [0.40\%]$ $\pm 0.00 [0.22\%]$
$\alpha_{\text{diboson_syst_CR_Gtt_0L_1}}$	$\pm 0.08 [0.27\%]$ $\pm 0.00 [0.00\%]$
$\alpha_{\text{diboson_syst_CR_Gtt_1L_0}}$	$\pm 0.00 [0.00\%]$ $\pm 0.02 [0.05\%]$ $\pm 0.00 [0.00\%]$
$\alpha_{\text{diboson_syst_VR_Gtt_0L_1}}$	$\pm 0.00 [0.00\%]$ $\pm 0.00 [0.00\%]$ $\pm 0.25 [1.1\%]$ $\pm 0.00 [0.00\%]$
$\alpha_{\text{st_syst_SR0_Gtt_1L_0}}$	$\pm 0.00 [0.00\%]$ $\pm 0.74 [41.7\%]$ $\pm 0.00 [0.00\%]$ $\pm 0.00 [0.00\%]$ $\pm 0.00 [0.00\%]$
$\alpha_{\text{st_syst_SR1_Gtt_1L_0}}$	$\pm 0.00 [0.00\%]$ $\pm 0.24 [23.4\%]$ $\pm 0.00 [0.00\%]$ $\pm 0.00 [0.00\%]$
$\alpha_{\text{st_syst_SR3_Gtt_1L_0}}$	$\pm 0.00 [0.00\%]$ $\pm 0.17 [18.3\%]$ $\pm 0.00 [0.00\%]$ $\pm 0.00 [0.00\%]$
$\alpha_{\text{st_syst_SR4_Gtt_0L_1}}$	$\pm 0.00 [0.00\%]$ $\pm 0.00 [0.00\%]$ $\pm 0.00 [0.00\%]$ $\pm 0.00 [0.00\%]$ $\pm 0.08 [5.0\%]$ $\pm 0.00 [0.00\%]$ $\pm 0.00 [0.00\%]$ $\pm 0.00 [0.00\%]$ $\pm 0.00 [0.00\%]$
$\alpha_{\text{st_syst_SR4_Gtt_1L_0}}$	$\pm 0.00 [0.00\%]$ $\pm 0.27 [18.6\%]$
$\alpha_{\text{st_syst_VR_Gtt_0L_1}}$	$\pm 0.00 [0.00\%]$ $\pm 0.00 [0.00\%]$ $\pm 4.22 [18.9\%]$ $\pm 0.00 [0.00\%]$
$\alpha_{\text{st_syst_VR_Gtt_1L_0}}$	$\pm 0.00 [0.00\%]$ $\pm 0.00 [0.00\%]$ $\pm 0.00 [0.00\%]$ $\pm 0.95 [3.7\%]$ $\pm 0.00 [0.00\%]$
$\alpha_{\text{topEW_syst_CR_Gtt_0L_1}}$	$\pm 2.13 [7.3\%]$ $\pm 0.00 [0.00\%]$
$\alpha_{\text{topEW_syst_CR_Gtt_1L_0}}$	$\pm 0.00 [0.00\%]$ $\pm 2.11 [6.2\%]$ $\pm 0.00 [0.00\%]$
$\alpha_{\text{topEW_syst_SR0_Gtt_1L_0}}$	$\pm 0.00 [0.00\%]$ $\pm 0.16 [9.0\%]$ $\pm 0.00 [0.00\%]$ $\pm 0.00 [0.00\%]$
$\alpha_{\text{topEW_syst_SR1_Gtt_1L_0}}$	$\pm 0.00 [0.00\%]$ $\pm 0.08 [7.7\%]$ $\pm 0.00 [0.00\%]$ $\pm 0.00 [0.00\%]$
$\alpha_{\text{topEW_syst_SR3_Gtt_1L_0}}$	$\pm 0.00 [0.00\%]$ $\pm 0.14 [15.1\%]$ $\pm 0.00 [0.00\%]$ $\pm 0.00 [0.00\%]$
$\alpha_{\text{topEW_syst_SR4_Gtt_0L_1}}$	$\pm 0.00 [0.00\%]$ $\pm 0.00 [0.00\%]$ $\pm 0.00 [0.00\%]$ $\pm 0.00 [0.00\%]$ $\pm 0.24 [15.1\%]$ $\pm 0.00 [0.00\%]$ $\pm 0.00 [0.00\%]$ $\pm 0.00 [0.00\%]$ $\pm 0.00 [0.00\%]$
$\alpha_{\text{topEW_syst_SR4_Gtt_1L_0}}$	$\pm 0.00 [0.00\%]$ $\pm 0.20 [13.8\%]$
$\alpha_{\text{topEW_syst_VR_Gtt_0L_1}}$	$\pm 0.00 [0.00\%]$ $\pm 0.00 [0.00\%]$ $\pm 1.07 [4.8\%]$ $\pm 0.00 [0.00\%]$
$\alpha_{\text{topEW_syst_VR_Gtt_1L_0}}$	$\pm 0.00 [0.00\%]$ $\pm 0.00 [0.00\%]$ $\pm 0.00 [0.00\%]$ $\pm 1.59 [6.1\%]$ $\pm 0.00 [0.00\%]$
$\alpha_{\text{ttbar_syst_SR0_Gtt_1L_0}}$	$\pm 0.00 [0.00\%]$ $\pm 0.67 [37.9\%]$ $\pm 0.00 [0.00\%]$ $\pm 0.00 [0.00\%]$
$\alpha_{\text{ttbar_syst_SR1_Gtt_1L_0}}$	$\pm 0.00 [0.00\%]$ $\pm 0.49 [47.0\%]$ $\pm 0.00 [0.00\%]$ $\pm 0.00 [0.00\%]$
$\alpha_{\text{ttbar_syst_SR3_Gtt_1L_0}}$	$\pm 0.00 [0.00\%]$ $\pm 0.40 [42.5\%]$ $\pm 0.00 [0.00\%]$ $\pm 0.00 [0.00\%]$
$\alpha_{\text{ttbar_syst_SR4_Gtt_0L_1}}$	$\pm 0.00 [0.00\%]$ $\pm 0.00 [0.00\%]$ $\pm 0.00 [0.00\%]$ $\pm 0.00 [0.00\%]$ $\pm 0.36 [22.5\%]$ $\pm 0.00 [0.00\%]$ $\pm 0.00 [0.00\%]$ $\pm 0.00 [0.00\%]$ $\pm 0.00 [0.00\%]$
$\alpha_{\text{ttbar_syst_SR4_Gtt_1L_0}}$	$\pm 0.00 [0.00\%]$ $\pm 0.75 [51.6\%]$
$\alpha_{\text{ttbar_syst_VR_Gtt_0L_1}}$	$\pm 0.00 [0.00\%]$ $\pm 0.00 [0.00\%]$ $\pm 4.97 [22.3\%]$ $\pm 0.00 [0.00\%]$
$\alpha_{\text{ttbar_syst_VR_Gtt_1L_0}}$	$\pm 0.00 [0.00\%]$ $\pm 0.00 [0.00\%]$ $\pm 0.00 [0.00\%]$ $\pm 3.16 [12.2\%]$ $\pm 0.00 [0.00\%]$

Table A.3: Breakdown of the dominant systematic uncertainties on background estimates in the Gtt_0L_1_Gtt_1L_2 signal regions. Note that the individual uncertainties can be correlated, and do not necessarily add up quadratically to the total background uncertainty. The percentages show the size of the uncertainty relative to the total expected background.

Uncertainty of channel	CR_Gtt_0L_1CR_Gtt_1L_2VR_Gtt_0L_1VR_Gtt_1L_2SR4_Gtt_0L_1SR0_Gtt_1L_2SR1_Gtt_1L_2SR3_Gtt_1L_2SR4_Gtt_1L_2								
Total background expectation	28.96	41.97	22.27	31.67	1.61	2.18	1.45	1.17	1.75
Total statistical ($\sqrt{N_{\text{exp}}}$)	± 5.38	± 6.48	± 4.72	± 5.63	± 1.27	± 1.48	± 1.20	± 1.08	± 1.32
Total background systematic	$\pm 5.57 [19.22\%]$	$\pm 6.46 [15.38\%]$	$\pm 8.98 [40.32\%]$	$\pm 11.96 [37.75\%]$	$\pm 1.26 [78.40\%]$	$\pm 1.46 [66.85\%]$	$\pm 1.48 [101.93\%]$	$\pm 0.83 [70.72\%]$	$\pm 1.64 [93.35\%]$
Lumi	$\pm 0.33 [1.2\%]$	$\pm 0.24 [0.56\%]$	$\pm 0.25 [1.1\%]$	$\pm 0.20 [0.64\%]$	$\pm 0.03 [1.9\%]$	$\pm 0.03 [1.3\%]$	$\pm 0.01 [0.67\%]$	$\pm 0.02 [1.4\%]$	$\pm 0.03 [1.5\%]$
$\mu_{\text{ttbar}}_{\text{Gtt}_0\text{L}_1}$	$\pm 6.50 [22.4\%]$	$\pm 0.00 [0.00\%]$	$\pm 5.06 [22.7\%]$	$\pm 0.00 [0.00\%]$	$\pm 0.20 [12.2\%]$	$\pm 0.00 [0.00\%]$	$\pm 0.00 [0.00\%]$	$\pm 0.00 [0.00\%]$	$\pm 0.00 [0.00\%]$
$\mu_{\text{ttbar}}_{\text{Gtt}_1\text{L}_2}$	$\pm 0.00 [0.00\%]$	$\pm 7.54 [18.0\%]$	$\pm 0.00 [0.00\%]$	$\pm 5.49 [17.3\%]$	$\pm 0.00 [0.00\%]$	$\pm 0.27 [12.4\%]$	$\pm 0.25 [17.1\%]$	$\pm 0.13 [11.3\%]$	$\pm 0.19 [10.8\%]$
$\gamma_{\text{stat}}_{\text{CR}_{\text{Gtt}_1\text{L}_2}}$	$\pm 0.00 [0.00\%]$	$\pm 2.86 [6.8\%]$	$\pm 0.00 [0.00\%]$	$\pm 0.00 [0.00\%]$	$\pm 0.00 [0.00\%]$	$\pm 0.00 [0.00\%]$	$\pm 0.00 [0.00\%]$	$\pm 0.00 [0.00\%]$	$\pm 0.00 [0.00\%]$
$\gamma_{\text{stat}}_{\text{SR0}_{\text{Gtt}_1\text{L}_2}}$	$\pm 0.00 [0.00\%]$	$\pm 0.00 [0.00\%]$	$\pm 0.00 [0.00\%]$	$\pm 0.00 [0.00\%]$	$\pm 0.00 [0.00\%]$	$\pm 0.46 [21.2\%]$	$\pm 0.00 [0.00\%]$	$\pm 0.00 [0.00\%]$	$\pm 0.00 [0.00\%]$
$\gamma_{\text{stat}}_{\text{SR1}_{\text{Gtt}_1\text{L}_2}}$	$\pm 0.00 [0.00\%]$	$\pm 0.00 [0.00\%]$	$\pm 0.00 [0.00\%]$	$\pm 0.00 [0.00\%]$	$\pm 0.00 [0.00\%]$	$\pm 0.00 [0.00\%]$	$\pm 0.25 [17.3\%]$	$\pm 0.00 [0.00\%]$	$\pm 0.00 [0.00\%]$
$\gamma_{\text{stat}}_{\text{SR3}_{\text{Gtt}_1\text{L}_2}}$	$\pm 0.00 [0.00\%]$	$\pm 0.00 [0.00\%]$	$\pm 0.00 [0.00\%]$	$\pm 0.00 [0.00\%]$	$\pm 0.00 [0.00\%]$	$\pm 0.00 [0.00\%]$	$\pm 0.00 [0.00\%]$	$\pm 0.23 [19.6\%]$	$\pm 0.00 [0.00\%]$
$\gamma_{\text{stat}}_{\text{SR4}_{\text{Gtt}_0\text{L}_1}}$	$\pm 0.00 [0.00\%]$	$\pm 0.00 [0.00\%]$	$\pm 0.00 [0.00\%]$	$\pm 0.00 [0.00\%]$	$\pm 0.29 [18.1\%]$	$\pm 0.00 [0.00\%]$	$\pm 0.00 [0.00\%]$	$\pm 0.00 [0.00\%]$	$\pm 0.00 [0.00\%]$
$\gamma_{\text{stat}}_{\text{SR4}_{\text{Gtt}_1\text{L}_2}}$	$\pm 0.00 [0.00\%]$	$\pm 0.00 [0.00\%]$	$\pm 0.00 [0.00\%]$	$\pm 0.00 [0.00\%]$	$\pm 0.00 [0.00\%]$	$\pm 0.00 [0.00\%]$	$\pm 0.00 [0.00\%]$	$\pm 0.00 [0.00\%]$	$\pm 0.39 [22.0\%]$
$\gamma_{\text{stat}}_{\text{VR}_{\text{Gtt}_0\text{L}_1}}$	$\pm 0.00 [0.00\%]$	$\pm 0.00 [0.00\%]$	$\pm 1.40 [6.3\%]$	$\pm 0.00 [0.00\%]$	$\pm 0.00 [0.00\%]$	$\pm 0.00 [0.00\%]$	$\pm 0.00 [0.00\%]$	$\pm 0.00 [0.00\%]$	$\pm 0.00 [0.00\%]$
$\gamma_{\text{stat}}_{\text{VR}_{\text{Gtt}_1\text{L}_2}}$	$\pm 0.00 [0.00\%]$	$\pm 0.00 [0.00\%]$	$\pm 0.00 [0.00\%]$	$\pm 2.33 [7.3\%]$	$\pm 0.00 [0.00\%]$	$\pm 0.00 [0.00\%]$	$\pm 0.00 [0.00\%]$	$\pm 0.00 [0.00\%]$	$\pm 0.00 [0.00\%]$
$\alpha_{\text{JER}1}$	$\pm 0.50 [1.7\%]$	$\pm 0.62 [1.5\%]$	$\pm 1.86 [8.4\%]$	$\pm 1.30 [4.1\%]$	$\pm 0.20 [12.6\%]$	$\pm 0.08 [3.8\%]$	$\pm 0.43 [29.7\%]$	$\pm 0.19 [16.6\%]$	$\pm 0.28 [16.0\%]$
$\alpha_{\text{JER}2}$	$\pm 0.86 [3.0\%]$	$\pm 0.51 [1.2\%]$	$\pm 1.50 [6.7\%]$	$\pm 1.75 [5.5\%]$	$\pm 0.20 [12.5\%]$	$\pm 0.23 [10.7\%]$	$\pm 0.34 [23.2\%]$	$\pm 0.25 [21.4\%]$	$\pm 0.30 [17.0\%]$
$\alpha_{\text{JER}3}$	$\pm 0.52 [1.8\%]$	$\pm 0.78 [1.9\%]$	$\pm 1.87 [8.4\%]$	$\pm 0.04 [0.12\%]$	$\pm 0.20 [12.2\%]$	$\pm 0.30 [13.8\%]$	$\pm 0.14 [10.0\%]$	$\pm 0.17 [15.0\%]$	$\pm 0.32 [18.2\%]$
$\alpha_{\text{JER}4}$	$\pm 0.74 [2.5\%]$	$\pm 0.47 [1.1\%]$	$\pm 1.59 [7.1\%]$	$\pm 0.99 [3.1\%]$	$\pm 0.28 [17.6\%]$	$\pm 0.32 [14.8\%]$	$\pm 0.10 [7.0\%]$	$\pm 0.22 [18.8\%]$	$\pm 0.23 [13.0\%]$
$\alpha_{\text{JER}5}$	$\pm 0.63 [2.2\%]$	$\pm 0.26 [0.61\%]$	$\pm 0.80 [3.6\%]$	$\pm 0.87 [2.8\%]$	$\pm 0.26 [16.1\%]$	$\pm 0.54 [25.0\%]$	$\pm 0.10 [6.6\%]$	$\pm 0.28 [24.3\%]$	$\pm 0.32 [18.0\%]$
$\alpha_{\text{JER}6}$	$\pm 0.27 [0.92\%]$	$\pm 0.01 [0.02\%]$	$\pm 1.63 [7.3\%]$	$\pm 0.23 [0.74\%]$	$\pm 0.30 [18.5\%]$	$\pm 0.60 [27.6\%]$	$\pm 0.04 [2.8\%]$	$\pm 0.27 [22.7\%]$	$\pm 0.29 [16.6\%]$
$\alpha_{\text{JER}7}$	$\pm 0.56 [1.9\%]$	$\pm 0.44 [1.1\%]$	$\pm 1.85 [8.3\%]$	$\pm 0.81 [2.6\%]$	$\pm 0.23 [14.2\%]$	$\pm 0.54 [24.6\%]$	$\pm 0.52 [35.6\%]$	$\pm 0.20 [17.1\%]$	$\pm 0.24 [13.9\%]$
$\alpha_{\text{JER}}_{\text{DataVsMC}}$	$\pm 0.63 [2.2\%]$	$\pm 0.05 [0.13\%]$	$\pm 1.33 [6.0\%]$	$\pm 0.57 [1.8\%]$	$\pm 0.31 [19.3\%]$	$\pm 0.44 [20.3\%]$	$\pm 0.08 [5.2\%]$	$\pm 0.38 [32.5\%]$	$\pm 0.32 [18.2\%]$
$\alpha_{\text{JES}1}$	$\pm 1.12 [3.9\%]$	$\pm 0.67 [1.6\%]$	$\pm 0.75 [3.4\%]$	$\pm 0.85 [2.7\%]$	$\pm 0.06 [4.0\%]$	$\pm 0.04 [2.0\%]$	$\pm 0.07 [4.7\%]$	$\pm 0.08 [6.9\%]$	$\pm 0.01 [0.39\%]$
$\alpha_{\text{JES}2}$	$\pm 0.93 [3.2\%]$	$\pm 0.46 [1.1\%]$	$\pm 0.68 [3.0\%]$	$\pm 0.16 [0.52\%]$	$\pm 0.12 [7.1\%]$	$\pm 0.07 [3.2\%]$	$\pm 0.13 [9.0\%]$	$\pm 0.08 [6.4\%]$	$\pm 0.06 [3.3\%]$
$\alpha_{\text{JES}3}$	$\pm 0.02 [0.07\%]$	$\pm 0.08 [0.18\%]$	$\pm 0.25 [1.1\%]$	$\pm 0.51 [1.6\%]$	$\pm 0.00 [0.08\%]$	$\pm 0.18 [8.3\%]$	$\pm 0.10 [6.7\%]$	$\pm 0.00 [0.06\%]$	$\pm 0.01 [0.41\%]$
$\alpha_{\text{JES}}_{\text{EtaInter_highE}}$	$\pm 0.23 [0.80\%]$	$\pm 0.00 [0.01\%]$	$\pm 1.29 [5.8\%]$	$\pm 0.04 [0.11\%]$	$\pm 0.38 [23.3\%]$	$\pm 0.34 [15.7\%]$	$\pm 0.00 [0.00\%]$	$\pm 0.11 [9.5\%]$	$\pm 0.29 [16.4\%]$
$\alpha_{\text{JES}}_{\text{EtaInter_negEta}}$	$\pm 0.34 [1.2\%]$	$\pm 0.01 [0.01\%]$	$\pm 0.24 [1.1\%]$	$\pm 0.07 [0.21\%]$	$\pm 0.18 [11.2\%]$	$\pm 0.00 [0.04\%]$	$\pm 0.00 [0.10\%]$	$\pm 0.00 [0.09\%]$	$\pm 0.00 [0.06\%]$
$\alpha_{\text{JES}}_{\text{EtaInter_posEta}}$	$\pm 0.11 [0.39\%]$	$\pm 0.01 [0.03\%]$	$\pm 0.04 [0.18\%]$	$\pm 0.13 [0.41\%]$	$\pm 0.17 [10.5\%]$	$\pm 0.00 [0.09\%]$	$\pm 0.01 [0.62\%]$	$\pm 0.00 [0.05\%]$	$\pm 0.00 [0.03\%]$
$\alpha_{\text{JET}}_{\text{Flavor_Response}}$	$\pm 0.75 [2.6\%]$	$\pm 0.40 [0.95\%]$	$\pm 0.54 [2.4\%]$	$\pm 1.28 [4.0\%]$	$\pm 0.01 [0.65\%]$	$\pm 0.04 [1.7\%]$	$\pm 0.01 [0.60\%]$	$\pm 0.03 [2.5\%]$	$\pm 0.01 [0.44\%]$

Uncertainty of channel	CR_Gtt_0L_1CR_Gtt_1L_2VR_Gtt_0L_1VR_Gtt_1L_2SR4_Gtt_0L_1SR0_Gtt_1L_2SR1_Gtt_1L_2SR3_Gtt_1L_2SR4_Gtt_1L_2
α_{JVT}	$\pm 0.12 [0.41\%]$ $\pm 0.08 [0.19\%]$ $\pm 0.12 [0.54\%]$ $\pm 0.12 [0.39\%]$ $\pm 0.01 [0.55\%]$ $\pm 0.01 [0.36\%]$ $\pm 0.01 [0.50\%]$ $\pm 0.01 [0.47\%]$ $\pm 0.02 [1.4\%]$
α_{MCMCHack}	$\pm 0.77 [2.6\%]$ $\pm 0.10 [0.24\%]$ $\pm 0.82 [3.7\%]$ $\pm 0.07 [0.23\%]$ $\pm 0.16 [10.1\%]$ $\pm 0.00 [0.00\%]$ $\pm 0.00 [0.00\%]$ $\pm 0.00 [0.00\%]$ $\pm 0.01 [0.47\%]$
$\alpha_{\text{RW_1CR}}$	$\pm 0.00 [0.00\%]$ $\pm 0.33 [0.79\%]$ $\pm 0.00 [0.00\%]$ $\pm 0.30 [0.94\%]$ $\pm 0.00 [0.00\%]$ $\pm 0.03 [1.6\%]$ $\pm 0.03 [1.8\%]$ $\pm 0.03 [2.5\%]$ $\pm 0.05 [2.9\%]$
$\alpha_{\text{WZ_ckkw_syst}}$	$\pm 2.30 [7.9\%]$ $\pm 0.02 [0.06\%]$ $\pm 2.08 [9.4\%]$ $\pm 0.01 [0.04\%]$ $\pm 0.73 [45.2\%]$ $\pm 0.00 [0.00\%]$ $\pm 0.00 [0.00\%]$ $\pm 0.00 [0.00\%]$ $\pm 0.00 [0.13\%]$
$\alpha_{\text{WZ_fac_syst}}$	$\pm 0.96 [3.3\%]$ $\pm 0.05 [0.13\%]$ $\pm 0.88 [3.9\%]$ $\pm 0.07 [0.21\%]$ $\pm 0.35 [21.5\%]$ $\pm 0.00 [0.00\%]$ $\pm 0.00 [0.00\%]$ $\pm 0.00 [0.00\%]$ $\pm 0.01 [0.43\%]$
$\alpha_{\text{WZ_qsf_syst}}$	$\pm 0.16 [0.55\%]$ $\pm 0.06 [0.14\%]$ $\pm 0.13 [0.58\%]$ $\pm 0.05 [0.16\%]$ $\pm 0.01 [0.37\%]$ $\pm 0.00 [0.00\%]$ $\pm 0.00 [0.00\%]$ $\pm 0.00 [0.00\%]$ $\pm 0.01 [0.37\%]$
$\alpha_{\text{WZ_renorm_syst}}$	$\pm 0.65 [2.2\%]$ $\pm 0.09 [0.22\%]$ $\pm 0.57 [2.5\%]$ $\pm 0.04 [0.12\%]$ $\pm 0.12 [7.2\%]$ $\pm 0.00 [0.00\%]$ $\pm 0.00 [0.00\%]$ $\pm 0.00 [0.00\%]$ $\pm 0.01 [0.75\%]$
$\alpha_{\text{bTag_B}}$	$\pm 0.31 [1.1\%]$ $\pm 0.24 [0.57\%]$ $\pm 0.13 [0.57\%]$ $\pm 0.33 [1.1\%]$ $\pm 0.00 [0.06\%]$ $\pm 0.05 [2.2\%]$ $\pm 0.00 [0.02\%]$ $\pm 0.02 [1.4\%]$ $\pm 0.02 [0.99\%]$
$\alpha_{\text{bTag_C}}$	$\pm 0.51 [1.8\%]$ $\pm 0.30 [0.71\%]$ $\pm 0.45 [2.0\%]$ $\pm 0.03 [0.10\%]$ $\pm 0.03 [2.0\%]$ $\pm 0.03 [1.4\%]$ $\pm 0.03 [2.1\%]$ $\pm 0.01 [0.55\%]$ $\pm 0.04 [2.1\%]$
$\alpha_{\text{bTag_L}}$	$\pm 0.38 [1.3\%]$ $\pm 0.26 [0.61\%]$ $\pm 0.33 [1.5\%]$ $\pm 0.28 [0.87\%]$ $\pm 0.01 [0.49\%]$ $\pm 0.00 [0.04\%]$ $\pm 0.00 [0.03\%]$ $\pm 0.01 [0.94\%]$ $\pm 0.00 [0.06\%]$
$\alpha_{\text{bTag_extrapol}}$	$\pm 0.12 [0.42\%]$ $\pm 0.04 [0.08\%]$ $\pm 0.06 [0.28\%]$ $\pm 0.05 [0.17\%]$ $\pm 0.00 [0.15\%]$ $\pm 0.00 [0.03\%]$ $\pm 0.01 [0.35\%]$ $\pm 0.00 [0.09\%]$ $\pm 0.01 [0.29\%]$
$\alpha_{\text{bTag_extrapol_charm}}$	$\pm 0.16 [0.54\%]$ $\pm 0.08 [0.19\%]$ $\pm 0.07 [0.30\%]$ $\pm 0.19 [0.59\%]$ $\pm 0.00 [0.29\%]$ $\pm 0.00 [0.11\%]$ $\pm 0.00 [0.08\%]$ $\pm 0.01 [1.2\%]$ $\pm 0.00 [0.12\%]$
$\alpha_{\text{diboson_syst_CR_Gtt_0L_1}}$	$\pm 0.08 [0.27\%]$ $\pm 0.00 [0.00\%]$
$\alpha_{\text{diboson_syst_CR_Gtt_1L_2}}$	$\pm 0.00 [0.00\%]$ $\pm 0.04 [0.08\%]$ $\pm 0.00 [0.00\%]$
$\alpha_{\text{diboson_syst_VR_Gtt_0L_1}}$	$\pm 0.00 [0.00\%]$ $\pm 0.00 [0.00\%]$ $\pm 0.25 [1.1\%]$ $\pm 0.00 [0.00\%]$
$\alpha_{\text{st_syst_SR0_Gtt_1L_2}}$	$\pm 0.00 [0.00\%]$ $\pm 0.31 [14.1\%]$ $\pm 0.00 [0.00\%]$ $\pm 0.00 [0.00\%]$ $\pm 0.00 [0.00\%]$
$\alpha_{\text{st_syst_SR3_Gtt_1L_2}}$	$\pm 0.00 [0.00\%]$ $\pm 0.16 [13.7\%]$ $\pm 0.00 [0.00\%]$
$\alpha_{\text{st_syst_SR4_Gtt_0L_1}}$	$\pm 0.00 [0.00\%]$ $\pm 0.00 [0.00\%]$ $\pm 0.00 [0.00\%]$ $\pm 0.00 [0.00\%]$ $\pm 0.08 [5.1\%]$ $\pm 0.00 [0.00\%]$ $\pm 0.00 [0.00\%]$ $\pm 0.00 [0.00\%]$ $\pm 0.00 [0.00\%]$
$\alpha_{\text{st_syst_SR4_Gtt_1L_2}}$	$\pm 0.00 [0.00\%]$ $\pm 0.82 [47.0\%]$
$\alpha_{\text{st_syst_VR_Gtt_0L_1}}$	$\pm 0.00 [0.00\%]$ $\pm 0.00 [0.00\%]$ $\pm 4.22 [19.0\%]$ $\pm 0.00 [0.00\%]$
$\alpha_{\text{st_syst_VR_Gtt_1L_2}}$	$\pm 0.00 [0.00\%]$ $\pm 0.00 [0.00\%]$ $\pm 0.00 [0.00\%]$ $\pm 1.20 [3.8\%]$ $\pm 0.00 [0.00\%]$
$\alpha_{\text{topEW_syst_CR_Gtt_0L_1}}$	$\pm 2.13 [7.4\%]$ $\pm 0.00 [0.00\%]$
$\alpha_{\text{topEW_syst_CR_Gtt_1L_2}}$	$\pm 0.00 [0.00\%]$ $\pm 1.91 [4.5\%]$ $\pm 0.00 [0.00\%]$
$\alpha_{\text{topEW_syst_SR0_Gtt_1L_2}}$	$\pm 0.00 [0.00\%]$ $\pm 0.28 [13.0\%]$ $\pm 0.00 [0.00\%]$ $\pm 0.00 [0.00\%]$ $\pm 0.00 [0.00\%]$
$\alpha_{\text{topEW_syst_SR1_Gtt_1L_2}}$	$\pm 0.00 [0.00\%]$ $\pm 0.17 [11.7\%]$ $\pm 0.00 [0.00\%]$
$\alpha_{\text{topEW_syst_SR3_Gtt_1L_2}}$	$\pm 0.00 [0.00\%]$ $\pm 0.23 [20.0\%]$ $\pm 0.00 [0.00\%]$
$\alpha_{\text{topEW_syst_SR4_Gtt_0L_1}}$	$\pm 0.00 [0.00\%]$ $\pm 0.00 [0.00\%]$ $\pm 0.00 [0.00\%]$ $\pm 0.00 [0.00\%]$ $\pm 0.24 [15.0\%]$ $\pm 0.00 [0.00\%]$ $\pm 0.00 [0.00\%]$ $\pm 0.00 [0.00\%]$ $\pm 0.00 [0.00\%]$
$\alpha_{\text{topEW_syst_SR4_Gtt_1L_2}}$	$\pm 0.00 [0.00\%]$ $\pm 0.17 [9.6\%]$
$\alpha_{\text{topEW_syst_VR_Gtt_0L_1}}$	$\pm 0.00 [0.00\%]$ $\pm 0.00 [0.00\%]$ $\pm 1.07 [4.8\%]$ $\pm 0.00 [0.00\%]$
$\alpha_{\text{topEW_syst_VR_Gtt_1L_2}}$	$\pm 0.00 [0.00\%]$ $\pm 0.00 [0.00\%]$ $\pm 0.00 [0.00\%]$ $\pm 1.76 [5.5\%]$ $\pm 0.00 [0.00\%]$
$\alpha_{\text{ttbar_syst_SR0_Gtt_1L_2}}$	$\pm 0.00 [0.00\%]$ $\pm 0.20 [9.2\%]$ $\pm 0.00 [0.00\%]$ $\pm 0.00 [0.00\%]$ $\pm 0.00 [0.00\%]$
$\alpha_{\text{ttbar_syst_SR1_Gtt_1L_2}}$	$\pm 0.00 [0.00\%]$ $\pm 0.19 [82.4\%]$ $\pm 0.00 [0.00\%]$ $\pm 0.00 [0.00\%]$
$\alpha_{\text{ttbar_syst_SR3_Gtt_1L_2}}$	$\pm 0.00 [0.00\%]$ $\pm 0.13 [11.3\%]$ $\pm 0.00 [0.00\%]$ $\pm 0.00 [0.00\%]$
$\alpha_{\text{ttbar_syst_SR4_Gtt_0L_1}}$	$\pm 0.00 [0.00\%]$ $\pm 0.00 [0.00\%]$ $\pm 0.00 [0.00\%]$ $\pm 0.00 [0.00\%]$ $\pm 0.36 [22.4\%]$ $\pm 0.00 [0.00\%]$ $\pm 0.00 [0.00\%]$ $\pm 0.00 [0.00\%]$ $\pm 0.00 [0.00\%]$
$\alpha_{\text{ttbar_syst_SR4_Gtt_1L_2}}$	$\pm 0.00 [0.00\%]$ $\pm 0.99 [56.6\%]$
$\alpha_{\text{ttbar_syst_VR_Gtt_0L_1}}$	$\pm 0.00 [0.00\%]$ $\pm 0.00 [0.00\%]$ $\pm 4.95 [22.2\%]$ $\pm 0.00 [0.00\%]$
$\alpha_{\text{ttbar_syst_VR_Gtt_1L_2}}$	$\pm 0.00 [0.00\%]$ $\pm 0.00 [0.00\%]$ $\pm 0.00 [0.00\%]$ $\pm 9.73 [30.7\%]$ $\pm 0.00 [0.00\%]$

Table A.4: Breakdown of the dominant systematic uncertainties on background estimates in the Gtt_0L_3_Gtt_1L_2 signal regions. Note that the individual uncertainties can be correlated, and do not necessarily add up quadratically to the total background uncertainty. The percentages show the size of the uncertainty relative to the total expected background.

Uncertainty of channel	CR_Gtt_0L_3CR_Gtt_1L_2VR_Gtt_0L_3VR_Gtt_1L_2SR4_Gtt_0L_3SR0_Gtt_1L_2SR1_Gtt_1L_2SR3_Gtt_1L_2SR4_Gtt_1L_2								
Total background expectation	36.88	42.00	24.44	31.72	1.24	2.19	1.45	1.17	1.76
Total statistical ($\sqrt{N_{\text{exp}}}$)	± 6.07	± 6.48	± 4.94	± 5.63	± 1.11	± 1.48	± 1.20	± 1.08	± 1.33
Total background systematic	± 6.09 [16.51%]	± 6.46 [15.38%]	± 14.20 [58.10%]	± 11.98 [37.76%]	± 0.79 [63.85%]	± 1.47 [67.39%]	± 1.48 [101.88%]	± 0.83 [70.80%]	± 1.65 [93.88%]
Lumi	± 0.30 [0.81%]	± 0.23 [0.56%]	± 0.21 [0.84%]	± 0.20 [0.64%]	± 0.02 [1.4%]	± 0.03 [1.3%]	± 0.01 [0.67%]	± 0.02 [1.4%]	± 0.03 [1.5%]
μ_{ttbar} _Gtt_0L_3	± 7.56 [20.5%]	± 0.00 [0.00%]	± 4.93 [20.2%]	± 0.00 [0.00%]	± 0.18 [14.7%]	± 0.00 [0.00%]	± 0.00 [0.00%]	± 0.00 [0.00%]	± 0.00 [0.00%]
μ_{ttbar} _Gtt_1L_2	± 0.00 [0.00%]	± 7.54 [18.0%]	± 0.00 [0.00%]	± 5.49 [17.3%]	± 0.00 [0.00%]	± 0.27 [12.3%]	± 0.25 [17.1%]	± 0.13 [11.3%]	± 0.19 [10.8%]
γ_{stat} _CR_Gtt_0L_3	± 2.86 [7.8%]	± 0.00 [0.00%]	± 0.00 [0.00%]	± 0.00 [0.00%]	± 0.00 [0.00%]	± 0.00 [0.00%]	± 0.00 [0.00%]	± 0.00 [0.00%]	± 0.00 [0.00%]
γ_{stat} _CR_Gtt_1L_2	± 0.00 [0.00%]	± 2.87 [6.8%]	± 0.00 [0.00%]	± 0.00 [0.00%]	± 0.00 [0.00%]	± 0.00 [0.00%]	± 0.00 [0.00%]	± 0.00 [0.00%]	± 0.00 [0.00%]
γ_{stat} _SR0_Gtt_1L_2	± 0.00 [0.00%]	± 0.00 [0.00%]	± 0.00 [0.00%]	± 0.00 [0.00%]	± 0.00 [0.00%]	± 0.46 [21.2%]	± 0.00 [0.00%]	± 0.00 [0.00%]	± 0.00 [0.00%]
γ_{stat} _SR1_Gtt_1L_2	± 0.00 [0.00%]	± 0.00 [0.00%]	± 0.00 [0.00%]	± 0.00 [0.00%]	± 0.00 [0.00%]	± 0.00 [0.00%]	± 0.25 [17.3%]	± 0.00 [0.00%]	± 0.00 [0.00%]
γ_{stat} _SR3_Gtt_1L_2	± 0.00 [0.00%]	± 0.00 [0.00%]	± 0.00 [0.00%]	± 0.00 [0.00%]	± 0.00 [0.00%]	± 0.00 [0.00%]	± 0.00 [0.00%]	± 0.23 [19.6%]	± 0.00 [0.00%]
γ_{stat} _SR4_Gtt_0L_3	± 0.00 [0.00%]	± 0.00 [0.00%]	± 0.00 [0.00%]	± 0.00 [0.00%]	± 0.29 [23.2%]	± 0.00 [0.00%]	± 0.00 [0.00%]	± 0.00 [0.00%]	± 0.00 [0.00%]
γ_{stat} _SR4_Gtt_1L_2	± 0.00 [0.00%]	± 0.00 [0.00%]	± 0.00 [0.00%]	± 0.00 [0.00%]	± 0.00 [0.00%]	± 0.00 [0.00%]	± 0.00 [0.00%]	± 0.00 [0.00%]	± 0.39 [22.0%]
γ_{stat} _VR_Gtt_0L_3	± 0.00 [0.00%]	± 0.00 [0.00%]	± 1.79 [7.3%]	± 0.00 [0.00%]	± 0.00 [0.00%]	± 0.00 [0.00%]	± 0.00 [0.00%]	± 0.00 [0.00%]	± 0.00 [0.00%]
γ_{stat} _VR_Gtt_1L_2	± 0.00 [0.00%]	± 0.00 [0.00%]	± 0.00 [0.00%]	± 2.33 [7.3%]	± 0.00 [0.00%]	± 0.00 [0.00%]	± 0.00 [0.00%]	± 0.00 [0.00%]	± 0.00 [0.00%]
α_{JER1}	± 0.28 [0.76%]	± 0.61 [1.5%]	± 0.15 [0.61%]	± 1.30 [4.1%]	± 0.13 [10.4%]	± 0.08 [3.7%]	± 0.43 [29.6%]	± 0.19 [16.4%]	± 0.28 [16.0%]
α_{JER2}	± 0.07 [0.19%]	± 0.51 [1.2%]	± 0.40 [1.6%]	± 1.75 [5.5%]	± 0.13 [10.7%]	± 0.24 [10.7%]	± 0.34 [23.1%]	± 0.25 [21.2%]	± 0.30 [17.0%]
α_{JER3}	± 0.47 [1.3%]	± 0.77 [1.8%]	± 1.49 [6.1%]	± 0.04 [0.13%]	± 0.06 [5.1%]	± 0.30 [13.9%]	± 0.14 [9.9%]	± 0.17 [14.8%]	± 0.32 [18.3%]
α_{JER4}	± 0.16 [0.44%]	± 0.47 [1.1%]	± 0.44 [1.8%]	± 0.99 [3.1%]	± 0.07 [5.5%]	± 0.33 [14.9%]	± 0.10 [7.0%]	± 0.22 [18.6%]	± 0.23 [13.1%]
α_{JER5}	± 0.27 [0.72%]	± 0.25 [0.61%]	± 2.13 [8.7%]	± 0.88 [2.8%]	± 0.02 [1.5%]	± 0.55 [25.0%]	± 0.10 [6.6%]	± 0.28 [24.2%]	± 0.32 [18.1%]
α_{JER6}	± 0.29 [0.78%]	± 0.01 [0.02%]	± 0.88 [3.6%]	± 0.23 [0.74%]	± 0.08 [6.8%]	± 0.60 [27.6%]	± 0.04 [2.8%]	± 0.26 [22.6%]	± 0.29 [16.6%]
α_{JER7}	± 0.63 [1.7%]	± 0.44 [1.0%]	± 1.91 [7.8%]	± 0.81 [2.6%]	± 0.08 [6.2%]	± 0.54 [24.6%]	± 0.52 [35.6%]	± 0.20 [17.0%]	± 0.25 [14.0%]
$\alpha_{\text{JER_DataVsMC}}$	± 0.72 [1.9%]	± 0.05 [0.13%]	± 2.04 [8.3%]	± 0.57 [1.8%]	± 0.03 [2.1%]	± 0.45 [20.4%]	± 0.08 [5.2%]	± 0.38 [32.3%]	± 0.32 [18.3%]
α_{JES1}	± 0.73 [2.0%]	± 0.67 [1.6%]	± 0.90 [3.7%]	± 0.86 [2.7%]	± 0.11 [8.7%]	± 0.04 [2.0%]	± 0.07 [4.7%]	± 0.08 [6.8%]	± 0.01 [0.38%]
α_{JES2}	± 1.29 [3.5%]	± 0.46 [1.1%]	± 0.84 [3.5%]	± 0.15 [0.46%]	± 0.10 [8.1%]	± 0.07 [3.3%]	± 0.13 [9.1%]	± 0.07 [6.1%]	± 0.06 [3.4%]
α_{JES3}	± 0.18 [0.48%]	± 0.08 [0.18%]	± 0.06 [0.23%]	± 0.51 [1.6%]	± 0.00 [0.20%]	± 0.18 [8.3%]	± 0.10 [6.7%]	± 0.00 [0.08%]	± 0.01 [0.42%]
$\alpha_{\text{JES_EtaInter_highE}}$	± 0.74 [2.0%]	± 0.01 [0.01%]	± 0.67 [2.8%]	± 0.19 [0.58%]	± 0.07 [5.3%]	± 0.34 [15.7%]	± 0.00 [0.00%]	± 0.11 [9.6%]	± 0.29 [16.4%]
$\alpha_{\text{JES_EtaInter_negEta}}$	± 0.35 [0.94%]	± 0.00 [0.01%]	± 0.02 [0.06%]	± 0.07 [0.22%]	± 0.04 [3.4%]	± 0.00 [0.02%]	± 0.00 [0.08%]	± 0.00 [0.16%]	± 0.00 [0.04%]
$\alpha_{\text{JES_EtaInter_posEta}}$	± 0.00 [0.01%]	± 0.01 [0.03%]	± 0.03 [0.12%]	± 0.13 [0.41%]	± 0.04 [3.5%]	± 0.00 [0.09%]	± 0.01 [0.61%]	± 0.00 [0.06%]	± 0.00 [0.03%]
$\alpha_{\text{JET_Flavor_Response}}$	± 0.44 [1.2%]	± 0.39 [0.94%]	± 1.07 [4.4%]	± 1.28 [4.0%]	± 0.10 [7.8%]	± 0.04 [1.8%]	± 0.01 [0.63%]	± 0.03 [2.3%]	± 0.01 [0.38%]

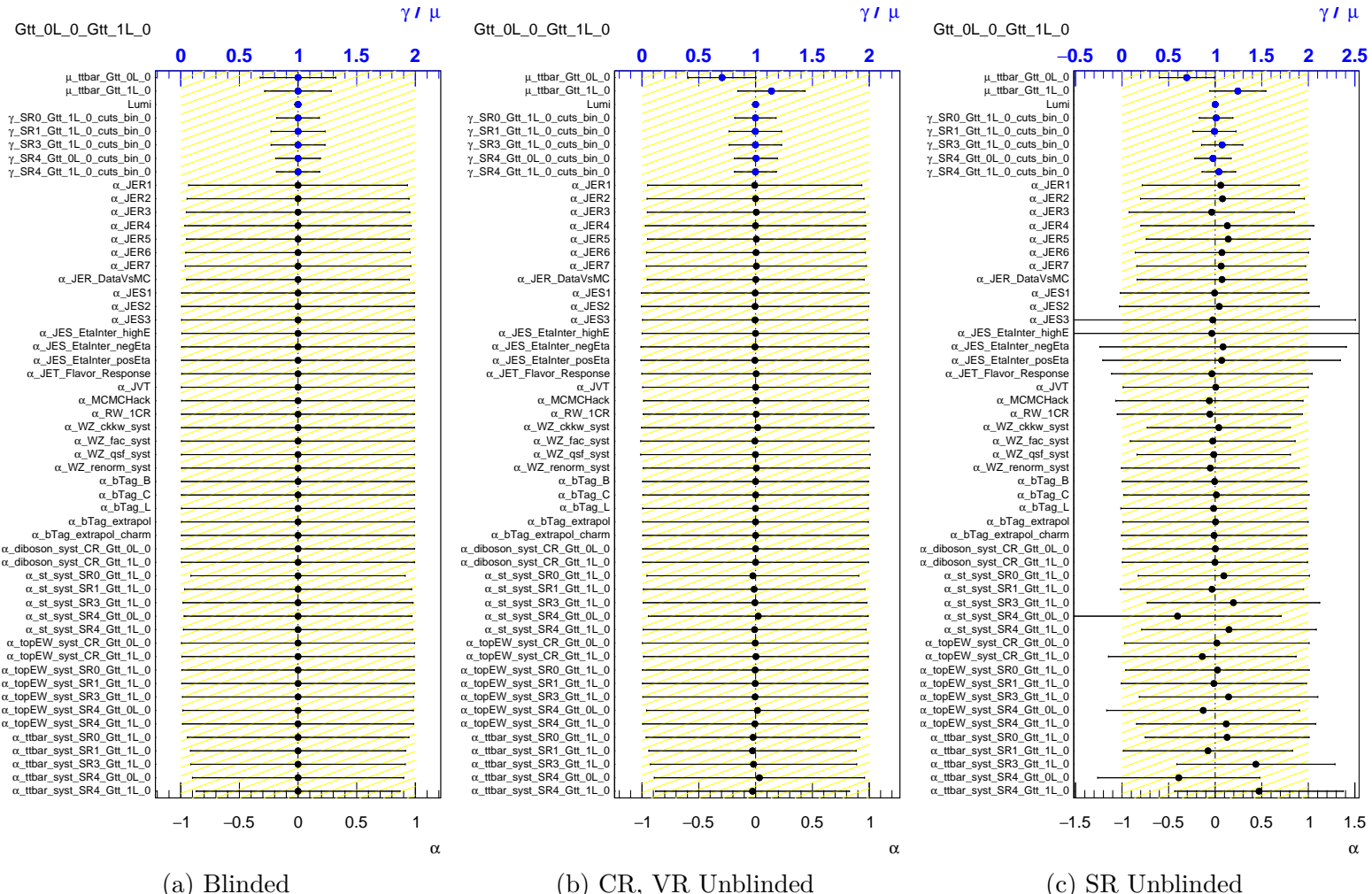
Uncertainty of channel	CR_Gtt_0L_3CR_Gtt_1L_2VR_Gtt_0L_3	VR_Gtt_1L_2SR4_Gtt_0L_3SR0_Gtt_1L_2SR1_Gtt_1L_2SR3_Gtt_1L_2SR4_Gtt_1L_2
α_{JVT}	$\pm 0.09 [0.25\%]$	$\pm 0.08 [0.19\%]$
α_{MCMCHack}	$\pm 0.98 [2.7\%]$	$\pm 0.10 [0.24\%]$
$\alpha_{\text{RW_1CR}}$	$\pm 0.00 [0.00\%]$	$\pm 0.33 [0.79\%]$
$\alpha_{\text{WZ_ckkw_syst}}$	$\pm 0.82 [2.2\%]$	$\pm 0.02 [0.06\%]$
$\alpha_{\text{WZ_fac_syst}}$	$\pm 0.22 [0.60\%]$	$\pm 0.05 [0.13\%]$
$\alpha_{\text{WZ_qsf_syst}}$	$\pm 0.63 [1.7\%]$	$\pm 0.06 [0.14\%]$
$\alpha_{\text{WZ_renorm_syst}}$	$\pm 1.38 [3.7\%]$	$\pm 0.09 [0.22\%]$
$\alpha_{\text{bTag_B}}$	$\pm 0.27 [0.73\%]$	$\pm 0.24 [0.57\%]$
$\alpha_{\text{bTag_C}}$	$\pm 0.26 [0.72\%]$	$\pm 0.30 [0.71\%]$
$\alpha_{\text{bTag_L}}$	$\pm 0.32 [0.88\%]$	$\pm 0.25 [0.61\%]$
$\alpha_{\text{bTag_extrapol}}$	$\pm 0.08 [0.23\%]$	$\pm 0.04 [0.08\%]$
$\alpha_{\text{bTag_extrapol_charm}}$	$\pm 0.04 [0.10\%]$	$\pm 0.08 [0.19\%]$
$\alpha_{\text{diboson_syst_CR_Gtt_1L_2}}$	$\pm 0.00 [0.00\%]$	$\pm 0.04 [0.08\%]$
$\alpha_{\text{diboson_syst_VR_Gtt_0L_3}}$	$\pm 0.00 [0.00\%]$	$\pm 0.00 [0.00\%]$
$\alpha_{\text{st_syst_SR0_Gtt_1L_2}}$	$\pm 0.00 [0.00\%]$	$\pm 0.00 [0.00\%]$
$\alpha_{\text{st_syst_SR3_Gtt_1L_2}}$	$\pm 0.00 [0.00\%]$	$\pm 0.00 [0.00\%]$
$\alpha_{\text{st_syst_SR4_Gtt_0L_3}}$	$\pm 0.00 [0.00\%]$	$\pm 0.00 [0.00\%]$
$\alpha_{\text{st_syst_SR4_Gtt_1L_2}}$	$\pm 0.00 [0.00\%]$	$\pm 0.00 [0.00\%]$
$\alpha_{\text{st_syst_VR_Gtt_0L_3}}$	$\pm 0.00 [0.00\%]$	$\pm 0.00 [0.00\%]$
$\alpha_{\text{st_syst_VR_Gtt_1L_2}}$	$\pm 0.00 [0.00\%]$	$\pm 0.00 [0.00\%]$
$\alpha_{\text{topEW_syst_CR_Gtt_0L_3}}$	$\pm 1.74 [4.7\%]$	$\pm 0.00 [0.00\%]$
$\alpha_{\text{topEW_syst_CR_Gtt_1L_2}}$	$\pm 0.00 [0.00\%]$	$\pm 1.90 [4.5\%]$
$\alpha_{\text{topEW_syst_SR0_Gtt_1L_2}}$	$\pm 0.00 [0.00\%]$	$\pm 0.00 [0.00\%]$
$\alpha_{\text{topEW_syst_SR1_Gtt_1L_2}}$	$\pm 0.00 [0.00\%]$	$\pm 0.00 [0.00\%]$
$\alpha_{\text{topEW_syst_SR3_Gtt_1L_2}}$	$\pm 0.00 [0.00\%]$	$\pm 0.00 [0.00\%]$
$\alpha_{\text{topEW_syst_SR4_Gtt_0L_3}}$	$\pm 0.00 [0.00\%]$	$\pm 0.00 [0.00\%]$
$\alpha_{\text{topEW_syst_SR4_Gtt_1L_2}}$	$\pm 0.00 [0.00\%]$	$\pm 0.00 [0.00\%]$
$\alpha_{\text{topEW_syst_VR_Gtt_0L_3}}$	$\pm 0.00 [0.00\%]$	$\pm 0.00 [0.00\%]$
$\alpha_{\text{topEW_syst_VR_Gtt_1L_2}}$	$\pm 0.00 [0.00\%]$	$\pm 0.00 [0.00\%]$
$\alpha_{\text{ttbar_syst_SR0_Gtt_1L_2}}$	$\pm 0.00 [0.00\%]$	$\pm 0.00 [0.00\%]$
$\alpha_{\text{ttbar_syst_SR1_Gtt_1L_2}}$	$\pm 0.00 [0.00\%]$	$\pm 0.00 [0.00\%]$
$\alpha_{\text{ttbar_syst_SR3_Gtt_1L_2}}$	$\pm 0.00 [0.00\%]$	$\pm 0.00 [0.00\%]$
$\alpha_{\text{ttbar_syst_SR4_Gtt_0L_3}}$	$\pm 0.00 [0.00\%]$	$\pm 0.00 [0.00\%]$
$\alpha_{\text{ttbar_syst_SR4_Gtt_1L_2}}$	$\pm 0.00 [0.00\%]$	$\pm 0.00 [0.00\%]$
$\alpha_{\text{ttbar_syst_VR_Gtt_0L_3}}$	$\pm 0.00 [0.00\%]$	$\pm 0.00 [0.00\%]$
$\alpha_{\text{ttbar_syst_VR_Gtt_1L_2}}$	$\pm 0.00 [0.00\%]$	$\pm 0.00 [0.00\%]$

Table A.5: Breakdown of the dominant systematic uncertainties on background estimates in the Gtt_0L_3_Gtt_1L_3 signal regions. Note that the individual uncertainties can be correlated, and do not necessarily add up quadratically to the total background uncertainty. The percentages show the size of the uncertainty relative to the total expected background.

Uncertainty of channel	CR_Gtt_0L_3CR_Gtt_1L_3 VR_Gtt_0L_3 VR_Gtt_1L_3 SR4_Gtt_0L_3SR4_Gtt_1L_3					
Total background expectation	36.95	45.02	24.44	29.36	1.25	1.62
Total statistical ($\sqrt{N_{\text{exp}}}$)	± 6.08	± 6.71	± 4.94	± 5.42	± 1.12	± 1.27
Total background systematic	± 6.10 [16.50%]	± 6.69 [14.85%]	± 14.18 [58.04%]	± 23.88 [81.32%]	± 0.80 [64.13%]	± 0.99 [61.41%]
Lumi	± 0.30 [0.81%]	± 0.27 [0.59%]	± 0.21 [0.85%]	± 0.15 [0.51%]	± 0.02 [1.4%]	± 0.02 [1.3%]
$\mu_{\text{ttbar}}\text{Gtt}_0\text{L}_3$	± 7.53 [20.4%]	± 0.00 [0.00%]	± 4.90 [20.0%]	± 0.00 [0.00%]	± 0.18 [14.6%]	± 0.00 [0.00%]
$\mu_{\text{ttbar}}\text{Gtt}_1\text{L}_3$	± 0.00 [0.00%]	± 8.01 [17.8%]	± 0.00 [0.00%]	± 5.41 [18.4%]	± 0.00 [0.00%]	± 0.20 [12.2%]
$\gamma_{\text{stat}}\text{CR}\text{Gtt}_0\text{L}_3$	± 2.86 [7.7%]	± 0.00 [0.00%]	± 0.00 [0.00%]	± 0.00 [0.00%]	± 0.00 [0.00%]	± 0.00 [0.00%]
$\gamma_{\text{stat}}\text{CR}\text{Gtt}_1\text{L}_3$	± 0.00 [0.00%]	± 3.26 [7.2%]	± 0.00 [0.00%]	± 0.00 [0.00%]	± 0.00 [0.00%]	± 0.00 [0.00%]
$\gamma_{\text{stat}}\text{SR4}\text{Gtt}_0\text{L}_3$	± 0.00 [0.00%]	± 0.00 [0.00%]	± 0.00 [0.00%]	± 0.00 [0.00%]	± 0.29 [23.2%]	± 0.00 [0.00%]
$\gamma_{\text{stat}}\text{SR4}\text{Gtt}_1\text{L}_3$	± 0.00 [0.00%]	± 0.00 [0.00%]	± 0.00 [0.00%]	± 0.00 [0.00%]	± 0.00 [0.00%]	± 0.40 [24.4%]
$\gamma_{\text{stat}}\text{VR}\text{Gtt}_0\text{L}_3$	± 0.00 [0.00%]	± 0.00 [0.00%]	± 1.79 [7.3%]	± 0.00 [0.00%]	± 0.00 [0.00%]	± 0.00 [0.00%]
$\gamma_{\text{stat}}\text{VR}\text{Gtt}_1\text{L}_3$	± 0.00 [0.00%]	± 0.00 [0.00%]	± 0.00 [0.00%]	± 3.08 [10.5%]	± 0.00 [0.00%]	± 0.00 [0.00%]
α_{JER1}	± 0.24 [0.64%]	± 0.05 [0.11%]	± 0.14 [0.58%]	± 2.22 [7.6%]	± 0.14 [10.8%]	± 0.06 [4.0%]
α_{JER2}	± 0.12 [0.32%]	± 0.27 [0.61%]	± 0.39 [1.6%]	± 1.37 [4.7%]	± 0.14 [11.1%]	± 0.15 [9.3%]
α_{JER3}	± 0.42 [1.1%]	± 0.47 [1.0%]	± 1.48 [6.1%]	± 1.23 [4.2%]	± 0.07 [5.5%]	± 0.27 [16.4%]
α_{JER4}	± 0.12 [0.32%]	± 0.31 [0.70%]	± 0.43 [1.8%]	± 1.90 [6.5%]	± 0.07 [5.9%]	± 0.07 [4.2%]
α_{JER5}	± 0.30 [0.82%]	± 0.20 [0.44%]	± 2.12 [8.7%]	± 0.15 [0.52%]	± 0.03 [2.0%]	± 0.11 [6.9%]
α_{JER6}	± 0.25 [0.67%]	± 0.72 [1.6%]	± 0.88 [3.6%]	± 2.44 [8.3%]	± 0.09 [7.2%]	± 0.07 [4.1%]
α_{JER7}	± 0.59 [1.6%]	± 0.28 [0.61%]	± 1.90 [7.8%]	± 1.06 [3.6%]	± 0.08 [6.7%]	± 0.04 [2.5%]
$\alpha_{\text{JER}}\text{DataVsMC}$	± 0.68 [1.8%]	± 1.02 [2.3%]	± 2.03 [8.3%]	± 0.97 [3.3%]	± 0.02 [1.6%]	± 0.08 [5.0%]
α_{JES1}	± 0.74 [2.0%]	± 0.68 [1.5%]	± 0.91 [3.7%]	± 0.26 [0.89%]	± 0.11 [8.7%]	± 0.09 [5.5%]
α_{JES2}	± 1.31 [3.5%]	± 0.54 [1.2%]	± 0.86 [3.5%]	± 1.05 [3.6%]	± 0.10 [8.4%]	± 0.12 [7.2%]
α_{JES3}	± 0.17 [0.47%]	± 0.04 [0.08%]	± 0.06 [0.24%]	± 0.13 [0.43%]	± 0.00 [0.20%]	± 0.04 [2.4%]
$\alpha_{\text{JES}}\text{EtaInter_highE}$	± 0.72 [1.9%]	± 1.23 [2.7%]	± 0.67 [2.7%]	± 0.89 [3.0%]	± 0.06 [4.9%]	± 0.12 [7.6%]
$\alpha_{\text{JES}}\text{EtaInter_negEta}$	± 0.37 [1.0%]	± 0.02 [0.04%]	± 0.02 [0.07%]	± 0.04 [0.14%]	± 0.05 [3.8%]	± 0.00 [0.04%]
$\alpha_{\text{JES}}\text{EtaInter_posEta}$	± 0.00 [0.01%]	± 0.00 [0.01%]	± 0.03 [0.11%]	± 0.02 [0.06%]	± 0.05 [3.8%]	± 0.00 [0.02%]
$\alpha_{\text{JET}}\text{Flavor_Response}$	± 0.44 [1.2%]	± 0.48 [1.1%]	± 1.07 [4.4%]	± 0.25 [0.86%]	± 0.10 [7.8%]	± 0.04 [2.6%]

Uncertainty of channel	CR_Gtt_0L_3	CR_Gtt_1L_3	VR_Gtt_0L_3	VR_Gtt_1L_3	SR4_Gtt_0L_3	SR4_Gtt_1L_3
α_{JVT}	$\pm 0.09 [0.25\%]$	$\pm 0.11 [0.24\%]$	$\pm 0.04 [0.16\%]$	$\pm 0.05 [0.16\%]$	$\pm 0.01 [0.46\%]$	$\pm 0.02 [1.4\%]$
α_{MCMCHack}	$\pm 0.98 [2.6\%]$	$\pm 0.04 [0.08\%]$	$\pm 0.52 [2.1\%]$	$\pm 0.06 [0.19\%]$	$\pm 0.05 [4.4\%]$	$\pm 0.01 [0.50\%]$
$\alpha_{\text{RW_1CR}}$	$\pm 0.00 [0.00\%]$	$\pm 0.34 [0.75\%]$	$\pm 0.00 [0.00\%]$	$\pm 0.17 [0.58\%]$	$\pm 0.00 [0.00\%]$	$\pm 0.04 [2.7\%]$
$\alpha_{\text{WZ_ckkw_syst}}$	$\pm 0.91 [2.5\%]$	$\pm 0.01 [0.02\%]$	$\pm 2.32 [9.5\%]$	$\pm 0.01 [0.02\%]$	$\pm 0.25 [20.1\%]$	$\pm 0.00 [0.13\%]$
$\alpha_{\text{WZ_fac_syst}}$	$\pm 0.18 [0.48\%]$	$\pm 0.04 [0.08\%]$	$\pm 1.08 [4.4\%]$	$\pm 0.05 [0.18\%]$	$\pm 0.12 [9.3\%]$	$\pm 0.01 [0.47\%]$
$\alpha_{\text{WZ_qsf_syst}}$	$\pm 0.60 [1.6\%]$	$\pm 0.03 [0.07\%]$	$\pm 0.02 [0.08\%]$	$\pm 0.03 [0.12\%]$	$\pm 0.00 [0.33\%]$	$\pm 0.01 [0.40\%]$
$\alpha_{\text{WZ_renorm_syst}}$	$\pm 1.35 [3.7\%]$	$\pm 0.06 [0.14\%]$	$\pm 0.28 [1.1\%]$	$\pm 0.02 [0.05\%]$	$\pm 0.04 [3.1\%]$	$\pm 0.01 [0.81\%]$
$\alpha_{\text{bTag_B}}$	$\pm 0.27 [0.74\%]$	$\pm 0.23 [0.51\%]$	$\pm 0.00 [0.01\%]$	$\pm 0.20 [0.69\%]$	$\pm 0.01 [0.60\%]$	$\pm 0.01 [0.61\%]$
$\alpha_{\text{bTag_C}}$	$\pm 0.27 [0.72\%]$	$\pm 0.38 [0.85\%]$	$\pm 0.10 [0.43\%]$	$\pm 0.06 [0.22\%]$	$\pm 0.01 [1.1\%]$	$\pm 0.03 [2.1\%]$
$\alpha_{\text{bTag_L}}$	$\pm 0.32 [0.88\%]$	$\pm 0.45 [1.00\%]$	$\pm 0.14 [0.57\%]$	$\pm 0.66 [2.3\%]$	$\pm 0.01 [0.48\%]$	$\pm 0.01 [0.31\%]$
$\alpha_{\text{bTag_extrapol}}$	$\pm 0.08 [0.23\%]$	$\pm 0.02 [0.04\%]$	$\pm 0.06 [0.25\%]$	$\pm 0.02 [0.05\%]$	$\pm 0.00 [0.09\%]$	$\pm 0.01 [0.32\%]$
$\alpha_{\text{bTag_extrapol_charm}}$	$\pm 0.04 [0.10\%]$	$\pm 0.07 [0.16\%]$	$\pm 0.16 [0.64\%]$	$\pm 0.20 [0.67\%]$	$\pm 0.01 [0.73\%]$	$\pm 0.01 [0.36\%]$
$\alpha_{\text{diboson_syst_VR_Gtt_0L_3}}$	$\pm 0.00 [0.00\%]$	$\pm 0.00 [0.00\%]$	$\pm 0.04 [0.17\%]$	$\pm 0.00 [0.00\%]$	$\pm 0.00 [0.00\%]$	$\pm 0.00 [0.00\%]$
$\alpha_{\text{st_syst_SR4_Gtt_0L_3}}$	$\pm 0.00 [0.00\%]$	$\pm 0.00 [0.00\%]$	$\pm 0.00 [0.00\%]$	$\pm 0.00 [0.00\%]$	$\pm 0.28 [22.4\%]$	$\pm 0.00 [0.00\%]$
$\alpha_{\text{st_syst_SR4_Gtt_1L_3}}$	$\pm 0.00 [0.00\%]$	$\pm 0.00 [0.00\%]$	$\pm 0.00 [0.00\%]$	$\pm 0.00 [0.00\%]$	$\pm 0.00 [0.00\%]$	$\pm 0.35 [21.5\%]$
$\alpha_{\text{st_syst_VR_Gtt_0L_3}}$	$\pm 0.00 [0.00\%]$	$\pm 0.00 [0.00\%]$	$\pm 3.77 [15.4\%]$	$\pm 0.00 [0.00\%]$	$\pm 0.00 [0.00\%]$	$\pm 0.00 [0.00\%]$
$\alpha_{\text{st_syst_VR_Gtt_1L_3}}$	$\pm 0.00 [0.00\%]$	$\pm 0.00 [0.00\%]$	$\pm 0.00 [0.00\%]$	$\pm 1.36 [4.6\%]$	$\pm 0.00 [0.00\%]$	$\pm 0.00 [0.00\%]$
$\alpha_{\text{topEW_syst_CR_Gtt_0L_3}}$	$\pm 1.75 [4.7\%]$	$\pm 0.00 [0.00\%]$	$\pm 0.00 [0.00\%]$	$\pm 0.00 [0.00\%]$	$\pm 0.00 [0.00\%]$	$\pm 0.00 [0.00\%]$
$\alpha_{\text{topEW_syst_CR_Gtt_1L_3}}$	$\pm 0.00 [0.00\%]$	$\pm 1.77 [3.9\%]$	$\pm 0.00 [0.00\%]$	$\pm 0.00 [0.00\%]$	$\pm 0.00 [0.00\%]$	$\pm 0.00 [0.00\%]$
$\alpha_{\text{topEW_syst_SR4_Gtt_0L_3}}$	$\pm 0.00 [0.00\%]$	$\pm 0.00 [0.00\%]$	$\pm 0.00 [0.00\%]$	$\pm 0.00 [0.00\%]$	$\pm 0.14 [10.9\%]$	$\pm 0.00 [0.00\%]$
$\alpha_{\text{topEW_syst_SR4_Gtt_1L_3}}$	$\pm 0.00 [0.00\%]$	$\pm 0.00 [0.00\%]$	$\pm 0.00 [0.00\%]$	$\pm 0.00 [0.00\%]$	$\pm 0.00 [0.00\%]$	$\pm 0.14 [8.4\%]$
$\alpha_{\text{topEW_syst_VR_Gtt_0L_3}}$	$\pm 0.00 [0.00\%]$	$\pm 0.00 [0.00\%]$	$\pm 1.52 [6.2\%]$	$\pm 0.00 [0.00\%]$	$\pm 0.00 [0.00\%]$	$\pm 0.00 [0.00\%]$
$\alpha_{\text{topEW_syst_VR_Gtt_1L_3}}$	$\pm 0.00 [0.00\%]$	$\pm 0.00 [0.00\%]$	$\pm 0.00 [0.00\%]$	$\pm 1.53 [5.2\%]$	$\pm 0.00 [0.00\%]$	$\pm 0.00 [0.00\%]$
$\alpha_{\text{ttbar_syst_SR4_Gtt_0L_3}}$	$\pm 0.00 [0.00\%]$	$\pm 0.00 [0.00\%]$	$\pm 0.00 [0.00\%]$	$\pm 0.00 [0.00\%]$	$\pm 0.51 [40.6\%]$	$\pm 0.00 [0.00\%]$
$\alpha_{\text{ttbar_syst_SR4_Gtt_1L_3}}$	$\pm 0.00 [0.00\%]$	$\pm 0.00 [0.00\%]$	$\pm 0.00 [0.00\%]$	$\pm 0.00 [0.00\%]$	$\pm 0.00 [0.00\%]$	$\pm 0.72 [44.2\%]$
$\alpha_{\text{ttbar_syst_VR_Gtt_0L_3}}$	$\pm 0.00 [0.00\%]$	$\pm 0.00 [0.00\%]$	$\pm 11.91 [48.7\%]$	$\pm 0.00 [0.00\%]$	$\pm 0.00 [0.00\%]$	$\pm 0.00 [0.00\%]$
$\alpha_{\text{ttbar_syst_VR_Gtt_1L_3}}$	$\pm 0.00 [0.00\%]$	$\pm 0.00 [0.00\%]$	$\pm 0.00 [0.00\%]$	$\pm 22.30 [75.9\%]$	$\pm 0.00 [0.00\%]$	$\pm 0.00 [0.00\%]$

A.6.2 Fitted Nuisance Parameters

FIGURE A.29: $\text{Gtt}_0\text{L}_0\text{--}\text{Gtt}_1\text{L}_0$ fitted nuisance parameters.

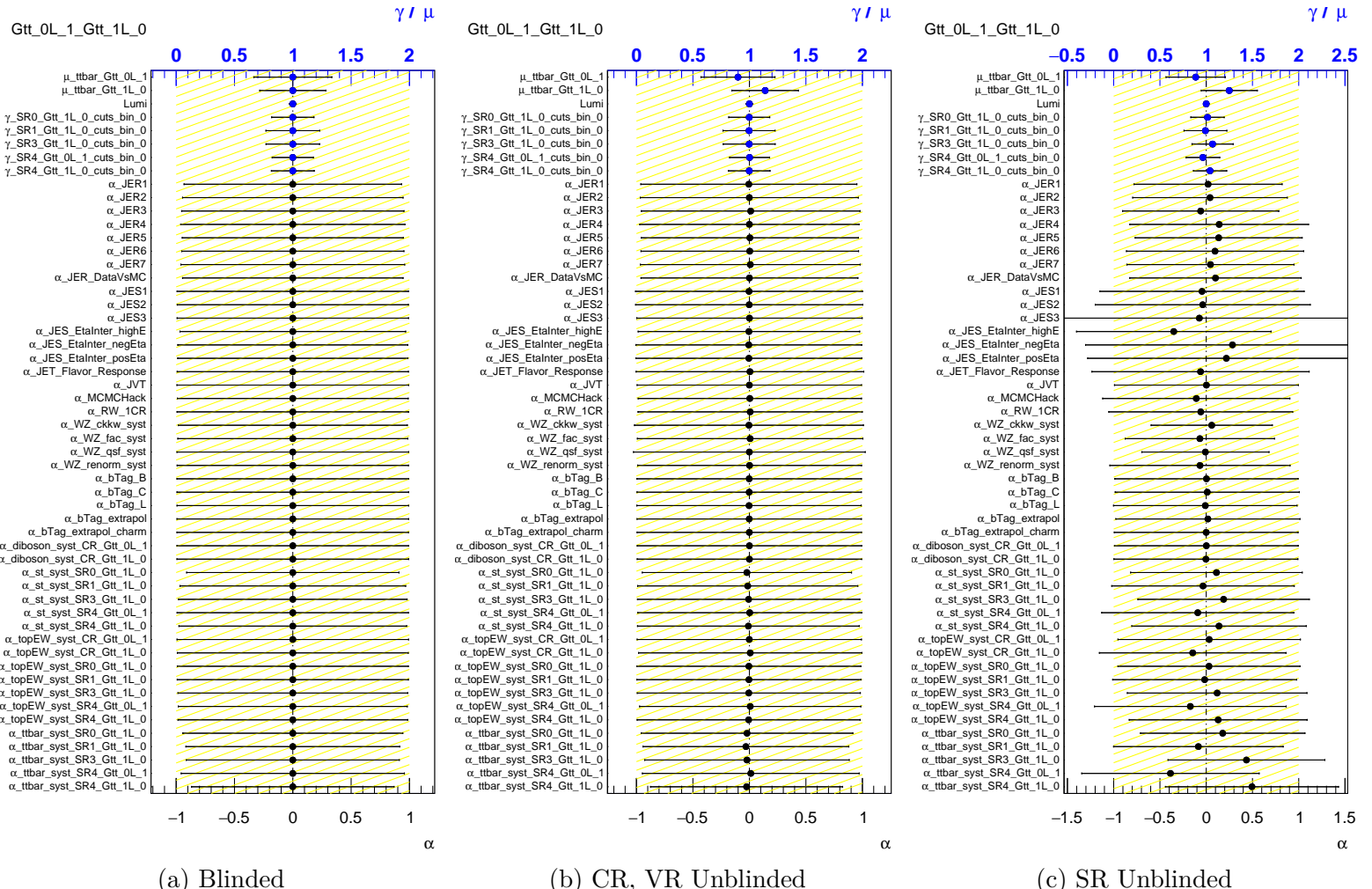


FIGURE A.30: $Gtt_0L_1_Gtt_1L_0$ fitted nuisance parameters.

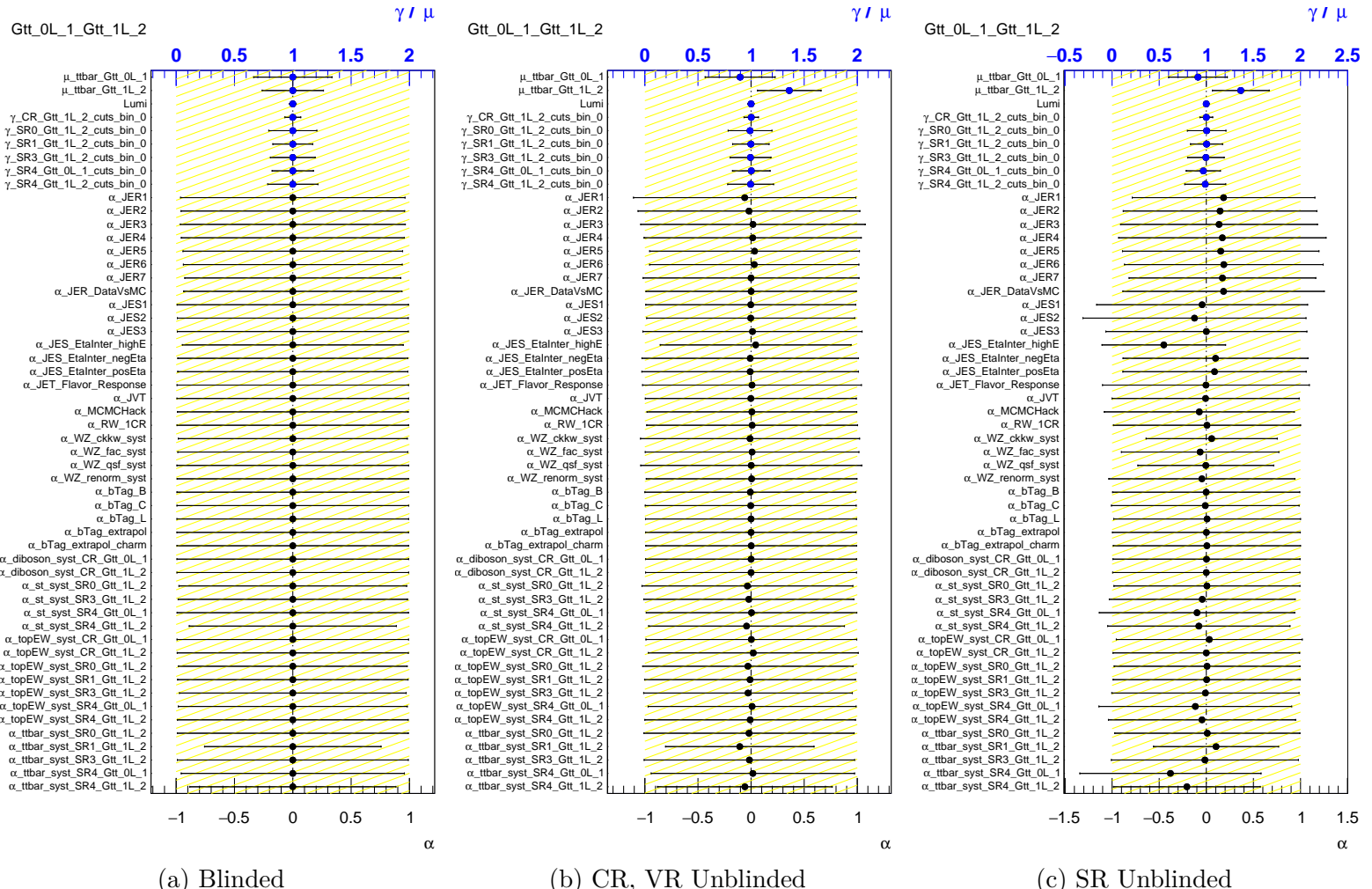
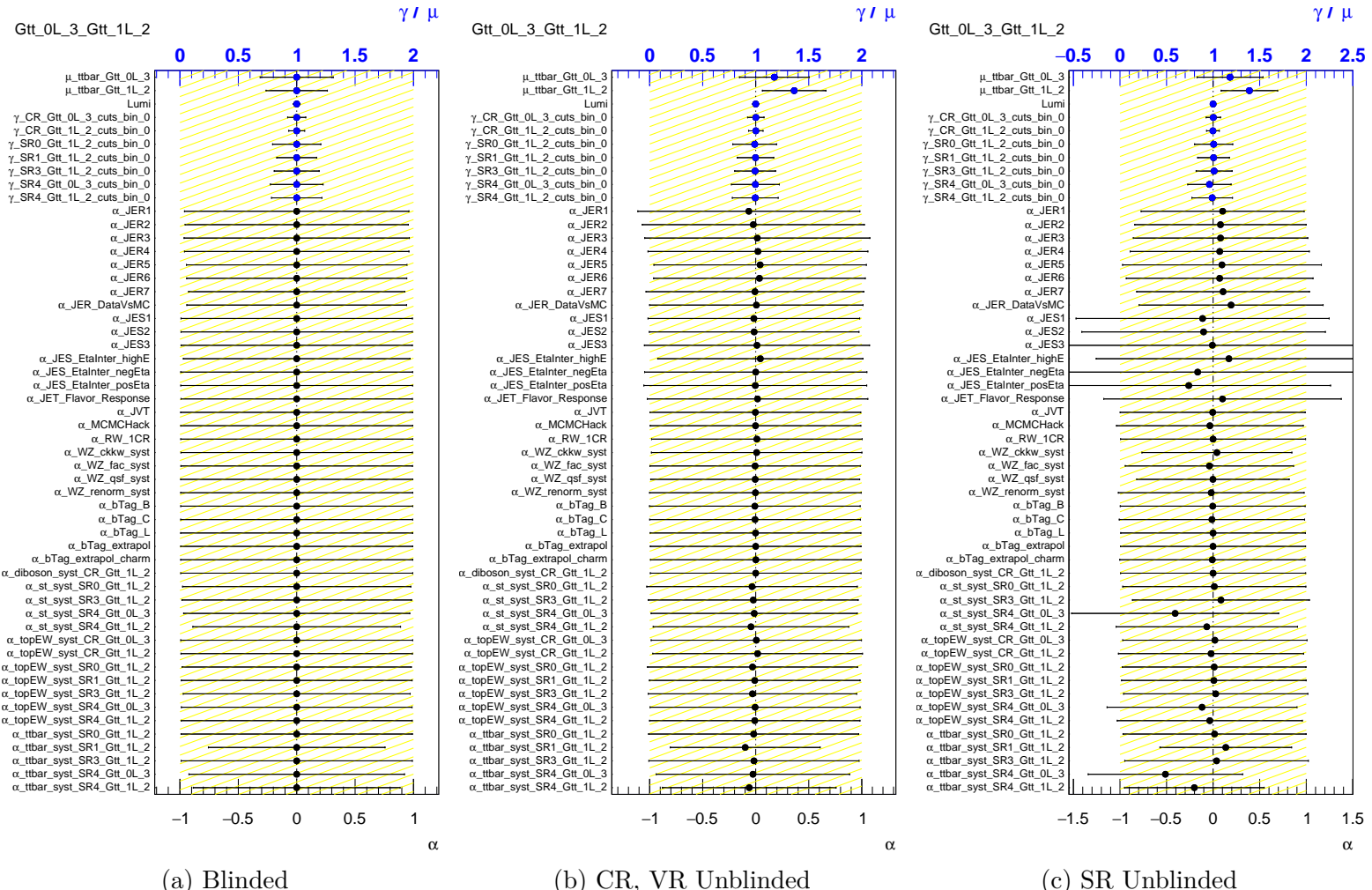
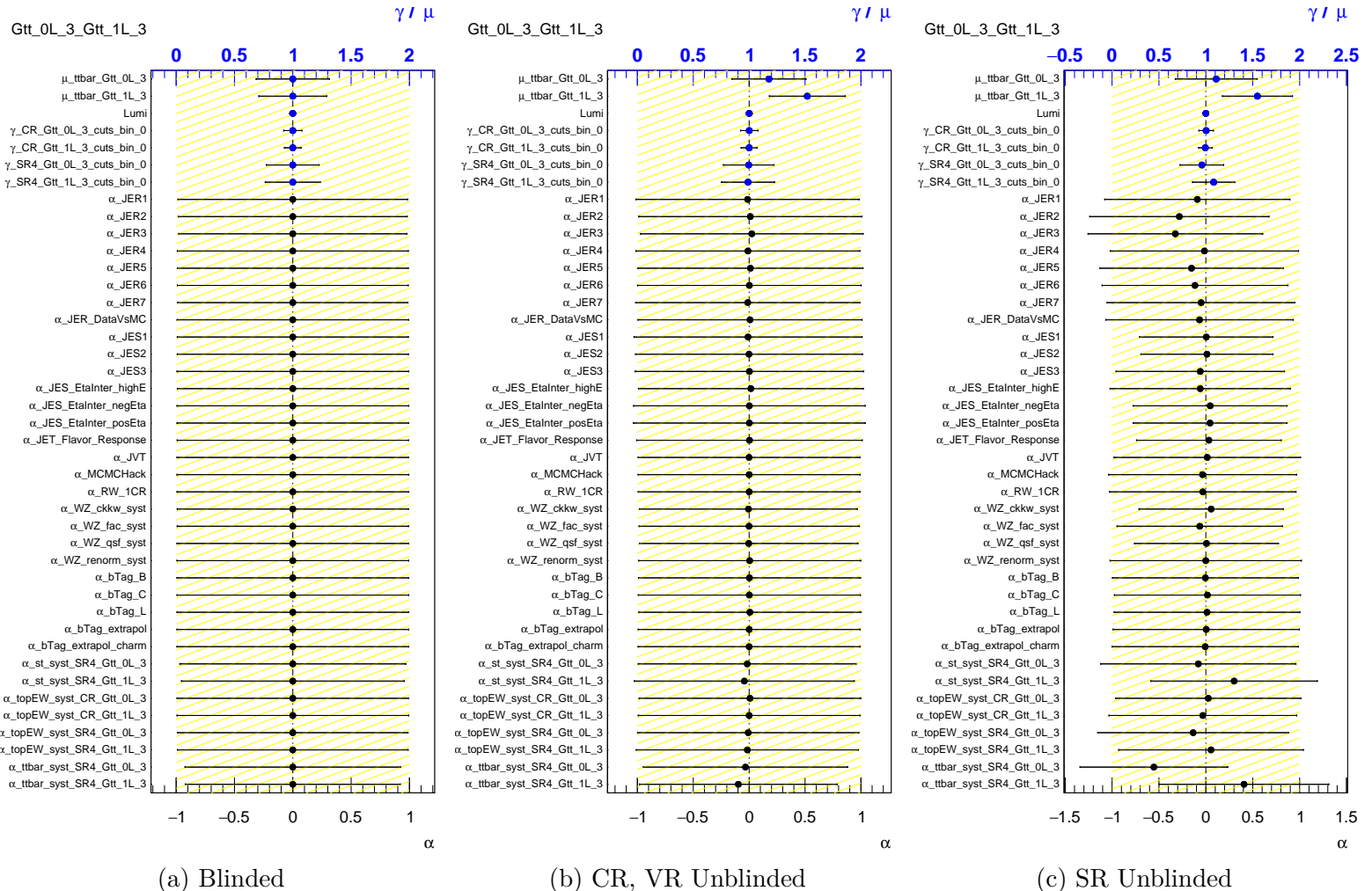


FIGURE A.31: $Gtt_0L_1_Gtt_1L_2$ fitted nuisance parameters.

FIGURE A.32: Gtt_0L_3_Gtt_1L_2 fitted nuisance parameters.

FIGURE A.33: $\text{Gtt}_0\text{L}_3 \text{Gtt}_1\text{L}_3$ fitted nuisance parameters.

A.7 Fit Construction

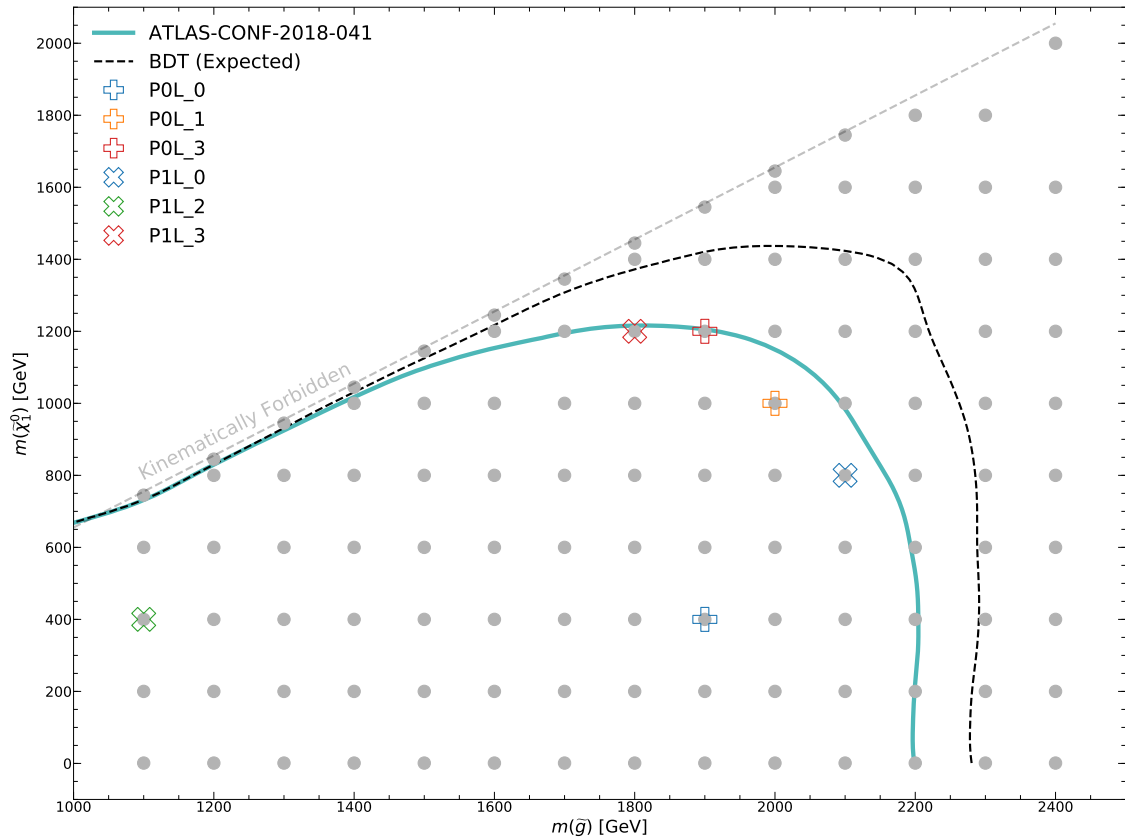
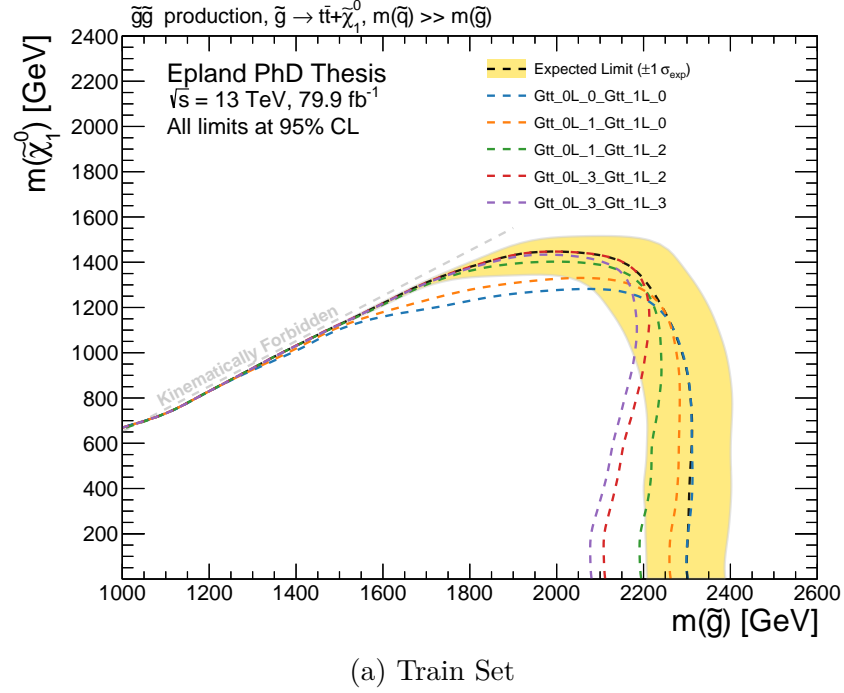
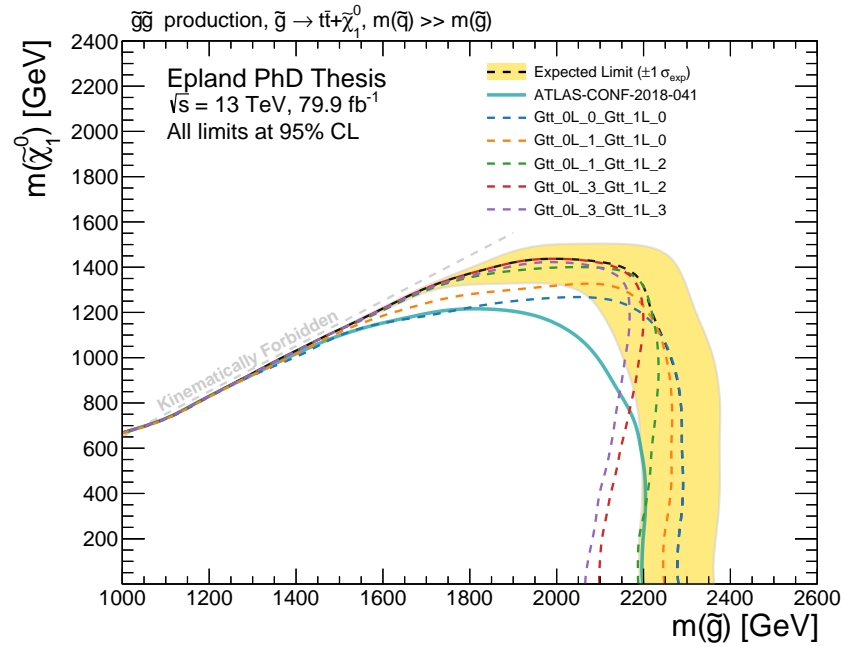


FIGURE A.34: Location of parameter points used in the final fit.



(a) Train Set



(b) Test Set

FIGURE A.35: Individual expected exclusion limits per lepton channel combination. The selected exclusion limits were chosen on the train set before unblinding with slightly different uncertainties applied, which is why Gtt_0L_3_Gtt_1L_3 does not appear to be useful in the final test set results. Note that combinations with boosted points drive the boosted limit and vice versa for compressed.

A.8 Results

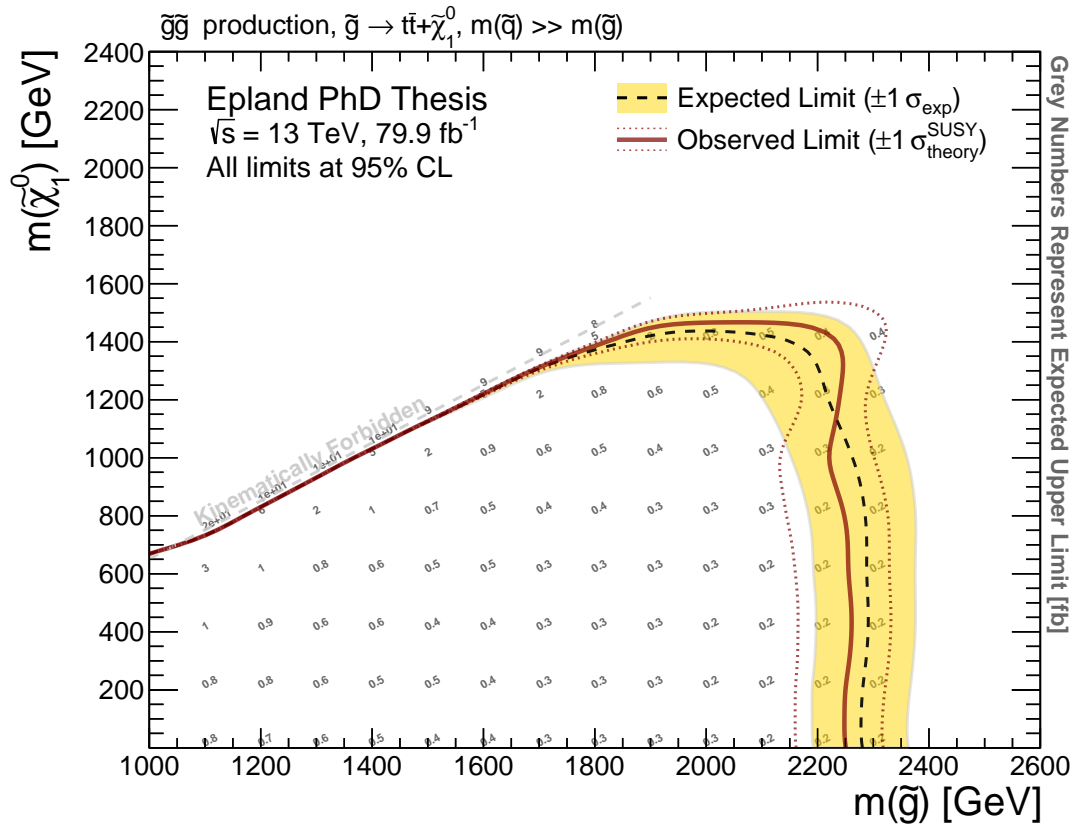


FIGURE A.36: Expected cross section limits for the 79.9 fb^{-1} BDT analysis. For the observed cross section limits see Figure 5.15b.

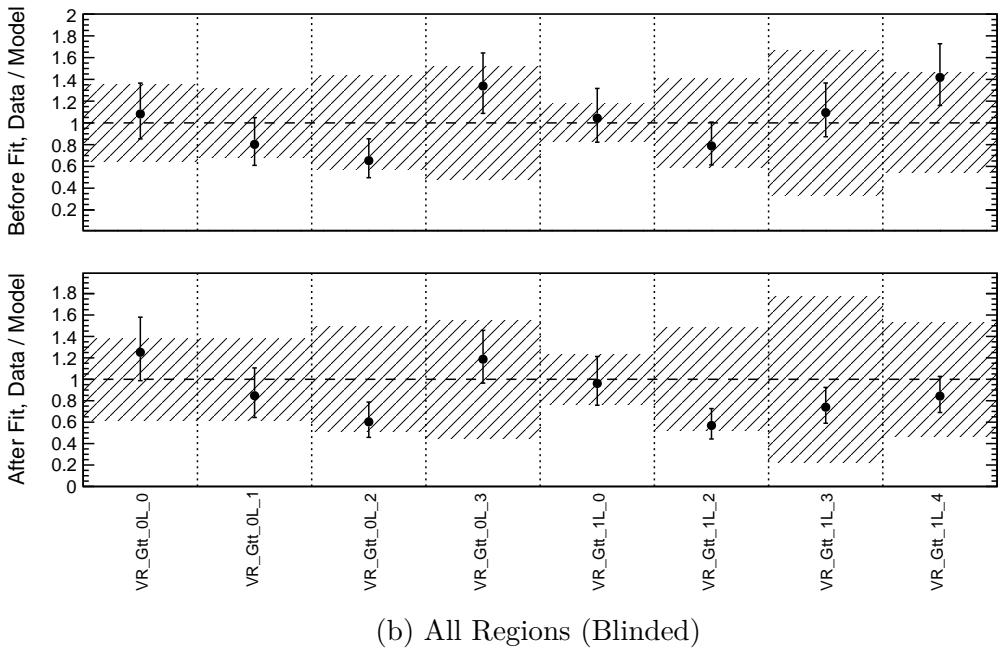
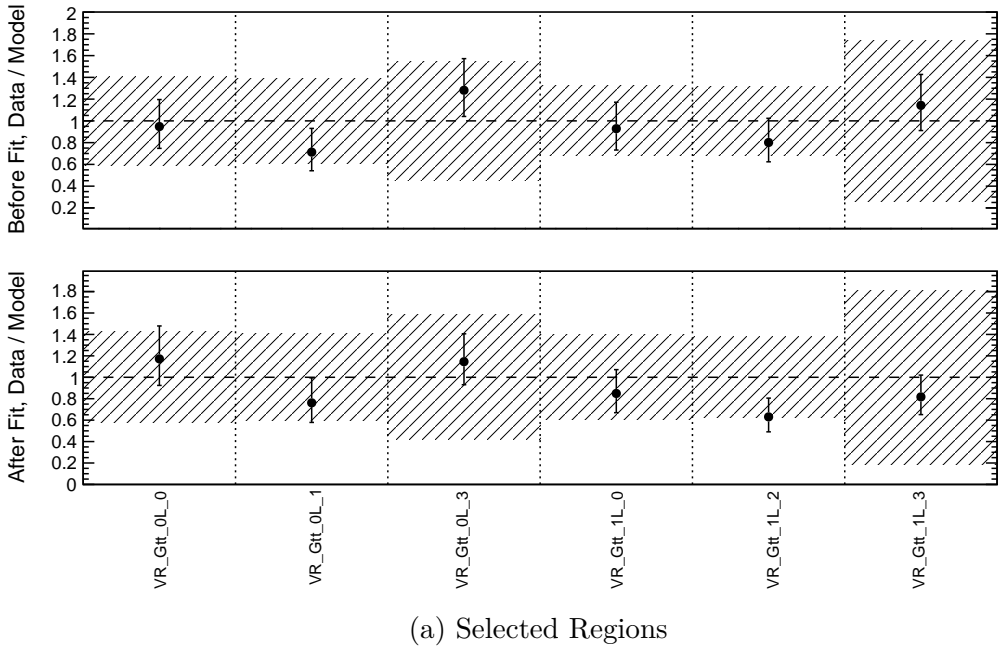


FIGURE A.37: Validation region data / MC before and after the fitted $t\bar{t}$ normalization factors are applied. Most of the selected regions showed an improvement in the agreement after the normalization factors were applied, or at least remained roughly the same. This is also seen in the validation regions which were dropped due to issues in their SR bins. Note that the blinded background fit is slightly different due to the reasons described in Section 4.4.5.

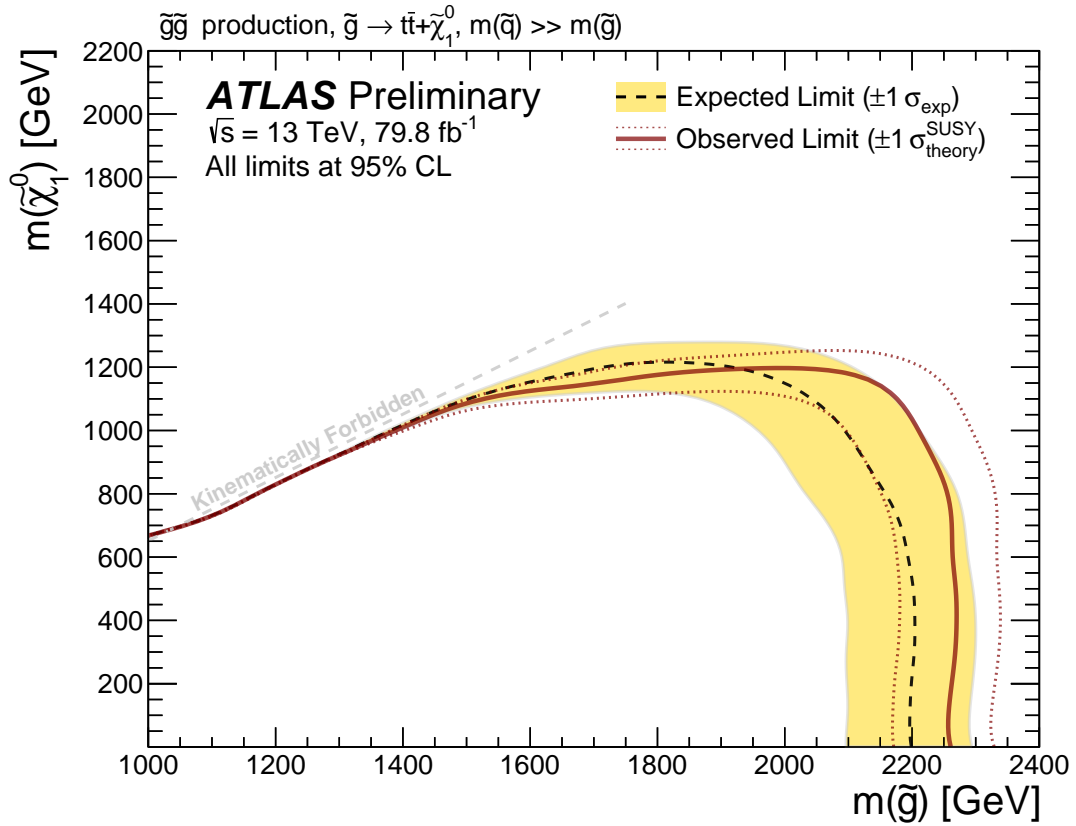


FIGURE A.38: Observed and expected exclusion limits from the standard 79.8 fb^{-1} multi- b analysis [4].

A.8.1 Individual Exclusion Limits

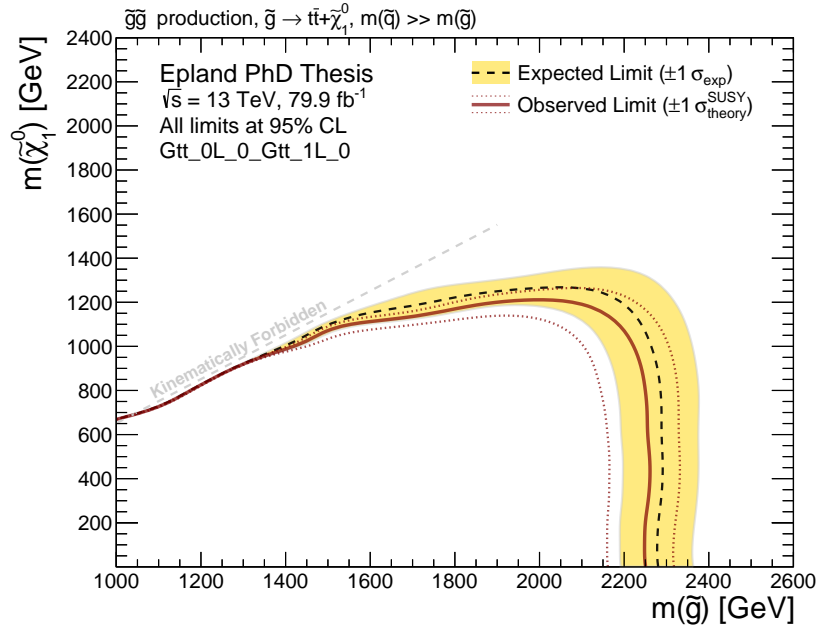


FIGURE A.39: Observed and expected exclusion limits for Gtt_0L_0_Gtt_1L_0.

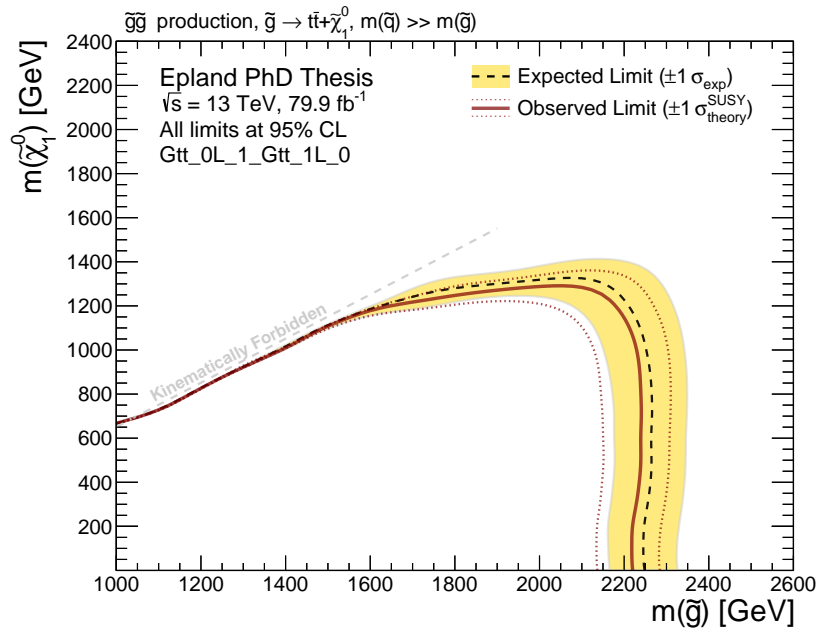


FIGURE A.40: Observed and expected exclusion limits for Gtt_0L_1_Gtt_1L_0.

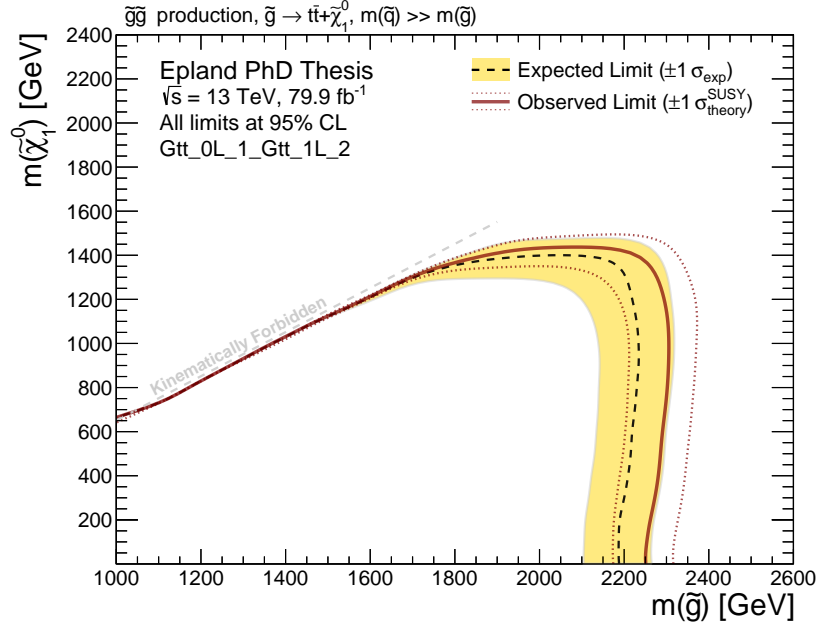


FIGURE A.41: Observed and expected exclusion limits for Gtt_0L_1_Gtt_1L_2.

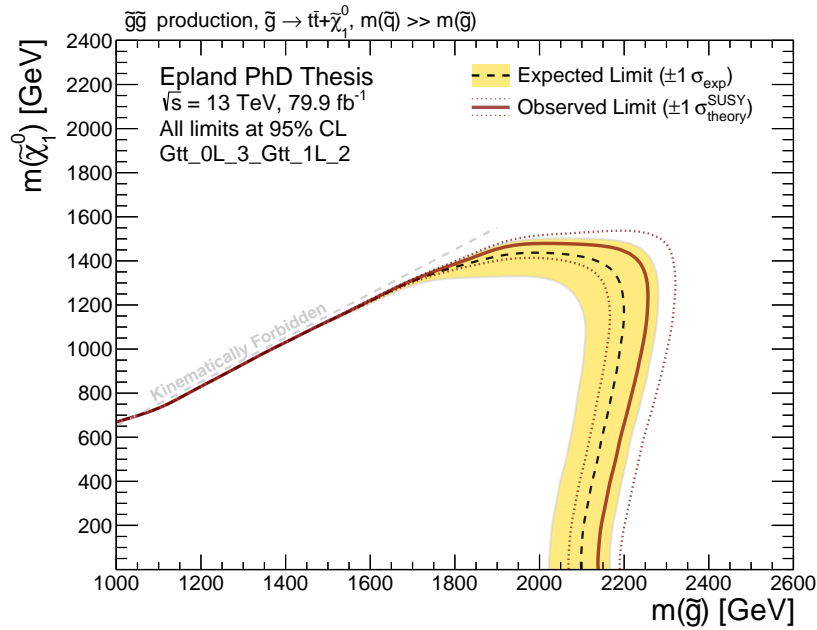


FIGURE A.42: Observed and expected exclusion limits for Gtt_0L_3_Gtt_1L_2.

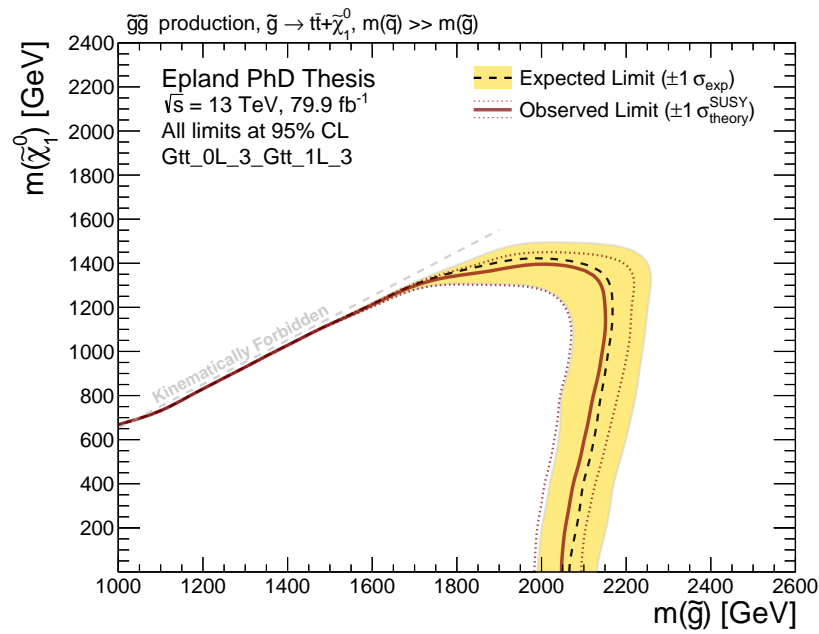


FIGURE A.43: Observed and expected exclusion limits for Gtt_0L_3_Gtt_1L_3.

A.8.2 Event Yields

Table A.6: Observed and fitted event yields for Gtt_0L_0, with MC expectations for comparison. The uncertainties shown are the statistical plus systematic, except for the SR background estimate, which is systematic only. Uncertainties on the fitted yields are symmetric by construction with any negative error truncated at zero.

	CR_Gtt_0L_0	VR_Gtt_0L_0	SR4_Gtt_0L_0
Observed events	26	22	0
Fitted background events	26.01 ± 5.51	18.77 ± 7.91	1.08 ± 0.62
Fitted $t\bar{t}$ events	14.57 ± 6.17	10.42 ± 6.94	$0.30^{+0.36}_{-0.30}$
Fitted single-top events	4.81 ± 1.94	3.37 ± 3.00	$0.19^{+0.71}_{-0.19}$
Fitted $t\bar{t} + X$ events	3.85 ± 3.04	1.66 ± 1.52	$0.39^{+0.80}_{-0.39}$
Fitted $W + \text{jets}$ events	0.98 ± 0.94	$1.89^{+2.49}_{-1.89}$	$0.13^{+0.26}_{-0.13}$
Fitted $Z + \text{jets}$ events	$1.38^{+3.58}_{-1.38}$	$1.04^{+2.70}_{-1.04}$	$0.07^{+0.20}_{-0.07}$
Fitted diboson events	0.42 ± 0.39	$0.40^{+0.76}_{-0.40}$	0.00 ± 0.00
MC exp. SM events	32.21	23.21	1.21
MC exp. $t\bar{t}$ events	20.75	14.85	0.43
MC exp. single-top events	4.81	3.37	0.19
MC exp. $t\bar{t} + X$ events	3.85	1.65	0.39
MC exp. $W + \text{jets}$ events	0.97	1.88	0.13
MC exp. $Z + \text{jets}$ events	1.41	1.06	0.08
MC exp. diboson events	0.42	0.40	0.00

Table A.7: Observed and fitted event yields for Gtt_0L_1, with MC expectations for comparison. The uncertainties shown are the statistical plus systematic, except for the SR background estimate, which is systematic only. Uncertainties on the fitted yields are symmetric by construction with any negative error truncated at zero.

	CR_Gtt_0L_1	VR_Gtt_0L_1	SR4_Gtt_0L_1
Observed events	29	17	0
Fitted background events	28.99 ± 5.56	22.32 ± 9.00	1.61 ± 1.25
Fitted $t\bar{t}$ events	17.48 ± 6.50	13.62 ± 7.47	0.53 ± 0.46
Fitted single-top events	5.32 ± 1.11	$4.52^{+4.53}_{-4.52}$	$0.19^{+0.83}_{-0.19}$
Fitted $t\bar{t} + X$ events	4.28 ± 3.38	2.13 ± 1.63	$0.49^{+0.94}_{-0.49}$
Fitted $W + \text{jets}$ events	0.76 ± 0.73	$0.65^{+0.66}_{-0.65}$	$0.10^{+0.17}_{-0.10}$
Fitted $Z + \text{jets}$ events	$1.00^{+2.69}_{-1.00}$	$0.89^{+2.42}_{-0.89}$	$0.31^{+0.93}_{-0.31}$
Fitted diboson events	$0.16^{+0.33}_{-0.16}$	$0.51^{+0.93}_{-0.51}$	0.00 ± 0.00
MC exp. SM events	31.01	23.85	1.67
MC exp. $t\bar{t}$ events	19.47	15.13	0.59
MC exp. single-top events	5.32	4.52	0.19
MC exp. $t\bar{t} + X$ events	4.28	2.14	0.48
MC exp. $W + \text{jets}$ events	0.76	0.66	0.10
MC exp. $Z + \text{jets}$ events	1.02	0.90	0.31
MC exp. diboson events	0.16	0.50	0.00

Table A.8: Observed and fitted event yields for Gtt_0L_3, with MC expectations for comparison. The uncertainties shown are the statistical plus systematic, except for the SR background estimate, which is systematic only. Uncertainties on the fitted yields are symmetric by construction with any negative error truncated at zero.

	CR_Gtt_0L_3	VR_Gtt_0L_3	SR4_Gtt_0L_3
Observed events	37	28	0
Fitted background events	36.88 ± 6.09	24.44 ± 14.20	1.24 ± 0.79
Fitted $t\bar{t}$ events	26.55 ± 7.04	17.30 ± 13.31	0.64 ± 0.58
Fitted single-top events	4.36 ± 1.98	$2.80^{+3.89}_{-2.80}$	$0.19^{+0.57}_{-0.19}$
Fitted $t\bar{t} + X$ events	3.51 ± 1.79	3.04 ± 1.73	0.27 ± 0.22
Fitted $W + \text{jets}$ events	$2.04^{+4.24}_{-2.04}$	$0.22^{+0.66}_{-0.22}$	$0.03^{+0.08}_{-0.03}$
Fitted $Z + \text{jets}$ events	$0.43^{+1.82}_{-0.43}$	$1.00^{+2.65}_{-1.00}$	$0.10^{+0.32}_{-0.10}$
Fitted diboson events	0.00 ± 0.00	$0.08^{+0.11}_{-0.08}$	0.00 ± 0.00
MC exp. SM events	32.91	21.85	1.15
MC exp. $t\bar{t}$ events	22.59	14.71	0.54
MC exp. single-top events	4.37	2.79	0.19
MC exp. $t\bar{t} + X$ events	3.50	3.04	0.27
MC exp. $W + \text{jets}$ events	2.00	0.22	0.03
MC exp. $Z + \text{jets}$ events	0.44	1.00	0.10
MC exp. diboson events	0.00	0.08	0.00

Table A.9: Observed and fitted event yields for Gtt_1L_0, with MC expectations for comparison. The uncertainties shown are the statistical plus systematic, except for the SR background estimate, which is systematic only. Uncertainties on the fitted yields are symmetric by construction with any negative error truncated at zero.

	CR_Gtt_1L_0	VR_Gtt_1L_0	SR0_Gtt_1L_0	SR1_Gtt_1L_0	SR3_Gtt_1L_0	SR4_Gtt_1L_0
Observed events	34	22	2	1	3	3
Fitted background events	34.01 ± 5.81	25.91 ± 10.25	$1.78^{+1.93}_{-1.78}$	1.04 ± 0.78	0.95 ± 0.74	1.46 ± 1.26
Fitted $t\bar{t}$ events	24.45 ± 6.60	16.98 ± 8.01	0.84 ± 0.81	0.66 ± 0.60	$0.40^{+0.55}_{-0.40}$	$0.64^{+0.84}_{-0.64}$
Fitted single-top events	4.99 ± 1.22	5.18 ± 2.05	$0.60^{+1.27}_{-0.60}$	$0.19^{+0.31}_{-0.19}$	$0.25^{+0.26}_{-0.25}$	$0.39^{+0.44}_{-0.39}$
Fitted $t\bar{t} + X$ events	4.26 ± 2.18	3.17 ± 1.96	$0.32^{+0.36}_{-0.32}$	$0.16^{+0.28}_{-0.16}$	0.29 ± 0.18	0.40 ± 0.32
Fitted $W+jets$ events	$0.22^{+0.76}_{-0.22}$	0.48 ± 0.36	$0.02^{+0.03}_{-0.02}$	$0.03^{+0.05}_{-0.03}$	0.00 ± 0.00	$0.02^{+0.03}_{-0.02}$
Fitted $Z+jets$ events	0.05 ± 0.04	$0.10^{+0.10}_{-0.10}$	0.00 ± 0.00	0.00 ± 0.00	$0.01^{+0.02}_{-0.01}$	0.00 ± 0.00
Fitted diboson events	$0.04^{+0.19}_{-0.04}$	0.00 ± 0.00				
MC exp. SM events	30.87	23.70	1.66	0.96	0.90	1.37
MC exp. $t\bar{t}$ events	21.32	14.77	0.73	0.58	0.35	0.55
MC exp. single-top events	5.00	5.18	0.60	0.19	0.25	0.39
MC exp. $t\bar{t} + X$ events	4.24	3.17	0.32	0.16	0.29	0.40
MC exp. $W+jets$ events	0.22	0.48	0.02	0.03	0.00	0.02
MC exp. $Z+jets$ events	0.05	0.10	0.00	0.00	0.01	0.00
MC exp. diboson events	0.04	0.00	0.00	0.00	0.00	0.00

Table A.10: Observed and fitted event yields for Gtt_1L_2, with MC expectations for comparison. The uncertainties shown are the statistical plus systematic, except for the SR background estimate, which is systematic only. Uncertainties on the fitted yields are symmetric by construction with any negative error truncated at zero.

	CR_Gtt_1L_2	VR_Gtt_1L_2	SR0_Gtt_1L_2	SR1_Gtt_1L_2	SR3_Gtt_1L_2	SR4_Gtt_1L_2
Observed events	42	20	2	2	2	1
Fitted background events	42.00 ± 6.46	31.72 ± 11.98	2.19 ± 1.47	$1.45^{+1.48}_{-1.45}$	1.17 ± 0.83	1.76 ± 1.65
Fitted $t\bar{t}$ events	33.87 ± 7.00	24.65 ± 11.75	1.21 ± 0.82	$1.11^{+1.58}_{-1.11}$	$0.59^{+0.81}_{-0.59}$	$0.86^{+1.06}_{-0.86}$
Fitted single-top events	4.04 ± 1.04	3.37 ± 1.55	$0.41^{+0.76}_{-0.41}$	0.00 ± 0.00	$0.11^{+0.35}_{-0.11}$	$0.55^{+1.22}_{-0.55}$
Fitted $t\bar{t} + X$ events	3.83 ± 2.16	3.51 ± 1.89	$0.57^{+0.81}_{-0.57}$	$0.34^{+0.46}_{-0.34}$	$0.47^{+0.48}_{-0.47}$	0.33 ± 0.31
Fitted W +jets events	$0.13^{+0.44}_{-0.13}$	$0.11^{+0.27}_{-0.11}$	0.00 ± 0.00	0.00 ± 0.00	0.00 ± 0.00	$0.02^{+0.04}_{-0.02}$
Fitted Z +jets events	0.05 ± 0.04	$0.08^{+0.12}_{-0.08}$	0.00 ± 0.00	0.00 ± 0.00	0.00 ± 0.00	0.00 ± 0.00
Fitted diboson events	$0.07^{+0.12}_{-0.07}$	0.00 ± 0.00				
MC exp. SM events	32.72	24.96	1.85	1.15	1.01	1.52
MC exp. $t\bar{t}$ events	24.58	17.90	0.88	0.81	0.43	0.62
MC exp. single-top events	4.05	3.36	0.40	0.00	0.11	0.54
MC exp. $t\bar{t} + X$ events	3.84	3.51	0.57	0.34	0.47	0.34
MC exp. W +jets events	0.13	0.11	0.00	0.00	0.00	0.02
MC exp. Z +jets events	0.05	0.08	0.00	0.00	0.00	0.00
MC exp. diboson events	0.07	0.00	0.00	0.00	0.00	0.00

Table A.11: Observed and fitted event yields for Gtt_1L_3, with MC expectations for comparison. The uncertainties shown are the statistical plus systematic, except for the SR background estimate, which is systematic only. Uncertainties on the fitted yields are symmetric by construction with any negative error truncated at zero.

	CR_Gtt_1L_3	VR_Gtt_1L_3	SR4_Gtt_1L_3
Observed events	45	24	4
Fitted background events	45.02 ± 6.69	29.36 ± 23.88	1.62 ± 0.99
Fitted $t\bar{t}$ events	35.78 ± 7.35	24.17 ± 23.27	0.88 ± 0.81
Fitted single-top events	5.59 ± 3.65	$2.00^{+3.22}_{-2.00}$	$0.44^{+0.64}_{-0.44}$
Fitted $t\bar{t} + X$ events	3.55 ± 2.54	3.05 ± 1.74	$0.27^{+0.38}_{-0.27}$
Fitted $W + \text{jets}$ events	$0.10^{+0.29}_{-0.10}$	$0.08^{+0.25}_{-0.08}$	$0.02^{+0.04}_{-0.02}$
Fitted $Z + \text{jets}$ events	0.00 ± 0.00	$0.06^{+0.11}_{-0.06}$	0.00 ± 0.00
Fitted diboson events	0.00 ± 0.00	0.00 ± 0.00	0.00 ± 0.00
MC exp. SM events	32.72	21.00	1.31
MC exp. $t\bar{t}$ events	23.47	15.84	0.58
MC exp. single-top events	5.59	1.97	0.44
MC exp. $t\bar{t} + X$ events	3.56	3.04	0.27
MC exp. $W + \text{jets}$ events	0.09	0.08	0.02
MC exp. $Z + \text{jets}$ events	0.00	0.06	0.00
MC exp. diboson events	0.00	0.00	0.00

A.8.3 Expectation Limit Changes When Unblinding

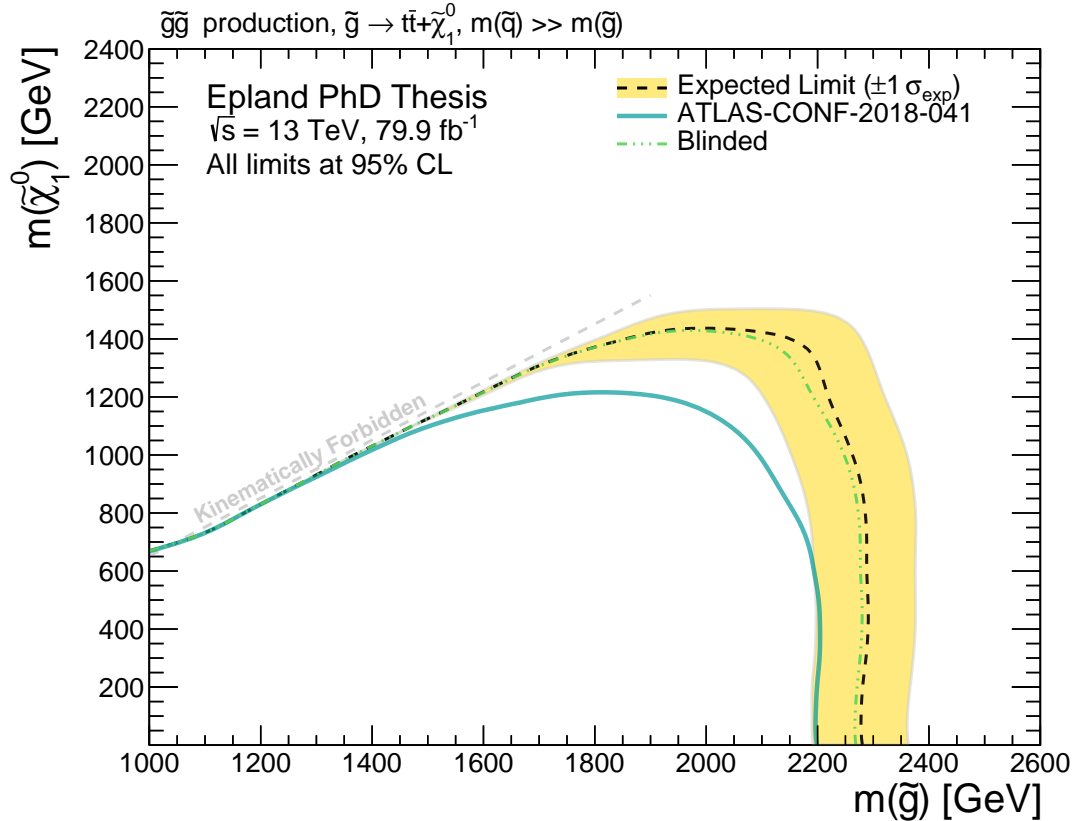


FIGURE A.44: Expected exclusion limits with blinded and unblinded SRs. As mentioned in Section 4.4.5 the expected exclusion limits indirectly depend on the observed data in the SRs through the profiled nuisance parameters. Here the expected exclusion limit improved by $\approx 5\text{--}25$ GeV when unblinded.

A.9 Overfitting Studies

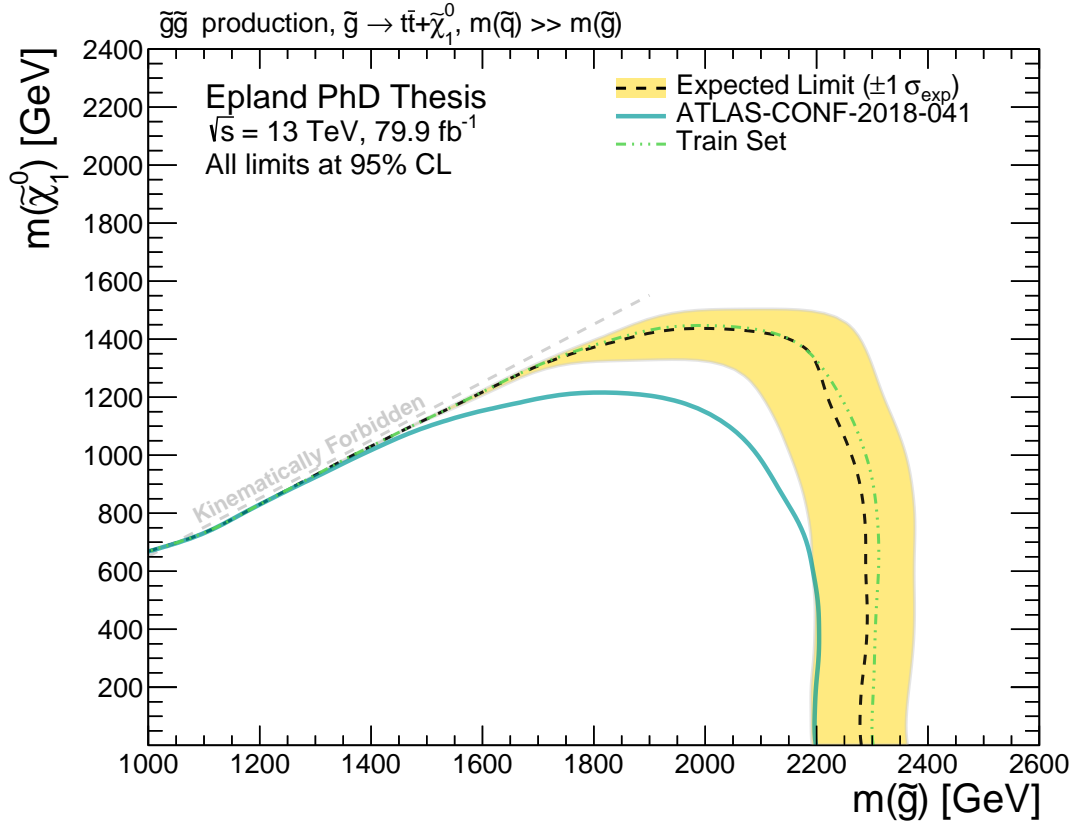


FIGURE A.45: Change in the expected exclusion limit between the train and test sets. Only a minor decrease of ≈ 25 GeV was found when moving to the test set, strong evidence that overfitting is not an issue with this analysis as all training and region building was performed on the train set.

Table A.12: 5-fold cross-validation results obtained by training the BDT multiple times on different combinations of folds. Here “physical” is calculated with the real MC event weights, while “training” is calculated with the reweighted training event weights which balance signal and background. The relatively small standard deviations give some confidence that the nominal model is likely not overfitted.

Metric	Mean \pm St. Dev.
Best Iteration	191 \pm 8
Best Score	0.05752 \pm 0.00029
Training Time (min)	1.95 \pm 0.06
Accuracy (Physical)	0.43388 \pm 0.00356
Accuracy (Training)	0.65297 \pm 0.00293
Sig Accuracy (Physical)	0.18029 \pm 0.00504
Bkg Accuracy (Physical)	0.99991 \pm 0.00003
Sig Accuracy (Training)	0.30604 \pm 0.00587
Bkg Accuracy (Training)	0.99991 \pm 0.00003

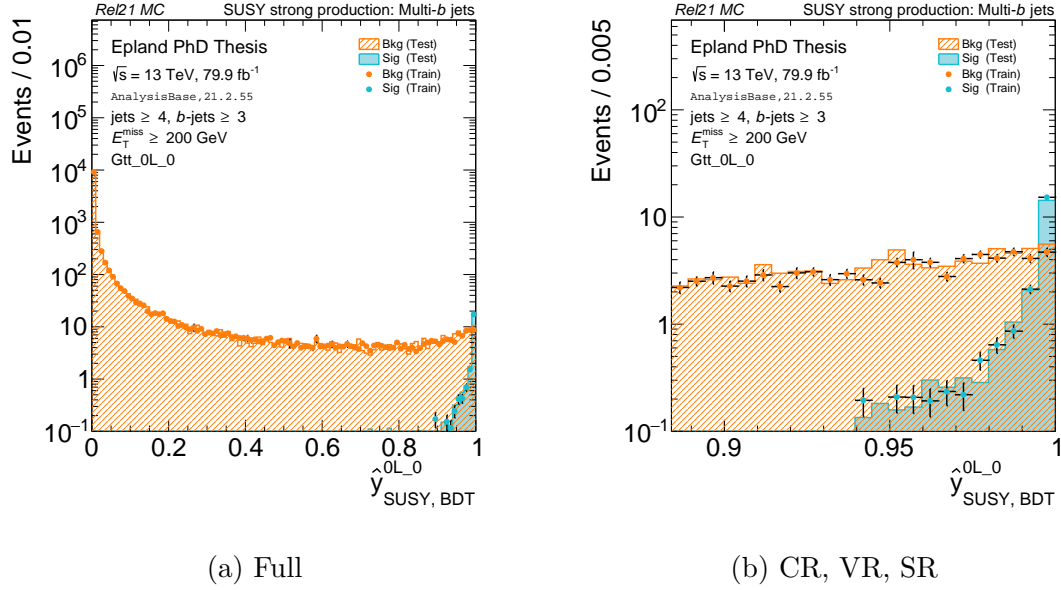


FIGURE A.46: Comparison of \hat{y} in the test and train sets for Gtt_0L_0.

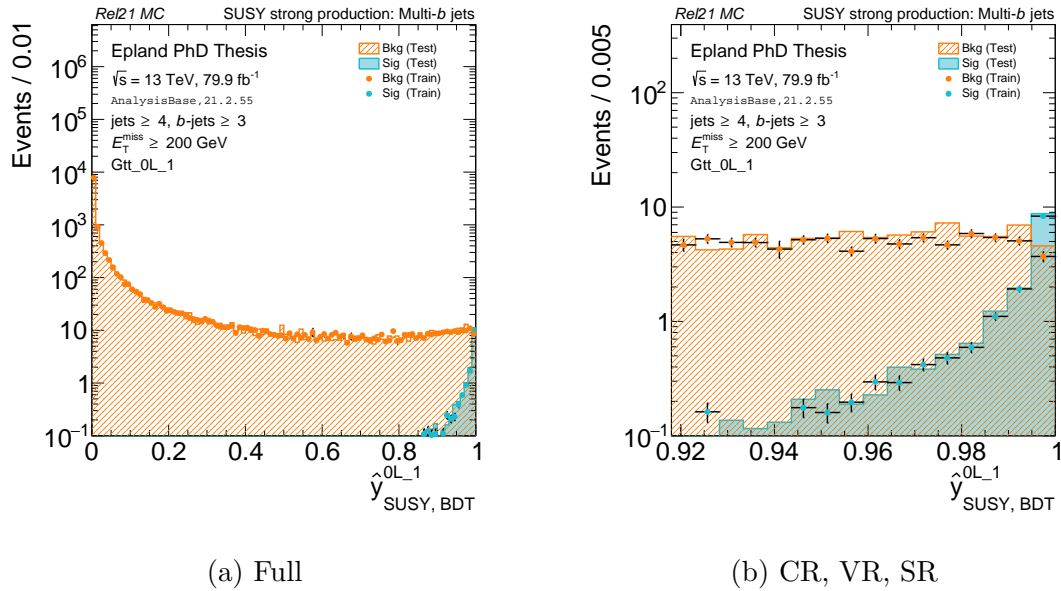


FIGURE A.47: Comparison of \hat{y} in the test and train sets for Gtt_0L_1.

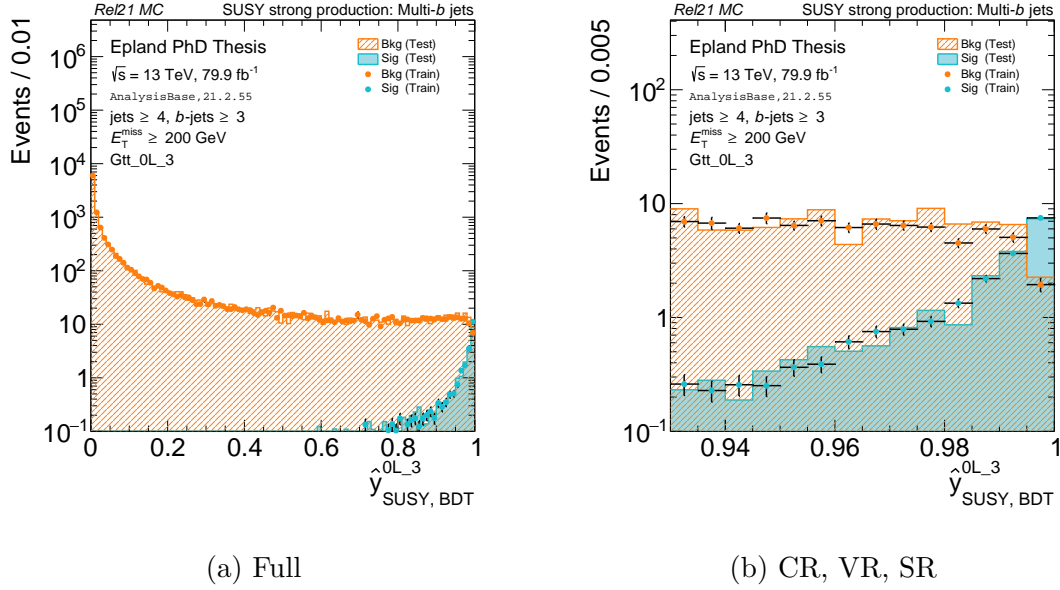


FIGURE A.48: Comparison of \hat{y} in the test and train sets for Gtt_0L_3.

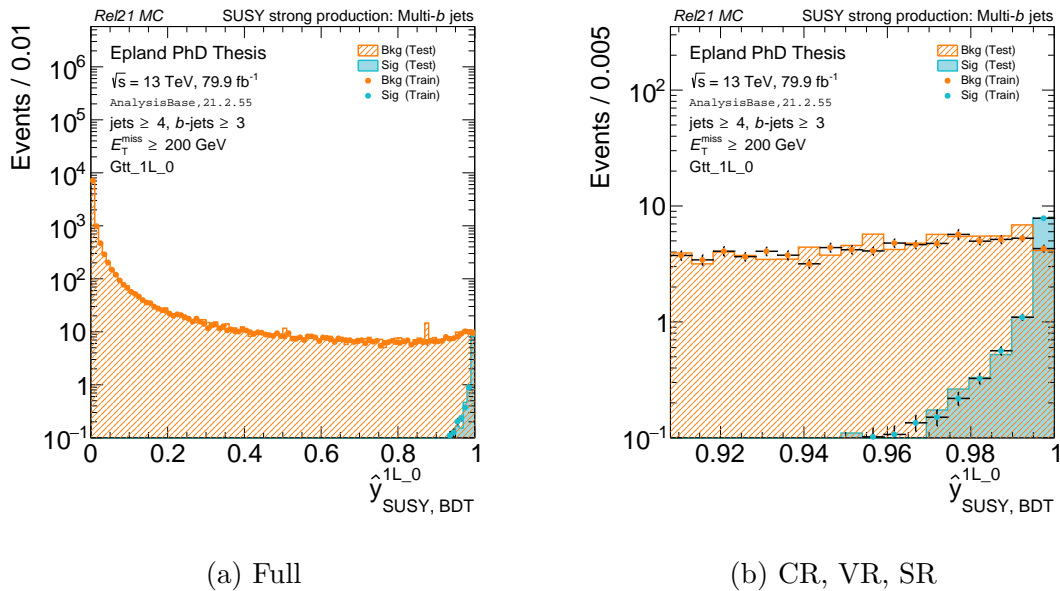


FIGURE A.49: Comparison of \hat{y} in the test and train sets for Gtt_1L_0.

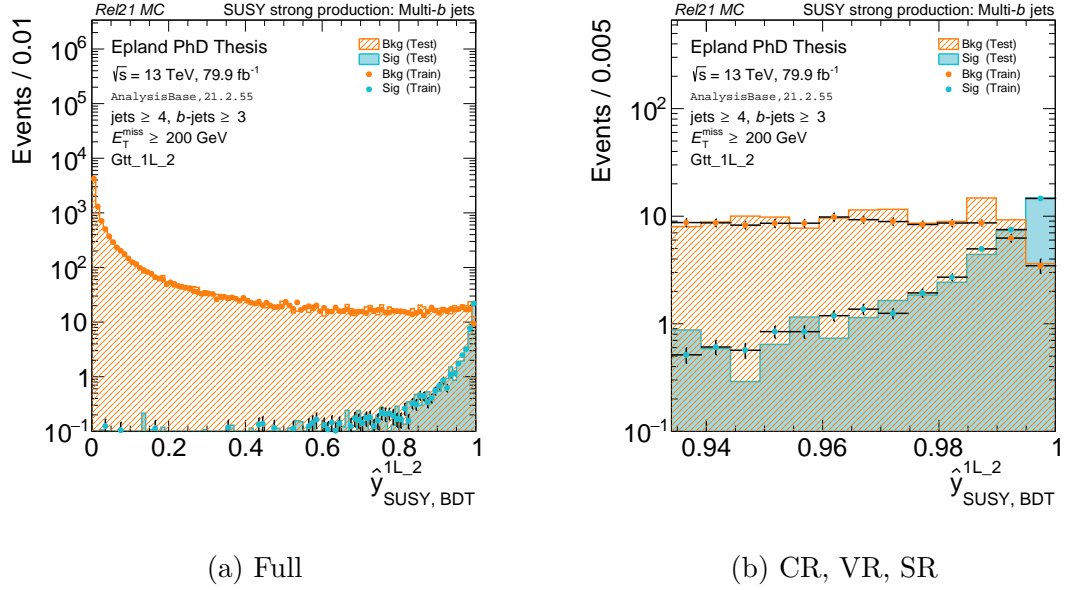


FIGURE A.50: Comparison of \hat{y} in the test and train sets for Gtt_1L_2.

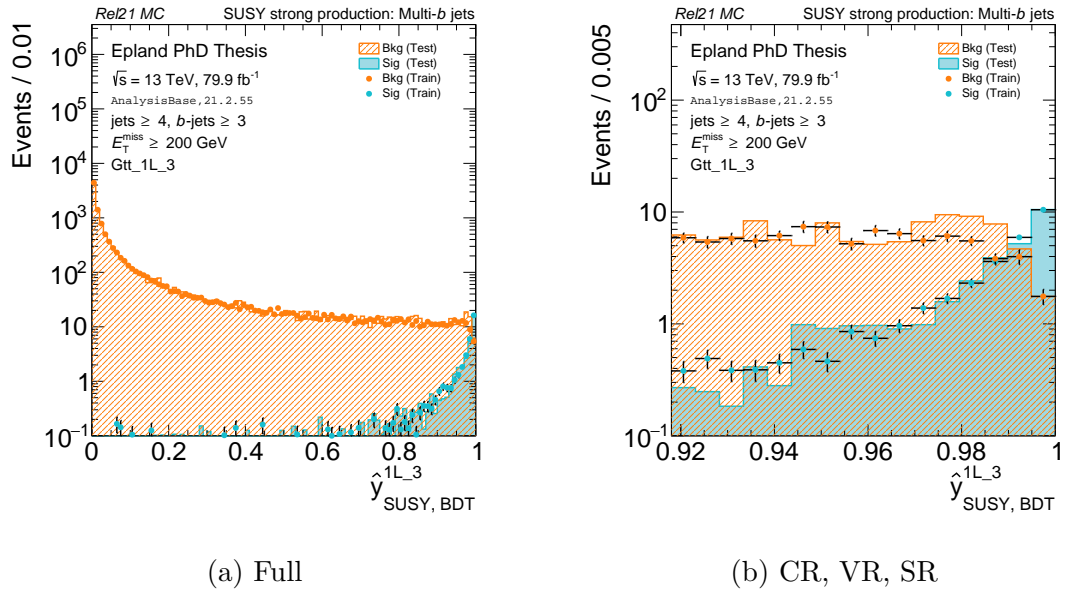


FIGURE A.51: Comparison of \hat{y} in the test and train sets for Gtt_1L_3.

A.10 Input Variables

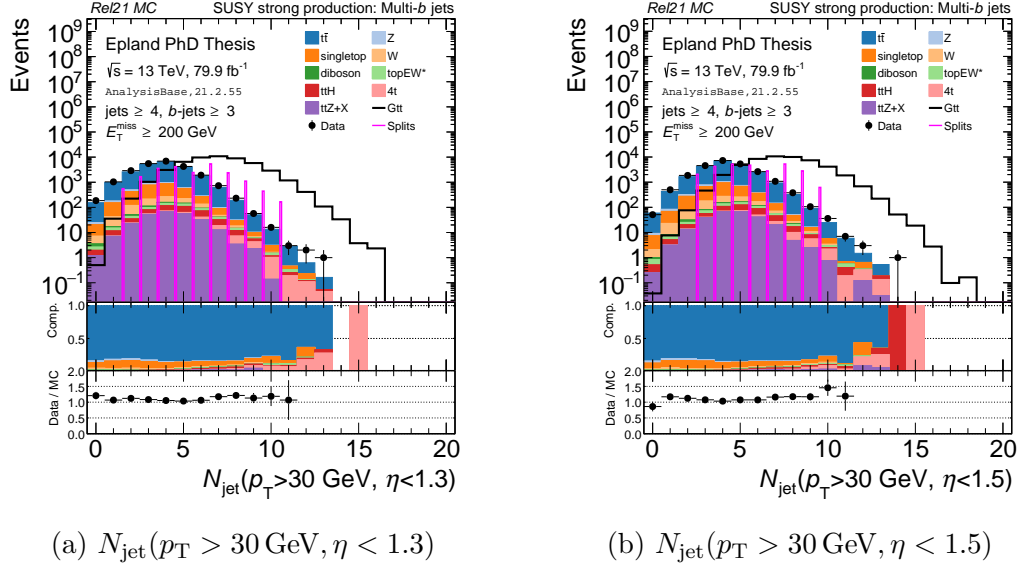


FIGURE A.52: $N_{\text{jet}}(p_{\text{T}} > 30 \text{ GeV}, \eta < 1.3)$ and $N_{\text{jet}}(p_{\text{T}} > 30 \text{ GeV}, \eta < 1.5)$ in data & MC with BDT split values.

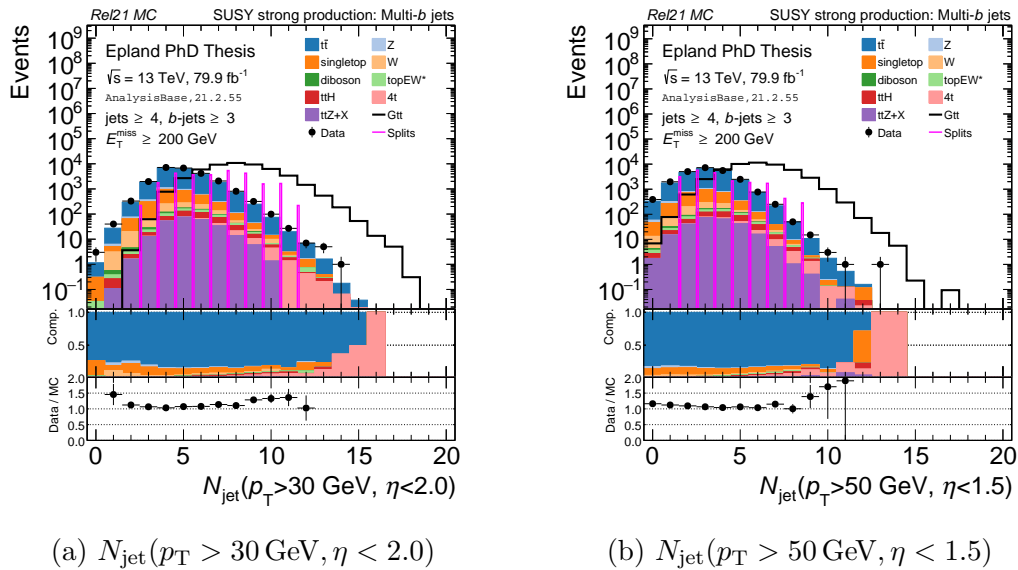


FIGURE A.53: $N_{\text{jet}}(p_{\text{T}} > 30 \text{ GeV}, \eta < 2.0)$ and $N_{\text{jet}}(p_{\text{T}} > 50 \text{ GeV}, \eta < 1.5)$ in data & MC with BDT split values.

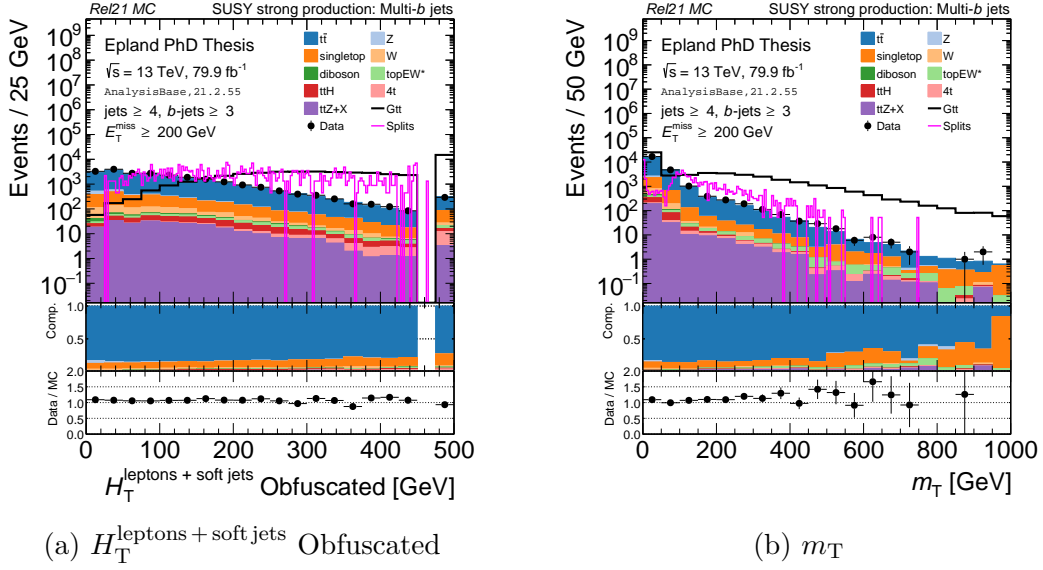


FIGURE A.54: $H_T^{\text{leptons} + \text{soft jets}}$ Obfuscated and m_T in data & MC with BDT split values.

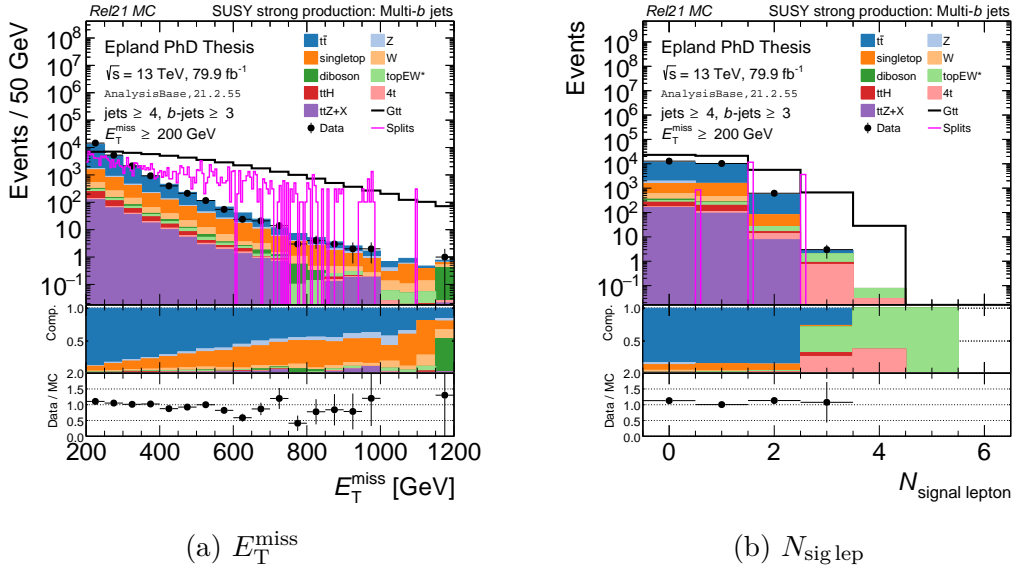


FIGURE A.55: E_T^{miss} and $N_{\text{sig lep}}$ in data & MC with BDT split values.

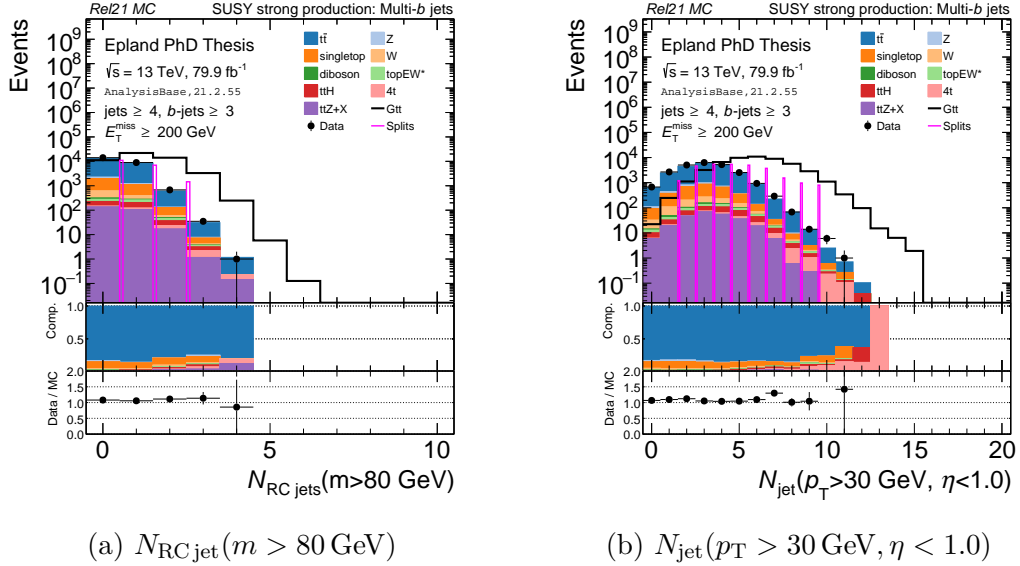


FIGURE A.56: $N_{\text{RCjet}}(m > 80 \text{ GeV})$ and $N_{\text{jet}}(p_{\text{T}} > 30 \text{ GeV}, \eta < 1.0)$ in data & MC with BDT split values.

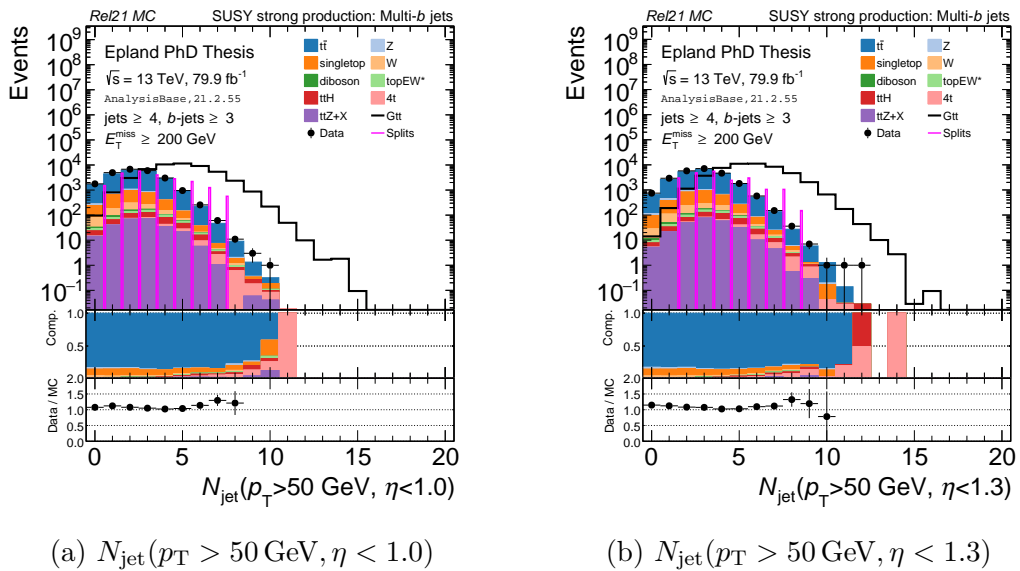


FIGURE A.57: $N_{\text{jet}}(p_{\text{T}} > 50 \text{ GeV}, \eta < 1.0)$ and $N_{\text{jet}}(p_{\text{T}} > 50 \text{ GeV}, \eta < 1.3)$ in data & MC with BDT split values.

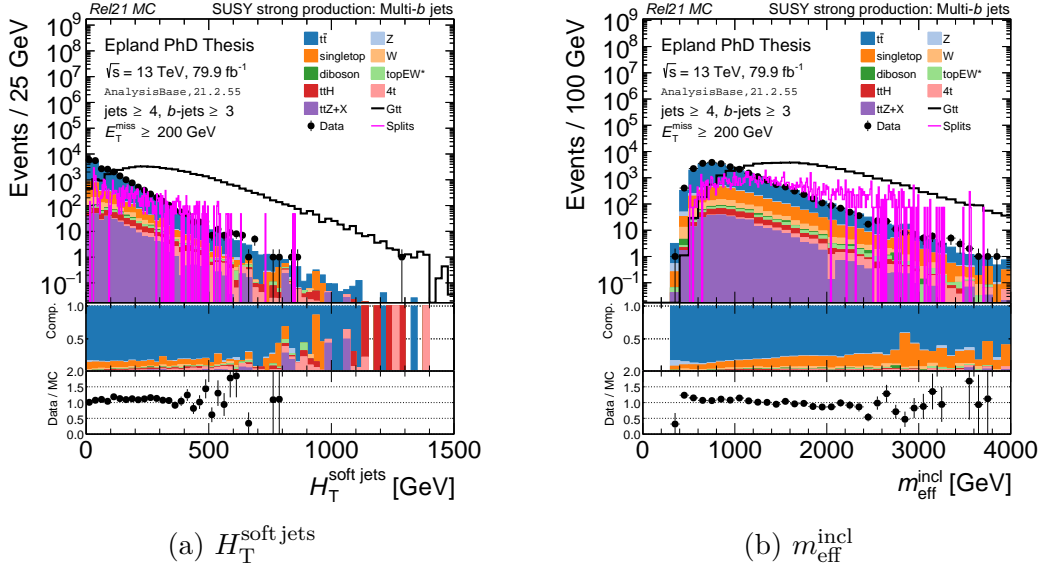


FIGURE A.58: $H_T^{\text{soft jets}}$ and $m_{\text{eff}}^{\text{incl}}$ in data & MC with BDT split values.

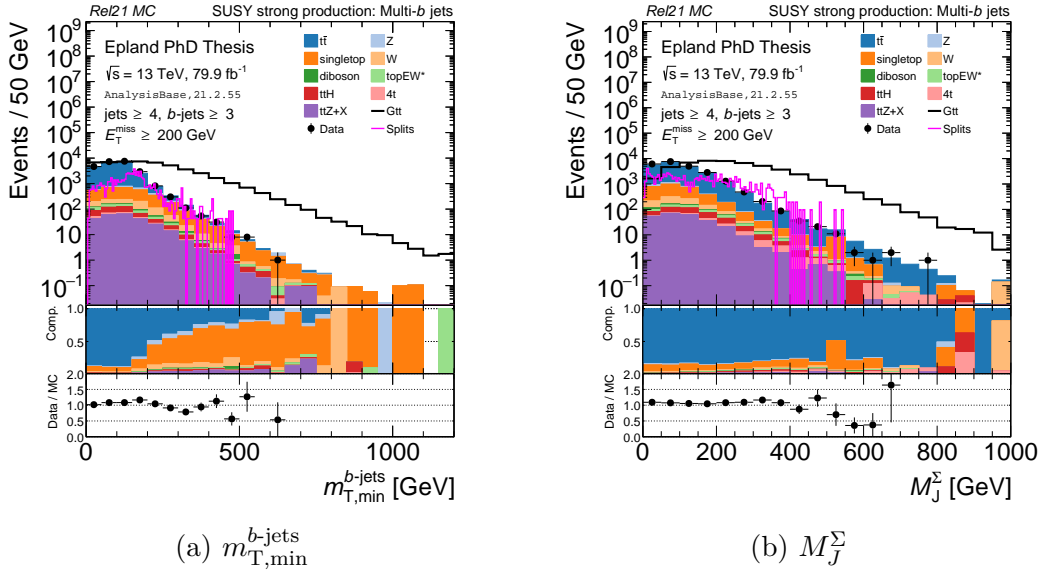


FIGURE A.59: $m_T^{b\text{-jets}}$ and M_J^Σ in data & MC with BDT split values.

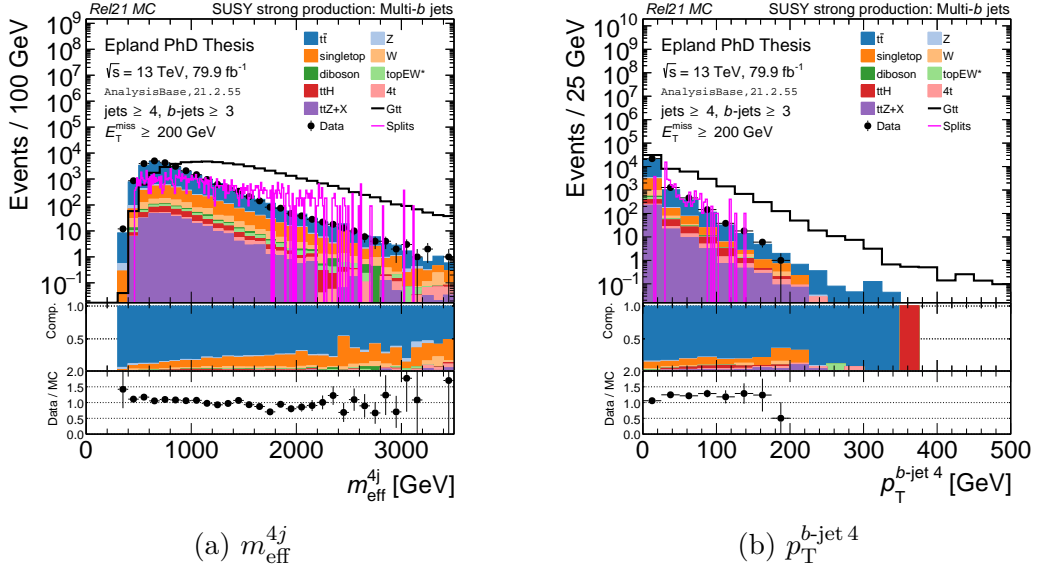


FIGURE A.60: m_{eff}^{4j} and $p_T^{b\text{-jet } 4}$ in data & MC with BDT split values.

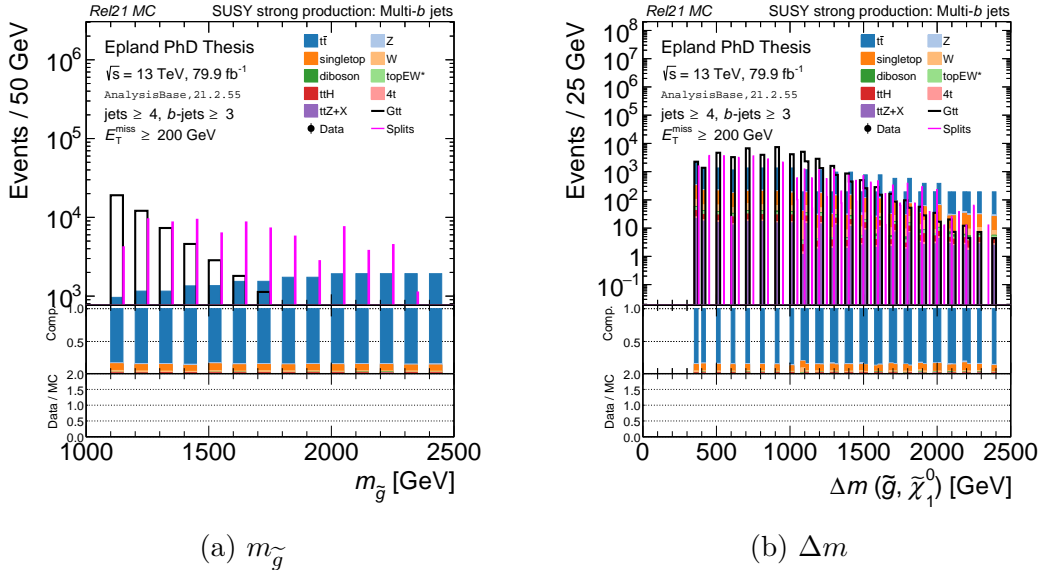


FIGURE A.61: $m_{\tilde{g}}$ and Δm in MC with BDT split values.

Appendix B

Maximum Performance Studies

The exact extent of the multi- b search’s exclusion limit is a function of many factors, which can be broadly grouped into two categories: cross section dependent and analysis dependent. The SM background and predicted Gtt production cross sections are fixed by theory, setting unavoidable constraints on the ratio of signal to background events available for measurement at any particular mass point. Of course, the total number of events at each point is a function of the detector’s integrated luminosity, but realistically this is also limited by time and funding. Taken together, then there is effectively some theoretical maximum exclusion limit attainable from the collected dataset.

In practice, a fraction of signal events will not be recorded by the detector or will otherwise fail to pass the triggers and preselections.¹ Additionally, a perfect signal background classifier does not exist² and systematic uncertainties must be incorporated. Within these experimental constraints we are free to optimize the

¹ The preselection efficiency is provided in Figure A.1.

² You will always be somewhere along a ROC curve making a tradeoff between false positives and false negatives.

analysis as best we can; by using a BDT, adjusting signal regions, trying to reduce systematics, *etc.*

It is straight forward to compare different analysis methods on the same channel and dataset, as is done in Figure 5.14a, to find their relative performance, but this does not show how close we are to the theoretical maximum performance. For example, while the BDT made noticeable gains over the standard analysis in the expected exclusion limit, is it brushing up on a statistical limit — or could a better classifier take things further?

One approach to answering this question is to grant the BDT 100 % signal efficiency, after trigger and preselection losses, by creating a “synthetic” output score which is always $\hat{y}_{\text{SUSY, BDT}} = 1.0$ for true Gtt MC events. This will force every Gtt signal event to appear in the top SR bin, artificially boosting the significance. The background event \hat{y} scores, fit regions, systematics, and everything else remain the same from the regular BDT analysis to keep some background events in the signal region for normalization, thereby helping control the systematic uncertainties.

Running on the train set we find that the resulting synthetic limit is only ≈ 100 GeV (≈ 200 GeV) beyond the expected limit in the boosted (compressed) region as displayed in Figure B.1. While these results are only a first attempt, it is encouraging to see that the BDT is already so close to the estimated maximum performance. The upper limit is also useful as a benchmark of indicating where the BDT’s performance could be pushed further, for example, by creating new variables targeting a specific region in phase space. Future work could expand on this approach by altering the triggers and preselections, implementing a more realistic, but still optimistic, ROC curve for the signal and background efficiencies, and optimizing the amount of background allowed into the signal regions.

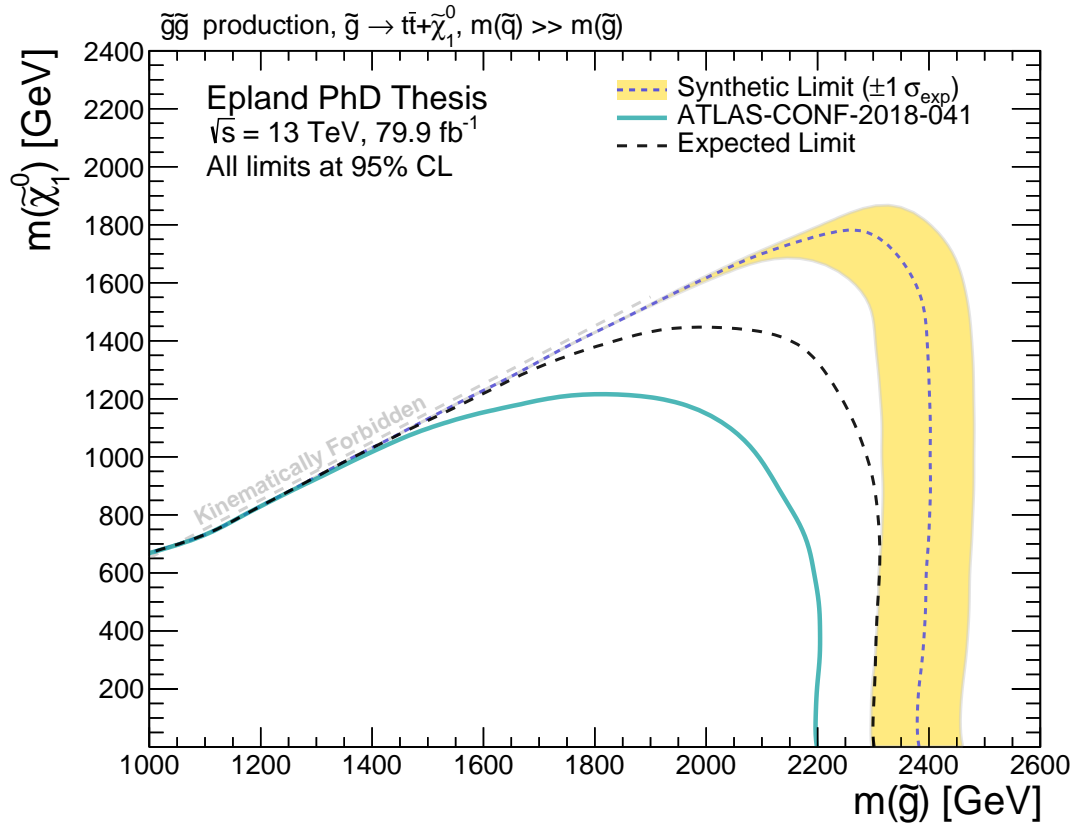


FIGURE B.1: Expected “synthetic” exclusion limit of the BDT analysis on the train set. The synthetic limit with boosted signal efficiency is only ≈ 100 GeV (≈ 200 GeV) beyond the expected BDT limit in the boosted (compressed) region.

Appendix C

The Look Elsewhere Effect

The look elsewhere effect [169, 213, 214, 215] is the term used by particle physicists to describe how a search’s expected significance in any particular location of parameter space relates to the significance over a wide range of parameter space. In essence, if we do not know the mass of a hypothesized particle *a priori* and must look for it everywhere, we are bound to see some apparently significant results just from statistical fluctuations. For example, if you make 100 hypothesis tests at different masses with a p -value threshold of only 0.05, you should expect to disprove a background-only null hypothesis in 5 tests just by chance alone! This is one motivation behind requiring such an extremely small p -value of only 2.87×10^{-7} to claim a discovery at 5σ .

Statistical techniques can be used to convert the local significance of a search to a global significance of discovery. This is fairly common practice for one-dimensional mass spectrum bump searches, such as the diboson resonance search [216]. In multidimensional SUSY searches, such as the Gtt search of this dissertation, the look elsewhere effect is of less concern as the model dependent exclusion limits are created by disproving a different null SUSY signal hypothesis at each mass parameter

point, rather than a single null SM background hypothesis everywhere. As such, the profile-likelihood statistics used in `HISTFITTER` make no explicit corrections for the look elsewhere effect. However, it is still a relevant statistical effect to keep in mind while designing signal regions, or if the search is changed to a model-independent discovery framework.

Appendix D

Pseudocode

D.1 Z_B

```
1 # NumPy/SciPy port of the RooStats function 'BinomialExpZ' by Louis-Guillaume Gagnon
2 # See: https://root.cern.ch/doc/master/NumberCountingUtils\_8cxx\_source.html#l00122
3
4 def significance(signalExp, backgroundExp, relativeBkgUncert):
5     tau = 1.0 / (backgroundExp * relativeBkgUncert*relativeBkgUncert)
6
7     x = 1.0 / (1.0 + tau)
8     y = signalExp + backgroundExp
9     z = 1 + backgroundExp * tau
10
11    P_B = scipy.special.betainc(y, z, x)
12    Z_B = -scipy.special.ndtri(P_B)
13
14    return Z_B
```

D.2 Optimized \hat{y} Threshold

```

1 def find_best_thr(y, y_pred, W, B, bkg_type_to_name, relativeBkgUncert, ttbar_stat_cut_threshold,
2                   bkg_cut_threshold=0.5):
3     fpr, tpr, thr = roc_curve(y, y_pred, sample_weight=W)
4
5     bkg_type_to_name_inverted = {v:int(k) for k,v in bkg_type_to_name.items()}
6     bkg_type_ttbar = bkg_type_to_name_inverted['ttbar']
7
8     # separate sig / bkg
9     sig_mask = np.where(y == 1)
10    bkg_mask = np.where(y != 1)
11    W_sig = W[sig_mask]
12    W_bkg = W[bkg_mask]
13    B_bkg = B[bkg_mask]
14    y_pred_bkg = y_pred[bkg_mask]
15
16    sigs = tpr*np.sum(W_sig)
17    bkgs = fpr*np.sum(W_bkg)
18
19    # compute all Z_B values (vectorized)
20    Zs = significance(sigs, bkgs, relativeBkgUncert)
21
22    # find max_Z
23    max_Z = -float('inf')
24    i_best = None
25    yield_sig_best = -float('inf')
26    yield_bkg_best = -float('inf')
27    limiting_constraint = 0
28    for i in range(Zs.shape[0]):
29        if Zs[i] > max_Z:
30
31            W_bkg_selected = W_bkg[np.where(y_pred_bkg > thr[i]) ]
32            W_bkg_selected_sum = np.sum(W_bkg_selected)
33
34            if W_bkg_selected_sum <= bkg_cut_threshold:
35                limiting_constraint = 1
36                continue
37
38            W_ttbar_selected = W_bkg[np.where( (y_pred_bkg > thr[i]) & (B_bkg == bkg_type_ttbar) ) ]
39            W_ttbar_selected_sum = np.sum(W_ttbar_selected)
40
41            if W_ttbar_selected_sum > 0:
42                ttbar_stat_uncert = np.sqrt(np.sum(np.square(W_ttbar_selected))) / W_ttbar_selected_sum
43                if not ttbar_stat_uncert < ttbar_stat_cut_threshold:
44                    limiting_constraint = 2
45                    continue
46            else:
47                # ttbar_stat_uncert = inf
48                limiting_constraint = 2
49                continue
50
51            max_Z = Zs[i]
52            i_best = i
53            yield_sig_best = sigs[i]
54            yield_bkg_best = bkgs[i]
55
56    limiting_constraint_dict = {0:'None', 1:'Bkg_Yield > {0:.1f}'.format(bkg_cut_threshold), 2:'ttbar_Stat_Uncert < {0:.0%}'.format(ttbar_stat_cut_threshold)}
57
58    return thr[i_best], max_Z, yield_sig_best, yield_bkg_best, limiting_constraint,
           limiting_constraint_dict

```

Appendix E

In Situ γ +Jet Calibration

During the author’s qualification process to be an ATLAS member they performed service work for the collaboration developing a large- R *in situ* γ +jet JES calibration. This work was a component of the first *in situ* calibrations for large- R LCW scale jets developed at ATLAS, circulated as a conference note in 2017 [217] and recently published as a paper [218]. The author also shared progress on the γ +jet calibration in numerous conference talks and poster sessions, of which [219] is the most recent example. This appendix describes the details of the large- R γ +jet calibration, as well as its connection to the multi- b analysis.

E.1 *In Situ* γ +Jet Calibration

Large- R jets are calibrated in roughly the same sequence as presented for small- R jets in Section 4.2. Following initial corrections and MC calibrations, data-driven *in situ* momentum balance calibrations are needed to address any residual mismodeling effects. The γ +jet final state is ideal for making an *in situ* measurement because photons showering electromagnetically in the ECAL are very well-measured in terms of

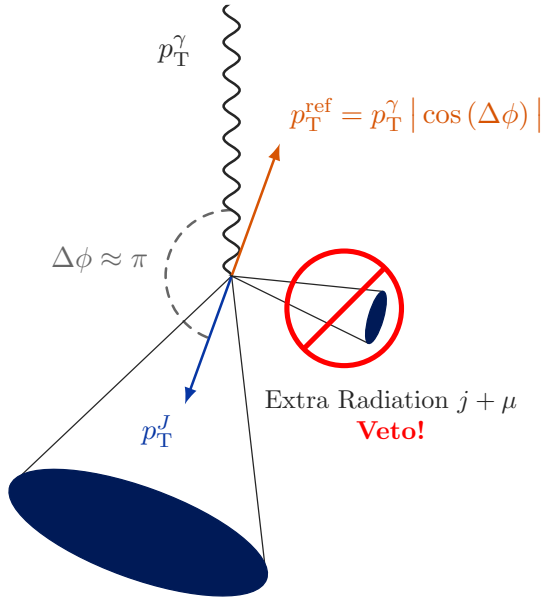


FIGURE E.1: Schematic representation of a well balanced γ +jet event.

their energies¹ and can be used as reference objects. For these events the momentum of the photon p_T^γ should precisely balance that of the jet, p_T^J , excluding the effects of any extra radiation. An illustration of a well balanced γ +jet event can be found in Figure E.1. The azimuthal separation angle $\Delta\phi$ is used to define a reference momentum p_T^{ref} (E.1) from the component of p_T^γ collinear with the jet.

$$p_T^{\text{ref}} = p_T^\gamma |\cos(\Delta\phi)| \quad (\text{E.1})$$

We then define the direct balance response² R_{DB} as the ratio:

$$R_{\text{DB}} = \frac{p_T^J}{p_T^{\text{ref}}}. \quad (\text{E.2})$$

By measuring R_{DB} in both data and MC we can compute the ratio $\langle R_{\text{DB}}^{\text{MC}} \rangle / \langle R_{\text{DB}}^{\text{Data}} \rangle$

¹ See Section 3.2.3, in particular (3.4).

² Equivalent to $\mathcal{R}_{\text{in situ}}$ (4.4) in the small- R jet calibration's notation.

Table E.1: γ +jet selections.

Object	Selection	Description
Photon (γ)	Lowest unprescaled single photon HLT	Trigger
	$p_T^\gamma > 140 \text{ GeV}$, $ \eta^\gamma < 1.37$	Preselection
	“Tight” [221, 222]	ID and Isolation
Large- R Jet (J)	$\Delta R(\text{Reco } \gamma, \text{ Truth } \gamma) < 0.2$	MC Truth Matching
	$p_T^J > 20 \text{ GeV}$	Preselection
Small- R Jet (j)	$\Delta R(\gamma, J) > 0.2$	Overlap Removal
	“BadLoose” [192]	Jet Cleaning
	$\text{JVT} \geq 0.59$ for $p_T < 60 \text{ GeV}$, $ \eta < 2.4$	Pileup Removal
Muons (μ)	$\Delta R(J, \mu) > 1.0$	Overlap Removal
	$\Delta\phi(\gamma, J) > 2.8$	Separation Angle
Topological	$p_T^{j+\mu} < \max(15 \text{ GeV}, 0.1 p_T^{\text{ref}})$	Extra-radiation Veto

that allows us to correct the JES calibration originally derived from MC alone. This ratio is the main result of the *in situ* JES calibration.

E.1.1 Event Selection

Events are selected by requiring the presence of a photon and large- R jet then applying the requirements in Table E.1. These selections are designed such that events passing them have nearly all of their p_T carried by the leading jet J and the leading photon γ , back-to-back with azimuthal separation angle $\Delta\phi(\gamma, J) \approx \pi$. Events with sub-leading small- R jets j and/or muons μ that have significant p_T are also rejected as this additional radiation is not included in the momentum balance. These selections are based on prior work [220] with some modifications and updates to match the latest ATLAS recommendations.

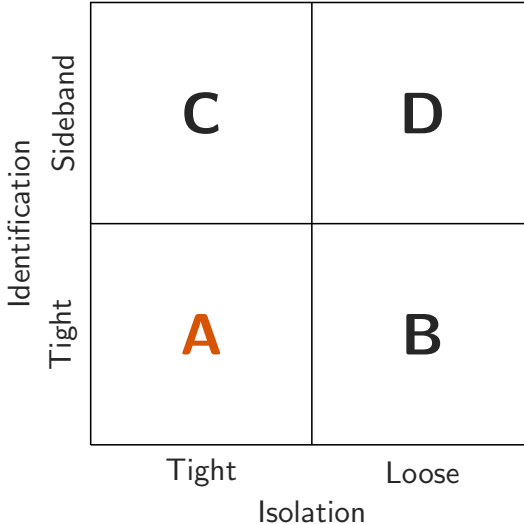


FIGURE E.2: Photon purity regions. A is the nominal selection on photon isolation and identification.

E.1.2 Photon Purity Correction

The photon selections are strict, but still allow the occasional jet or electron to pass through as a fake photon. These events will skew the nominal p_T balance unless they are accounted for. The photon purity correction is derived from data and MC by using a 2D-sideband, or ABCD, method [223, 224]. The photon identification and isolation selections are used to separate events in a 2D plane divided in four regions as shown in Figure E.2. Nominal events are located in region A, events failing the isolation requirement in B, events failing identification in C, and events failing both in D.

The response R_{DB}^X and number of events N_X are then found for each region X individually. We can estimate the probability of a real photon event being in region X from the MC sample, which consists of only real photons due to the truth matching selection, as $e_X = N_X^{\text{MC}} / \sum_{A,B,C,D} N_i^{\text{MC}}$. Assuming that there is no correlation between the isolation and identification selections, and letting f_1, f_2 be their respective fake rates, we can construct the following system of equations:

$$N_A = e_A N_\gamma + f_1 f_2 N_j , \quad (\text{E.3a})$$

$$N_B = e_B N_\gamma + (1 - f_1) f_2 N_j , \quad (\text{E.3b})$$

$$N_C = e_C N_\gamma + f_1 (1 - f_2) N_j , \quad (\text{E.3c})$$

$$N_D = e_D N_\gamma + (1 - f_1) (1 - f_2) N_j . \quad (\text{E.3d})$$

Solving for N_γ results in the nominal photon purity $P_A = e_A N_\gamma / N_A$ which can then finally be used along with $R_{\text{DB}}^{\text{not } \gamma} \approx R_{\text{DB}}^D$ to correct the nominal response (E.4) in region A. The photon purity displayed in Figure E.3 is always $> 94\%$. As can be seen in Figure E.4 the purity correction of $\approx 2\%$ is crucial, but actually ends up contributing an almost negligible amount to the final systematic uncertainty.

$$\begin{aligned} R_{\text{DB}}^A &= R_{\text{DB}}^\gamma P_A + R_{\text{DB}}^{\text{not } \gamma} (1 - P_A) \rightarrow \\ R_{\text{DB}}^\gamma &= \frac{R_{\text{DB}}^A}{P_A} + R_{\text{DB}}^D \left(1 - \frac{1}{P_A}\right) \end{aligned} \quad (\text{E.4})$$

E.1.3 Systematic Uncertainties

The systematic uncertainties on the calibration arise in four main areas; extra radiation outside the jet affecting the balance, the measurement of the photon, the presence of pileup jets, and the MC physics modeling. The effects of extra radiation on the balance are assessed by varying the topological selections, as well as varying the overlap removal $\Delta R(J, j)$ between the large- R and small- R jets. The effects of the photon measurement are assessed by varying the energy scale and resolution of the photon calibration [226, 227], as well as by varying the measured photon purity in the purity correction. The effects of pileup jets on the calibration are estimated by varying the JVT [208] selection threshold. Lastly, the analysis is repeated with alternative SHERPA 2.1 samples to assess the modeling uncertainty on the nominal

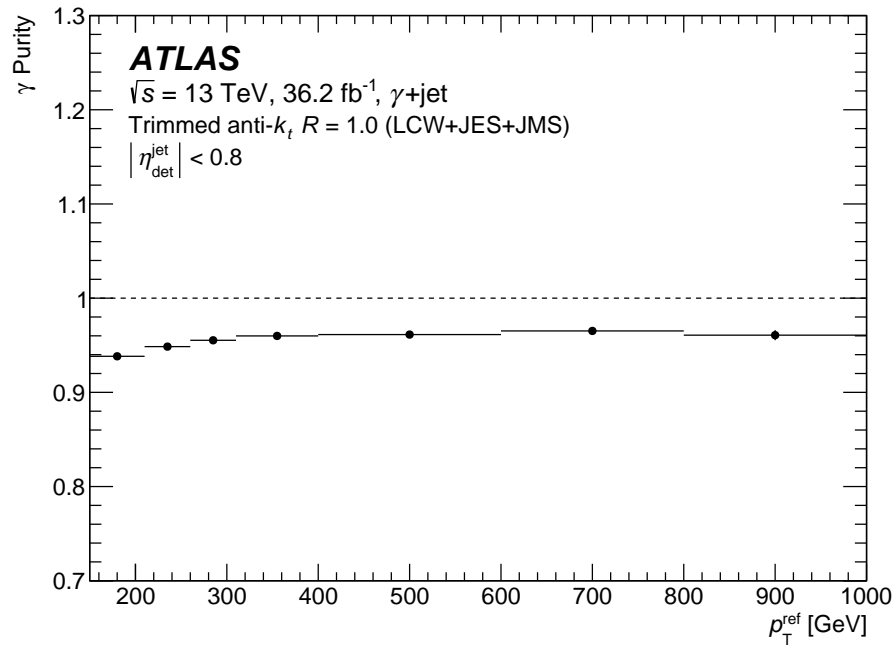


FIGURE E.3: Photon purity in the nominal region A [225].

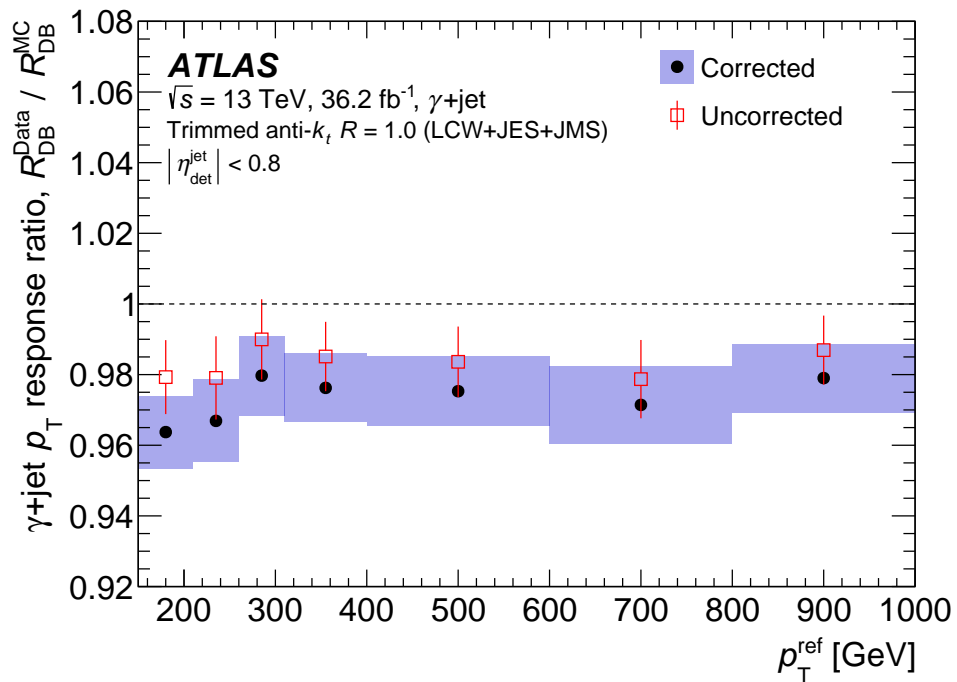


FIGURE E.4: $\gamma + \text{jet}$ response with and without photon purity correction [225].

Table E.2: γ +jet systematic variation values.

Variable	Up	Down	Description
$p_T^{j+\mu} < \max()$	20 GeV, 0.15 p_T^{ref}	10 GeV, 0.05 p_T^{ref}	Extra-radiation Veto
$\Delta\phi(\gamma, J) >$	2.9	2.7	Separation Angle
$\Delta R(J, j) >$	1.6	1.2	Overlap Removal
γ E Scale and Res.	$+1\sigma$	-1σ	Photon Calibration
γ Purity	$P + \sigma_P$	$P - \sigma_P$	Photon Purity Correction
JVT \geq	0.91	0.11	Pileup Removal

PYTHIA 8 samples. For specific details on each variation see Table E.2. The photon energy scale uncertainty is the dominate systematic uncertainty for all p_T values.

E.1.4 Results

The mean R_{DB} for data and MC is found by fitting the balance distributions in bins of p_T^{ref} and jet η . The fit is performed with a Gaussian function in two iterations. In order to minimize the impact of non-Gaussian tails on the result the second fit is constrained to the central subdomain $|R_{\text{DB}} - \mu_{R_{\text{DB}}}| \leq 2\sigma_{R_{\text{DB}}}$ derived from the first.

The statistical uncertainty on R_{DB} in each $p_T^{\text{ref}} - \eta$ bin is evaluated using pseudo-experiments, otherwise known as the bootstrap method. For 500 pseudo-experiments every event in data and MC is counted n times, where n is sampled from a Poisson distribution with a mean of one. The root mean square of R_{DB} over the pseudo-experiments is then the statistical uncertainty.

The calibration is measured with a 36.2 fb^{-1} sample of events from 2015–2016 $\sqrt{s} = 13 \text{ TeV}$ collision data. After fitting the R_{DB} distribution and computing the uncertainties in bins of p_T^{ref} all results are converted³ to being in terms of p_T^J for later application to uncalibrated jets. The fitted value of $\langle R_{\text{DB}} \rangle$ from the central $|\eta| < 0.8$ bin as a function of p_T^J for data and MC can be seen in Figure E.5. The MC to

³ By centering the new p_T^J bins at $\langle p_T^J \rangle$ of the original p_T^{ref} bins, and merging very small bins when necessary.

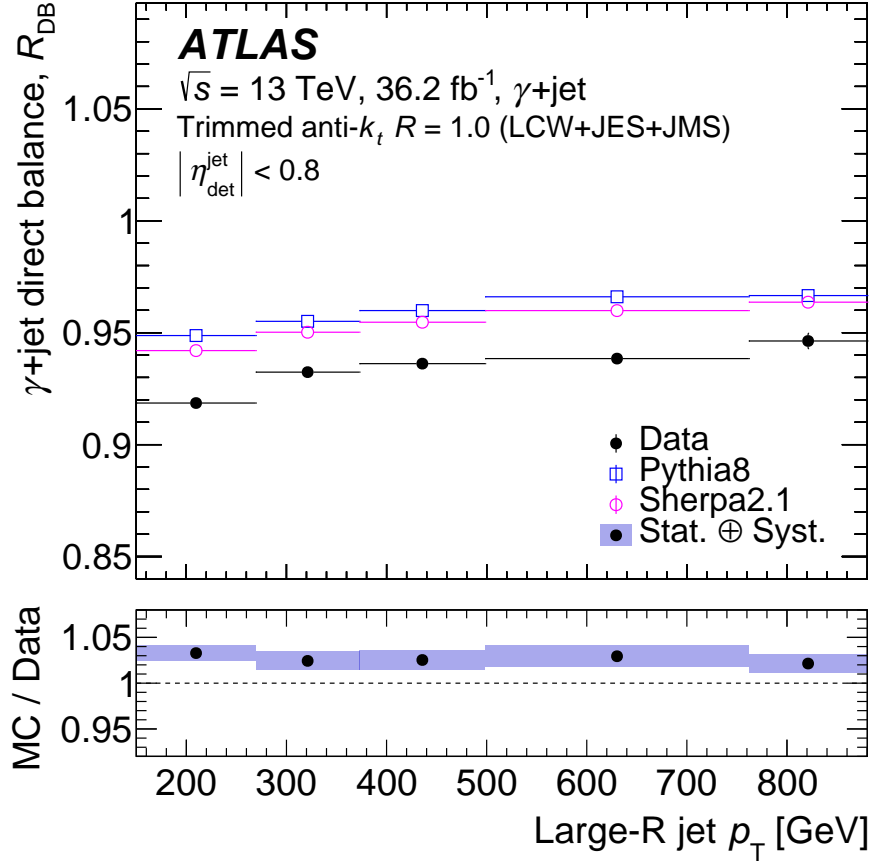


FIGURE E.5: Mean γ +jet transverse momentum balance in data and MC, and their ratio [218]. The error bars on the upper inset only show the statistical uncertainty, while those on the lower inset include the systematic uncertainties.

data ratio shown in the lower inset corresponds to the *in situ* γ +jet JES calibration. The systematics are plotted individually along with the statistical uncertainty in Figure E.6. The overall combined systematic and statistical uncertainty is $\approx 1\%$ for the majority of the p_T range.

E.2 *In Situ* Combination

The γ +jet direct balance method is only one component of the full *in situ* calibration, with Z +jet and multijet balance (MJB) measurements also being performed as in the small- R calibration of Section 4.2. The three *in situ* methods are combined in

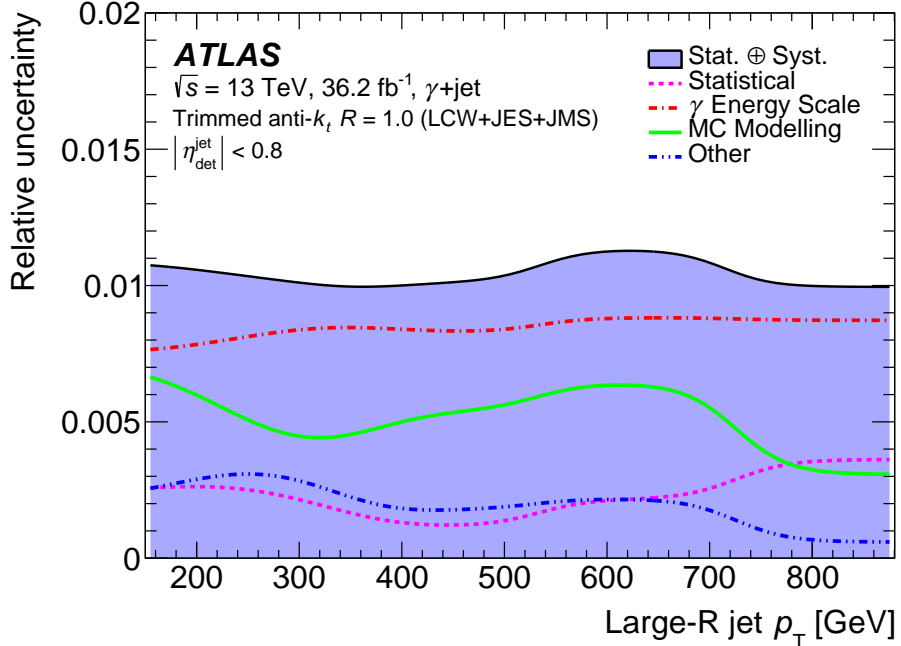


FIGURE E.6: Systematic and statistical uncertainties on the γ +jet transverse momentum balance [218]. Smoothed with a Gaussian kernel of width 70 GeV.

a weighted average based on a χ^2 -minimization, where the weights are functions of the statistical and systematic uncertainties, correlations, and different bin sizes. The response is 2–3 % higher in MC than data, with a relative JES uncertainty of 1–2 % for $200 \text{ GeV} < p_T < 2 \text{ TeV}$. γ +jet is the leading measurement for ≈ 400 –880 GeV and helps constrain the combined uncertainty elsewhere. The combined *in situ* response and the combination weights are displayed in Figures E.7 and E.8.

E.3 Re-clustered Jet Studies

During the γ +jet analysis supplementary studies were made with re-clustered large- R jets. The procedure remained the same as the nominal γ +jet analysis, but with $R = 1.0$ jets re-clustered from standard $R = 0.4$ small- R EM scale jets and trimmed with $f_{\text{cut}} = 0.1$ as the target object. The input $R = 0.4$ jets were first fully calibrated following the steps in Section 4.2. This made the re-clustered γ +jet results a cross

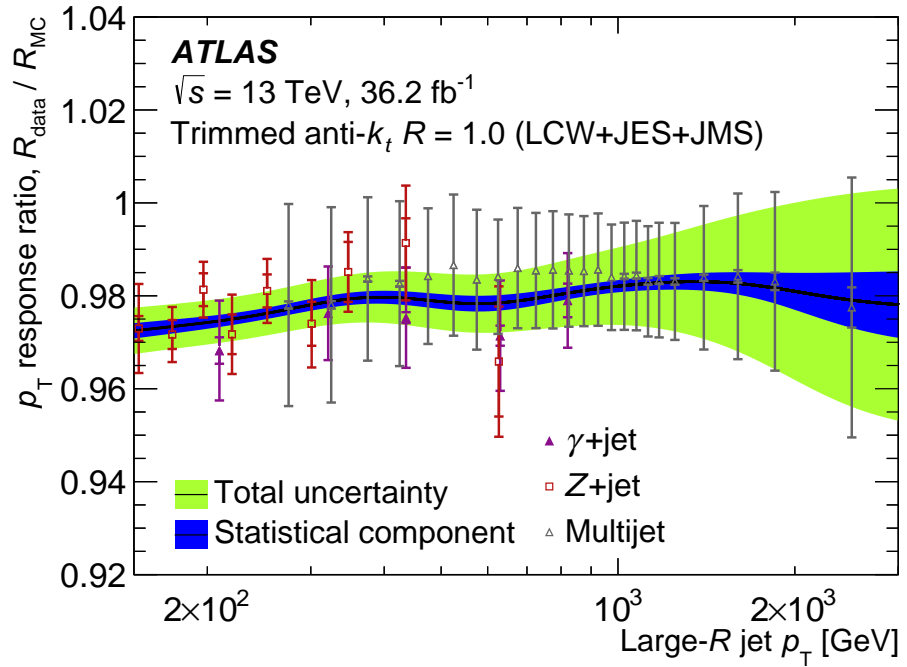


FIGURE E.7: Data to MC ratio of the combined large- R *in situ* measurements, smoothed with a sliding Gaussian kernel [218].

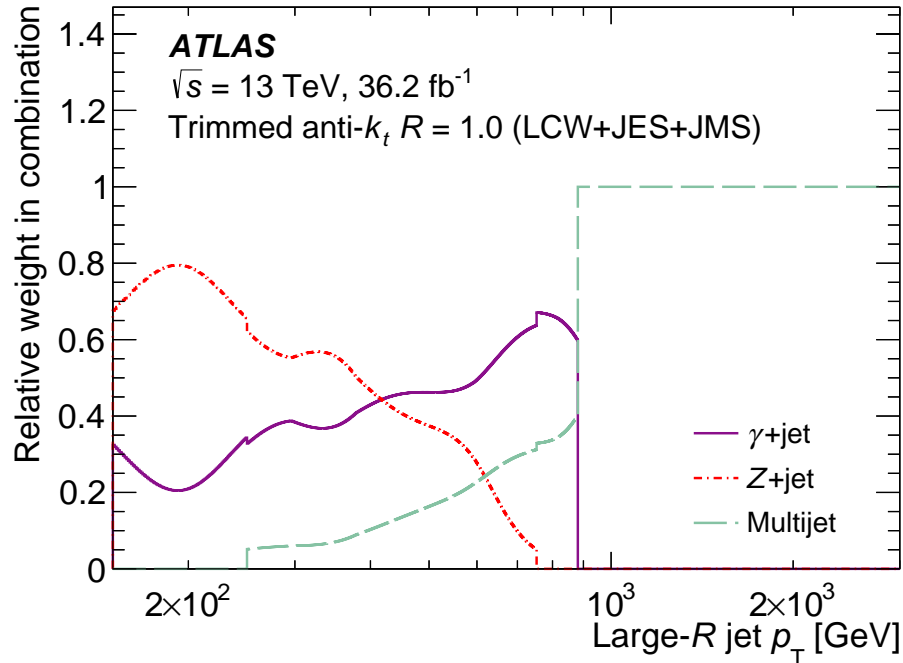


FIGURE E.8: Weight of each *in situ* measurement in the combination average as a function of the large- R jet p_T [218].

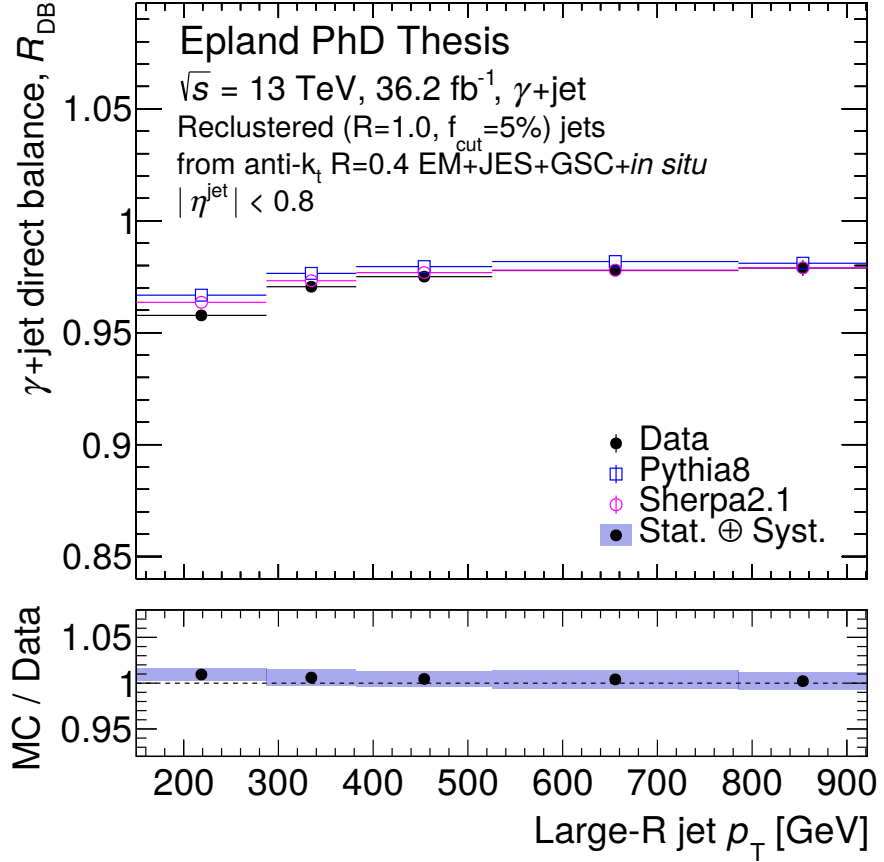


FIGURE E.9: Mean $\gamma + \text{jet}$ transverse momentum balance in data and MC for $R = 1.0$ re-clustered jets. The re-clustered jets are made up of fully calibrated $R = 0.4$ small- R jets. The error bars on the upper inset only show the statistical uncertainty, while those on the lower data to MC ratio include the systematic uncertainties.

check of the small- R calibration. As can be seen in Figure E.9, the MC to data ratio is 1.0 within error bars for the majority of the p_T range, demonstrating the validity of the original small- R calibration. Similar performance can be expected of the $R = 0.8$ re-clustered jets used by the multi- b analysis.

Bibliography

- [1] C. Autermann, *Experimental status of supersymmetry after the LHC Run-I*, Prog. Part. Nucl. Phys. **90** (2016) 125–155, [arXiv:1609.01686 \[hep-ex\]](https://arxiv.org/abs/1609.01686). Cited on page 2.
- [2] ATLAS Collaboration, *Summary of the ATLAS experiment’s sensitivity to supersymmetry after LHC Run 1 — interpreted in the phenomenological MSSM*, JHEP **10** (2015) 134, [arXiv:1508.06608 \[hep-ex\]](https://arxiv.org/abs/1508.06608). Cited on page 2.
- [3] ATLAS Collaboration, *Summary plots from the ATLAS Supersymmetry physics group*, July, 2018. <https://atlas.web.cern.ch/Atlas/GROUPS/PHYSICS/CombinedSummaryPlots/SUSY>. Cited on pages 3 and 4.
- [4] ATLAS Collaboration, *Search for supersymmetry in final states with missing transverse momentum and multiple b-jets in proton–proton collisions at $\sqrt{s} = 13$ TeV with the ATLAS detector*, ATLAS-CONF-2018-041, 2018, <https://cds.cern.ch/record/2632347>. Cited on pages 2, 3, 4, 66, 86, 87, 88, 93, 106, 107, 117, 119, and 158.
- [5] ATLAS Collaboration, *Search for supersymmetry in final states with missing transverse momentum and multiple b-jets in proton–proton collisions at $\sqrt{s} = 13$ TeV with the ATLAS detector*, JHEP **06** (2018) 107, [arXiv:1711.01901 \[hep-ex\]](https://arxiv.org/abs/1711.01901). Cited on pages 2, 79, 86, 89, 102, 106, 107, and 133.
- [6] CMS Collaboration, *Search for supersymmetry in pp collisions at $\sqrt{s} = 13$ TeV in the single-lepton final state using the sum of masses of large-radius jets*, Phys. Rev. Lett. **119** (2017) 151802, [arXiv:1705.04673 \[hep-ex\]](https://arxiv.org/abs/1705.04673). Cited on page 2.
- [7] CMS Collaboration, *Search for supersymmetry in multijet events with missing transverse momentum in proton–proton collisions at 13 TeV*, Phys. Rev. D **96** (2017) 032003, [arXiv:1704.07781 \[hep-ex\]](https://arxiv.org/abs/1704.07781). Cited on page 2.

- [8] CMS Collaboration, *Search for new phenomena with the M_{T2} variable in the all-hadronic final state produced in proton–proton collisions at $\sqrt{s} = 13$ TeV*, *Eur. Phys. J. C* **77** (2017) 710, [arXiv:1705.04650 \[hep-ex\]](https://arxiv.org/abs/1705.04650). Cited on page 2.
- [9] ATLAS Collaboration, *Search for supersymmetry in final states with two same-sign or three leptons and jets using 36 fb^{-1} of $\sqrt{s} = 13$ TeV pp collision data with the ATLAS detector*, *JHEP* **09** (2017) 084, [arXiv:1706.03731 \[hep-ex\]](https://arxiv.org/abs/1706.03731). Cited on pages 2 and 4.
- [10] CMS Collaboration, *Search for physics beyond the standard model in events with two leptons of same sign, missing transverse momentum, and jets in proton–proton collisions at $\sqrt{s} = 13$ TeV*, *Eur. Phys. J. C* **77** (2017) 578, [arXiv:1704.07323 \[hep-ex\]](https://arxiv.org/abs/1704.07323). Cited on page 2.
- [11] ATLAS Collaboration, *Summary of the searches for squarks and gluinos using $\sqrt{s} = 8$ TeV pp collisions with the ATLAS experiment at the LHC*, *JHEP* **10** (2015) 054, [arXiv:1507.05525 \[hep-ex\]](https://arxiv.org/abs/1507.05525). Cited on page 4.
- [12] C. N. Yang and R. L. Mills, *Conservation of Isotopic Spin and Isotopic Gauge Invariance*, *Phys. Rev.* **96** (1954) 191–195. Cited on page 5.
- [13] ATLAS Collaboration, *Summary plots from the ATLAS Standard Model physics group*, July, 2018. <https://atlas.web.cern.ch/Atlas/GROUPS/PHYSICS/CombinedSummaryPlots/SM>. Cited on page 6.
- [14] ZEUS Collaboration, *Limits on the effective quark radius from inclusive ep scattering at HERA*, *Physics Letters B* **757** (2016) 468–472. Cited on page 7.
- [15] CPEP, *Fundamental Particles and Interactions*, <http://www.cpepphysics.org/particle-chart.html>. Cited on page 7.
- [16] D. Galbraith and C. Burgard, *Standard model of the standard model*, CERN Webfest 2012. <http://www.texample.net/tikz/examples/model-physics>. Cited on page 8.
- [17] S. L. Glashow, *Partial-symmetries of weak interactions*, *Nuclear Physics* **22** (1961) 579–588. Cited on page 7.
- [18] S. Weinberg, *A Model of Leptons*, *Phys. Rev. Lett.* **19** (1967) 1264–1266. Cited on page 7.

- [19] A. Salam, *Weak and Electromagnetic Interactions*, Conf. Proc. **C680519** (1968) 367–377, <https://www.osti.gov/biblio/4767615>. Cited on page 7.
- [20] Particle Data Group Collaboration, C. Patrignani et al., *Review of Particle Physics*, Chin. Phys. **C40** (2016) 100001. Cited on pages 8, 15, 20, 22, 28, 29, 30, 31, 51, and 54.
- [21] A. Pich, *The Standard Model of Electroweak Interactions*, 2008. [arXiv:0705.4264 \[hep-ph\]](https://arxiv.org/abs/0705.4264). Cited on pages 8, 9, 11, and 12.
- [22] F. Englert and R. Brout, *Broken Symmetry and the Mass of Gauge Vector Mesons*, Phys. Rev. Lett. **13** (1964) 321–323. Cited on page 12.
- [23] P. W. Higgs, *Broken Symmetries and the Masses of Gauge Bosons*, Phys. Rev. Lett. **13** (1964) 508–509. Cited on page 12.
- [24] G. S. Guralnik, C. R. Hagen, and T. W. B. Kibble, *Global Conservation Laws and Massless Particles*, Phys. Rev. Lett. **13** (1964) 585–587. Cited on page 12.
- [25] Username “Just Ask”. Tex StackExchange. <https://tex.stackexchange.com/questions/229178>. Cited on page 13.
- [26] J. Goldstone, *Field Theories with Superconductor Solutions*, Nuovo Cim. **19** (1961) 154–164. Cited on page 13.
- [27] B. Pontecorvo, *Inverse beta processes and nonconservation of lepton charge*, Sov. Phys. JETP **7** (1958) 172–173. Cited on page 15.
- [28] Z. Maki, M. Nakagawa, and S. Sakata, *Remarks on the Unified Model of Elementary Particles*, Progress of Theoretical Physics **28** (1962) 870–880. Cited on page 15.
- [29] R. Davis, D. S. Harmer, and K. C. Hoffman, *Search for Neutrinos from the Sun*, Phys. Rev. Lett. **20** (1968) 1205–1209. Cited on page 15.
- [30] Super-Kamiokande Collaboration, *Evidence for Oscillation of Atmospheric Neutrinos*, Phys. Rev. Lett. **81** (1998) 1562–1567. Cited on page 15.
- [31] N. Cabibbo, *Unitary Symmetry and Leptonic Decays*, Phys. Rev. Lett. **10** (1963) 531–533. Cited on page 15.
- [32] M. Kobayashi and T. Maskawa, *CP Violation in the Renormalizable Theory of Weak Interaction*, Prog. Theor. Phys. **49** (1973) 652–657. Cited on page 15.

- [33] ATLAS Collaboration, *Observation of a new particle in the search for the Standard Model Higgs boson with the ATLAS detector at the LHC*, *Phys. Lett. B* **716** (2012) 1, [arXiv:1207.7214 \[hep-ex\]](#). Cited on page 15.
- [34] CMS Collaboration, *Observation of a new boson at a mass of 125 GeV with the CMS experiment at the LHC*, *Phys. Lett. B* **716** (2012) 30, [arXiv:1207.7235 \[hep-ex\]](#). Cited on page 15.
- [35] D. J. Gross and F. Wilczek, *Ultraviolet Behavior of Non-Abelian Gauge Theories*, *Phys. Rev. Lett.* **30** (1973) 1343–1346. Cited on page 15.
- [36] H. D. Politzer, *Reliable Perturbative Results for Strong Interactions?*, *Phys. Rev. Lett.* **30** (1973) 1346–1349. Cited on page 15.
- [37] D. J. Gross and F. Wilczek, *Asymptotically Free Gauge Theories. I*, *Phys. Rev. D* **8** (1973) 3633–3652. Cited on pages 15 and 17.
- [38] R. K. Ellis, W. J. Stirling, and B. R. Webber, *QCD and Collider Physics*, Camb. Monogr. Part. Phys. Nucl. Phys. Cosmol. **8** (1996). Cited on pages 15, 16, 17, 18, and 20.
- [39] L. Faddeev and V. Popov, *Feynman diagrams for the Yang-Mills field*, *Physics Letters B* **25** (1967) 29–30. Cited on page 16.
- [40] H. D. Politzer, *Asymptotic freedom: An approach to strong interactions*, *Physics Reports* **14** (1974) 129–180. Cited on page 17.
- [41] K. G. Wilson, *Confinement of Quarks*, *Phys. Rev. D* **10** (1974) 2445–2459. Cited on page 18.
- [42] S. Höche, *Introduction to parton-shower event generators*, [arXiv:1411.4085 \[hep-ph\]](#). Cited on page 19.
- [43] T. Sjostrand, S. Mrenna, and P. Z. Skands, *A Brief Introduction to PYTHIA 8.1*, *Comput. Phys. Commun.* **178** (2008) 852–867, [arXiv:0710.3820 \[hep-ph\]](#). Cited on page 18.
- [44] B. Andersson, G. Gustafson, and C. Peterson, *A Semiclassical Model for Quark Jet Fragmentation*, *Z. Phys. C1* (1979) 105. Cited on page 18.
- [45] T. Gleisberg et al., *Event generation with SHERPA 1.1*, *JHEP* **02** (2009) 007, [arXiv:0811.4622 \[hep-ph\]](#). Cited on pages 18 and 88.

- [46] M. Bähr et al., *Herwig++ Physics and Manual*, *Eur. Phys. J. C* **58** (2008) 639–707, [arXiv:0803.0883 \[hep-ph\]](https://arxiv.org/abs/0803.0883). Cited on page 18.
- [47] J. Bellm et al., *Herwig++ 2.7 Release Note*, [arXiv:1310.6877 \[hep-ph\]](https://arxiv.org/abs/1310.6877). Cited on pages 18 and 106.
- [48] R. D. Field and S. Wolfram, *A QCD Model for e^+e^- Annihilation*, *Nucl. Phys. B* **213** (1983) 65–84. Cited on page 18.
- [49] J.-C. Winter, F. Krauss, and G. Soff, *A modified cluster hadronization model*, *Eur. Phys. J. C* **36** (2004) 381–395, [arXiv:hep-ph/0311085 \[hep-ph\]](https://arxiv.org/abs/hep-ph/0311085). Cited on page 19.
- [50] J. C. Collins, D. E. Soper, and G. F. Sterman, *Factorization of Hard Processes in QCD*, *Adv. Ser. Direct. High Energy Phys.* **5** (1989) 1–91, [arXiv:hep-ph/0409313 \[hep-ph\]](https://arxiv.org/abs/hep-ph/0409313). Cited on page 20.
- [51] M. E. Peskin and D. V. Schroeder, *An Introduction to Quantum Field Theory*. Addison-Wesley, Reading, USA, 1995.
<http://www.slac.stanford.edu/~mpeskin/QFT.html>. Cited on page 20.
- [52] R. Brock et al., *Handbook of Perturbative QCD*, *Rev. Mod. Phys.* **67** (1995) 157–248. Cited on page 20.
- [53] V. N. Gribov and L. N. Lipatov, *Deep inelastic ep scattering in perturbation theory*, *Sov. J. Nucl. Phys.* **15** (1972) 438–450. Cited on page 20.
- [54] G. Altarelli and G. Parisi, *Asymptotic Freedom in Parton Language*, *Nucl. Phys. B* **126** (1977) 298–318. Cited on page 20.
- [55] Y. L. Dokshitzer, *Calculation of the Structure Functions for Deep Inelastic Scattering and e^+e^- Annihilation by Perturbation Theory in Quantum Chromodynamics.*, *Sov. Phys. JETP* **46** (1977) 641–653. Cited on page 20.
- [56] R. D. Ball et al., *Parton distributions from high-precision collider data*, *The European Physical Journal C* **77** (2017) 663. Cited on page 21.
- [57] Particle Data Group Collaboration, M. Tanabashi et al., *Review of Particle Physics*, *Phys. Rev. D* **98** (2018) 030001. Cited on page 21.
- [58] Planck Collaboration, *Planck 2015 Results - XIII. Cosmological Parameters*, *A&A* **594** (2016) A13. Cited on page 22.

- [59] Y. Ali-Haïmoud, J. Chluba, and M. Kamionkowski, *Constraints on Dark Matter Interactions with Standard Model Particles from Cosmic Microwave Background Spectral Distortions*, Phys. Rev. Lett. **115** (2015) 071304. Cited on page 22.
- [60] D. Clowe, M. Bradac, A. H. Gonzalez, M. Markevitch, S. W. Randall, C. Jones, and D. Zaritsky, *A direct empirical proof of the existence of dark matter*, Astrophys. J. **648** (2006) L109–L113, arXiv:astro-ph/0608407 [astro-ph]. Cited on page 22.
- [61] E. V. Karukes, P. Salucci, and G. Gentile, *The dark matter distribution in the spiral NGC 3198 out to 0.22 R_{vir}* , Astron. Astrophys. **578** (2015) A13, arXiv:1503.04049 [astro-ph.GA]. Cited on pages 22 and 23.
- [62] S. P. Martin, *A Supersymmetry Primer*, Adv. Ser. Direct. High Energy Phys. **18** (1998) 1, arXiv:hep-ph/9709356 [hep-ph]. Cited on pages 22, 23, 24, 25, 26, 27, 30, 31, 32, and 33.
- [63] J. Wess and B. Zumino, *Supergauge Transformations in Four-Dimensions*, Nucl. Phys. B **70** (1974) 39. Cited on pages 24 and 26.
- [64] J. Wess and B. Zumino, *Supergauge Invariant Extension of Quantum Electrodynamics*, Nucl. Phys. B **78** (1974) 1. Cited on page 24.
- [65] S. Ferrara and B. Zumino, *Supergauge Invariant Yang-Mills Theories*, Nucl. Phys. B **79** (1974) 413. Cited on page 24.
- [66] A. Salam and J. A. Strathdee, *Supersymmetry and Nonabelian Gauges*, Phys. Lett. B **51** (1974) 353. Cited on page 24.
- [67] J. Ellis and K. A. Olive, *Supersymmetric Dark Matter Candidates*, 2010. arXiv:1001.3651 [astro-ph.CO]. Cited on pages 24 and 32.
- [68] J. L. Lopez, K. Yuan, and D. Nanopoulos, *Supersymmetry Breaking and Dark Matter*, Physics Letters B **267** (1991) 219–226. Cited on pages 24 and 32.
- [69] R. Haag, J. T. Łopuszański, and M. Sohnius, *All possible generators of supersymmetries of the S-matrix*, Nuclear Physics B **88** (1975) 257–274. Cited on page 25.
- [70] S. Coleman and J. Mandula, *All Possible Symmetries of the S Matrix*, Phys. Rev. **159** (1967) 1251–1256. Cited on page 25.

- [71] L. Girardello and M. T. Grisaru, *Soft Breaking of Supersymmetry*, Nucl. Phys. B **194** (1982) 65. Cited on page 27.
- [72] J. R. Ellis and S. Rudaz, *Search for Supersymmetry in Toponium Decays*, Phys. Lett. B **128** (1983) 248. Cited on page 28.
- [73] R. Barbieri and G. F. Giudice, *Upper Bounds on Supersymmetric Particle Masses*, Nucl. Phys. B **306** (1988) 63. Cited on page 28.
- [74] P. Fayet, *Supersymmetry and Weak, Electromagnetic and Strong Interactions*, Phys. Lett. B **64** (1976) 159. Cited on page 28.
- [75] P. Fayet, *Spontaneously Broken Supersymmetric Theories of Weak, Electromagnetic and Strong Interactions*, Phys. Lett. B **69** (1977) 489. Cited on page 28.
- [76] P. Fayet, *Supergauge invariant extension of the Higgs mechanism and a model for the electron and its neutrino*, Nucl. Phys. B **90** (1975) 104. Cited on page 29.
- [77] G. R. Farrar and P. Fayet, *Phenomenology of the Production, Decay, and Detection of New Hadronic States Associated with Supersymmetry*, Phys. Lett. B **76** (1978) 575. Cited on page 32.
- [78] J. R. Ellis, J. S. Hagelin, D. V. Nanopoulos, K. A. Olive, and M. Srednicki, *Supersymmetric Relics from the Big Bang*, Nucl. Phys. B **238** (1984) 453. Cited on pages 32 and 34.
- [79] C. Giunti, C. W. Kim, and U. W. Lee, *Running Coupling Constants and Grand Unification Models*, Modern Physics Letters A **6** (1991) 1745–1755. Cited on page 32.
- [80] U. Amaldi, W. de Boer, and H. Fürstenau, *Comparison of grand unified theories with electroweak and strong coupling constants measured at LEP*, Physics Letters B **260** (1991) 447–455. Cited on page 32.
- [81] N. Sakai, *Naturalness in Supersymmetric GUTS*, Z. Phys. C **11** (1981) 153. Cited on page 32.
- [82] S. Dimopoulos, S. Raby, and F. Wilczek, *Supersymmetry and the Scale of Unification*, Phys. Rev. D **24** (1981) 1681. Cited on page 32.

- [83] L. E. Ibanez and G. G. Ross, *Low-Energy Predictions in Supersymmetric Grand Unified Theories*, Phys. Lett. B **105** (1981) 439. Cited on page 32.
- [84] S. Dimopoulos and H. Georgi, *Softly Broken Supersymmetry and SU(5)*, Nucl. Phys. B **193** (1981) 150. Cited on page 32.
- [85] J. Alwall, P. Schuster, and N. Toro, *Simplified Models for a First Characterization of New Physics at the LHC*, Phys. Rev. D **79** (2009) 075020. Cited on page 33.
- [86] D. Alves et al., *Simplified Models for LHC New Physics Searches*, J. Phys. G **39** (2012) 105005. Cited on page 33.
- [87] K. Cranmer and I. Yavin, *RECAST — Extending the Impact of Existing Analyses*, Journal of High Energy Physics **2011** (2011) 38. Cited on page 33.
- [88] A. Arvanitaki, M. Baryakhtar, X. Huang, K. Van Tilburg, and G. Villadoro, *The last vestiges of naturalness*, Journal of High Energy Physics **2014** (2014) 22. Cited on page 34.
- [89] S. Chakraborty, A. Martin, and T. S. Roy, *Charting generalized supersoft supersymmetry*, Journal of High Energy Physics **2018** (2018) 176. Cited on page 34.
- [90] W. Beenakker, C. Borschensky, M. Krämer, A. Kulesza, and E. Laenen, *NNLL-fast: Predictions for coloured supersymmetric particle production at the LHC with threshold and Coulomb resummation*, Journal of High Energy Physics **2016** (2016) 133. Cited on page 35.
- [91] L. Evans and P. Bryant, *LHC Machine*, Journal of Instrumentation **3** (2008) S08001. Cited on pages 37 and 39.
- [92] Service graphique, CERN, *Overall view of the LHC*, <https://cds.cern.ch/record/1708849>. Cited on page 38.
- [93] E. Mobs, *The CERN accelerator complex*, <https://cds.cern.ch/record/2197559>. Cited on page 38.
- [94] R. Bruce et al., *LHC Run 2: Results and Challenges*, in *Proceedings, 57th ICFA Advanced Beam Dynamics Workshop on High-Intensity and High-Brightness Hadron Beams (HB2016): Malmö, Sweden*. July, 2016. Cited on page 39.

- [95] ATLAS Collaboration, *Luminosity Public Results Run 2*, Public Results. <https://twiki.cern.ch/twiki/bin/view/AtlasPublic/LuminosityPublicResultsRun2>. Cited on pages 39 and 40.
- [96] ATLAS Collaboration, *The ATLAS Experiment at the CERN Large Hadron Collider*, JINST **3** (2008) S08003. Cited on pages 41, 46, 47, 48, 50, 51, 52, 53, 54, 55, 57, and 59.
- [97] M. Bajko et al., *Report of the Task Force on the Incident of 19th September 2008 at the LHC*, Mar, 2009. <https://cds.cern.ch/record/1168025>. Cited on page 41.
- [98] J. Pequenao and P. Schaffner, *An computer generated image representing how ATLAS detects particles*, Jan, 2013. <https://cds.cern.ch/record/1505342>. Cited on page 42.
- [99] J. Pequenao, *Computer generated image of the whole ATLAS detector*, Mar, 2008. <https://cds.cern.ch/record/1095924>. Cited on page 43.
- [100] ATLAS Collaboration, K. Potamianos, *The upgraded Pixel detector and the commissioning of the Inner Detector tracking of the ATLAS experiment for Run-2 at the Large Hadron Collider*, PoS EPS-HEP2015 (2015), [arXiv:1608.07850 \[physics.ins-det\]](https://arxiv.org/abs/1608.07850). Cited on page 45.
- [101] ATLAS Collaboration, *ATLAS Insertable B-Layer Technical Design Report*, Sep, 2010. <https://cds.cern.ch/record/1291633>. Cited on pages 44 and 46.
- [102] ATLAS Collaboration, A. L. Rosa, *The ATLAS Insertable B-Layer: From Construction to Operation*, Journal of Instrumentation **11** (2016) C12036. Cited on page 44.
- [103] ATLAS Collaboration, N. Wermes and G. Hallewel, *ATLAS Pixel Detector: Technical Design Report*, 1998. <http://cds.cern.ch/record/381263>. Cited on page 44.
- [104] ATLAS Collaboration, G. Aad et al., *ATLAS pixel detector electronics and sensors*, Journal of Instrumentation **3** (2008) P07007. Cited on page 44.
- [105] ATLAS Collaboration, A. Ahmad et al., *The silicon microstrip sensors of the ATLAS semiconductor tracker*, Nucl. Instrum. Meth. **A578** (2007) 98–118. Cited on page 44.

- [106] ATLAS Collaboration, *Operation and performance of the ATLAS semiconductor tracker*, JINST **9** (2014) P08009, [arXiv:1404.7473 \[hep-ex\]](https://arxiv.org/abs/1404.7473). Cited on page 44.
- [107] ATLAS Collaboration, *The ATLAS Transition Radiation Tracker (TRT) Proportional Drift Tube: Design and Performance*, Journal of Instrumentation **3** (2008) P02013. Cited on page 46.
- [108] ATLAS Collaboration, *Particle Identification Performance of the ATLAS Transition Radiation Tracker*, ATLAS-CONF-2011-128, 2011, <https://cds.cern.ch/record/1383793>. Cited on pages 46 and 48.
- [109] ATLAS Collaboration, *Performance of the ATLAS Transition Radiation Tracker in Run 1 of the LHC: tracker properties*, JINST **12** (2017) P05002, [arXiv:1702.06473 \[hep-ex\]](https://arxiv.org/abs/1702.06473). Cited on pages 46 and 48.
- [110] D. Richter, *Energy Loss Measurements with the ATLAS Transition Radiation Tracker Using Test Beam Data*, Master's thesis, Humboldt University of Berlin, 2008. http://atlas-archiv.desy.de/theses/Richter_dipl.pdf. Cited on page 47.
- [111] J. D. Jackson, *Classical Electrodynamics*. Wiley, 1998. Cited on page 48.
- [112] ATLAS Collaboration, *ATLAS Calorimeter Performance: Technical Design Report*, 1996. [http://cds.cern.ch/record/331059](https://cds.cern.ch/record/331059). Cited on page 48.
- [113] ATLAS Collaboration, *ATLAS Liquid-Argon Calorimeter: Technical Design Report*, 1996. <https://cds.cern.ch/record/331061>. Cited on page 48.
- [114] ATLAS Collaboration, *ATLAS Tile Calorimeter: Technical Design Report*, 1996. <https://cds.cern.ch/record/331062>. Cited on page 48.
- [115] C. Grupen and B. Schwartz, *Particle Detectors*. Cambridge Univ. Pr., 2008. <http://www.cambridge.org/9780521840064>. Cited on pages 49, 50, 51, 52, 53, and 54.
- [116] J. Pequenao, *Computer generated image of the ATLAS calorimeter*, Mar, 2008. <https://cds.cern.ch/record/1095927>. Cited on page 49.
- [117] ATLAS Collaboration, K.-J. Grahn, *A Layer Correlation Technique for Pion Energy Calibration at the 2004 ATLAS Combined Beam Test*, [arXiv:0911.2639 \[physics.ins-det\]](https://arxiv.org/abs/0911.2639). Cited on pages 53 and 54.

- [118] ATLAS Collaboration, *Topological cell clustering in the ATLAS calorimeters and its performance in LHC Run 1*, *Eur. Phys. J. C* **77** (2017) 490, [arXiv:1603.02934 \[hep-ex\]](https://arxiv.org/abs/1603.02934). Cited on page 54.
- [119] ATLAS Collaboration, *ATLAS Muon Spectrometer: Technical Design Report*, 1997. <https://cds.cern.ch/record/331068>. Cited on page 54.
- [120] ATLAS Collaboration, S. Palestini, *The muon spectrometer of the ATLAS experiment*, *Nuclear Physics B - Proceedings Supplements* **125** (2003) 337–345. Cited on page 54.
- [121] J. Pequenao, *Computer generated image of the ATLAS muons subsystem*, Mar, 2008. <https://cds.cern.ch/record/1095929>. Cited on page 55.
- [122] ATLAS Collaboration, D. Drakoulakos, E. Gschwendtner, J. M. Maugain, F. Rohrbach, and Yu. Sedykh, *The high precision X-ray tomograph for quality control of the ATLAS MDT muon spectrometer*, 1997. <https://cds.cern.ch/record/335977>. Cited on page 57.
- [123] ATLAS Collaboration, *ATLAS Level-1 Trigger: Technical Design Report*, 1998. <https://cds.cern.ch/record/381429>. Cited on page 56.
- [124] ATLAS Collaboration, *ATLAS High-Level Trigger, Data-Acquisition and Controls: Technical Design Report*, 2003. <https://cds.cern.ch/record/616089>. Cited on page 56.
- [125] ATLAS Collaboration, *Performance of the ATLAS trigger system in 2015*, *Eur. Phys. J. C* **77** (2017) 317, [arXiv:1611.09661 \[hep-ex\]](https://arxiv.org/abs/1611.09661). Cited on pages 56 and 58.
- [126] ATLAS Collaboration, *Fast TracKer (FTK): Technical Design Report*, Jun, 2013. [http://cds.cern.ch/record/1552953](https://cds.cern.ch/record/1552953). Cited on page 58.
- [127] T. Cornelissen, M. Elsing, I. Gavrilenko, W. Liebig, E. Moyse, and A. Salzburger, *The new ATLAS track reconstruction (NEWT)*, *Journal of Physics: Conference Series* **119** (2008) 032014. Cited on pages 60 and 61.
- [128] ATLAS Collaboration, *Performance of the ATLAS track reconstruction algorithms in dense environments in LHC Run 2*, *Eur. Phys. J. C* **77** (2017) 673, [arXiv:1704.07983 \[hep-ex\]](https://arxiv.org/abs/1704.07983). Cited on page 60.

- [129] ATLAS Collaboration, *Vertex Reconstruction Performance of the ATLAS Detector at $\sqrt{s} = 13$ TeV*, ATL-PHYS-PUB-2015-026, 2015, <https://cds.cern.ch/record/2037717>. Cited on page 61.
- [130] ATLAS Collaboration, S. Boutle et al., *Primary vertex reconstruction at the ATLAS experiment*, *J. Phys. Conf. Ser.* **898** (2017) 042056. Cited on page 61.
- [131] ATLAS Collaboration, A. Salzburger, *The ATLAS Track Extrapolation Package*, ATL-SOFT-PUB-2007-005, ATL-COM-SOFT-2007-010, Jun, 2007, <https://cds.cern.ch/record/1038100>. Cited on page 62.
- [132] M. Cacciari, G. P. Salam, and G. Soyez, *The Anti- $k(t)$ Jet Clustering Algorithm*, *JHEP* **04** (2008) 063, [arXiv:0802.1189 \[hep-ph\]](https://arxiv.org/abs/0802.1189). Cited on pages 62 and 64.
- [133] D. Krohn, J. Thaler, and L.-T. Wang, *Jet Trimming*, *JHEP* **02** (2010) 084, [arXiv:0912.1342 \[hep-ph\]](https://arxiv.org/abs/0912.1342). Cited on page 63.
- [134] S. D. Ellis and D. E. Soper, *Successive combination jet algorithm for hadron collisions*, *Phys. Rev.* **D48** (1993) 3160–3166, [arXiv:hep-ph/9305266 \[hep-ph\]](https://arxiv.org/abs/hep-ph/9305266). Cited on page 63.
- [135] ATLAS Collaboration, *Jet mass reconstruction with the ATLAS Detector in early Run 2 data*, ATLAS-CONF-2016-035, 2016, <https://cds.cern.ch/record/2200211>. Cited on page 63.
- [136] B. Nachman, P. Nef, A. Schwartzman, M. Swiatlowski, and C. Wanotayaroj, *Jets from Jets: Re-clustering as a tool for large radius jet reconstruction and grooming at the LHC*, *JHEP* **02** (2015) 075, [arXiv:1407.2922 \[hep-ph\]](https://arxiv.org/abs/1407.2922). Cited on page 64.
- [137] ATLAS Collaboration, *Expected performance of the ATLAS b-tagging algorithms in Run-2*, ATL-PHYS-PUB-2015-022, 2015, <https://cds.cern.ch/record/2037697>. Cited on page 65.
- [138] ATLAS Collaboration, *Optimisation of the ATLAS b-tagging performance for the 2016 LHC Run*, ATL-PHYS-PUB-2016-012, 2016, <https://cds.cern.ch/record/2160731>. Cited on pages 65, 66, 67, and 106.
- [139] ATLAS Collaboration, *Optimisation and performance studies of the ATLAS b-tagging algorithms for the 2017-18 LHC run*, ATL-PHYS-PUB-2017-013, 2017, <https://cds.cern.ch/record/2273281>. Cited on pages 65, 66, and 106.

- [140] ATLAS Collaboration, *E_T^{miss} performance in the ATLAS detector using 2015–2016 LHC pp collisions*, ATLAS-CONF-2018-023, 2018, <https://cds.cern.ch/record/2625233>. Cited on page 68.
- [141] ATLAS Collaboration, *Performance of missing transverse momentum reconstruction with the ATLAS detector in the first proton–proton collisions at $\sqrt{s} = 13$ TeV*, ATL-PHYS-PUB-2015-027, 2015, <https://cds.cern.ch/record/2037904>. Cited on page 68.
- [142] ATLAS Collaboration, *Expected performance of missing transverse momentum reconstruction for the ATLAS detector at $\sqrt{s} = 13$ TeV*, ATL-PHYS-PUB-2015-023, 2015, <https://cds.cern.ch/record/2037700>. Cited on page 68.
- [143] ATLAS Collaboration, *Jet energy scale measurements and their systematic uncertainties in proton–proton collisions at $\sqrt{s} = 13$ TeV with the ATLAS detector*, Phys. Rev. D **96** (2017) 072002, [arXiv:1703.09665 \[hep-ex\]](https://arxiv.org/abs/1703.09665). Cited on pages 68, 69, 71, 72, and 106.
- [144] M. Cacciari and G. P. Salam, *Pileup subtraction using jet areas*, Physics Letters B **659** (2008) 119 – 126, [arXiv:0707.1378 \[hep-ph\]](https://arxiv.org/abs/0707.1378). Cited on page 68.
- [145] ATLAS Collaboration, *Jet energy measurement with the ATLAS detector in proton–proton collisions at $\sqrt{s} = 7$ TeV*, Eur. Phys. J. C **73** (2013) 2304, [arXiv:1112.6426 \[hep-ex\]](https://arxiv.org/abs/1112.6426). Cited on page 69.
- [146] ATLAS Collaboration, *A method for the construction of strongly reduced representations of ATLAS experimental uncertainties and the application thereof to the jet energy scale*, ATL-PHYS-PUB-2015-014, 2015, <https://cds.cern.ch/record/2037436>. Cited on page 71.
- [147] ATLAS Collaboration, *Jet energy resolution in 2017 data and simulation*, Public Results, Sept, 2018. <https://atlas.web.cern.ch/Atlas/GROUPS/PHYSICS/PLOTS/JETM-2018-005/>. Cited on page 73.
- [148] T. Hastie, R. Tibshirani, and J. H. Friedman, *The Elements of Statistical Learning: Data Mining, Inference, and Prediction, 2nd Edition*. Springer, 2009. <http://www.worldcat.org/oclc/300478243>. Cited on page 74.
- [149] L. Breiman, J. H. Friedman, R. A. Olshen, and C. J. Stone, *Classification and Regression Trees*. Wadsworth, Monterey, CA, 1984. <https://cds.cern.ch/record/2253780>. Cited on pages 74 and 77.

- [150] Y. Freund and R. E. Schapire, *A Decision-Theoretic Generalization of On-Line Learning and an Application to Boosting*, *Journal of Computer and System Sciences* **55** (1997) 119 – 139. Cited on page 75.
- [151] J. Friedman, T. Hastie, and R. Tibshirani, *Additive Logistic Regression: A statistical view of boosting (With discussion and a rejoinder by the authors)*, *The Annals of Statistics* **28** (2000) 337–407. Cited on page 75.
- [152] T. Chen and C. Guestrin, *XGBoost: A Scalable Tree Boosting System*, CoRR [abs/1603.02754](#) (2016), [arXiv:1603.02754 \[cs.LG\]](#). Cited on pages 75, 77, and 93.
- [153] J. H. Friedman, *Greedy Function Approximation: A Gradient Boosting Machine*, *The Annals of Statistics* **29** (2001) 1189–1232, <http://www.jstor.org/stable/2699986>. Cited on page 76.
- [154] J. H. Friedman, *Stochastic Gradient Boosting*, *Computational Statistics & Data Analysis* **38** (2002) 367 – 378, Nonlinear Methods and Data Mining. Cited on page 76.
- [155] G. Ke, Q. Meng, T. Finley, T. Wang, W. Chen, W. Ma, Q. Ye, and T.-Y. Liu, *LightGBM: A Highly Efficient Gradient Boosting Decision Tree*, Advances in Neural Information Processing Systems 30, 2017. <http://papers.nips.cc/paper/6907-lightgbm-a-highly-efficient-gradient-boosting-decision-tree.pdf>. Cited on page 77.
- [156] A. V. Dorogush, V. Ershov, and A. Gulin, *CatBoost: Gradient Boosting with Categorical Features Support*, CoRR [abs/1810.11363](#) (2018), [arXiv:1810.11363 \[cs.LG\]](#). Cited on page 77.
- [157] A. Hoecker et al., *TMVA - Toolkit for Multivariate Data Analysis*, 2007, [arXiv:physics/0703039 \[physics.data-an\]](#). Cited on page 77.
- [158] C. Adam-Boudarios, G. Cowan, C. Germain, I. Guyon, B. Kégl, and D. Rousseau, *The Higgs Boson Machine Learning Challenge*, Proceedings of the NIPS 2014 Workshop on High-Energy Physics and Machine Learning, Dec, 2015. <http://proceedings.mlr.press/v42/cowa14.html>. Cited on page 77.
- [159] G. Cowan and E. Gross, *Discovery significance with statistical uncertainty in the background estimate*, ATLAS Statistics Forum (2008), <https://www.pp.rhul.ac.uk/~cowan/stat/notes/SigCalcNote.pdf>. Cited on page 78.

- [160] R. Brun and F. Rademakers, *ROOT: An object oriented data analysis framework*, Nucl. Instrum. Meth. **A389** (1997) 81–86. Cited on pages 79 and 81.
- [161] E. Jones, T. Oliphant, P. Peterson, et al., *SciPy: Open source scientific tools for Python*, 2001–. <http://www.scipy.org/>. Cited on page 79.
- [162] R. D. Cousins, J. T. Linnemann, and J. Tucker, *Evaluation of three methods for calculating statistical significance when incorporating a systematic uncertainty into a test of the background-only hypothesis for a Poisson process*, arXiv:physics/0702156 [physics.data-an]. Cited on page 79.
- [163] D. J. Hand and R. J. Till, *A Simple Generalisation of the Area Under the ROC Curve for Multiple Class Classification Problems*, Machine Learning **45** (2001) 171–186. Cited on page 79.
- [164] M. Baak, G. J. Besjes, D. Côte, A. Koutsman, J. Lorenz, and D. Short, *HistFitter software framework for statistical data analysis*, Eur. Phys. J. **C75** (2015) 153, arXiv:1410.1280 [hep-ex]. Cited on pages 81 and 83.
- [165] ROOT Collaboration, K. Cranmer, G. Lewis, L. Moneta, A. Shibata, and W. Verkerke, *HistFactory: A tool for creating statistical models for use with RooFit and RooStats*, Jan, 2012. <http://cds.cern.ch/record/1456844>. Cited on page 81.
- [166] L. Moneta, K. Belasco, K. S. Cranmer, S. Kreiss, A. Lazzaro, D. Piparo, G. Schott, W. Verkerke, and M. Wolf, *The RooStats Project*, PoS **ACAT2010** (2010) 057, arXiv:1009.1003 [physics.data-an]. Cited on page 81.
- [167] W. Verkerke and D. P. Kirkby, *The RooFit toolkit for data modeling*, eConf (2005), arXiv:physics/0306116 [physics.data-an], Statistical Problems in Particle Physics, Astrophysics and Cosmology (PHYSTAT 05): Proceedings, Oxford, UK. Cited on page 81.
- [168] G. Cowan, K. Cranmer, E. Gross, and O. Vitells, *Asymptotic formulae for likelihood-based tests of new physics*, Eur. Phys. J. **C71** (2011) 1554, arXiv:1007.1727 [physics.data-an], [Erratum: Eur. Phys. J.C73,2501(2013)]. Cited on pages 83, 84, and 85.
- [169] G. Ranucci, *The profile likelihood ratio and the look elsewhere effect in high energy physics*, Nucl. Instrum. Meth. **A661** (2012) 77–85, arXiv:1201.4604 [physics.data-an]. Cited on pages 83 and 182.

- [170] J. Neyman and E. S. Pearson, *On the Problem of the Most Efficient Tests of Statistical Hypotheses*, Philosophical Transactions of the Royal Society of London Series A **231** (1933) 289–337. Cited on page 84.
- [171] S. S. Wilks, *The Large-Sample Distribution of the Likelihood Ratio for Testing Composite Hypotheses*, Annals Math. Statist. **9** (1938) 60–62. Cited on page 85.
- [172] A. L. Read, *Presentation of search results: The $CL(s)$ technique*, J. Phys. **G28** (2002) 2693–2704. Cited on page 85.
- [173] ATLAS Collaboration, *Search for strong production of supersymmetric particles in final states with missing transverse momentum and at least three b -jets at $\sqrt{s} = 8$ TeV proton–proton collisions with the ATLAS detector*, JHEP **10** (2014) 024, [arXiv:1407.0600 \[hep-ex\]](#). Cited on page 86.
- [174] S. Alioli, P. Nason, C. Oleari, and E. Re, *A general framework for implementing NLO calculations in shower Monte Carlo programs: The POWHEG BOX*, JHEP **06** (2010) 043, [arXiv:1002.2581 \[hep-ph\]](#). Cited on page 87.
- [175] NNPDF Collaboration, R. D. Ball et al., *Parton distributions for the LHC Run II*, JHEP **04** (2015) 040, [arXiv:1410.8849 \[hep-ph\]](#). Cited on page 87.
- [176] C. Borschensky et al., *Squark and gluino production cross sections in pp collisions at $\sqrt{s} = 13, 14, 33$ and 100 TeV*, Eur. Phys. J. C **74** (2014) 3174, [arXiv:1407.5066 \[hep-ph\]](#). Cited on pages 87, 88, and 107.
- [177] W. Beenakker, R. Hopker, M. Spira, and P. Zerwas, *Squark and gluino production at hadron colliders*, Nucl. Phys. B **492** (1997) 51, [arXiv:hep-ph/9610490 \[hep-ph\]](#). Cited on page 88.
- [178] A. Kulesza and L. Motyka, *Threshold resummation for squark-antisquark and gluino-pair production at the LHC*, Phys. Rev. Lett. **102** (2009) 111802, [arXiv:0807.2405 \[hep-ph\]](#). Cited on page 88.
- [179] A. Kulesza and L. Motyka, *Soft gluon resummation for the production of gluino-gluino and squark-antisquark pairs at the LHC*, Phys. Rev. D **80** (2009) 095004, [arXiv:0905.4749 \[hep-ph\]](#). Cited on page 88.
- [180] W. Beenakker, S. Brensing, M. Kramer, A. Kulesza, E. Laenen, et al., *Soft-gluon resummation for squark and gluino hadroproduction*, JHEP **12** (2009) 041, [arXiv:0909.4418 \[hep-ph\]](#). Cited on page 88.

- [181] W. Beenakker et al., *Squark and gluino hadroproduction*, *Int. J. Mod. Phys. A* **26** (2011) 2637, [arXiv:1105.1110 \[hep-ph\]](https://arxiv.org/abs/1105.1110). Cited on page 88.
- [182] M. Czakon and A. Mitov, *Top++: A Program for the Calculation of the Top-Pair Cross-Section at Hadron Colliders*, *Comput. Phys. Commun.* **185** (2014) 2930, [arXiv:1112.5675 \[hep-ph\]](https://arxiv.org/abs/1112.5675). Cited on page 88.
- [183] N. Kidonakis, *Next-to-next-to-leading-order collinear and soft gluon corrections for t-channel single top quark production*, *Phys. Rev. D* **83** (2011) 091503, [arXiv:1103.2792 \[hep-ph\]](https://arxiv.org/abs/1103.2792). Cited on page 88.
- [184] N. Kidonakis, *Two-loop soft anomalous dimensions for single top quark associated production with a W^- or H^-* , *Phys. Rev. D* **82** (2010) 054018, [arXiv:1005.4451 \[hep-ph\]](https://arxiv.org/abs/1005.4451). Cited on page 88.
- [185] N. Kidonakis, *NNLL resummation for s-channel single top quark production*, *Phys. Rev. D* **81** (2010) 054028, [arXiv:1001.5034 \[hep-ph\]](https://arxiv.org/abs/1001.5034). Cited on page 88.
- [186] J. Alwall et al., *The automated computation of tree-level and next-to-leading order differential cross sections, and their matching to parton shower simulations*, *JHEP* **07** (2014) 079, [arXiv:1405.0301 \[hep-ph\]](https://arxiv.org/abs/1405.0301). Cited on page 88.
- [187] LHC Higgs Cross Section Working Group Collaboration, J. R. Andersen et al., *Handbook of LHC Higgs Cross Sections: 3. Higgs Properties*, Cern-2013-004, 10.5170/cern-2013-004, 2013, [arXiv:1307.1347 \[hep-ph\]](https://arxiv.org/abs/1307.1347). Cited on page 88.
- [188] S. Höche, F. Krauss, M. Schönherr, and F. Siegert, *QCD matrix elements + parton showers: The NLO case*, *JHEP* **04** (2013) 027, [arXiv:1207.5030 \[hep-ph\]](https://arxiv.org/abs/1207.5030). Cited on page 88.
- [189] S. Catani, L. Cieri, G. Ferrera, D. de Florian, and M. Grazzini, *Vector boson production at hadron colliders: A fully exclusive QCD calculation at NNLO*, *Phys. Rev. Lett.* **103** (2009) 082001, [arXiv:0903.2120 \[hep-ph\]](https://arxiv.org/abs/0903.2120). Cited on page 88.
- [190] ATLAS Collaboration, *Electron efficiency measurements with the ATLAS detector using the 2015 LHC proton–proton collision data*, ATLAS-CONF-2016-024, 2016, <https://cds.cern.ch/record/2157687>. Cited on page 87.

- [191] ATLAS Collaboration, *Muon reconstruction performance of the ATLAS detector in proton–proton collision data at $\sqrt{s} = 13$ TeV*, *Eur. Phys. J. C* **76** (2016) 292, [arXiv:1603.05598 \[hep-ex\]](https://arxiv.org/abs/1603.05598). Cited on page 88.
- [192] ATLAS Collaboration, *Selection of jets produced in 13 TeV proton–proton collisions with the ATLAS detector*, ATLAS-CONF-2015-029, 2015, <https://cds.cern.ch/record/2037702>. Cited on pages 88 and 188.
- [193] ATLAS Collaboration, *Performance of pile-up mitigation techniques for jets in pp collisions at $\sqrt{s} = 8$ TeV using the ATLAS detector*, *Eur. Phys. J. C* **76** (2016) 581, [arXiv:1510.03823 \[hep-ex\]](https://arxiv.org/abs/1510.03823). Cited on page 88.
- [194] Scikit-HEP, *uproot*, 2016–. <https://github.com/scikit-hep/uproot>. Cited on page 93.
- [195] W. McKinney, *Data Structures for Statistical Computing in Python*, in *Proceedings of the 9th Python in Science Conference*. 2010. <https://pandas.pydata.org/>. Cited on page 93.
- [196] T. Oliphant, *NumPy: A guide to NumPy*, USA: Trelgol Publishing, 2006–. <http://www.numpy.org/>. Cited on page 93.
- [197] P. Baldi, K. Cranmer, T. Faucett, P. Sadowski, and D. Whiteson, *Parameterized neural networks for high-energy physics*, *The European Physical Journal C* **76** (2016) 235. Cited on page 93.
- [198] E. Brochu, V. M. Cora, and N. de Freitas, *A Tutorial on Bayesian Optimization of Expensive Cost Functions, with Application to Active User Modeling and Hierarchical Reinforcement Learning*, CoRR (2010), [arXiv:1012.2599 \[cs.LG\]](https://arxiv.org/abs/1012.2599). Cited on page 96.
- [199] Z. Wang, F. Hutter, M. Zoghi, D. Matheson, and N. de Freitas, *Bayesian Optimization in a Billion Dimensions via Random Embeddings*, *J. Artif. Int. Res.* **55** (2016) 361–387, [arXiv:1301.1942 \[stat.ML\]](https://arxiv.org/abs/1301.1942). Cited on page 96.
- [200] T. Head et al., *Scikit-Optimize v0.5.2*, Mar, 2018. <https://doi.org/10.5281/zenodo.1207017>. Cited on page 96.
- [201] M. Borisov, *Lecture. Black-Box Optimization: Bayesian Optimization, Variational Optimization*, Fourth Machine Learning in High Energy Physics Summer School, August, 2018. <https://github.com/yandexdataschool/mlhep2018/blob/master/day4-Fri/Black-Box.pdf>. Cited on page 96.

- [202] F. Hutter, H. H. Hoos, and K. Leyton-Brown, *Sequential Model-Based Optimization for General Algorithm Configuration*, 2011.
<http://www.cs.ubc.ca/~hutter/papers/10-TR-SMAC.pdf>. Cited on page 96.
- [203] F. Hutter, H. Hoos, and K. Leyton-Brown, *An Efficient Approach for Assessing Hyperparameter Importance*, Proceedings of the 31st International Conference on Machine Learning – Volume 32, 2014.
<http://proceedings.mlr.press/v32/hutter14.pdf>. Cited on page 96.
- [204] A. A. Hagberg, D. A. Schult, and P. J. Swart, *Exploring network structure, dynamics, and function using NetworkX*, in *Proceedings of the 7th Python in Science Conference (SciPy2008)*.
<http://math.lanl.gov/~hagberg/Papers/hagberg-2008-exploring.pdf>. Cited on page 98.
- [205] V. D. Blondel, J.-L. Guillaume, R. Lambiotte, and E. Lefebvre, *Fast unfolding of communities in large networks*, Journal of Statistical Mechanics: Theory and Experiment **2008** (2008) P10008,
<http://stacks.iop.org/1742-5468/2008/i=10/a=P10008>. Cited on page 98.
- [206] T. Aynaud, *python-louvain, Louvain Community Detection*, 2011–.
<https://github.com/taynaud/python-louvain>. Cited on page 98.
- [207] ATLAS Collaboration, *Search for top squark pair production in final states with one isolated lepton, jets, and missing transverse momentum using 36 fb^{-1} of $\sqrt{s} = 13 \text{ TeV}$ pp collision data with the ATLAS detector*, ATLAS-CONF-2017-037, 2017, <https://cds.cern.ch/record/2266170>. Cited on page 102.
- [208] ATLAS Collaboration, *Tagging and suppression of pileup jets with the ATLAS detector*, ATLAS-CONF-2014-018, 2014,
<https://cds.cern.ch/record/1700870>. Cited on pages 106 and 190.
- [209] ATLAS Collaboration, *Luminosity determination in pp collisions at $\sqrt{s} = 8 \text{ TeV}$ using the ATLAS detector at the LHC*, *Eur. Phys. J. C* **76** (2016) 653, [arXiv:1608.03953 \[hep-ex\]](https://arxiv.org/abs/1608.03953). Cited on page 106.
- [210] P. Z. Skands, *Tuning Monte Carlo Generators: The Perugia Tunes*, *Phys. Rev. D* **82** (2010) 074018, [arXiv:1005.3457 \[hep-ph\]](https://arxiv.org/abs/1005.3457). Cited on page 106.

- [211] P. Kant, O. M. Kind, T. Kintscher, T. Lohse, T. Martini, S. Mölbitz, P. Rieck, and P. Uwer, *Hathor for single top-quark production: Updated predictions and uncertainty estimates for single top-quark production in hadronic collisions*, *Comput. Phys. Commun.* **191** (2015) 74–89, [arXiv:1406.4403 \[hep-ph\]](https://arxiv.org/abs/1406.4403). Cited on page 107.
- [212] A. Shibata and B. Clement, *Tagging Rate Function B-Tagging*, Jun, 2007. <http://cds.cern.ch/record/1042972>. Cited on page 107.
- [213] L. Demortier, *P Values and Nuisance Parameters*, Statistical issues for LHC physics. Proceedings, Workshop, PHYSTAT-LHC, Geneva, Switzerland, June 27-29, 2007. <https://cds.cern.ch/record/1099967>. Cited on page 182.
- [214] L. Lyons, *Open Statistical Issues in Particle Physics*, *Ann. Appl. Stat.* **2** (2008) 887–915, [arXiv:0811.1663 \[stat.AP\]](https://arxiv.org/abs/0811.1663). Cited on page 182.
- [215] E. Gross and O. Vitells, *Trial factors for the look elsewhere effect in high energy physics*, *The European Physical Journal C* **70** (2010) 525–530, [arXiv:1005.1891 \[physics.data-an\]](https://arxiv.org/abs/1005.1891). Cited on page 182.
- [216] ATLAS Collaboration, *Search for diboson resonances with boson-tagged jets in pp collisions at $\sqrt{s} = 13$ TeV with the ATLAS detector*, *Phys. Lett. B* **777** (2018) 91, [arXiv:1708.04445 \[hep-ex\]](https://arxiv.org/abs/1708.04445). Cited on page 182.
- [217] ATLAS Collaboration, *In-situ measurements of the ATLAS large-radius jet response in 13 TeV pp collisions*, ATLAS-CONF-2017-063, 2017, <https://cds.cern.ch/record/2275655>. Cited on page 186.
- [218] ATLAS Collaboration, M. Aaboud et al., *In situ calibration of large-radius jet energy and mass in 13 TeV proton–proton collisions with the ATLAS detector*, *The European Physical Journal C* **79** (2019) 135, [arXiv:1807.09477 \[hep-ex\]](https://arxiv.org/abs/1807.09477). Cited on pages 186, 193, 194, and 195.
- [219] ATLAS Collaboration, M. Epland, *Large- R γ +Jet In Situ Calibration*, BOOST Conference, Paris, Jul, 2018. <https://cds.cern.ch/record/2632438>. Cited on page 186.
- [220] ATLAS Collaboration, *Determination of the jet energy scale and resolution at ATLAS using Z/γ -jet events in data at $\sqrt{s} = 8$ TeV*, ATLAS-CONF-2015-057, 2015, <https://cds.cern.ch/record/2059846>. Cited on page 188.
- [221] ATLAS Collaboration, *Photon identification in 2015 ATLAS data*, ATL-PHYS-PUB-2016-014, 2016, <https://cds.cern.ch/record/2203125>. Cited on page 188.

- [222] ATLAS Collaboration, *Measurement of the photon identification efficiencies with the ATLAS detector using LHC Run-1 data*, *Eur. Phys. J. C* **76** (2016) 666, [arXiv:1606.01813 \[hep-ex\]](https://arxiv.org/abs/1606.01813). Cited on page 188.
- [223] ATLAS Collaboration, *Measurement of the inclusive isolated prompt photon cross section in pp collisions at $\sqrt{s} = 7$ TeV with the ATLAS detector*, *Phys. Rev. D* **83** (2011) 052005, [arXiv:1012.4389 \[hep-ex\]](https://arxiv.org/abs/1012.4389). Cited on page 189.
- [224] ATLAS Collaboration, *Measurement of the cross section for inclusive isolated-photon production in pp collisions at $\sqrt{s} = 13$ TeV using the ATLAS detector*, *Phys. Lett. B* **770** (2017) 473, [arXiv:1701.06882 \[hep-ex\]](https://arxiv.org/abs/1701.06882). Cited on page 189.
- [225] ATLAS Collaboration, *In situ calibration of large-radius jet energy and mass in 13 TeV proton–proton collisions with the ATLAS detector — Auxiliary Material*, July, 2018. <https://atlas.web.cern.ch/Atlas/GROUPS/PHYSICS/PAPERS/JETM-2018-02>. Cited on page 191.
- [226] ATLAS Collaboration, *Electron and photon energy calibration with the ATLAS detector using data collected in 2015 at $\sqrt{s} = 13$ TeV*, ATL-PHYS-PUB-2016-015, 2016, <https://cds.cern.ch/record/2203514>. Cited on page 190.
- [227] ATLAS Collaboration, *Electron and photon energy calibration with the ATLAS detector using LHC Run 1 data*, *Eur. Phys. J. C* **74** (2014) 3071, [arXiv:1407.5063 \[hep-ex\]](https://arxiv.org/abs/1407.5063). Cited on page 190.

Biography

Matthew Epland attended the University of Minnesota, Twin Cities where he earned a B.S. in physics *summa cum laude* and B.S. in mathematics in 2014. He completed his Ph.D. studies in experimental particle physics at Duke University in 2019. As an incoming graduate student at Duke he was supported by the Goshaw Family Fellowship.